ISSN 1345-1065

Advances in Polar Upper Atmosphere Research

No. 19

August 2005

National Institute of Polar Research

Tokyo

This document is provided by JAXA.

In the past the proceedings of symposia sponsored by the National Institute of Polar Research have been published as "Memoirs of National Institute of Polar Research, Special Issue".

Since 1987, new series of "Proceedings of the NIPR Symposium" for each discipline have been published as follows:

Proceedings of the NIPR Symposium on Upper Atmosphere Physics
Proceedings of the NIPR Symposium on Polar Meteorology and Glaciology
Proceedings of the NIPR Symposium on Antarctic Geosciences
Proceedings of the NIPR Symposium on Antarctic Meteorites
Proceedings of the NIPR Symposium on Polar Biology

Since 1999, "Proceedings of the NIPR Symposium on Upper Atmosphere Physics" has been renamed to:

"*Advances in Polar Upper Atmosphere Research*"

Editorial Board
Editor-in-Chief: Masaki Ejiri, *National Institute of Polar Research, Research Organization of Information and Systems (NIPR, ROIS)*
Editors: Mitsuo Fukuchi, *NIPR, ROIS*
Hideo Ishizuka, *Kochi University*
Hideyasu Kojima, *NIPR, ROIS*
Satoru Kojima, *Tokyo Woman's Christian University*
Kouichi Nishimura, *National Research Institute for Earth Science and Disaster Prevention*
Takayuki Ono, *Tohoku University*
Kazuo Shibuya, *NIPR, ROIS*
Masashi Takada, *Nara Women's University*
Takashi Yamanouchi, *NIPR, ROIS*

This document is provided by JAXA.

Foreword

This volume 19 is the seventh volume of the "Advances in Polar Upper Atmosphere Research (APUAR)" which succeeded the "Proceedings of the NIPR Symposium on Upper Atmosphere Physics" in 1999 and includes papers presented at or related to "The Twenty-eighth Symposium on Space and Upper Atmospheric Sciences in the Polar Regions" held at the National Institute of Polar Research (NIPR) in summer 2004. The annual Symposium is devoted to discuss significant scientific results of studies on the upper atmosphere, including the ionosphere and the magnetosphere in the polar regions. The journal extensively accepts contributed papers which do mark the advance of research works on the polar upper atmospheric sciences in recent years.

The present volume contains 12 refereed scientific papers, research notes, review and report. We sincerely hope that this will be valuable to those who are interested in the polar upper atmospheric sciences and to those who are engaged in Arctic and Antarctic research activities.

Editorial Board of APUAR
Editor-in-Chief: Akira Kadokura
Editors: Takayuki Ono
Takehiko Aso
Tadahiko Ogawa
Natsuo Sato
Hisao Yamagishi
Kazuo Makita
Hiroshi Miyaoka
Yasuhiro Murayama
Makoto Taguchi
Editorial Secretary:
Nobuko Takahama

This document is provided by JAXA.

This document is provided by JAXA.

Advances in Polar Upper Atmosphere Research

No. 19

CONTENTS

Boundary between the near-Earth ($< 10 R_E$) plasma sheet and outer plasma sheet: Equatorial observations at 9–15 R_E by Geotail
..... *Hisato Shirai, Tomoaki Hori and Toshifumi Mukai*... 1

Seasonal and solar cycle dependences of the correlation between auroral kilometric radiation and the AE index
..... *Atsushi Kumamoto, Takayuki Ono and Masahide Iizima*... 10

Extreme magnetic field variations during the October 2003 superstorm
..... *Tohru Sakurai and Yutaka Tonegawa*... 21

Subionospheric LF monitoring of ionospheric perturbations prior to the Tokachi-oki earthquake and a possible mechanism of lithosphere-ionosphere coupling
..... *Masashi Hayakawa, Alexandre V. Shvets and Shinko Maekawa*... 42

Model calculations of possible ionospheric backscatter echo area for a mid-latitude HF radar
..... *Nozomu Nishitani and Tadahiko Ogawa*... 55

Research notes

Relationship between thermospheric vertical wind and the location of ionospheric current in the polar region
..... *Mamoru Ishii*... 63

High-resolution simulation of propagation of interplanetary shock wave caused by a coronal mass ejection observed on November 13, 2003
..... *Tomoya Ogawa, Mitsue Den, Takashi Tanaka, and Kazuyuki Yamashita*... 71

Plasma flow characteristics in converging field line geometry in anisotropic plasmas
..... *Osuke Saka*... 80

The effect of magnetic mirror force on the field-aligned acceleration of plasmas
..... *Osuke Saka, Shigeru Fujita and Daniel N. Baker*... 84

This document is provided by JAXA.

VHF data transmission experiments using MBC equipment conducted during the period from JARE-43 to JARE-45
..... *Kaiji Mukumoto, Akira Fukuda, Masashi Nagasawa, Yasuaki Yoshihiro, Kei Nakano, Satoshi Ohichi, Hisao Yamagishi, Natsuo Sato, Akira Kadokura, Huigen Yang, Ming Wu Yao, Sen Zhang, Guojing He and Li-Jun Jin* ... 89

Review
Inner magnetospheric plasma interactions and coupling with the ionosphere
..... *Mei-Ching Fok, Yusuke Ebihara and Thomas E. Moore* ... 106

Report
Development of the Virtual Earth's Magnetosphere System (VEMS)
..... *Ken T. Murata, Kazunori Yamamoto, Daisuke Matsuoka, Eizen Kimura, Hiroshi Matsumoto, Masaki Okada, Toshifumi Mukai, Jhon B. Sigwarth, Shigeru Fujita, Takashi Tanaka, Kiyohumi Yumoto, Tatsuki Ogino, Kazuo Shiokawa, Nikolai A. Tsyganenko, James L. Green and Tsugunobu Nagai* ... 135

Note to contributors 152
Author index 154

This document is provided by JAXA.

Adv. Polar Upper Atmos. Res., 19, 1-9, 2005
© 2005 National Institute of Polar Research

Boundary between the near-Earth ($<10R_E$) plasma sheet and outer plasma sheet: Equatorial observations at 9–15 R_E by Geotail

Hisato Shirai[1]*, Tomoaki Hori[2] and Toshifumi Mukai[3]

[1]*Ichinoseki National College of Technology, Hagisyo, Ichinoseki 021-8511*
[2]*National Institute of Information and Communications Technology, Koganei-shi, Tokyo 184-8795*
[3]*Institute of Space and Astronautical Science, Sagamihara-shi 229-8510*
**Corresponding author. E-mail: shirai@ichinoseki.ac.jp*

(Received December 10, 2004; Accepted January 28, 2005)

Abstract: Equatorial observations of a boundary between the near-Earth ($<10R_E$) plasma sheet and outer plasma sheet in the magnetotail are reported in the present paper. Analyzing energy-time spectrograms of low energy particles obtained by the Geotail spacecraft, we find that there often exists a boundary between the near-Earth plasma sheet and the tail plasma sheet. At this boundary, fluctuating particle spectra in the magnetotail change to stable spectra in the near-Earth region and energy flux of particles increases rapidly. Repeated observations of these signatures suggest that there often exists a spatial boundary between the two regions. In the present paper, we call this boundary "near-Earth plasma sheet boundary (NEPS boundary)" and examine it in detail. We show that the NEPS boundary is located usually at distances of around 9–15R_E on the night side near the magnetospheric equator. We also discuss a new method of mapping, in which the NEPS boundary is used as a tracer to map auroral regions to the magnetosphere without using field-line models.

key words: new boundary, plasma sheet, magnetotail

1. Introduction

Recent papers have pointed out importance of the equatorial region of geocentric distances of around 10–15R_E. Shiokawa *et al.* (1998) have analyzed magnetic field and particle data obtained by six satellites at distances between 5R_E and 20R_E. They suggested that braking of earthward plasma flows occurring at the boundary (10–20 R_E) between dipolar and tail-like field may be a key to solving a discrepancy between substorm onset models; for example, there is a discrepancy between the current disruption model (*e.g.*, Lui, 1991) and the neutral line model (*e.g.*, Hones, 1976). The former explains the onset by tail current disruption beginning in the near-Earth region ($<10R_E$), while the latter accounts for the onset by formation of magnetic neutral lines in the magnetotail ($>15R_E$). Delcourt and Belmont (1998) have examined behaviors of ions in the plasma sheet at 8–15R_E by performing numerical calculations of ion trajectories in the magnetotail. The results indicated that ion behaviors near the equator at distances of around 9–10R_E are chaotic, and an intense tail current is generated at this distance. Zelenyi *et al.* (2002) have also examined ion behaviors in

This document is provided by JAXA.

the magnetotail and proposed a model of current sheet evolution. In this model, a thin current sheet is formed in the magnetotail and evolves through a positive feedback process. In this process, the tail current producing the thin current sheet is enhanced by non-adiabatic ion motions, and the rate of non-adiabatic ions increases with decreasing thickness of the tail current sheet.

Analyzing auroral particle data obtained at low altitudes is another method to obtain information on physics in the equatorial region of distances of 10–15R_E. However, comparison of auroral phenomena with magnetospheric phenomena occurring in this region has been difficult for the following reason. We usually utilize field line models like Tsyganenko models (Tsyganenko, 1987, 1989) for mapping of auroral regions to the magnetosphere (*e.g.*, Weiss *et al.*, 1992). In these models, the field configuration changes from dipolar-like to tail-like field at distances of 10–20R_E rapidly and thus the projection on the equatorial region of 10–20R_E highly depends on the field line models. For this reason, it is difficult to map auroral regions to the magnetosphere without ambiguity due to a large dependence on field line models.

As proposed in later sections, we have another method for mapping in which field-line models are not utilized. It is the mapping using boundary signatures based on particle observations. If we know a boundary observed both at low and high altitudes, we can use it as a tracer. A number of particle boundaries have been discovered at auroral altitudes and in the magnetosphere. Although there is a problem of terminology (*i.e.*, the same boundary is occasionally called by different names), we can mention several of the boundaries in the following way; when a satellite surveys auroral regions from high to low latitudes, it will observe (A1) the polar cap boundary at the high-latitude edge of the auroral oval, (A2) the low-latitude boundary between the velocity-dispersed ion signature (*e.g.*, Saito *et al.*, 1992), (A3) the low-latitude boundary of the ion gap (*e.g.*, Bosqued *et al.*, 1993), (A4) the boundary between the discrete and the diffuse aurora, (A5) the isotropy boundary (Sergeev *et al.*, 1993), (A6) the high-latitude boundary of the ion drop-off band (Shirai *et al.*, 1997), (A7) the low-latitude edge of auroral electron precipitation, and (A8) the low-latitude edge of auroral ion precipitation. This summary of low-altitude boundaries is not complete nor generally accepted but is a list of boundaries which we can find in the E-t spectrograms obtained by the Akebono spacecraft on the nightside auroral region. More comprehensive survey of low-altitude boundaries was made by Newell *et al.* (1996) using the DMSP data with quantitative definitions of boundaries.

On the other hand, when a satellite surveys the magnetosphere, it will observe (B1) the boundary between the lobe and the plasma sheet boundary layer (PSBL), (B2) the boundary between the PSBL and the plasma sheet (*e.g.*, Saito *et al.*, 1998), (B6) the outer boundary of the ion drop-off band (Shirai *et al.*, 1994), (B7) the plasmapause, and (B8) the inner boundary of the plasma sheet (*e.g.*, Kerns *et al.*, 1994). The boundaries A1, A2, A6, A7, and A8 detected at auroral altitudes have been interpreted as the ionospheric projection of the boundaries B1, B2 (*e.g.*, Zelenyi *et al.*, 1990), B6 (Shirai *et al.*, 1994; Yermolaev, 2000), B7, and B8 (*e.g.*, Fairfield and Vinas, 1984) in the magnetosphere, respectively. Since these boundaries are observed at both altitudes, we can utilize the boundaries as tracers and compare auroral phenomena with magnetospheric phenomena observed around these boundaries. Although we found

This document is provided by JAXA.

the boundaries B1, B2, B6–B8 corresponding to the auroral boundaries A1, A2, A6–A8, we have not discovered the magnetospheric boundaries corresponding to the auroral boundaries A3, A4, and A5. Since it is difficult to detect the isotropy boundary (*i.e.*, the boundary corresponding to A5) near the magnetospheric equator because of anisotropy in pitch angle distributions of particles decreasing with increasing altitudes, the boundaries we may find in the magnetosphere are the boundaries corresponding to A3 and A4.

In addition to the low-energy particle boundaries, a high-energy (>30 keV) particle boundary has been found recently at low altitudes of 3–4 R_E using the Cluster spacecraft (Sergeev *et al.*, 2003). The Cluster data indicated that there exists a sharp boundary between the inner magnetosphere and active outer plasma sheet. The inner magnetosphere was filled with a larger flux of high-energy (>30 keV) electrons, and the outer region had a lower ion pressure. The boundary was observed at latitudes of 64–65 degrees, which is mapped to the geocentric distance of about 10 R_E near the magnetospheric equator when we utilize the field line model of Tsyganenko 1989. They supposed that the boundary is a short-lived structure as suggested by rare appearance and could be generated by a sudden braking of localized bursty fast flows produced by magnetic reconnection.

In this paper, we report equatorial observations of a boundary between the near-Earth ($<10 R_E$) plasma sheet and outer plasma sheet in the magnetotail by Geotail. We propose to interpret this boundary as the field-aligned projection of the low-latitude boundary of the ion gap, that is, the boundary corresponding to A3 stated above.

2. Observation

The Geotail spacecraft surveyed the distant magnetotail from 1992 to 1994. After that, its apogee distance was lowered to 50 R_E in 1994 and to 30 R_E in 1995. The data analyzed in this paper were obtained in 1995 and later years at geocentric distances of around 9–30 R_E. Energy-time (E-t) spectrograms of 10 eV–40 keV particles were obtained by the LEP instrument (Mukai *et al.*, 1994).

Figure 1 presents an example of near-equatorial observations by Geotail. E-t spectrograms of ions (top) and electrons (bottom) obtained for the interval from 1100 UT to 2100 UT on June 27, 2002 are shown in two panels. For this interval, the geomagnetic condition was quiet ($Kp=0+, 1$) and any substorm activity was not observed. The Geotail spacecraft surveyed the equatorial magnetosphere near the perigee on this day. The trajectory for this interval is plotted on the X_{GSM}-Y_{GSM} plane in Fig. 2. As seen in Fig. 1, the spacecraft was first in the plasma sheet boundary layer (PSBL) or in the lobe (at 1100–1200 UT). The PSBL can be identified by coexistence of velocity-dispersed ion signature in higher-energy range (>1 keV) and a weak flux of cold ions in lower-energy range (<1 keV), which was detected at 1100–1120 UT and 1140–1200 UT. The lobe is characterized by very weak (or no) particle fluxes, which were detected at 1120–1140 UT. After that, the spacecraft observed fluctuating fluxes of ions and electrons until 1830 UT. We can notice that characteristics of particle spectra changed rapidly around 1830 UT. The fluctuation disappeared, and stable particle spectra with intense fluxes appeared around 1830 UT. From the long-term

This document is provided by JAXA.

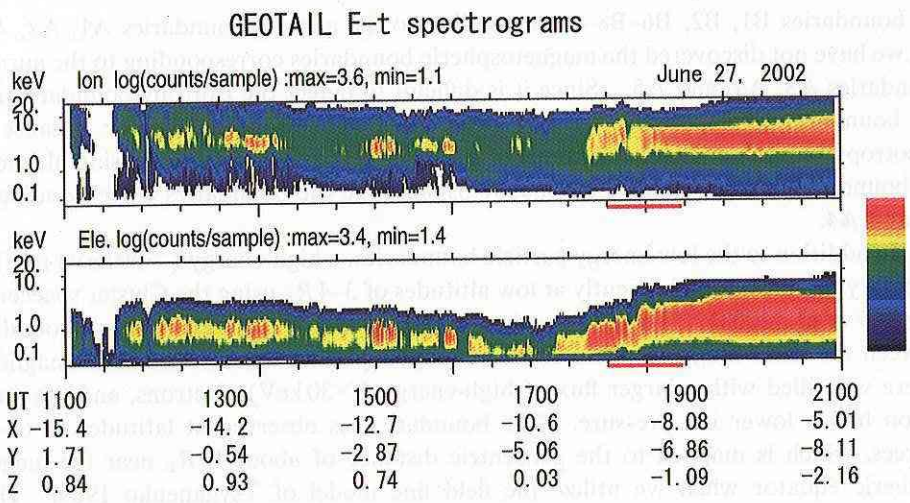


Fig. 1. Geotail observations for the interval of 1100 UT to 2100 UT on June 27, 2002. Energy-time spectrograms of omnidirectional ions (top) and electrons (bottom) show clear changes in particle features between 1800 UT and 1900 UT. A red line below each panel indicates the time interval for which changes are most remarkable.

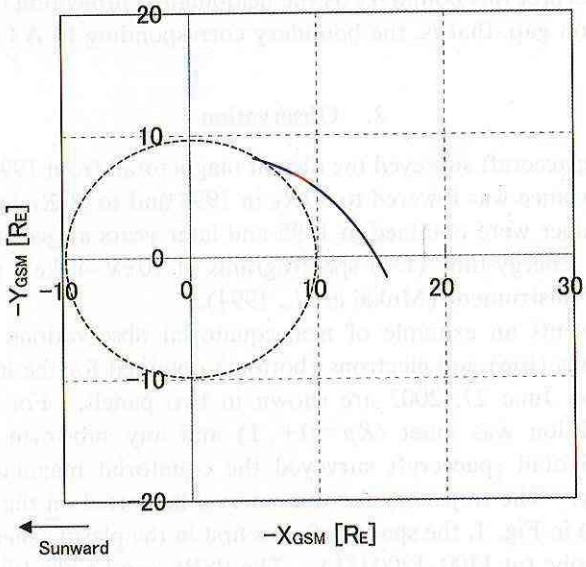


Fig. 2. The Geotail trajectory for the interval of 1100 UT to 2100 UT on June 27, 2002 plotted on the X_{GSM}-Y_{GSM} plane. Geotail crossed the NEPS boundary in the time interval indicated by a red line.

observation performed by Geotail, we have found that this rapid transition is often observed near the perigee of 9–10 R_E. Repeated observations of this signature suggest that there often exists a spatial boundary between the near-Earth plasma sheet and outer

This document is provided by JAXA.

plasma sheet in the magnetotail. We call this boundary "near-Earth plasma sheet (NEPS) boundary" in this paper.

3. Position of the NEPS boundary

In order to examine position of the NEPS boundary, we have analyzed the data obtained in three years of 1995–1997 and found 57 crossings of the NEPS boundary by Geotail. The following procedure was utilized for identification of the NEPS boundary. (1) First, we examined whether or not the spacecraft obtained stable particle spectra near the perigee. Flux variation of particles in the near-Earth ($< 10 R_E$) plasma sheet was often so small that we can separate it from a large flux variation in the outer plasma sheet clearly. (2) After we found stable particle spectra, we checked whether the spacecraft surveyed the outer plasma sheet in the magnetotail after/before the perigee observation. We chose only spectral changes occurring between the near-Earth region and the magnetotail but not changes observed at the dayside magnetopause or at the LLBL. (3) After that, we checked whether the changes took place within one hour or more than two hours. When the change took place within one hour, we regarded it as a boundary. Through this procedure, we have identified 57 examples of the NEPS boundary crossings in three-year data of Geotail. The crossing time is defined as the center of the time interval of 60 min for which spectral change is most remarkable.

Figure 3 shows positions of the 57 crossings of the NEPS boundary plotted on the X_{GSM}-Y_{GSM} plane. As shown in the figure, the NEPS boundary exists usually at 9–15 R_E. It would be noteworthy that the width of the distribution in the radial direction is not very large but narrow especially in the midnight sector. In Fig. 4, the number of

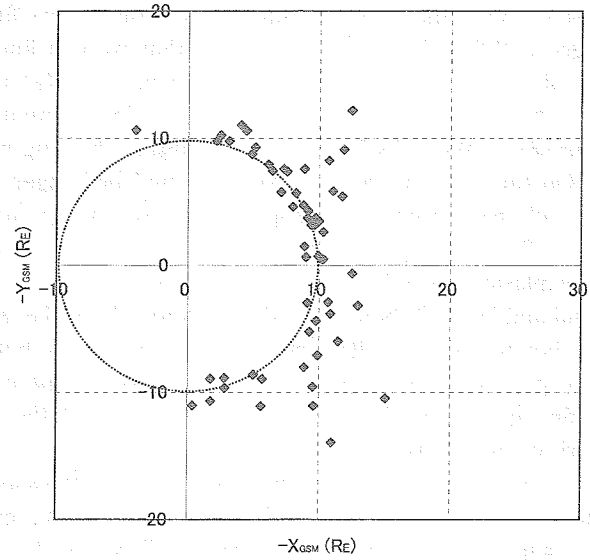


Fig. 3. Position of the NEPS boundary crossings by Geotail. The crossings occurred at distances of 9–15 R_E on the night side.

This document is provided by JAXA.

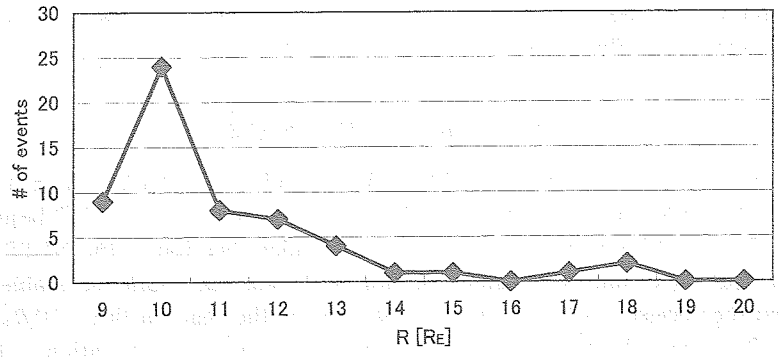


Fig. 4. The distribution of occurrence of the NEPS boundary crossing. The number of occurrence is plotted against the radial distance, $R=(X_{GSM}^2+Y_{GSM}^2)^{1/2}$.

occurrence of the NEPS boundary crossings is plotted against the radial distance from the Earth. The positions are mostly distributed in the width of about $5R_E$ between 9 R_E and $14R_E$. (The earthward termination of the distribution may be attributable to the limit of coverage of the Geotail observations.)

4. Discussion

This paper has reported equatorial observations of the NEPS boundary. The Geotail data have shown that there often exists a spatial boundary between the near-Earth (<9–$15R_E$) plasma sheet and outer plasma sheet in the magnetosphere. Firstly, we discuss influence of temporal variability of the plasma sheet on identification of the NEPS boundary. One may suppose that we can observe very fluctuating spectra even near the perigee ($\sim 9R_E$) during substorms, or that we can find prolonged time periods of stable particle spectra near the Geotail apogee ($\sim 30R_E$) during quiet conditions. In fact, we have found several examples in which fluctuating spectra were observed near the perigee. We classified them as examples showing no crossing of the NEPS boundary. On the other hand, we have not found prolonged (>4 hours) time periods of stable particle spectra near the apogee. This result supports our interpretation that the outer (>9–$15R_E$) plasma sheet is usually variable and is distinguishable from the stable inner plasma sheet.

In order to avoid ambiguity in boundary identification, Newell *et al.* (1996) defined low-altitude particle boundaries quantitatively and investigated the boundary locations. Their study is more precise than previous studies. If we compare our results with theirs, we need to find quantitative criteria for identification of the NEPS boundary. This is a future work of our study.

Secondly, we discuss three boundaries observed at low altitudes as a counterpart of the low-altitude side. One is the low-latitude boundary of the ion gap (*e.g.* Bosqued *et al.*, 1993). The ion gap is a region with very weak ion fluxes in the auroral oval. At the low-latitude boundary of the ion gap, fluctuating particle spectra with very weak fluxes change to stable ones with strong fluxes. The change is very similar to that

This document is provided by JAXA.

occurring at the NEPS boundary. In addition to this similarity, we can point out the following similarity between these boundaries. The low-latitude boundary of the ion gap is observed between the VDIS near the polar cap boundary and the ion drop-off band (IDB) (Shirai *et al.*, 1997). On the other hand, the NEPS boundary is observed between the VDIS in the PSBL and the near-Earth ($<9R_E$) magnetosphere, in which IDBs have been detected by Geotail (Shirai *et al.*, 1994) and by Interball (Yermolaev, 2000). From these similarities, we propose that the NEPS boundary is the magnetospheric projection of the low-latitude boundary of the ion gap observed at auroral altitudes.

Another boundary we discuss here is the boundary between the two regions termed "CPS" and "BPS" by Winningham *et al.* (1975). They analyzed the low-altitude satellites, ISIS-1 and 2, to examine electron precipitation on the night side. The electron precipitation region was divided into two regions. One is a relatively stable electron region at lower latitudes, which they call the central region of the plasma sheet (CPS). The other is a higher latitude region with electron structures changing dynamically in response to substorms, which they call the outer boundary layers of the plasma sheet (BPS). Although there is still a terminological problem on these regions due to ambiguity of their definition, their CPS/BPS boundary is often interpreted as the discrete/diffuse auroral boundary. One may suppose that the discrete/diffuse auroral boundary is the field-aligned projection of the NEPS boundary, since fluctuating electron spectra change to stable ones at this boundary. However, this interpretation is not acceptable because the discrete/diffuse auroral boundary does not coincide with the location at which electron energy flux increases rapidly. The latitude of the former is often lower than that of the latter. In order to reveal the association of the NEPS boundary with the discrete/diffuse auroral boundary, we need more thorough study on low- and high-altitude particle boundaries.

The other low-altitude boundary we discuss is the Energetic Electron Wall (EEW) reported by Sergeev *et al.* (2003). In their paper, the EEW was defined as a sudden increase of energetic (>30 keV) electron fluxes. The thickness of the EEW was estimated to be comparable to the ion gyro-radius of 50 km, which is much smaller than that of the NEPS boundary. This boundary was detected at the latitude of 64–65 degrees, which was expected to be mapped to the distance of about $10R_E$ near the equator using the field line model of Tsyganenko 1989. They also reported that an intense Alfvenic wave activity toward the ionosphere was detected on the outside of the EEW, and a gradual increase in ion pressure was observed at the same time as the EEW crossing. These signatures are similar to those of the NEPS boundary. A difference from the NEPS boundary is its rare appearance. The EEW was interpreted as a short-lived structure that could be generated by a sudden braking and azimuthal deflection of localized bursty fast flows produced by the magnetic reconnection in the near tail. Comparing the EEW and the NEPS boundary, we suppose that the field configuration which changes from dipolar to tail-like rapidly at distances of around 9–$15R_E$ may explain the similar signatures (*i.e.*, a larger fluctuation on the outside and an increase in ion pressure at the boundaries), and substorm activity may account for the difference in the thickness and occurrence frequency. However, we need more detailed analyses of the Geotail and the Cluster data to understand their formation mechanisms.

This document is provided by JAXA.

Finally, we discuss a new method of mapping in which the NEPS boundary and other boundaries are utilized as tracers. As stated in the previous sections, the projection of auroral regions by utilizing field line models highly depends on our choice of models, especially in mapping to the outer ($>10R_E$) equatorial region. Here we propose to use the boundaries observed both at high and low altitudes. The following boundaries can be utilized as tracers; (1) the low-latitude boundary of auroral electron precipitation, which can be mapped to the earthward boundary of plasma sheet electrons and almost corresponds to the plasmapause (4–$6R_E$) (*e.g.*, Fairfield and Vinas, 1984). (2) The high-latitude boundary of the IDB (Shirai *et al.*, 1997) observed at auroral altitudes can be mapped to the outer boundary of the IDB (7–$9R_E$) in the magnetosphere (Shirai *et al.* 1994; Yermolaev, 2000). (3) The VDIS observed near the polar cap boundary has been interpreted as the projection of the VDIS in the PSBL (*e.g.*, Zelenyi *et al.*, 1990). In addition to these boundaries, we can utilize the NEPS boundary as a useful tracer. This boundary would be very helpful for mapping to the outer ($>10R_E$) region, since the method using field line models have a large difficulty especially in mapping to distances larger than about $10R_E$, at which the NEPS boundary is observed. Examining the latitude of the Ion Gap boundary and comparing it with the position of the NEPS boundary to obtain the information on the latitudes mapped to the equatorial region of 9–$15R_E$ are left as future works.

5. Summary

We can summarize this paper in the following way; (1) we have shown that the Geotail spacecraft often observes a boundary between the near-Earth ($<10R_E$) plasma sheet and outer plasma sheet in the magnetotail. Particle spectra have shown a large flux variation and weak intensity of particles in the outer plasma sheet, while they have a small flux variation and strong intensity in the near-Earth region. We call this boundary "the NEPS boundary". (2) The statistics using three-year data of Geotail have shown that the NEPS boundary is usually located around 9–$15R_E$. (3) We have proposed an interpretation that the NEPS boundary is the magnetospheric projection of the low-latitude boundary of the Ion Gap. This interpretation enables us to utilize the NEPS boundary as a helpful tracer for mapping of auroral regions to the outer (>10 R_E) magnetosphere.

Acknowledgments

The work was supported by National Institute of Polar Research. The work was also carried out as a joint research program of the Solar-Terrestrial Environmental Laboratory, Nagoya University, and supported by JSPS Grant-in-Aid for Scientific Research (C) 16540409.

The editor thanks Drs. K. Shiokawa and V.A. Sergeev for their help in evaluating this paper.

This document is provided by JAXA.

References

Bosqued, J.M., Ashour-Abdalla, M., Alaoui, M.E., Zelenyi, L.M. and Berthelier, A. (1993): AUREOL-3 observations of new boundaries in the auroral ion precipitation. Geophys. Res. Lett., **20**, 1203–1206.

Delcourt, D.C. and Belmont, G. (1998): Ion dynamics at the earthward termination of the magnetotail current sheet. J. Geophys. Res., **103**, 4605–4613.

Fairfield, D.H. and Vinas, A.F. (1984): The inner edge of the plasma sheet and the diffuse aurora. J. Geophys. Res., **89**, 841–854.

Hones, E.W., Jr. (1976): The magnetotail: Its generation and dissipation. Physics of Solar Planetary Environments, ed. by D.J. Williams. Washington, D.C., AGU, 559–571.

Kerns, K.J., Hardy, D.A. and Gussenhoven, M.S. (1994): Modeling of convection boundaries seen by CRRES in 120-eV to 28-keV particles. J. Geophys. Res., **99**, 2403–2414.

Lui, A.T.Y. (1991): A synthesis of magnetospheric substorm models. J. Geophys. Res., **96**, 1849–1856.

Mukai, T., Machida, S., Saito, Y., Hirahara, M., Terasawa, T., Kaya, N., Obara, T., Ejiri, M. and Nishida, A. (1994): The Low-Energy Particle (LEP) experiment onboard the GEOTAIL satellite. J. Geomagn. Geoelectr., **46**, 669–692.

Newell, P.T., Feldstein, T.I., Galperin, Y.I. and Meng, C.I. (1996): Morphology of nightside precipitation. J. Geophys. Res., **101**, 10737–10748.

Saito, Y., Mukai, T., Hirahara, M., Machida, S. and Kaya, N. (1992): Distribution function of precipitating ion beams with velocity dispersion observed near the poleward edge of the nightside auroral oval. Geophys. Res. Lett., **19**, 2155–2158.

Saito, Y., Mukai, T. and Teresawa, T. (1998): Kinetic structure of the slow-mode shocks in the Earth's magnetotail. Perspectives on the Earth's magnetotail, ed. by A. Nishida *et al.* Washington, D.C., AGU, 103–115.

Sergeev, V.A., Malkov, M. and Mursula, K. (1993): Testing the isotropic boundary algorithm method to evaluate the magnetic field configuration in the tail. J. Geophys. Res., **98**, 7609–7620.

Sergeev, V.A., Sauvaud, J.-A., Reme, H., Balogh, A., Daly, P., Zong, Q.-G., Angelopoulos, V., Andre, M. and Vaivads, A. (2003): Sharp boundary between the inner magnetosphere and active outer plasma sheet. Geophys. Res. Lett., **30**, 1799–1802.

Shiokawa, K., Baumjohann, W., Haerendel, G., Paschmann, G., Fennel, J.F., Friis-Christensen, E., Luhr, H., Reeves, G.D., Russell, C.T., Sutcliffe, P.R. and Takahashi, K. (1998): High-speed ion flow, substorm current wedge, and multiple Pi 2 pulsations. J. Geophys. Res., **103**, 4491–4507.

Shirai, H., Maezawa, K., Mukai, T. and Kaya, N. (1994): Band-like lack of ions around 10 keV observed by the Akebono and the Geotail satellites. EOS; Trans., **75**, 559.

Shirai, H., Maezawa, K., Fujimoto, M., Mukai, T., Saito, Y. and Kaya, N. (1997): Monoenergetic ion drop-off in the inner magnetosphere. J. Geophys. Res., **102**, 19873–19881.

Tsyganenko, N.A. (1987): Global quantitative models of geomagnetic field in the cislunar magnetosphere for different disturbance levels. Planet. Space Sci., **35**, 1347–1358.

Tsyganenko, N.A. (1989): A magnetospheric magnetic field model with a warped tail current sheet. Planet. Space Sci., **37**, 5–20.

Weiss, L.A., Reiff, P.H., Hilmer, R.V., Winningham, J.D. and Lu, G. (1992): Mapping the auroral oval into the magnetotail using dynamics explorer plasma data. J. Geomagn. Geoelectr., **44**, 1121–1144.

Winningham, J.D., Yasuhara, F., Akasofu, S.-I. and Heikkila, W.J. (1975): The latitudinal morphology of 10-eV to 10-keV electron fluxes during magnetically quiet and disturbed times in the 2100–0300 MLT sector. J. Geophys. Res., **80**, 3148–3171.

Yermolaev, Y.I. (2000): Ion gap locations: INTERBALL/TAIL observations. Proceedings of International Symposium, From solar corona through interplanetary space, into Earth's magnetosphere and ionosphere: Interball, ISTP satellites, and ground based observations, 58–59.

Zelenyi, L.M., Kovrazkhin, R.A. and Bosqued, J.M. (1990): Velocity-dispersed ion beams in the nightside auroral zone: AUREOL 3 observations. J. Geophys. Res., **95**, 12119–12139.

Zelenyi, L.M., Delcourt, D.C., Malova, H.V. and Sharma, A.S. (2002): "Aging" of the magnetotail thin current sheets. Geophys. Res. Lett., **29**, 1608–1611.

This document is provided by JAXA.

Adv. Polar Upper Atmos. Res., 19, 10–20, 2005
© 2005 National Institute of Polar Research

Seasonal and solar cycle dependences of the correlation between auroral kilometric radiation and the AE index

Atsushi Kumamoto[1]*, Takayuki Ono[1] and Masahide Iizima[1]

[1]*Department of Geophysics, Graduate School of Science, Tohoku University, 6-3, Aoba, Aramaki, Aoba, Sendai 980-8578*

**Corresponding author. E-mail: kumamoto@stpp1.geophys.tohoku.ac.jp*

(Received December 19, 2004; Accepted April 29, 2005)

Abstract: Seasonal and solar cycle dependences of the correlation between auroral kilometric radiation (AKR) and the auroral electrojet (AE) index have been investigated based on the plasma wave data obtained by the Akebono satellite. Under any seasonal and solar activity conditions, a clear correlation has been found between the AKR power flux and the AE index. The properties of the correlation, however, vary depending on season and solar activity. AKR power flux increases as about the 1.2 power of AE index in all seasonal and solar activity conditions. However, even for the same AE index, AKR power flux during solar minimum is 5 dB larger than that during solar maximum. As for the seasonal variations, the AKR power flux in winter is 22 dB larger than that in summer even for the same AE index. The results suggest that long-term variations of AKR depend not only on auroral current variations but also on factors associated with the total energy flux of auroral electrons and the generation process of AKR.

key words: auroral kilometric radiation, AE index, seasonal dependence, solar cycle dependence, AKR index

1. Introduction

It is widely known that auroral kilometric radiation (AKR) is closely correlated with auroral phenomena. The coincidence of AKR enhancement and discrete aurora appearance was pointed out by Gurnett (1974). Voots *et al.* (1977) showed close correlation between AKR power flux and auroral electrojet (AE) index and proposed to use the AKR power flux as a reliable indicator of geomagnetic disturbances. The idea was developed by studies on "AKR index" (Murata *et al.*, 1997; Kurth *et al.*, 1998; Kurth and Gurnett, 1998). In these studies, the averaged power flux of AKR in frequency range from 50 kHz to 800 kHz was defined as the AKR index and its correlation with Kp and Dst indices were investigated. Furthermore, the AKR index was also used for identification of the substorm onset in order to discuss the dynamics of plasmoids in the geomagnetic tail (Slavin *et al.*, 1993; Murata *et al.*, 1995).

It has also come to be known that AKR depends not only on geomagnetic conditions but also on seasonal and solar activity conditions. Seasonal variation of AKR is found by statistical studies of long-term plasma wave data obtained by the

This document is provided by JAXA.

Geotail spacecraft and the Akebono (EXOS-D) satellite (Kasaba *et al.*, 1997; Kumamoto and Oya, 1998; Kumamoto *et al.*, 2001). Based on the 13-years of plasma wave data obtained by the Akebono satellite, a solar cycle dependence of AKR was also discovered (Kumamoto *et al.*, 2003a, b). Consistent results were reported based on the statistical analyses of Polar/IMAGE plasma wave datasets (Green *et al.*, 2004). The conditions of the polar ionosphere are likely to be a main control factor of AKR seasonal and solar cycle variations. However, control mechanisms have not been clarified and remain controversial.

In previous studies on AKR index, the seasonal and solar cycle effects on AKR were not taken into account, as pointed out by Green *et al.* (2004). The main purpose of this study is, therefore, to clarify the seasonal and solar cycle effects on the correlation between AKR power flux and AE index by using plasma wave data obtained by the Akebono satellite, and to discuss control factors of AKR seasonal and solar cycle variations.

2. Datasets and methods of analysis

AKR power fluxes were derived from high gain and medium gain plasma wave datasets obtained by the plasma waves and sounder (PWS) instrument onboard the Akebono satellite. The instrumentations of the PWS were precisely described by Oya *et al.* (1990). AE indices were provided by World Data Center (WDC) for Geomagnetism, Kyoto. Simultaneous AE indices are available for AKR power flux data in a period from 1990 to 1995. However, it should be noted that the AE index in the period is not final but the provisional one.

In order to investigate seasonal and solar activity dependences of correlations between AKR power flux and AE index, datasets were divided into four groups: Datasets (1) in northern summer during solar maximum, (2) in northern winter during solar maximum, (3) in northern summer during solar minimum, and (4) in northern winter during solar minimum. In this study, summer and winter were defined as three months around the solstice for the northern hemisphere. The period from 1990 to 1991, and the period from 1994 to 1995 were defined as solar maximum and solar minimum, respectively.

The AKR power flux was determined by averaging S_{30R_E}, normalized power flux at $30R_E$, in frequency range from 250 kHz to 800 kHz for 1 min:

$$S_{AKR}(t)=\frac{1}{1\,\mathrm{min}}\int_t^{t+1\,\mathrm{min}}\left[\frac{1}{550\,\mathrm{kHz}}\int_{250\,\mathrm{kHz}}^{800\,\mathrm{kHz}}S_{30R_E}(f,t)\,df\right]dt'. \quad (1)$$

Normalized power flux S_{30R_E} was obtained by

$$S_{30R_E}(f,t)=\left[\frac{r_{sat}(t)-r_{f=f_{ce}}(t)}{30R_E}\right]^2 S_{sat}(f,t), \quad (2)$$

where S_{sat}, r_{sat} and $r_{f=f_{ce}}$ respectively indicate wave power flux at the satellite, geocentric distance of the satellite, and the location at which wave frequency f equals the local electron cyclotron frequency f_{ce}. In order to avoid plasma wave data out of the

This document is provided by JAXA.

dynamic range of the PWS in high gain observation mode, only plasma wave data within a power flux range from 3×10^{-17} to 1×10^{-13} $Wm^{-2}Hz^{-1}$ at the satellite were utilized for the calculations. As for the period from 1990 to 1991, the medium gain plasma wave data, whose dynamic range is from 3×10^{-15} to 1×10^{-11} $Wm^{-2}Hz^{-1}$, are also available. However, the amount of the medium gain plasma wave data is much smaller than that of the high gain plasma wave data in the same period. Assuming that AKR is generated near the electron cyclotron frequency at the source and propagates upward, AKR can not be observed below the electron cyclotron frequency at the satellite. In order to determine the AKR power fluxes based on the entire AKR spectrum in the frequency range from 250 to 800 kHz, whose sources are located within a geocentric distance of $1.85R_E$, plasma wave data obtained within a geocentric distance of $2R_E$, were excluded from the analysis. It is also known that AKR mainly occurs in auroral regions in the evening sector (Gurnett, 1974). It should be also considered that AE index is determined by geomagnetic variations observed in the northern polar region. Therefore, only AKR power fluxes obtained in the northern polar area with an invariant latitude range from 70 to 75 degrees and with a magnetic local time (MLT) range from 2200 to 2400 were utilized for the analysis.

3. Results

Correlations between the AE index and the normalized AKR power flux, S_{AKR}, in the four seasonal and solar activity cases, which are derived from high gain plasma wave datasets, are shown in Figs. 1–4. In each figure, upper panel and lower panel respectively show scatter plot and occurrence time plot of normalized AKR power flux as a function of AE index. Saturation limits of normalized AKR power flux are indicated in the right side of the scatter plot. It should be noted that they depend on the distance between AKR sources and the satellite, which is larger than $0.15R_E$ in this analysis because AKR sources in a frequency range above 250 kHz is located within $1.85R_E$ and plasma wave data observed within $2.0R_E$ are excluded from the analysis. Although the data points are very scattered, we can see the positive correlation between AKR power flux and AE index. In order to investigate seasonal and solar cycle dependence of the correlations, the data points are fitted to $\log_{10}S_{AKR}=a\log_{10}AE+b$ by least mean square (LMS) method. The determined parameters are shown in Table 1. Due to scattered property of datasets, correlation coefficients are about 50% or lower in all cases. The fitted lines are also indicated in Figs. 1–4 and summarized in Fig. 6. In summer, AKR power flux increases as about 1.2 power of AE index both during solar maximum and during minimum. However, even for the same AE index, AKR power flux during solar minimum is 5 dB larger than that during solar maximum. In winter, AKR power flux increases as about 1.0 or less power of AE index. However, it should be noted that considerable portion of winter AKR data were excluded from the analysis because they are beyond the saturation level. Due to lack of those data, the slopes of the fitted line can be smaller than it would be if there were no saturation limit. In order to avoid saturation limit effects, plasma wave data obtained by medium gain observation were also utilized for the analysis.

Correlation between the AE index and the normalized AKR power flux in winter

This document is provided by JAXA.

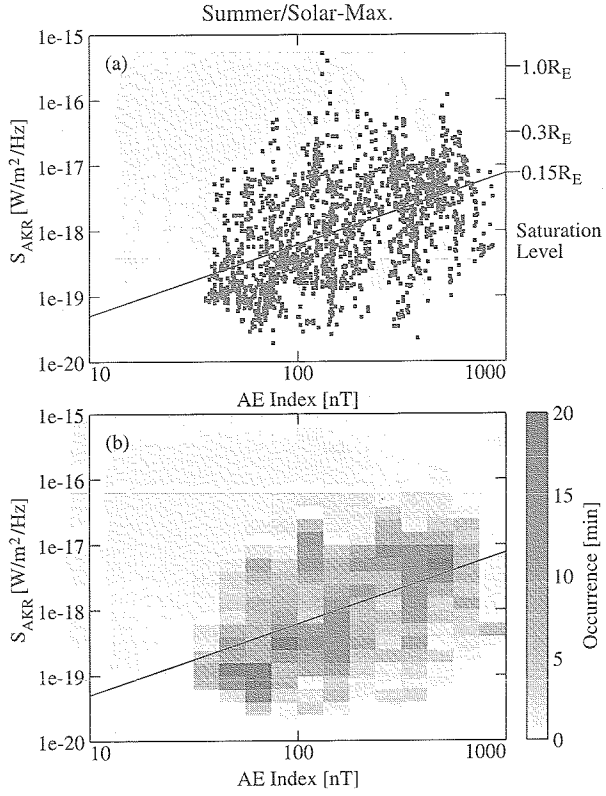


Fig. 1. Scatter plot (a) and occurrence time plot (b) of the normalized AKR power flux as a function of AE index in summer during solar maximum. Normalized AKR power flux and its occurrence time were derived from high gain plasma wave dataset. Fitted line is also indicated by solid line.

during solar maximum, which is derived from medium gain plasma wave dataset obtained in the period from 1990 to 1991, is shown in Fig. 5. Saturation level of medium gain observation is 20 dB larger than those of high gain observation. Therefore, the main portion of winter AKR data can be included in the analysis. Fitted line is shown in Fig. 5 by solid line, and also in Fig. 2 by broken line. In winter during solar maximum, normalized AKR power flux increases about 1.2 power of AE index, which is quite similar to the summer case. During solar maximum, normalized AKR power flux in winter is 22 dB larger than that in summer even for the same AE index.

4. Discussion and conclusions

The results indicated in the previous section clearly suggest that there is a correlation between AKR power flux and AE index in all seasonal and solar activity cases. However the properties of the correlation change depending on season and solar activity. Thus, AKR index proposed in the previous studies should be corrected if it is

This document is provided by JAXA.

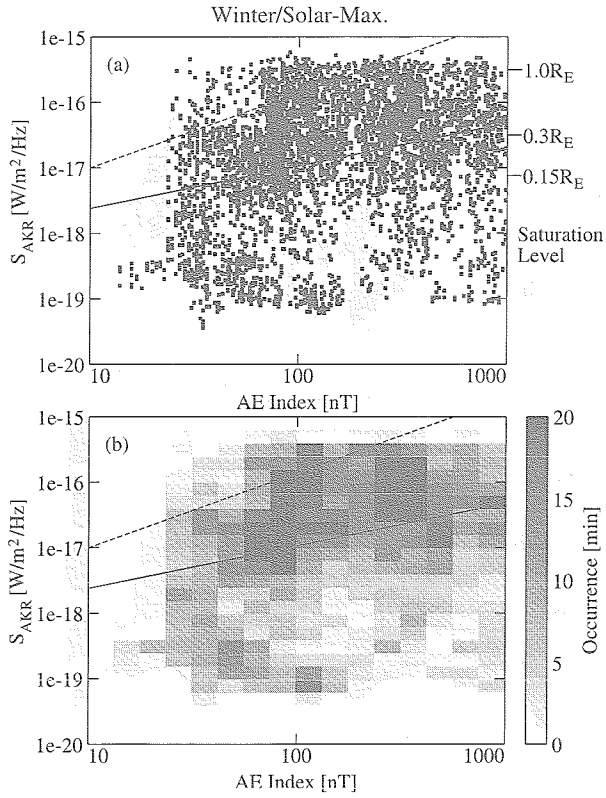


Fig. 2. Scatter plot (a) and occurrence time plot (b) of normalized AKR power flux as a function of AE index in winter during solar maximum. Normalized AKR power flux and its occurrence time were derived from high gain plasma wave dataset. Fitted lines based on high gain and medium gain plasma wave datasets are also indicated by solid line and broken line, respectively.

used under different seasonal and solar activity conditions. Even for the same AE index, there are 5 dB difference between AKR power fluxes during solar maximum and during solar minimum and 22 dB difference between those in the summer and winter polar regions. In the present study, the normalized AKR power flux in winter derived from high gain plasma wave dataset seems to be underestimated due to effects by saturation limit. As for the winter case, the normalized AKR power flux derived from medium gain plasma wave dataset are more reliable than that based on high gain plasma wave dataset.

The AE index were originally defined by Davis and Sugiura (1966) as an indicator of global electrojet activity in the auroral zone. The AE index is derived from geomagnetic variations in the H (horizontal) component observed at selected stations distributed along the auroral zone in the northern hemisphere. The higher and lower envelopes of the H-component perturbation are defined as the AU and AL index. The AE index is determined by AE=AU-AL. The AE index from 10 to 1000 nT corre-

This document is provided by JAXA.

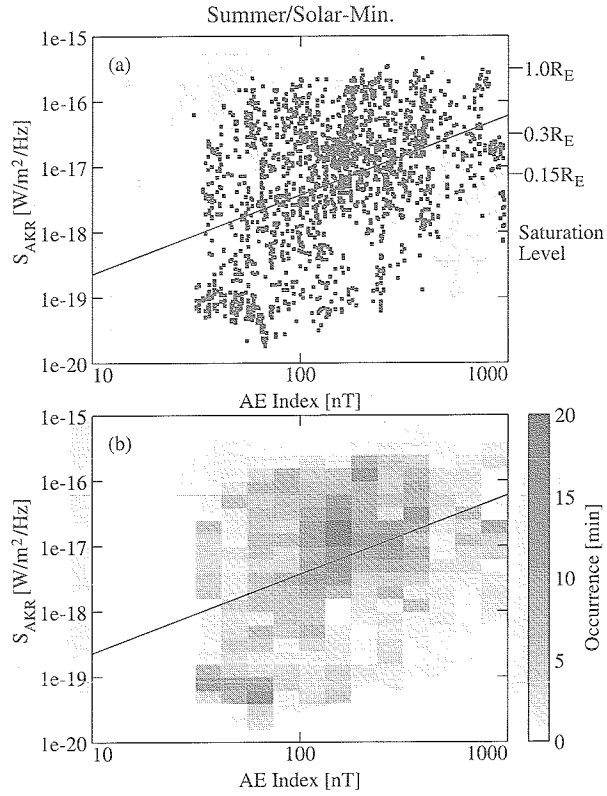


Fig. 3. Same as Fig. 1 but for in summer during solar minimum.

sponds to the current in a range from 10^4 to 10^6 A in the ionosphere. Based on recent statistical studies on long-term variations of the AE index, it has been reported that the AE index during solar minimum is larger than that during solar maximum (Fres Saba *et al.*, 1997; Ahn and Moon, 2003), which are consistent with the results shown in the present study. On the other hand, based on statistical analysis on annual variation of the AE index, it has been also reported that the AE index increases around the equinox (Lyatsky *et al.*, 2001; Benkevitch *et al.*, 2002). Focusing on the deference between correlations of summer and winter AKR with the AE index, the equinoctial period data were not included into the analyses in the present study. Therefore, the issue on the equinoctial maximum of the AE index and effects on AKR variations are deferred to the future works.

Based on the plasma wave datasets obtained by Imp 6, it has been reported by Voots *et al.* (1977) that correlation between AKR power flux and AE index is given by

$$\log_{10} S_{AKR} = 1.2 \log_{10} AE - 19 \quad (AE > 100\,\mathrm{nT}), \tag{3}$$
$$\log_{10} S_{AKR} = 2 \log_{10} AE - 20.5 \quad (AE < 100\,\mathrm{nT}). \tag{4}$$

These correlations are within fitted lines determined in the present study in summer and winter during solar maximum cases, which is probably because the dataset used by Voots

This document is provided by JAXA.

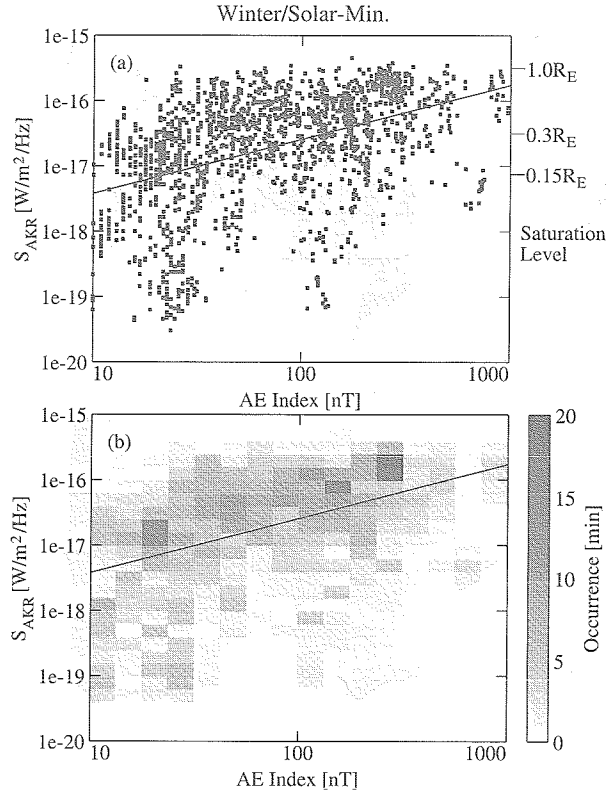


Fig. 4. Same as Fig. 1 but for in winter during solar minimum.

et al. (1977) covers autumn and winter during solar maximum. In our results, however, it was difficult to find another slope in AE index range below 100 nT by the LMS method.

Lyons *et al.* (1979) found an empirical relation between the total energy flux of auroral electrons E_{tot} and the field aligned potential V, which is given by

$$E_{tot}=\alpha \cdot V^2. \tag{5}$$

It was also shown by Fridman and Lamaire (1980) that the parameter α is given by

$$\alpha=N_{e,M}\frac{e^2}{(2\pi m_e)^{1/2}}\frac{(E_{0\parallel})^{1/2}}{E_{0\perp}}, \tag{6}$$

where e, m_e, $N_{e,M}$, $E_{0\parallel}$, and $E_{0\perp}$ are charge and mass of electron, number density of hot electrons in the magnetospheric source region such as plasmasheeet, and thermal energy parallel and perpendicular to the magnetic field, respectively. Assuming a proportional relation between auroral current and field aligned potential drop as shown by Knight (1973), auroral current is given by

$$I\approx N_e e v_{Te,\parallel}\frac{eV}{T_{e,\perp}}=KV, \tag{7}$$

This document is provided by JAXA.

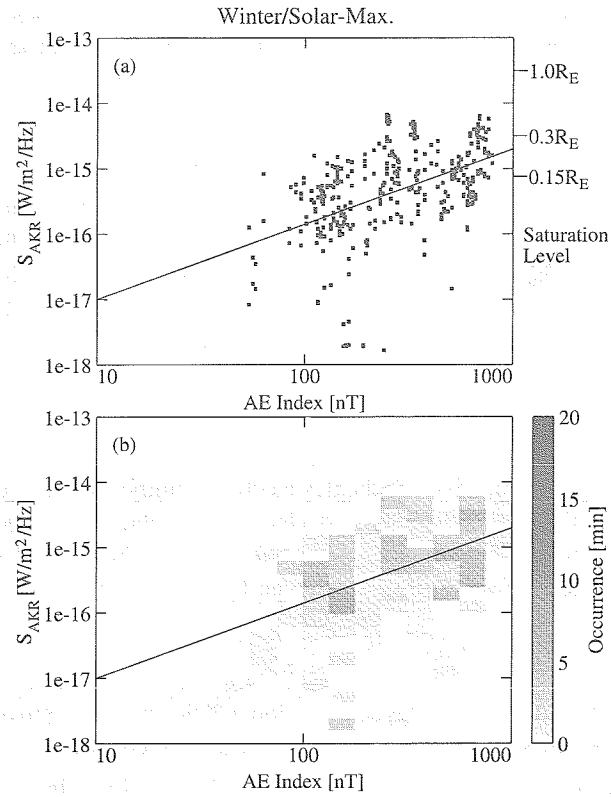


Fig. 5. Same as Fig. 1 but for in winter during solar maximum and from medium gain plasma wave dataset.

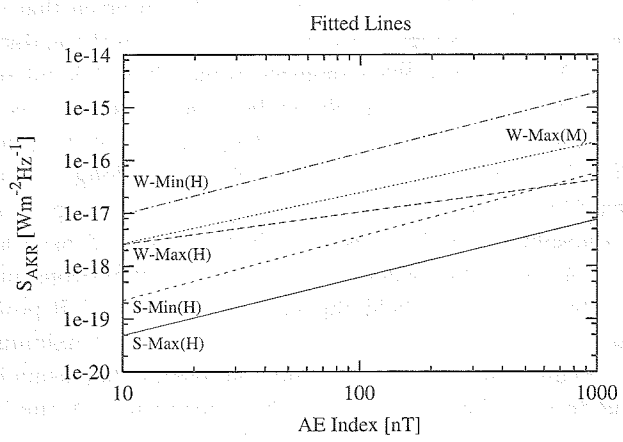


Fig. 6. Seasonal and solar activity dependences of fitted lines for correlations of normalized AKR power flux with AE index. The lines labeled S-Max(H), W-Max(H), S-Min(H), W-Min(H), and W-Max(M) indicated fitted lines for correlations in summer during solar maximum, in winter during solar maximum, in summer during solar minimum, in winter during solar minimum derived from high gain plasma wave datasets, and in winter during solar maximum derived from medium gain plasma wave dataset, respectively.

This document is provided by JAXA.

Table 1. Seasonal and solar activity dependences of least mean square (LMS) fitting parameter a and b for correlation of AKR power flux with AE index. σ_a, σ_b, R and N indicate the standard deviations of a and b, correlation coefficient, and data number, respectively.

Dataset	Conditions		$\log_{10} S_{AKR}=a \log_{10} AE+b$					
			$\bar{a}$	σ_a	$\bar{b}$	σ_b	R	N
Gain-H	Solar Max.	Summer	1.096	0.044	−20.408	0.097	0.494	1949
		Winter	0.068	0.031	−18.196	0.068	0.277	4789
	Solar Min.	Summer	1.207	0.062	−19.858	0.135	0.412	1884
		Winter	0.960	0.039	−18.532	0.074	0.516	1650
Gain-M	Solar Max.	Winter	1.154	0.118	−18.173	0.286	0.472	337

where N_e, $v_{Te,\parallel}$ and $T_{e,\perp}$ respectively indicates electron number density, electron thermal velocity parallel to the magnetic field and electron temperature perpendicular to the magnetic field around the field-aligned potential drops in the auroral regions. Using eqs. (5) and (7), AKR power flux S_{AKR} is given by

$$S_{AKR}=\beta E_{tot}=\beta\frac{\alpha}{K^2}I^{\gamma}, \tag{8}$$

where $\gamma=2$, and β indicates energy conversion efficiency from auroral electrons to AKR. However, as for S_{AKR} obtained in this study and in Voots *et al.* (1977), γ is ~1.2. This discrepancy is probably caused not by the change of γ itself but by the changes of other parameter such as β and α. It is possible that β become small due to some nonlinear saturation mechanisms as the energy flux of auroral electrons increase, as discussed by Voots *et al.* (1977). In addition, it is also inferred that auroral electron precipitation causes loss of hot plasma sources in the magnetosphere, due to which α can decrease. Ono and Morishima (1994) reported some observational results, in which the apparent γ is less than 2. This is probably because α decreases as I increases.

In this study, seasonal and solar cycle dependences of the correlation between AKR power flux and the AE index have been clarified based on the long-term datasets. They are probably attributed to the change of β/K^2 caused by seasonal and solar cycle variations in the ionosphere. K depends on ambient electron density and temperature in an altitude range of several km, where field-aligned potential drops and AKR sources are generated. Even for the same field aligned potentials, or AKR power flux, auroral current varies depending on K. In summer or during solar maximum, S_{AKR} can decrease due to an increase of K. In this condition, ambient cold plasma in AKR sources becomes dense due to upwelling plasma from the ionosphere. Assuming that AKR is generated via the cyclotron maser instability (CMI) process, β is also inferred to be small in a dense cold plasma (Wu and Lee, 1979; Hewitt *et al.*, 1982).

In this study, AKR power flux clearly depends on the AE index under any seasonal and solar cycle conditions. Therefore, AKR index without seasonal and solar activity correction is sufficiently useful for the purposes such as identification of substorm onsets. However, it should be noted that long-term variations of the AE and AKR indices are

This document is provided by JAXA.

different due to the seasonal and solar activity dependence of β and K, which is probably caused by variations in the ionosphere. More quantitative investigation of these control factors will be needed for understanding long-term variations of AKR power flux and wide application of the AKR index.

Acknowledgments

We would like to thank all the staff of the Akebono satellite team. The provisional AE index in the period from 1990 to 1995 was provided by World Data Center (WDC) for Geomagnetism, Kyoto.

The editor thanks Dr. Y. Kasaba and another referee for their help in evaluating this paper.

References

Ahn, B.-H. and Moon, G.-H. (2003): Seasonal and universal time variations of the AU, AL and Dst indices. J. Korean Astron. Soc., **36**, S93–S99.

Benkevitch, L.V., Lyatsky, W.B., Koustov, A.V., Sofko, G.J. and Hamza, A.M. (2002): Substorm onset times as derived from geomagnetic indices. Geophys. Res. Lett., **29** (10), 10.1029/2001GL014386.

Davis, T.N. and Sugiura, M. (1966): Auroral electrojet activity index AE and its universal time variations. J. Geophys. Res., **71**, 785–801.

Fres Saba, M.M., Gonzalez, W.D. and Clua de Gonzalez, A.L. (1997): Relationship between the AE, ap and Dst indices near solar minimum (1974) and at solar maximum (1979). Ann. Geophys., **15**, 1265–1270.

Fridman, M. and Lemaire, J. (1980): Relationship between auroral electrons fluxes and field aligned electric potential differences. J. Geophys. Res., **85**, 664–670.

Green, J.L., Boardsen, S., Garcia, L., Fung, S.F. and Reinisch, B.W. (2004): Seasonal and solar cycle dynamics of the auroral kilometric radiation source region. J. Geophys. Res., **109**, A05223, doi: 10.1029/2003JA010311.

Gurnett, D.A. (1974): The earth as a radio source: terrestrial kilometric radiation. J. Geophys. Res., **79**, 4227–4238.

Hewitt, R.G., Melrose, D.B. and Ronmark, K.G. (1982): The loss-cone driven electron-cyclotron maser. Aust. J. Phys., **35**, 447–471.

Kasaba, Y., Matsumoto, Hashimoto, K. and Anderson, R.R. (1997): The angular distribution of auroral kilometric radiation observed by the GEOTAIL spacecraft. Geophys. Res. Lett., **24**, 2483–2486.

Knight, S. (1973): Parallel electric fields. Planet. Space Sci., **21**, 741–750.

Kumamoto, A. and Oya, H. (1998): Asymmetry of occurrence-frequency and intensity of AKR between summer polar region and winter polar region sources. Geophys. Res. Lett., **25**, 2369–2372.

Kumamoto, A., Ono, T. and Oya, H. (2001): Seasonal dependence of the vertical distributions of auroral kilometric radiation sources and auroral particle acceleration regions observed by the Akebono satellite. Adv. Polar Upper Atmos. Res., **15**, 32–42.

Kumamoto, Ono, T., Iizima, M. and Oya, H. (2003a): Seasonal and solar cycle variations of the vertical distribution of the occurrence probability of auroral kilometric radiation sources and of upflowing ion events. J. Geophys. Res., **108** (A1), 1032, doi: 10.1029/2002JA009522.

Kumamoto, A., Ono, T., Iizima, M. and Oya, H. (2003b): Control factor of solar cycle variation of auroral kilometric radiation. Adv. Polar Upper Atmos. Res., **17**, 48–59.

Kurth, W.S. and Gurnett, D.A. (1998): Auroral kilometric radiation integrated power flux as proxy for AE. Adv. Space Res., **22**, 73–77.

Kurth, W.S., Murata, T., Lu, G., Gurnett, D.A. and Matsumoto, H. (1998): Auroral kilometric radiation and the auroral electrojet index for the January 1997 magnetic cloud event. Geophys. Res. Lett., **25**,

This document is provided by JAXA.

3027–3030.

Lyatsky, W., Newell, P.T. and Hamza, A. (2001): Solar illumination as cause of the equinoctial preference for geomagnetic activity. Geophys. Res. Lett., **28**, 2353–2356.

Lyons, L.R., Evans, D.S. and Lundin, R. (1979): An observed relation between magnetic field aligned electric fields and downward electron energy fluxes in the vicinity of auroral forms. J. Geophys. Res., **84**, 457–461.

Murata, T., Matsumoto, H., Kojima, H., Fujita, A., Nagai, T., Yamamoto, T. and Anderson, R.R. (1995): Estimation of tail reconnection lines by AKR onsets and plasmoid entries observed with GEOTAIL spacecraft. Geophys. Res. Lett., **22**, 1849–1852.

Murata, T., Matsumoto, H., Kojima, H. and Iyemori, T. (1997): Correlations of AKR index with Kp and Dst indecies. Proc. NIPR Symp. Upper Atmos. Phys., **10**, 64–68.

Ono, T. and Morishima, K. (1994): Energy parameters of precipitating auroral electrons obtained by using photometric observations. Geophys. Res. Lett., **21**, 261–264.

Oya, H., Morioka, A., Kobayashi, K., Iizima, M., Ono, T., Miyaoka, H., Okada, T. and Obara, T. (1990): Plasma wave observation and sounder experiments (PWS) using the Akebono (EXOS-D) satellite-instrumentation and initial results including discovery of the high altitude equatorial plasma turbulence. J. Geomagn. Geoelectr., **42**, 411–442.

Slavin, J.A., Smith, M.F., Mazur, E.L., Baker, D.N., Hones, E.W., Iyemori, T. and Greenstadt, E.W (1993): ISEE 3 observations of traveling compression regions in the earth's magnetotail. J. Geophys. Res., **98**, 15425–15446.

Voots, G.R., Gurnett, D.A. and Akasofu, S.-I. (1977): Auroral kilometric radiation as an indicator of auroral magnetic disturbances. J. Geophys. Res., **82**, 2259–2266.

Wu, C.S. and Lee, L.C. (1979): A theory of the terrestrial kilometric radiation. Astrophys. J., **230**, 621–626.

This document is provided by JAXA.

Adv. Polar Upper Atmos. Res., 19, 21-41, 2005
© 2005 National Institute of Polar Research

Extreme magnetic field variations during the October 2003 superstorm

Tohru Sakurai[1]* and Yutaka Tonegawa[1]

[1] *Department of Aeronautics and Astronautics, School of Engineering, Tokai University, 1117 Kitakaname, Hiratsuka 259-1292*
**Corresponding author. E-mail: sakurai@keyaki.cc.u-tokai.ac.jp*

(Received December 24, 2004; Accepted April 25, 2005)

Abstract: From October to November, 2003 the sun became very active. The plural numbers of active region appeared on the solar surface. The most prominent one was the number 486, which yielded extremely large flares X17/4B at 0951 UT on October 28, and X10/2B at 2037 UT on October 29. These big flares hurled massive coronal mass ejections (CMEs) toward the earth. In this paper the solar-terrestrial relationship during the October super magnetic storms is discussed. Two fast moving clouds of gas from the sun swept the earth and sparked extreme geomagnetic storms producing the big ground magnetic field depressions of approximately −350 nT and −400 nT of Dst.

Several interesting magnetic field variations observed in interplanetary space and their relationships to the ground magnetic field variations are discussed. Topics are as follows: 1) magnetic field polarity changes of the north-south component B_z of interplanetary magnetic field conveyed with the interplanetary coronal mass ejections (ICMEs) and their response to the magnetic field variations on the ground, 2) large amplitude tail flapping motions observed in the distant tail at about $-160\,R_e$, 3) large amplitude Pc 5 oscillations globally observed on the ground during the recovery phase of the super magnetic storm, and 4) large amplitude Pc 3 ULF waves observed in space from upstream through the magnetosheath to the dusk-side outer magnetosphere.

key words: coronal mass ejection, interplanetary magnetic field, geomagnetic storm, MHD waves

1. Introduction

Solar activity occurred on October to November 2003, that yielded violent super magnetic storms in the terrestrial magnetosphere. The magnetic activity occurred in less than a day from the beginning of the solar flares. The solar wind speed was extremely high. In order to predict the geo-effectiveness of such solar activity accurate knowledge of the solar-terrestrial relationship is desired. This storm event is a suitable example for this study. In this paper the important geomagnetic phenomena that occurred during this super magnetic storm and their relationships to solar wind features are examined in detail. In Section 2 the observed extremely high-speed solar wind and CMEs are examined. A typical relationship between ICMEs and their geo-effectiveness is discussed in Section 3. The relationships between the solar wind conditions observed by the ACE satellite in the region upstream, and tail flapping motions observed by the

This document is provided by JAXA.

WIND satellite in the distant tail downstream are examined in Section 4. Extremely large amplitude Pc 5 oscillations and their characteristics are examined in Section 5. Pc 3 pulsations (10–50 s in period) observed in interplanetary space, the magnetosheath and the dusk-side outer magnetosphere observed by the GEOTAIL satellite are examined in Section 6. Summary and discussions are described in Section 7.

2. Extremely high-speed solar wind

Large X-ray flares occurred at 0951 UT on October 28, and 2037 UT on October 29. Ejected coronal materials were hurled toward the earth, and observed in interplanetary space following shocks. The first and second shocks were observed at 0559 UT on October 29, and at 1620 UT on October 30 by ACE, at $230R_e$ upstream. The first shock was identified clearly accompanied with the associated shock sheath, while the second shock was not clear and did not accompany the shock sheath. During this period the WIND satellite stayed in the distant tail at $-160R_e$ and observed these interplanetary coronal mass ejections (ICMEs). WIND observed the first shock at 0618 UT. The second shock was not identified clearly in the magnetic field. The plasma data of both satellite, ACE and WIND were not available for this storm period. This was due to the instrument damage for these severe storms. From the observations of onsets times of flares and sscs we can estimate transit times of these shocks from the sun to the earth, which were 20.3 hrs and 20.0 hrs for the first and second shocks, respectively, which are amongst the highest speed ever observed. These observations are summarized in Table 1.

Table 1. A summary of flare onset times and shock transit times of October 2003 storm.

		1st flare	2nd flare
1	Flare onset time	0951 UT Oct 28, 2003	2037 UT Oct 29, 2003
2	Shock observed time at ACE ($230R_e$)	0559 UT Oct 29, 2003	1620 UT Oct 30, 2003
3	ssc onset time	0611 UT Oct 29, 2003	1637 UT Oct 30, 2003
4	Shock observed time at WIND ($-160R_e$)	0618 UT Oct 29, 2003	Not identified
5	Shock speed estimated from ACE and WIND arrival times	2189 km/s	Not calculated
6	Travel time from the sun to the earth	20.3 hrs	20.0 hrs
7	Shock speed estimated from travel time from the sun to the earth	2049 km/s	2193 km/s

We tried to examine a relationship between arrival times of super magnetic storms with Dst < -200 nT observed in this solar cycle from 1996 to 2003 and corresponding initial speeds of CMEs. The initial speeds of CMEs are employed from the LASCO CME CATALOG (http://cdaw.gsfc.nasa.gov/cme_list/). The arrival times of sscs for sampled 12 super magnetic storms and the initial speeds of the CMEs corresponding to these storms are tabulated in Table 2. The relationship is shown in Fig. 1. By taking into account of the initial speeds of the first and second CMEs of the October 2003 superstorms, the arrival times of the ssc are clearly understood to be shortest amongst the ever observed sscs. Therefore, this relationship is very useful to predict the 1 AU arrival time of ssc.

This document is provided by JAXA.

Table 2. Relationship between Halo Type CME and SSC Storm with Dst<−200 nT from 1996 to 2003.

No.	Year	SSC MM/DD/UT	Dst MM/DD	Dst (nT)	Lag time (hh:mm)	CME MM/DD	CME UT	Type	V1 (km/s)
1	1998	5/3/1743	5/4	−205	42:03	5/1	2340:09	Halo	585
2	2000	4/6/1640	4/7	−288	48:08	4/4	1632:37	Halo	1188
3	2000	7/15/1439	7/16	−301	27:45	7/14	1054:07	Halo	1674
4	2000	8/11/1846	8/12	−235	50:16	8/9	1630:05	Halo	702
5	2000	9/17/1316	9/17	−201	31:58	9/16	0518:04	Halo	1215
6	2001	3/31/0052	3/31	−387	38:26	3/29	1026:05	Halo	942
7	2001	4/11/1345	4/11	−271	32:15	4/10	0530:00	Halo	2411
8	2001	11/6/0152	11/6	−288	32:17	11/4	1635:05	Halo	1810
9	2001	11/24/0555	11/24	−221	33:25	11/22	2030:05	Halo	1437
10	2003	10/29/0611	10/30	−363	18:41	10/28	1130:05	Halo	2459
11	2003	10/30/1637	10/30	−401	19:43	10/29	2054:05	Halo	2029
12	2003	11/20/0804	11/20	−472	47:14	11/18	0850:05	Halo	1660

Lag time (hh:mm) = SSC Onset Time − Observed Time of V1.
V1 (km/s): Initial speed of Halo Type CME.

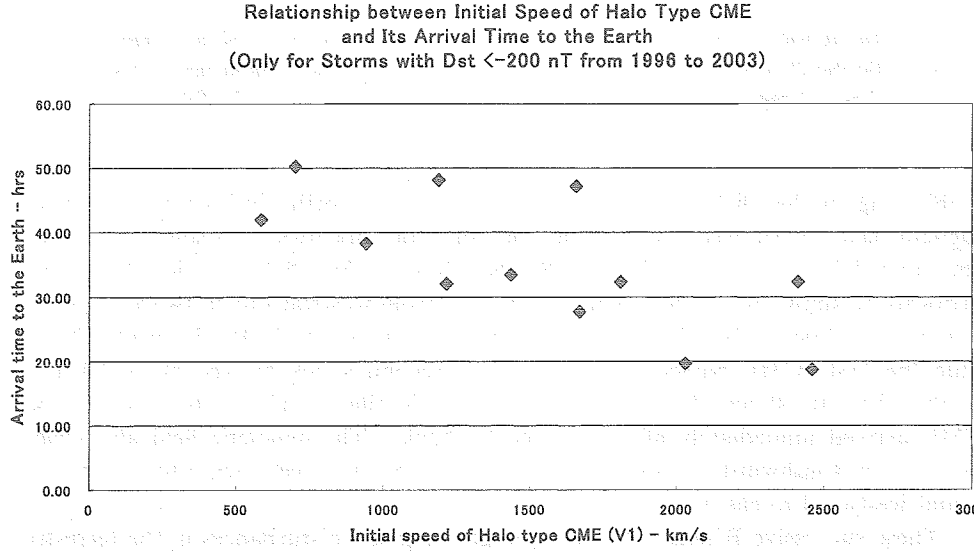


Fig. 1. The relationship between the arrival times of superstorms (Dst<−200 nT) and the initial speeds of the corresponding Halo type CMEs.

3. Field rotations of ICMEs and corresponding geomagnetic disturbances

Figure 2 shows the ICMEs successively observed by ACE on October 29–30, which is a typical example of ICME observed in interplanetary space. Clear field rotations of IMF can be seen. The first shock was observed at 0558 UT on October 29, accompanied with a sharp increase of the magnetic field intensity, and also followed by the shock sheath, in which the magnetic field varied violently, and thereafter the ICME

This document is provided by JAXA.

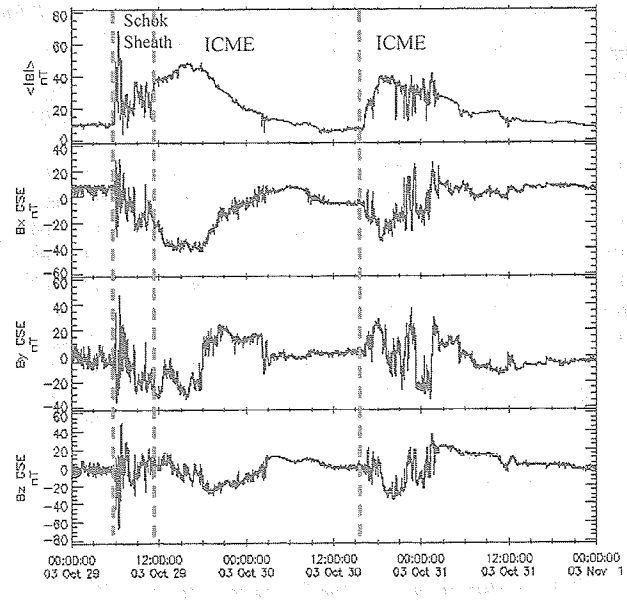


Fig. 2. The ICMEs observed by ACE at 230 R_e upstream in the super magnetic storm period from October 29 to 31, 2003. From the top to bottom panels are the magnetic field intensity, and three components of the magnetic field in the GSE coordinates. The field rotations are clearly identified in all of the components.

exhibitcd again clear field rotations. In particular, the north-south component of the magnetic field, B_z showed a clear field rotation from northward to southward. The other two field components, B_x and B_y also showed clear field rotations, *i.e.*, from earthward to sunward for the B_x component, and from westward to eastward for the B_y component, respectively. These field rotations continued until 03 UT on October 30 while the first ICME passed the earth. The second shock arrived at 1618 UT on October 30. Its shock sheath was not clearly identified. The body of the second ICME arrived immediately after the second shock. The magnetic field also clearly rotated from southward to northward for the B_z component, earthward to sunward for B_x and westward to eastward for B_y, respectively.

These successive ICMEs produced big geomagnetic disturbances in the terrestrial magnetosphere. This is shown in Fig. 3, which shows the geomagnetic disturbances observed at the IMAGE chain magnetometer stations (http://www.ava.fmi.fi/image/index.html). The storm sudden commencement (ssc) was observed at 0611 UT at all of the stations, indicating the shock arrival at the ground. After the first ssc the geomagnetic field showed disturbances, in particular, from 0800–1000 UT on October 29, 2003. There were some negative bay signatures at high latitude stations. This might be caused by fluctuation of IMF B_z around 0 nT. Then the activity remained quiet for a while. This is due to the geo-effectiveness for the north–south component of the IMF B_z, almost zero. That continued for about 9 hrs until 15 UT on October 29. Around 15 UT the IMF B_z turned negative and geomagnetic activity became active, *i.e.*, substorm activity began to develop and continued for about 12 hrs. Around 03 UT on

This document is provided by JAXA.

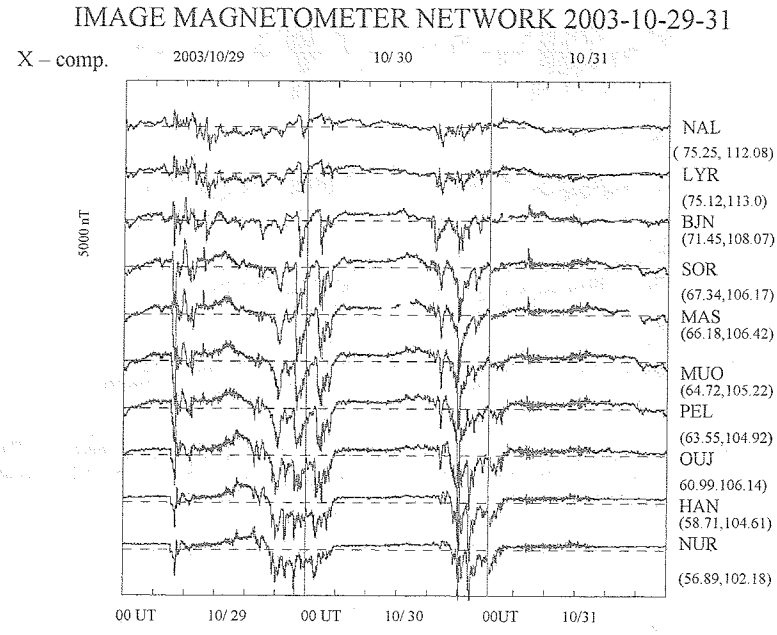


Fig. 3. The magnetic field variations observed at IMAGE chain stations during the October 2003 super storm.

October 30 the IMF B_z turned positive, and then, geomagnetic activity subsided and remained quiet until 15 UT. At that moment the second ICME passed past the earth. The large negative IMF B_z followed. The geomagnetic field then became active again, while enhanced substorm activity that continued for about 8 hrs. Around 00 UT on October 31 the IMF B_z turned positive. Geomagnetic activity suddenly subsided again. However, thereafter the activity of ULF pulsations enhanced. Large amplitude Pc 5 waves were observed during this period.

Therefore, a clear relationship between the field rotation of the IMF B_z component and geomagnetic activity existed throughout this storm. It is evident that the behavior of the IMF B_z primarily controls geomagnetic field activities although specific features in the magnetosphere are controlled by the other solar wind parameters examined in the following sections.

4. Tail flapping oscillations

During the super magnetic storm of October 29–31 WIND stayed in the nightside distant tail at about $X=-160R_e$, where WIND measured large amplitude tail flapping oscillations as shown in Fig. 4. The oscillations were exhibited only in the X component of the magnetic field as indicated with solid circles. The lack of oscillations in the B_y and B_z components suggests that the oscillation was confined to the magnetic field, oriented parallel to the sun-earth line in a X–Z plane. The period of the oscillations was 10–30 min. The peak-to-peak amplitude was about 30–40 nT, and the oscillations were

This document is provided by JAXA.

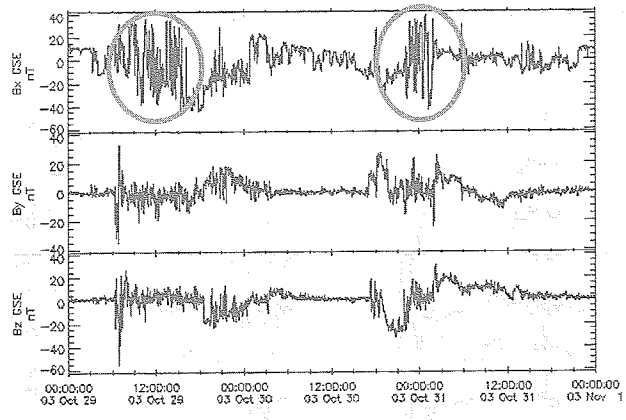


Fig. 4. The WIND observation of the magnetic field variations during the storm period. From the top to bottom panels are B_x, B_y and B_z components of magnetic field in the GSE coordinates. Large amplitude tail flapping oscillations are exhibited only in the B_x component indicated with two circles.

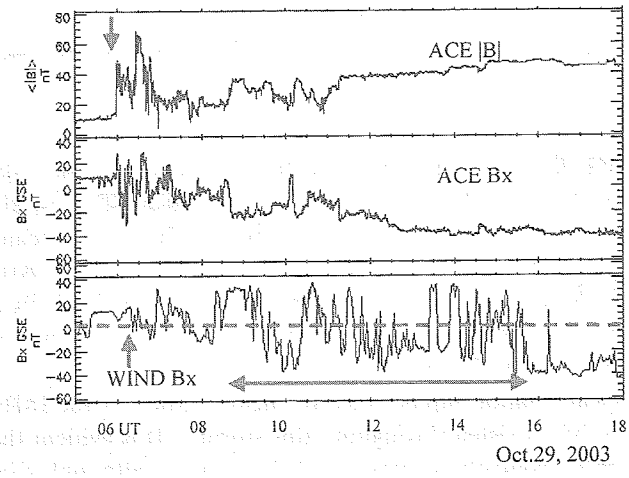


Fig. 5. The tail flapping oscillations observed by WIND at $-167R_e$ immediately after passing of the first ICME. No oscillations observed by ACE upstream at $230R_e$.

quite symmetric about $B_x=0$, which means the boundary displacements associated with this oscillation were in equal magnitude and direction. Therefore, the oscillation mode corresponds to the anti-symmetric mode by Siscoe (1969). He pointed out that this oscillation mode is similar to a rigid oscillation of the outer boundary about a central line.

In order to clarify their characteristics in detail, the oscillations exhibited in the WIND magnetogram are compared with the magnetic field variations measured by the ACE satellite located at about $230R_e$ upstream of the bow shock. Figure 5 shows that there are no periodic oscillations in the magnetic field intensity, $|B|$, and the X

This document is provided by JAXA.

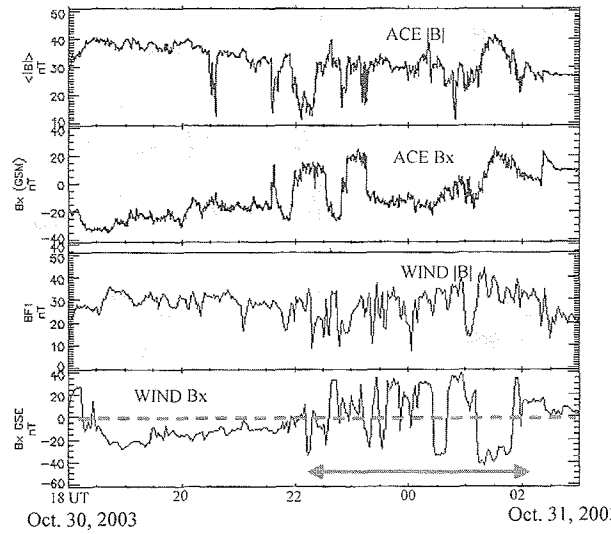


Fig. 6. The tail flapping oscillations observed by WIND immediately after passing of the second ICME. The upper and lower two panels indicate the magnetic field variations of the intensity and the B_x component in the GSE coordinates observed by ACE and WIND, respectively.

component of the magnetic field, B_x, of the ACE magnetograms, as shown in the upper panel of the figure. The bottom panel shows the oscillations, which are identified only in the B_x component of the magnetogram observed by WIND with the period of about 10–30 m. The oscillations continued from 08 UT to 16 UT on October 29 as indicated with a horizontal arrow. This oscillation occurred immediately after the passing of the first shock by WIND.

Another example of such oscillations was observed immediately after the second shock as shown in Fig. 6, in which the magnetic fields observed by ACE and WIND are given in the upper and the lower panels, respectively. In the upper panel there are no clear oscillations of the magnetic field intensity and X component at ACE. In the lower panel the oscillations are clearly identified in the X component from 22 UT on October 30 to 02 UT on October 31 as indicated with a horizontal arrow. The magnetic field of the X component varied with a period of about 10–30 m and amplitude of $\pm$30–40 nT. Moreover, the oscillation was symmetric about $B_x=0$, suggesting that the oscillation is anti-symmetric about the central line.

5. Large amplitude Pc 5 oscillation

During the recovery phase of the super magnetic storm, IMF B_z continued northward with the amplitude of about 20 nT. In this period ULF wave activity became active. In particular, two intervals of large amplitude Pc 5 oscillations were observed from 0537 to 0740 UT, and from 11 to 14 UT. Figure 7 shows a typical example of such large amplitude Pc 5 oscillations observed at a high latitude station,

This document is provided by JAXA.

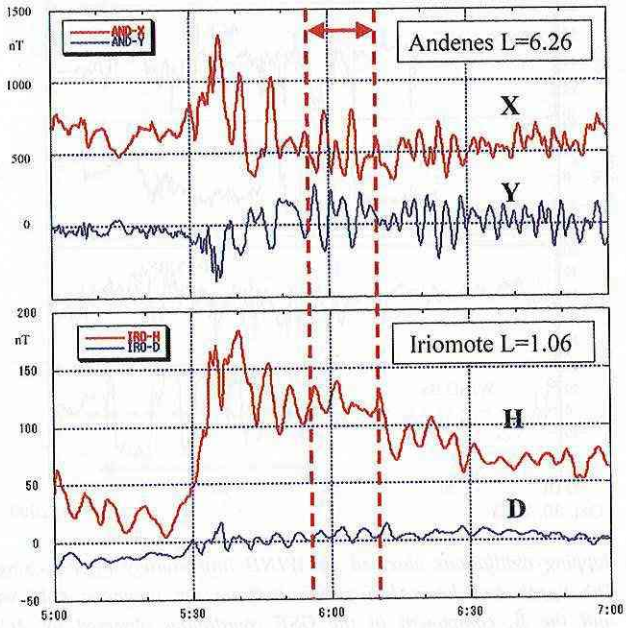


Fig. 7. Comparison of Pc 5 magnetic field oscillations, X and Y components (upper panel) at a high latitude station, Andenes (L=6.26) and H and D components (lower panel) at a low latitude station, Iriomote (L=1.06). Pc 5 oscillations were observed similarly between them. The interval of vertical dotted lines is used for a calculation of power spectrum shown in Fig. 8.

Andenes (geomag. latitude=66.5°N, geomag. long.=100.4°E), as a representative station of the Image chain stations in the auroral zone, and a low latitude station, Iriomote (geomag. lat.=13.6°N, geomag. long.=193.6°E). The Pc 5 oscillations were observed simultaneously at both stations, suggesting that this Pc 5 oscillation might be excited over a large scale in latitude and longitude from high to low latitude and from early morning to evening. Iriomote was located in the evening side at this local time. Power spectra are shown in Fig. 8 for an interval of 15 m from 0555 UT to 0610 UT as indicated with the vertical lines in Fig. 7. The Pc 5 spectral peak occurs at about 4 mHz at both stations.

From these observations we can summarize that large amplitude Pc 5 oscillations can be simultaneously observed over a large range of latitude and longitude with a similar spectral frequency of about 4 mHz. The important characteristics for this Pc 5 event are the large amplitude and the long period oscillations. The reason why this Pc 5 occurred with such a large amplitude and with such a long period is a question. We surveyed the solar wind parameters at this moment. Figure 9 shows the solar wind parameters observed by ACE during this interval, in which the solar wind proton density, solar wind bulk speed and B_z component of the magnetic field are given in the upper, middle and lower panels, respectively. Two successive solar wind density enhancements were observed during the northward IMF B_z approximately at 0500 UT and 1020 UT. The density jumps were from 1 #/cc to 4 #/cc, and from 1 #/cc to 10

This document is provided by JAXA.

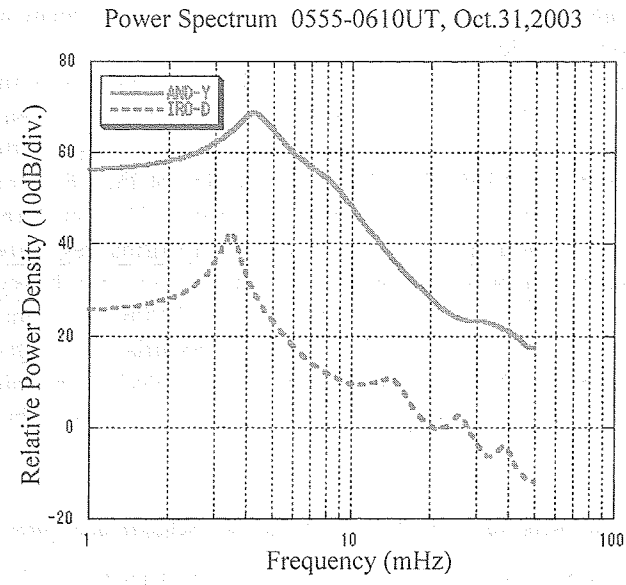


Fig. 8. Comparison of power spectra of the Y and D component magnetic field Pc 5 oscillations during the interval of 15 min from 0555 UT to 0610 UT indicated with the dotted vertical lines in the previous figure, observed at Andenes (solid curve) and Iriomote (dotted curve). Spectral peaks stand at about 4 mHz. However, the power is larger with approximately 20 dB at Andenes compared with that at Iriomote.

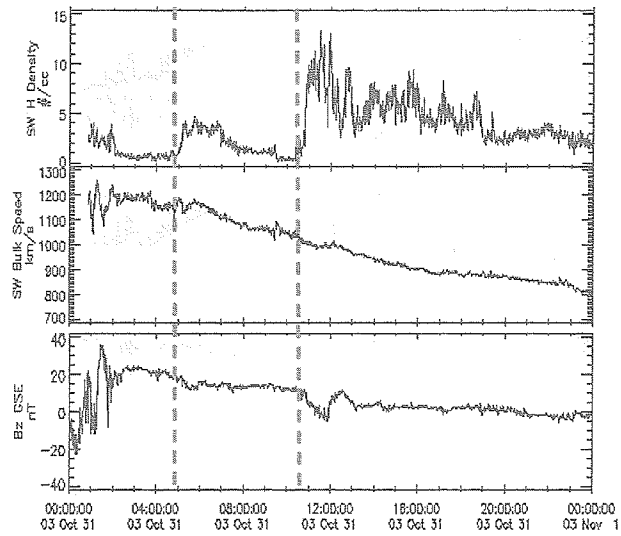


Fig. 9. Solar wind density enhancements (top panel) observed by the ACE satellite, indicated with the dashed lines at the times, 0500 UT and 1030 UT during the northward IMF, B_z (lower panel). The variation of the solar wind bulk speed is shown in the middle panel.

This document is provided by JAXA.

#/cc for the first and second case. The second density enhancement was severer and continued for a longer period.

Therefore, we can suppose that these Pc 5's might be triggered by sudden compressions of the magnetosphere due to the sudden enhancements of solar wind density. Moreover, these Pc 5 events occurred during the recovery phase of the storm in the prevailed intense northward IMF B_z. From the turning of IMF B_z to northward at 00 UT on October 31 ULF wave activity became enhanced. Furthermore, the Dst index attained −350 nT and −400 nT for the first and second storms, respectively, suggesting that the ring current developed during these storms. Therefore, heavy ions might be expected to be injected into the inner magnetosphere during the main phase. These solar wind and magnetospheric conditions seem to be essential for triggering these large amplitude and long period Pc 5 in the magnetosphere. Therefore, we can conclude that these Pc 5's happened to occur when these conditions are matched in between the solar wind and the magnetosphere by chance.

6. Pc 3 ULF waves observed in the foreshock, magnetosheath and outer magnetosphere

Another topic related to this storm is an intense Pc 3 ULF wave activity observed by GEOTAIL in space. During later phase of the first ICME, when the IMF was strongly northward, the GEOTAIL satellite traversed from the upstream region of the quasi-perpendicular shock, through the dusk-side magnetosheath and to the outer magnetosphere. Large amplitude Pc 3 waves were observed throughout the trajectory

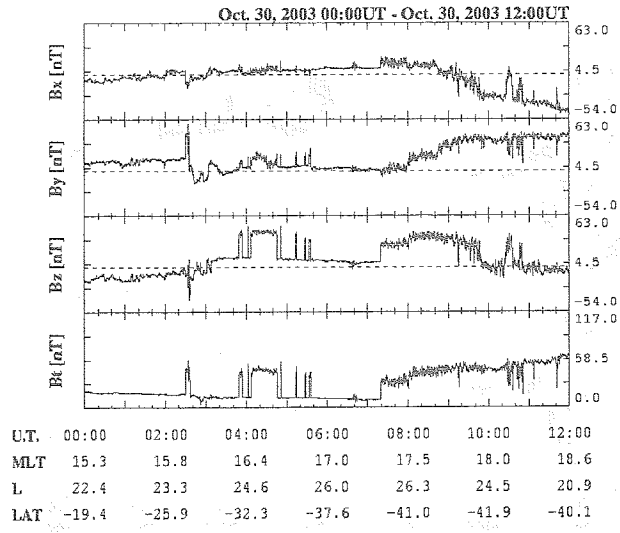


Fig. 10. An overview of the magnetic field variations observed in the upstream region to the dusk-side outer magnetosphere along the GEOTAIL satellite trajectory during the interval of 12 hrs from 0000 UT to 1200 UT on October 30. From top to bottom the panels are three components of the magnetic fields, B_x, B_y, and B_z in GSM coordinates, and the magnetic field intensity, respectively.

This document is provided by JAXA.

of GEOTAIL. The peak-to-peak amplitude was approximately 3 nT in the upstream region, and 6–7 nT in the magnetosheath and in the outer magnetosphere. The observed characteristics of the Pc 3 waves are summarized as follows: (i) The dominant frequency was observed at 20–30 mHz. (ii) The spectral peak power was approximately $5\times10\,nT^2/Hz$ in the upstream region, $8\times10\,nT^2/Hz$ in the magnetosheath and $1.5\times10^2\,nT^2/Hz$ in the outer magnetosphere. (iii) The dominant oscillation was different in each region; transverse in the upstream and the magnetosheath region near the bow shock, and compressional in the magnetosheath near the magnetopause and in the outer magnetosphere. (iv) Wave energy propagated earthward and duskward, perpendicular to the magnetic field-line with the Poynting flux of approximately $3\text{–}4\times10^{-6}\,W/m^2$ on average.

Figure 10 shows the observed magnetic field variations from 00 h to 12 h UT on October 30, when the satellite traversed upstream of the quasi-perpendicular shock to the dusk-side outer magnetosphere. Three components of magnetic field, B_x, B_y and B_z in the GSM coordinates, the magnetic field intensity, B_t, are presented from the top to the bottom panels, respectively. Multiple crossings of the bow shock are observed from 02 UT to 06 UT, which are characterized by impulsive or rectangular sudden changes in the magnetic field variations. Pc 3 ULF waves are recognized throughout the interval.

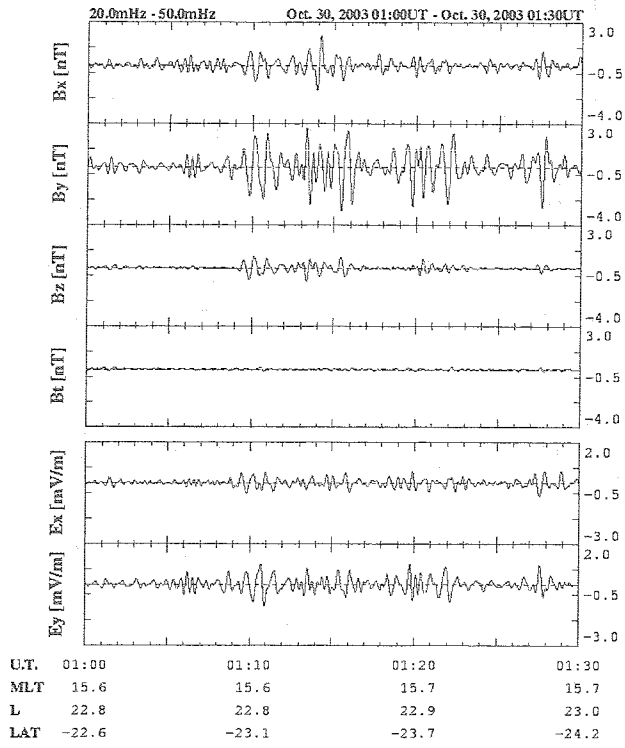


Fig. 11. A typical example of Pc 3 oscillations observed in the upstream region. The transverse oscillation is clearly identified with the largest oscillations in the B_y component of the magnetic field in the MFA coordinates.

This document is provided by JAXA.

They appear as being crowded with high-frequency variations. In particular, the large amplitude oscillations are clearly recognized in the later phase from 07 UT, when the satellite passed through the dusk-side magnetosheath and the outer magnetosphere. The observed characteristics of Pc 3 waves in each region are presented in order as follows.

An example of Pc 3 waves seen upstream of quasi-perpendicular shock is shown in Fig. 11 with representing traces of filtered Pc 3, band-pass filtered from 20 mHz to 50 mHz, from 0100 UT (1536 MLT) to 0130 UT (1542 MLT). From the top to bottom panels are three components of the magnetic field and two components of the electric field. The traces are presented with the field-aligned coordinates (MFA), in which the Z axis is parallel to the local mean-magnetic field, which is calculated every 10 min. The Y axis is taken in a plane perpendicular to the plane containing the satellite and the center of the earth. The X axis is set to the direction of a vector product between Y and Z axes. The horizontal axis of the figure indicates universal time (UT), magnetic local time (MLT), L-values and magnetic latitude (LAT). Tick marks are given each minute with a large mark at every 10 min. The Pc 3 oscillations seem to be coherent in

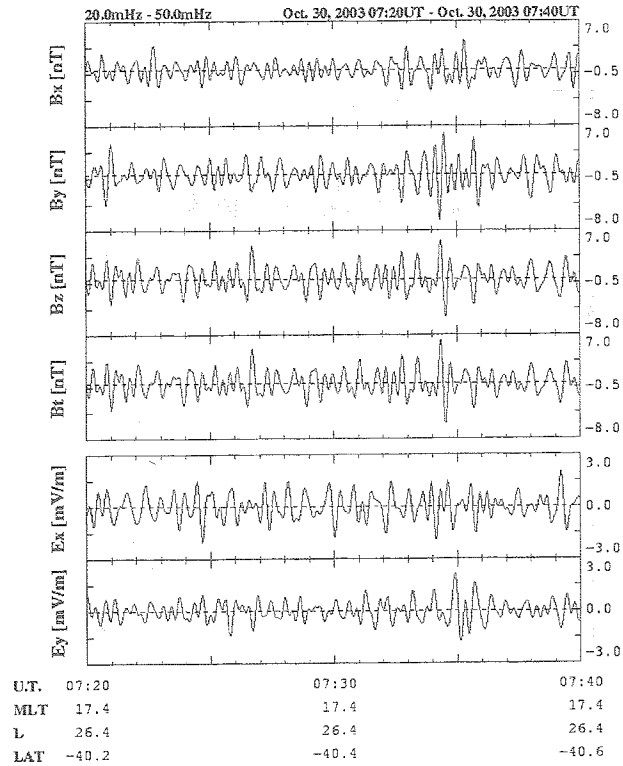


Fig. 12. A typical example of Pc 3 oscillations observed in the magnetosheath immediately after the bow shock crossing during the interval of 20 min from 0720 UT to 0740 UT. The large amplitude oscillations (6–8 nT in peak-peak) are clearly observed in all components of the magnetic field, and in the magnetic field intensity.

This document is provided by JAXA.

both fields. The largest amplitude oscillations are seen in the B_x and B_y components of the magnetic field, attaining 6–7 nT peak to peak in the B_y component. For the electric field the peak to peak amplitude is 2 mV/m in the E_y component. Therefore, the oscillations are known as transverse oscillations.

Figure 12 shows traces of the magnetic and electric field variations during the period of 20 min from 0720 UT to 0740 UT (1724 MLT) when the satellite traversed through the dusk-side magnetosheath immediately after crossing the bow shock. The peak-to-peak amplitude of the oscillation is 6–7 nT, almost the same for the three components of magnetic field. Therefore, the magnetic field oscillation exhibits both transverse and compressional modes. The electric field oscillates coherently to the magnetic field oscillation with amplitude of 2–3 mV/m. The power spectra of the magnetic field are shown in Fig. 13. From the figure two dominant spectral peaks can be recognized at 30 mHz and 60 mHz. These spectral peak powers are approximately same in both oscillation components, B_y and B_z, with the power of $7\times10\,\mathrm{nT^2/Hz}$.

Another interval is examined for 15 min from 0740 UT to 0755 UT when the satellite stayed in the magnetosheath closely to the magnetopause. The filtered traces of three components of the magnetic field and two components of the electric field are shown in Fig. 14. Inspecting the figure the oscillation amplitude is largest in the B_z component. The peak-to-peak amplitude is about 7–8 nT. While, for the transverse components the amplitude is 3–5 nT on average. Therefore, the dominant oscillation changed to the oscillation parallel to the magnetic field-line, which means the compressional mode.

The Poynting flux is given in Fig. 15. The Poynting flux reaches approximately to

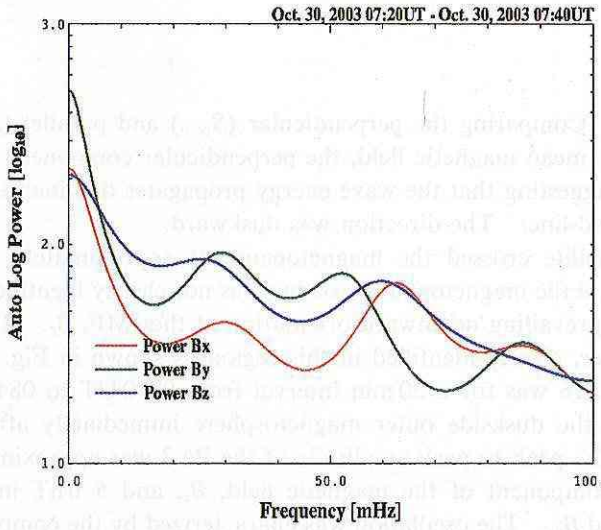


Fig. 13. Power spectra of Pc 3 for the interval of 20 m from 0720 to 0740 UT. Two spectral peaks can be identified in each field component at the frequency of 30 mHz and 60 mHz, respectively. The spectral powers of the transverse (B_y) and compressional (B_z) components are almost same.

This document is provided by JAXA.

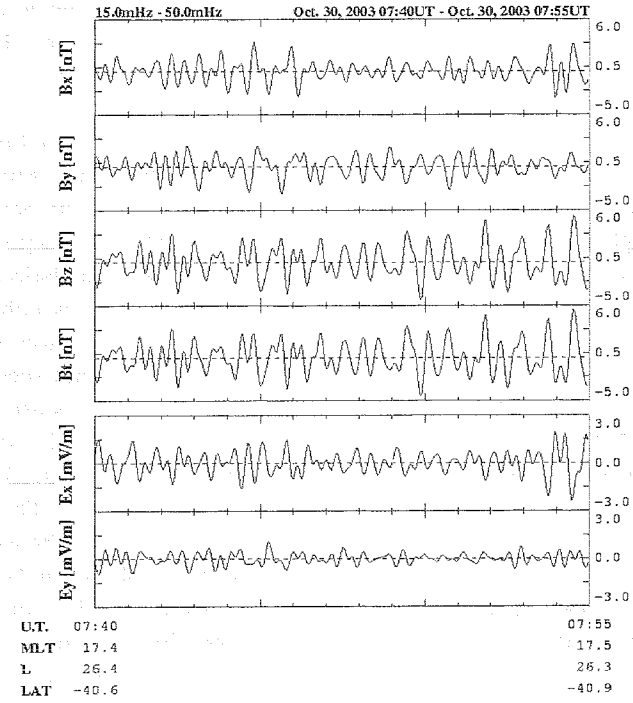


Fig. 14. A typical example of Pc 3 oscillations observed in the magnetosheath close to the magnetopause. The compressional component of the magnetic field, B_z is superior to the other two transverse components, B_x and B_y, and extends to approximately 6–7 nT on average.

$1\text{–}2\times10^{-6}$ W/m^2. Comparing the perpendicular (S_{perp}) and parallel (S_z) components with respect to the mean magnetic field, the perpendicular component was superior to the parallel one, suggesting that the wave energy propagates dominantly perpendicular to the magnetic field-line. The direction was duskward.

Then, the satellite crossed the magnetopause at approximately 0800 UT (1730 MLT). In this case the magnetopause crossing was not clearly identified. This might be masked by the prevailing northward orientation of the IMF, B_z. The Pc 3 oscillations were, however, clearly identified in this region as shown in Fig. 10. The wave trace given in Fig. 16 was for a 30 min interval from 0810 UT to 0840 UT when the satellite stayed in the duskside outer magnetosphere immediately after crossing the magnetopause. The peak to peak amplitude of the Pc 3 was approximately 6–7 nT in the field-aligned component of the magnetic field, B_z, and 5–6 nT in the transverse components, B_x and B_y. The oscillation was characterized by the compressional mode, almost the same seen in the magnetosheath near the outside of the magnetopause. The dominant power was 1×10^2 nT^2/Hz at the frequency of 30 mHz in the compressional component, B_z. The Poynting flux was approximately $2\text{–}3\times10^{-6}$ W/m^2 and dominant in the perpendicular component, whose propagation was tailward.

This document is provided by JAXA.

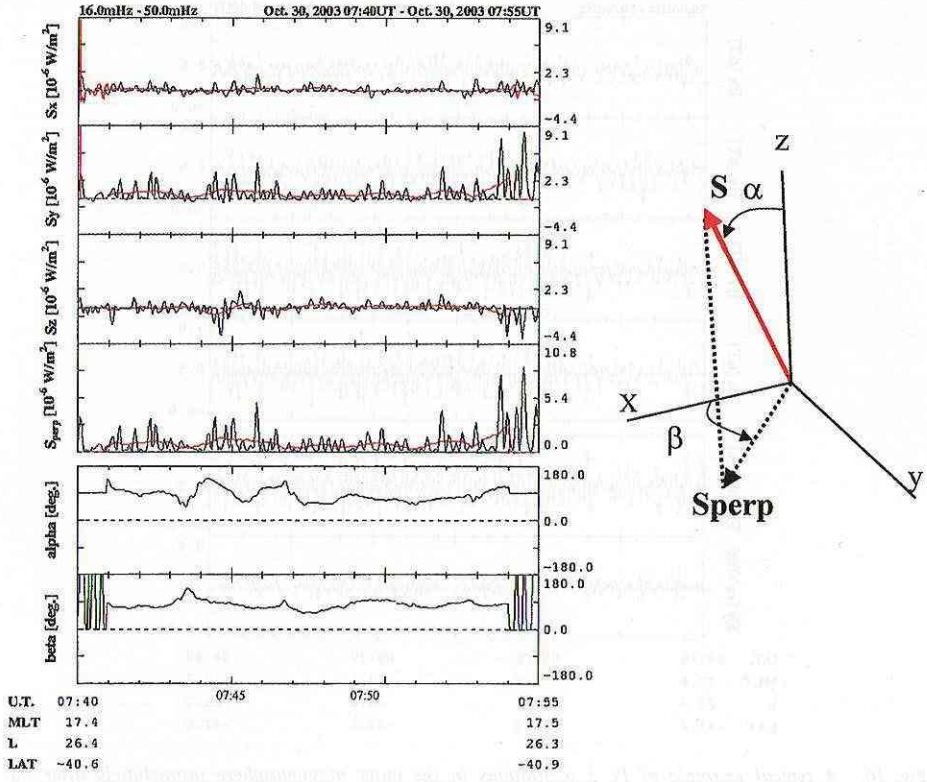


Fig. 15. Poynting flux of the Pc 3. From top to bottom the Poynting flux X, Y and Z-components, S_x, S_y and S_z, respectively, and the perpendicular component to the magnetic field, S_{perp}, and angles of Poynting flux respective to a direction of magnetic field, the polar angle, Alpha and the azimuth angle, Beta. The S_y component of the Poynting flux is superior to the others, and the Alpha=90°, and the Beta=90°, indicating that the Pc 3 wave energy propagates predominantly duskward perpendicular to the magnetic field-line.

Summarizing, on October 30, 2003 GEOTAIL traversed from the upstream region to the dusk-side outer magnetosphere through the magnetosheath. The amplitude of Pc 3 observed in these regions was very large, almost the same in the magnetosheath and in the outer magnetosphere, 6–8 nT, and amongst the largest ever observed in these regions. Usually the amplitude of Pc 3 is larger in the magnetosheath than in the outer magnetosphere, and the transmission rate is 10^{-2}–10^{-3}. However, in this case the amplitude of Pc 3 in the outer magnetosphere was almost the same to that observed in the magnetosheath. This might be due to the matching of several conditions of the solar wind in this storm period: the solar wind dynamic pressure was very large, the IMF B_z was very intense and northward throughout this interval.

The oscillation mode was different in the upstream, magnetosheath and outer magnetosphere regions. In the upstream region transverse oscillations were dominant and it may be generated by a cyclotron instability. On the other hand, in the

This document is provided by JAXA.

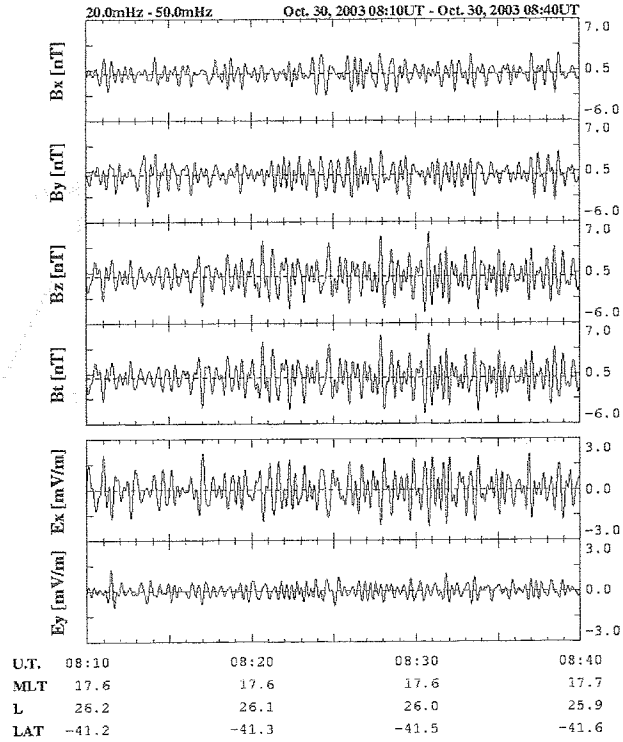


Fig. 16. A typical example of Pc 3 oscillations in the outer magnetosphere immediately after the magnetopause crossing. The compressional component of the magnetic field, B_z is superior to the other two transverse components, B_x and B_y. The amplitude of B_z is larger and extends to 6–7 nT on average.

magnetosheath near the magnetopause the oscillation changed to the compressional mode. The compressibility seemed to increase as the satellite approached the magnetopause. This might be due to the mixing of the conveyed cyclotron waves from the upstream region with the waves generated in the magnetosheath, where the mirror mode instability may be dominant as suggested by Anderson and Fuselier (1993), Anderson *et al.* (1994), Gray and Winske (1993), and Song *et al.* (1992, 1994). In the outer magnetosphere the compressional mode was dominant. This might be due to the transmission of the magnetosheath waves. The average direction of the Poynting flux was duskward, perpendicular to the average magnetic field, which indicates that Pc 3 wave energy in the dusk-side magnetosheath and the outer magnetoshere propagates duskward along with the draped duskward magnetic field and bulk flow in this region.

7. Summary and discussions

The primary importance in this study is that the causal relationship between the solar flares and their produced CMEs and the ICMEs, and their geo-effectiveness to the

This document is provided by JAXA.

terrestrial magnetosphere. The extremely large flares that occurred on October 28 and 29, 2003, produced extremely high-speed interplanetary coronal mass ejections and some of the largest magnetic field variations in the terrestrial magnetosphere ever recorded. A variety of enhanced activity was studied both in the space and on the ground. The observations by ACE and WIND revealed the peculiar magnetic and plasma structures in the interplanetary space in regions, upstream and downstream of the earth. The results from GEOTAIL clarified the properties of Pc 3 ULF waves from upstream and downstream of the bow shock, and in the dusk-side outer magnetosphere. The ground observations provide us a new insight into the dynamic response of the magnetosphere to these interplanetary disturbances. All of these contributed to establish a new perspective for the space weather prediction. The results from the examination of these satellite and ground observations during this super magnetic storm are summarized as follows:

1) Extremely high-speed solar wind hurled from the big flares was observed approximately as 2000 km/s.
2) The transit time of this high-speed solar wind from the sun to the earth was about 20 hrs.
3) This high-speed solar wind produced large amplitude magnetotail flapping motions.
4) A series of ICMEs yielded typical magnetic field rotations of the IMF, with the B_z component turnings of the north-south and south-north directions.
5) These IMF B_z polarization changes produced a typical response of the magnetic field activity of the terrestrial magnetosphere.
6) The southward orientation of the IMF, B_z produced substorm activities and large negative Dst variations extending to -350 nT and/or -400 nT, on the ground.
7) The northward orientation of the IMF, B_z enhanced magnetic pulsation activity in the magnetosphere.
8) During the northward IMF large amplitude Pc 5 oscillations were observed over the regions extending from the early morning to the pre-midnight, and from high to low latitude.
9) Enhanced Pc 3 wave activity was observed from the upstream region, through the magnetosheath, and to the dusk-side outer magnetosphere.
10) The amplitude of the Pc 3 was 4–5 nT in the upstream region, and 6–7 nT in the magnetosheath and the outer magnetosphere. These observed amplitudes are amongst the largest ever observed there.
11) Very high transmission efficiency of the Pc 3 waves from the magnetosheath to the outer magnetosphere was observed during this period.
12) The Poynting flux of the Pc 3 showed tailward propagation, dominantly perpendicular to the magnetic field-line.

A variety of magnetic field variations were examined in this study. First of all the transit time of the ICME was found to be surprisingly very short, about 20 hrs for both CMEs occurred on October 28, and 29, 2003. Gopalswamy *et al.* (2001) studied statistically the relationship between the transit time and the initial speed of the CME. However, they have no data for such a high solar wind speed in their study. The initial speeds of the CMEs occurred on October, 28 and 29, 2003 were approximately 2459 km/s, and 2029 km/s. Moreover, by comparing arrival times by ACE and WIND satellites

This document is provided by JAXA.

staying upstream of the bow shock and downstream in the distant tail, respectively, the speed for the first shock was estimated as 2189 km/s. The high speed of this shock suggests that the deceleration of the initial speed of CME is not effective to the distance of 1 AU. Therefore, the observed high initial speeds of CMEs for this October superstorm can not be directly compared with the result obtained by Gopalswamy *et al.* (2001). The relationship should be considered in more detail. This is our future work.

The relationship between transit times of super magnetic storms (Dst<-200 nT) and initial speeds of CMEs is shown in Fig. 1. This figure suggests that the observation of initial speed of CME is important for prediction of arrival time of super magnetic storms.

Tail flapping oscillations were observed in the very distant tail at $-160R_e$ in this study. Such a distant tail observation of flapping oscillations has never been reported. Much of the observation of the tail flapping motion reported so far were at most the distance to -30~$-60R_e$. The previous studies reported by Mihalov *et al.* (1970), Toichi and Miyazaki (1976), and Nishida and Lyon (1972) were based on satellite observations performed by Explorer 33, 34 and 35 within such distances. The typical characteristics of the flapping motion of the magnetotail reported by them were 3–8 min for the period and at most about 10 nT for the amplitude.

However, in this study the WIND satellite encountered the high-speed solar wind at the distant tail of about $-160R_e$ during this storm. The amplitude of the observed tail flapping motions was very large, about 30–40 nT. In general it is not considered that such large amplitude tail flapping motions might be due to the intrinsic geomagnetic field in such a distant tail. Therefore, the observed oscillations might be the magnetic field variations when they reconnected to the magnetic field of the ICMEs only in the X component.

The oscillations were observed only in the X component of the magnetic field. This means that the oscillation occurred alternately in the earthward and tailward oriented magnetic field in a X-Z plane. The amplitude of the alternate oscillations of the magnetic field was almost same. Therefore, the oscillation might be symmetric about the central line of the tail. Three decades ago Siscoe (1969) reported that there was a possibility of two types of the tail flapping oscillation in the magnetotail, *i.e.*, one is symmetric and the other is anti-symmetric. The observed characteristics in this study are in good agreement with the anti-symmetric oscillation mode since the magnetotail oscillated as a rigid oscillation of the outer boundaries about the center.

Large amplitude Pc 5 waves were observed during the recovery phase of the magnetic storm. This Pc 5 was characterized with a very coherent oscillation over widely spaced ground stations. The reason why such a coherent Pc 5 oscillation was observed might be due to the fact that it oscillated globally, like as a global mode, excited by a sudden compression of the magnetosphere due to the sudden enhancement of solar wind dynamic pressure, and the reason why the amplitude of the oscillation was very large might be due to the fact that it occurred during the intense northward IMF B_z, and also in the recovery phase of this super magnetic storm.

The condition of the magnetosphere during this period seemed to be very suitable for excitation of ULF waves. It has been well known that the Kelvin-Hermholtz

This document is provided by JAXA.

instability at the magnetospheric boundary is easily excited in such conditions (Miura, 1995). Moreover, the solar wind density was enhanced at that moment. This might be another important factor to trigger the Pc 5. This solar wind density enhancement was also observed by GEOTAIL. Large amplitude density oscillations were observed by GEOTAIL at the dawn side magnetopause. However, the period of the density oscillation observed by GEOTAIL was longer than that of the observed Pc 5 on the ground. At this moment the longitudinal location of GEOTAIL was almost similar to that of the IMAGE chain stations. Therefore, the oscillation observed on the ground might be of intrinsically magnetospheric origin and due to a global mode oscillation of the magnetosphere.

Another interesting observation during this storm period was Pc 3 oscillations observed in space by the GEOTAIL satellite, from upstream and downstream of the bow shock, and in the dusk-side outer magnetosphere. The observation was from 04 h UT to 09 h UT on October 30, when the north-south component of the IMF was completely northward with the intensity of 5–10 nT.

Surprisingly, the amplitude of the Pc 3 was almost the same in the magnetosheath and the outer magnetosphere. This was peculiar. Usually the amplitude of Pc 3 observed in the magnetosphere is much less than that observed in the magnetosheath. The transmission coefficient is known to be 1/100–1/1000. The reason for the present case might be due to the northward orientation of IMF, B_z.

Another important result concerns the oscillation characteristics of Pc 3. These varied from transverse oscillations observed in the upstream region to compressional oscillations near the magnetopause. The compressibility increased when the satellite approached the magnetopause. Anderson *et al.* (1994) reported the association of magnetic field fluctuations with the plasma depletion layer downstream of the quasi-perpendicular shock, mainly in the stagnation region, and found that there were two dominant spectral features. One was compressional fluctuations which related to the mirror mode instability, and the other was transverse fluctuations closely related to the cyclotron instability of H^+ and He^{2+}. They concluded that these magnetic field signatures and plasma properties were found to progress from mirror waves with high $\beta_{\|p}$ and low A_p in the magnetsheath proper to H^+ and He^{2+} cyclotron waves associated with the high A_p and low $\beta_{\|p}$ in the plasma depletion layer, where $\beta_{\|p}$ and A_p mean a beta ratio and an anisotropy factor, respectively. The above results in our study might be due to similar reasons discussed by Anderson *et al.* (1994).

In this study plasma data are not available to use due to the improper operation of low energy plasma instruments (LEP) onboard GEOTAIL during the storm period. Therefore, the plasma characteristics could not be identified in this study. However, both types of oscillations were observed in the magnetosheath. Therefore, they might correspond to the mirror waves and ion cyclotron waves, respectively.

Lee *et al.* (1988) studied a simulation of waves generated in the magnetosheath under the assumption of a high ion temperature anisotropy, from which they found that a large temperature anisotropy generates a mirror wave downstream of a quasi-perpendicular shock, and in the earth's bow shock large amplitude (perturbed B almost equal to B_0) mirror waves develop downstream of the shock ramp. The large amplitude Pc 3 waves observed in the magnetosheath might be supported by this simulation study.

This document is provided by JAXA.

Compressional mode oscillations dominated the transverse mode in the dusk side outer magnetosphere. This result is consistent with our previous study of Pc 3 oscillations using the GEOTAIL magnetic field observation for the satellite trajectory along with the dayside magnetopause, in which the compressional oscillation was dominant near the magnetopause boundary. When the satellite trajectory was separated from the magnetopause to the magnetosphere, the oscillation characteristics changed to the transverse oscillation and the signature of the field-line resonance was much clearly identified (Sakurai *et al.*, 1999).

8. Conclusion

The causal relationship between the solar flares and their produced magnetic field variations in the terrestrial magnetosphere can be studied on the basis of a variety of phenomenon observed in the interplanetary space, in the magnetosphere and on the ground during the period of the super magnetic storm occurred from October 29 to 31, 2003. The most important observation was the very high solar wind. The high stream solar winds successively produced big disturbances in the terrestrial magnetosphere. The period is the declining phase of the solar activity of the solar cycle 23. Why did such big flares occur during this phase? This question is most important to be resolved, but it remains still unresolved. However, we were able to obtain many valuable insights into the solar-terrestrial relationship throughout this study.

Acknowledgments

We have to acknowledge to use the SOHO LASCO CME CATALOG, which is generated and maintained by the Center for Solar Physics and Space Weather, The Catholic University of America in cooperation with the Naval Research Laboratory and NASA. SOHO is a project of international cooperation between ESA and NASA, and to use the magnetic field and plasma data measured by ACE, WIND, GOES 10 and GEOTAIL satellites through the Coordinated Data Analysis Web (CDAWeb). We also thank the institutes who maintain the IMAGE magnetometer array. The Dst index is due to the World Data Center C2 at the Kyoto University. We also thank the referees for their valuable comments on our original manuscript.

The editor thanks Drs. M. Nose and F.W. Menk for their help in evaluating this paper.

References

Anderson, B.J. and Fuselier, S.A. (1993): Magnetic pulsations from 0.1 to 4 Hz and associated plasma properties in the Earth's subsolar magnetosheath and plasma depletion layer. J. Geophys. Res., **98**, 1461–1479.

Anderson, B.J., Stephen, A., Fuselier, S.A., Gary, P. and Denton, R.E. (1994): Magnetic spectral signatures in the Earth's magnetosheath and plasma depletion layer. J. Geophys. Res., **99**, 5877–5891.

Gopalswamy, N., Lara, A., Yashiro, S., Kaiser, M.L. and Howard, R.A. (2001): Predicting the 1-AU arrival times of coronal mass ejections. J. Geophys. Res., **106**, 29207–29217.

Gray, S.P. and Winske, D. (1993): Simulations of ion cyclotron anisotropy instabilities in the terrestrial

This document is provided by JAXA.

magnetosheath. J. Geophys. Res., **98**, 9171–9179.
Lee, L.C., Price, P.P. and Wu, G.S. (1988): A study of mirror waves generated downstream of a quasi-perpendicular shock. J. Geophys. Res., **93**, 247–250.
Mihalov, J.D., Sonett, C.P. and Colburn, D.S. (1970): Reconnection and noise in the geomagnetic tail. Cosm. Electrodyn., **1**, 178–204.
Miura, A. (1995): Kelvin-Helmholtz instability at the magnetopause: Computer simulation. Physics of the Magnetopause, ed. by P. Song *et al.* Washington, D.C., Am. Geophys. Union, 285–291 (Geophysical Monograph 90).
Nishida, A. and Lyon, E.F. (1972): Plasma sheet at lunar distance structure and solar wind dependence. J. Geophys. Res., **77**, 4086–4099.
Sakurai, T., Tonegawa, Y., Kitagawa, T., Yumoto, K., Yamamoto, T., Kokubun, S., Mukai, T. and Tsuruda, K. (1999): Dayside magnetopause Pc 3 and Pc 5 ULF waves observed by the GEOTAIL satellite. Earth Planets Space, **51**, 965–978.
Siscoe, G.L. (1969): Resonant compressional waves in the geomagnetic tail. J. Geophys. Res., **74**, 6482–6486.
Song, P., Russell, C.T. and Thomsen, M.F. (1992): Waves in the inner magnetosheath: A case study. Geophys. Res. Lett., **19**, 2191–2194.
Song, P., Russell, C.T. and Gary, S.P. (1994): Identification of low-frequency fluctuations in the terrestrial magnetosheath. J. Geophys. Res., **99**, 6011–6025.
Toichi, T. and Miyazaki, T. (1976): Flapping motions of the tail plasma sheet induced by the interplanetary magnetic field variations. Planet. Space Sci., **24**, 147–159.

This document is provided by JAXA.

Adv. Polar Upper Atmos. Res., 19, 42–54, 2005
© 2005 National Institute of Polar Research

Subionospheric LF monitoring of ionospheric perturbations prior to the Tokachi-oki earthquake and a possible mechanism of lithosphere-ionosphere coupling

Masashi Hayakawa[1]*, Alexandre V. Shvets[1,2] and Shinko Maekawa[1]

[1] *The University of Electro-Communications, 1–5–1, Chofugaoka, Chofu-shi, Tokyo 182-8585*
[2] *Usikov Institute for Radiophysics and Electronics, 12 Academician Proskury Street, Kharkov 61085 Ukraine*
**Corresponding author. E-mail: hayakawa@whistler.ee.uec.ac.jp*

(Received December 10, 2004; Accepted June 28, 2005)

Abstract: We first present the results of simultaneous monitoring of subionospheric LF propagation over two different paths prior to a very strong Tokachi-oki earthquake (near the east coast of Hokkaido Island on September 25, 2003) with magnitude 8.3. Nighttime amplitude fluctuations of the Japanese Time Standard Transmitter (JJY, 40 kHz) signal received at Moshiri (Japan, geographic coordinates 44°N, 142°E) and at Petropavlovsk-Kamchatski, Russia (53°N, 158°E) were analyzed. As a possible precursory signature we observed synchronous intensification of quasi-periodic 16-day variations of the dispersion in the signals received at both observation stations before the earthquake. The strongest deviations observed as a rule were depletions of signal amplitude probably connected with an increase in loss in the ionosphere by the enhancement of turbulence. This is due to dissipation of internal gravity waves (IGW) at the lower ionospheric heights. A scenario of interconnection between seismo-activity, atmospheric gravity waves and planetary waves, is proposed to explain the observed association with strong earthquakes.

key words: subionospheric LF propagation, earthquakes, ionospheric perturbations

1. Introduction

The effect of earthquakes has been expected to take place mainly in the Earth's crust, but we have found recently a lot of electromagnetic phenomena in the atmosphere as well as in the ionosphere (Hayakawa, 1999; Hayakawa and Molchanov, 2002). It is recently believed that the ionosphere is extremely sensitive to the seismic activity since the clear discovery of ionospheric perturbations for the Kobe earthquake by means of subionospheric VLF monitoring (Hayakawa *et al.*, 1996).

VLF/LF subionospheric radio sounding techniques have been studied as a solution of the short-term earthquake prediction for the last decade. These techniques are based on the detection of disturbances in the lower ionosphere, which can be of seismic origin. Some promising results demonstrate anomalous deviations in the VLF phase or/and amplitude (Gokhberg *et al.*, 1989; Morgounov *et al.*, 1994) and terminator time position (Hayakawa *et al.*, 1996; Molchanov and Hayakawa, 1998) in the diurnal patterns

This document is provided by JAXA.

of radio signals propagated over paths across the areas of future strong earthquakes.

The possible mechanisms of the energy transmission from processes in the earth's crust related to earthquake preparation, to the lower ionosphere have been discussed recently by Hayakawa and NASDA's Earthquake Remote Sensing Frontier Research (2001), Pilipenko *et al.* (2001) and Hayakawa *et al.* (2004). Three types of the lithosphere-atmosphere-ionosphere coupling have been proposed in those papers. 1) Electromagnetic coupling is connected with the direct penetration of the DC atmospheric electric field induced due to the appearance of seismo-related electric charges on the earth's surface. It can lead to the substantial modifications of ionospheric properties. 2) Chemical coupling is determined by variations of the fair weather electric field in the lower ionosphere due to the enhancement of conductivity of the lower atmospheric layers ionized by radon emanating from seismic faults. 3) Acoustic coupling implies an influence of atmospheric wave processes originating near the earth's surface onto the lower ionosphere. It is known that the atmosphere serves as an amplifier for upward propagating acoustic and internal gravity waves due to the exponential decrease in its density with altitude. So, even very small-amplitude (but large scale as we can assume for the tectonic processes) atmospheric oscillations originated from the near-ground sources can be transformed to high-amplitude waves at the lower ionospheric heights. The possible mechanisms of IGW generation in the lithosphere outlined by Hayakawa and NASDA's Earthquake Remote Sensing Frontier Research (2001) and Pilipenko *et al.* (2001) include so-called seismo-gravitational oscillations of the Earth with periods from a few tens of minutes to a few hours (Lin'kov *et al.*, 1998), gas yield from preparatory zone (Voitov and Dobrovolsky, 1994), and periodic heating of seismic faults (Gokhberg *et al.*, 1996).

As shown by Molchanov and Hayakawa (1998), some precursory signatures in VLF signal appeared as an intensification of background quasi-periodic variations with periods 5–16 days coinciding with the frequency range of planetary waves. Our initially proposed hypothesis on the excitation of PWs by shocks in an earthquake preparatory zone met considerable problems connected partially with too long time of propagation of PWs from the ground to the lower ionosphere. Later the gravity waves modulated by planetary waves were considered as a faster energy carrier from the lithosphere to the ionosphere in order to explain the effects observed in subionospheric VLF radio signals (Molchanov *et al.*, 2001).

Consistent with the present-day concepts, PWs originate in the troposphere and stratosphere and penetrate into the lower ionospheric heights (*e.g.* Namboothiri *et al.*, 2002 and references therein). The upward propagation of PWs is strongly determined by regular stratospheric winds. As predicted by the theory by Salby (1981a,b), PWs will be trapped by the westward winds that dominate during summer and they can propagate through the eastward winter winds to lower ionosphere heights. This prediction is confirmed experimentally by the radar observation of wind variations in the mesosphere and lower thermosphere (MLT) that show seasonal variability of PW activity reaching maximal intensity during winter months. The existence of minor summer maxima in the PW activity in the MLT region is explained by different causes. These are the penetration of PWs from the winter hemisphere, and breaking of gravity waves whose transmission through the stratosphere is modulated by PWs (Smith, 1996;

This document is provided by JAXA.

Namboothiri *et al.*, 2002 and references therein).

We present results of subionospheric LF monitoring performed simultaneously at two widely separated receiving stations during the Tokachi-oki earthquake with magnitude greater than 8. In this study we show an additional evidence for PW influence on the lower ionosphere through the modulation of the upward propagating IGW, and we compare our observational results with the above-mentioned concept of the PW activity in the MLT region.

2. Data acquisition

A signal transmitted by Japanese Time Standard LF station (JJY, 40 kHz) located at the geographic coordinates (37.37°N, 140.85°E) in Fukushima prefecture was monitored at two different locations. These are the Moshiri station in Hokkaido and the station at Petropavlovsk-Kamchatski that is operated as a part of the Russian-Japanese complex geophysical observatory (Uyeda *et al.*, 2002). The third Fresnel zone is plotted in Fig. 1 for each signal propagation path. The positions of the events corresponding to the Tokachi-oki earthquakes are marked with large empty circles in the map (Fig. 1).

For receiving and logging of the VLF/LF signals, JAPAL system (a modification

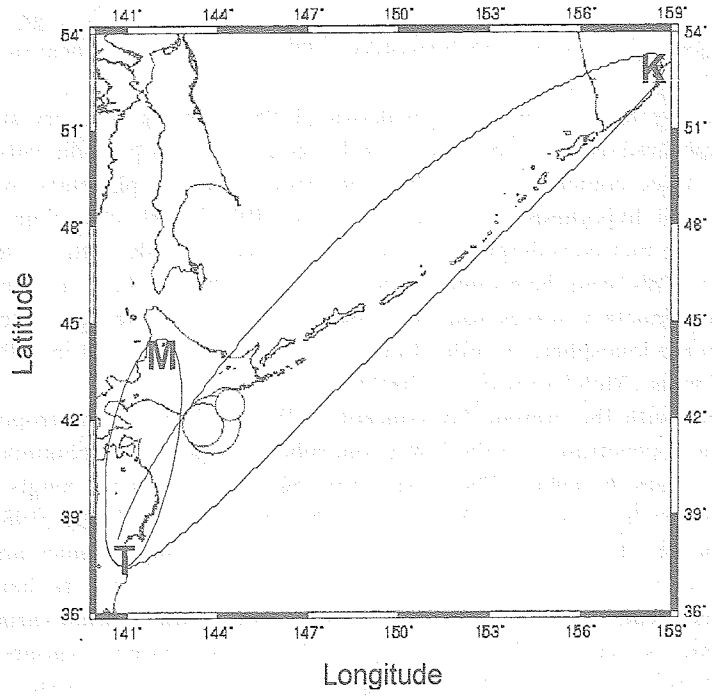


Fig. 1. A map of Tokachi earthquakes and LF propagation paths used for the study. Moshiri and Petropavlovsk-Kamchatski observatories, and JJY transmitter are marked in the figure with the bold letters M, K, and T respectively.

This document is provided by JAXA.

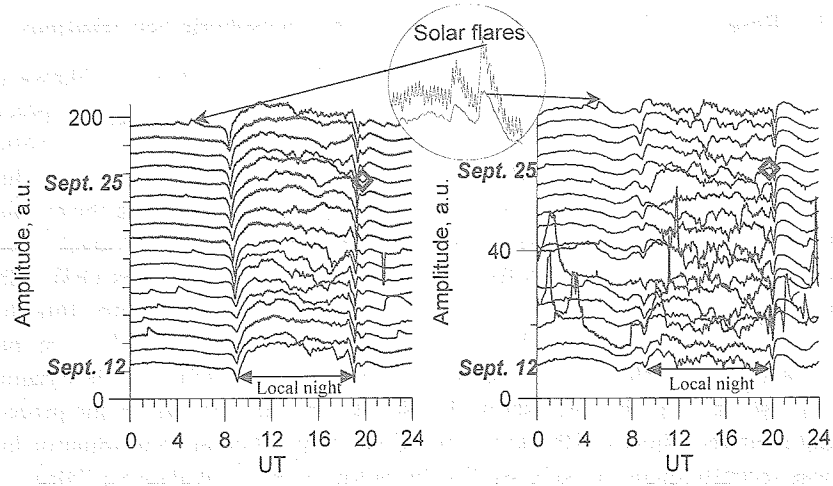


Fig. 2. Examples of daily amplitude variations measured in Petropavlovsk-Kamchatski (left) and Moshiri (right) around the date of the Tokachi earthquake. The earthquake time September 25, 2003, 1950 UT (or September 26, 0450 JST) is marked by a rhomb. The nighttime conditions over both propagation paths are marked by two-sided arrows. Synchronous perturbations in the signals caused by solar flares are demonstrated in the inset.

of the OmniPAL receiver) (Dowden and Adams, 1988) was used. The vertical electric component was received with a rod antenna installed on the roof of laboratory buildings at both locations.

Daily amplitude variations measured at both observatories around the date of the earthquake are plotted in Fig. 2. The different nature of the diurnal dependencies of the signal at these two places is connected with both the different orientation of the propagation paths to the terminator and their different lengths. For the shorter path (JJY–Moshiri) we note stronger fluctuations during the nighttime period in comparison with the longer path possibly due to its proximity to the interference minimum as it can be concluded from a comparison of average day-time and night-time levels. It is known that strong disturbances in VLF/LF signals occur during daytime due to additional ionization of the lower ionosphere by X-ray solar flares. They lead to increases in the VLF/LF signal amplitudes because of increased conductivity of the upper waveguide wall. Such disturbances in the signals are observed simultaneously, and they are shown in an inset of Fig. 2. Very strong (about 10 times over regular signal level) positive excursions of the amplitude of the signal observed at Moshiri during the daytime have a shape that is not typical for solar flare effects (fast growth and relatively slow decay), and seems to be unexplained in terms of waveguide propagation theory. So, we have to suppose another source for these disturbances in the signal. Possibly they are of artificial local origin.

This document is provided by JAXA.

3. Results of the LF data processing on the ionospheric perturbations

In a case study of different strong earthquakes Molchanov and Hayakawa (1998) have shown effectiveness of the terminator time method in revealing any precursory phenomena in VLF signals. Terminator times are determined by the positions of characteristic minima occurring in the diurnal dependencies of amplitude (and phase) of VLF/LF signals when the terminator crosses a propagation path during the evening and morning periods of time. Maekawa and Hayakawa (2005) have investigated the characteristics of terminator times for different propagation directions (EW, NS) and for short and long paths, and we expect clear changes in the terminator time for EW paths. Terminator minima are known to occur due to the interference between different waveguide modes. Their positions are sensitive to ionospheric irregularities along the propagation path as was shown by Hayakawa *et al.* (1996) for the propagation path being relatively short (~1000 km) and nearly perpendicular to terminator line and also as was recently quantitatively studied by Soloviev and Hayakawa (2004).

To explore a possibility of applying the terminator time method to the Tokachi-oki earthquake case, we demonstrate the evolution of the terminator time deviations around the date of the earthquake for both observatories in Fig. 3. We can find that the behavior of these deviations appears to be quiet. Maximal deviations do not exceed 15 min for both observation locations, which is much smaller than the effect (~45 min) observed for the Kobe earthquake (Hayakawa *et al.*, 1996). Possibly reduced sensitivity of the VLF signals to the ionospheric disturbances during the day-night transition period is connected with a specific (near meridian) orientation of the propagation paths (Maekawa and Hayakawa, 2005; Soloviev and Hayakawa, 2004).

In this study we use a technique based on the dispersion of the nighttime deviations of the LF signal amplitude from $\pm$8-day running mean diurnal runs. We choose the 17-day window lag for averaging to achieve a compromise of contradictive requirements between removing seasonal changes of night time duration and smoothing stochastic fluctuations in the signal amplitude. Figure 4 illustrates an example of the average amplitude $<A>$, current amplitude $A(t)$, and difference $A(t)-<A>$. It demonstrates an anomalous nighttime deviation observed at Petropavlovsk-Kamchatski on September 18. To emphasize and distinguish more clearly the deviations in the signal amplitude we applied a nonlinear transform to the original LF data records. The linear scaling of the signal emphasizes the large excursions in amplitude which could be short in time (spikes). The logarithmic scaling acts in an opposite way: it diminishes the large excursions and emphasizes low amplitude variations with high dynamic range. We choose an alternative to the linear and logarithmic scaling that is determined by the next expression: $A(a)=\exp[\log(a)]$. In such a way we reduce both the influence of low and high abnormal deviations that are important in the analysis of integral parameters of the signal. So, below we will operate formally with the value $A(a)$ instead of the signal amplitude. Amplitude dependencies were normalized by an average nighttime signal level to make comparable the relative deviations measured at both observatories.

To search for the most informative parameters together with the total values of the dispersion D we also analyzed its fractions composed of both positive D_p and negative D_n

This document is provided by JAXA.

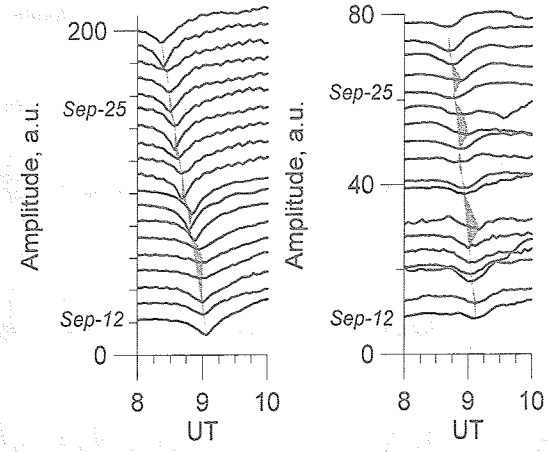


Fig. 3. Deviations in the terminator time on the signals received at Petropavlovsk-Kamchatski (left) and Moshiri (right), demonstrating a relatively quiet behavior. Because the maximal deviations do not exceed 15 min. Black paths indicate the deviation from the average terminator time variation expressed by a dotted line.

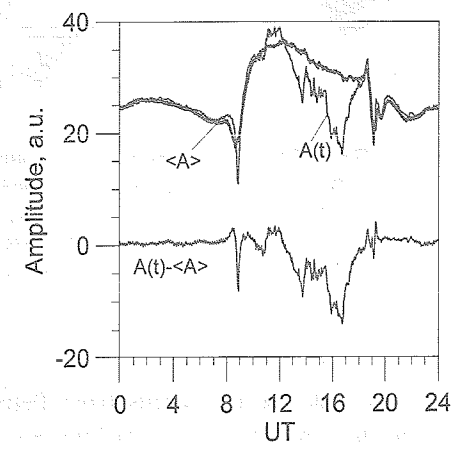


Fig. 4. An example of anomalous fading of the amplitude on September 18, 7 days before the date of the Tokachi earthquake. The variations of average amplitude $<A(t)>$, current amplitude $A(t)$ and differential amplitude $A(t)-<A>$, of the signal received at Petropavlovsk-Kamchatski are presented on this particular day.

deviations and their difference D_{pn}. The dispersion of the amplitude fluctuations was calculated over local nighttime specific for a chosen propagation path and a day of year. Presented in Fig. 5 are the results of analysis from the beginning of June to the end of October, for which simultaneously recorded data for both propagation paths are available. The dispersion dependencies smoothed by 5-day running mean are also plotted in Fig. 5. The time of the Tokachi-oki earthquake (September 25, 2003) is

This document is provided by JAXA.

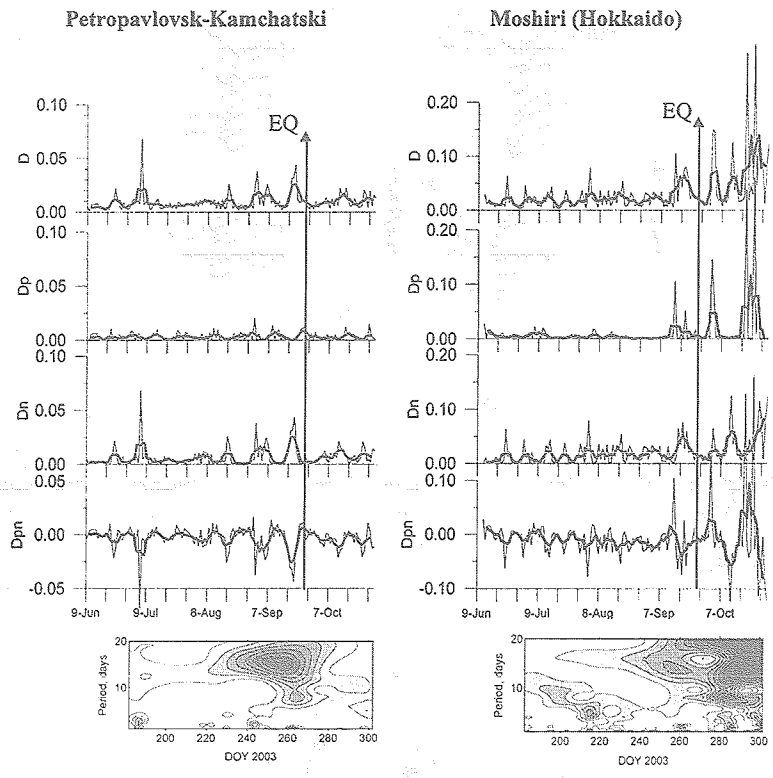


Fig. 5. Day-to-day variations of different fractions of dispersion of the nighttime deviations in the signal of JJY received at Petropavlovsk-Kamchatski (left) and Moshiri (right). The spectrograms at lower parts of the graphs show the Morlet wavelet transforms of the $D_{pn} = D_p - D_n$ *dependencies. The earthquake time is shown by the vertical arrow. In the upper panels thin line refers to the daily value and the full line, its corresponding running average ever 5 days.*

marked by vertical arrows. Considering the results from Petropavlovsk-Kamchatski presented in the left column in Fig. 5 we can find anomalous deviations of the LF signal. Such perturbations start from August 18 and are characterized by considerable fading of the signal that is demonstrated in Fig. 4. The strongest peaks appear in the "negative" fraction of the dispersion a week before the earthquake (September 18–20) and a day before the earthquake in the "positive" fraction of the dispersion. Such enhancements a week before the earthquake date are simultaneously observed in both the positive and negative fractions in deviations of the signal received at Moshiri.

A wave-like behavior of deviation intensity with the period of quasi 16-day PW becomes clearest from the D_{pn} dependences at both stations in Fig. 5. We can observe a swinging of this parameter before the earthquake with a gradual increase of its amplitude that reaches a maximal value a week before the earthquake. And just after the event the wave process is seen to shrink. The stronger perturbations in the signal received at Moshiri after the time of the earthquake could take place as a result of

This document is provided by JAXA.

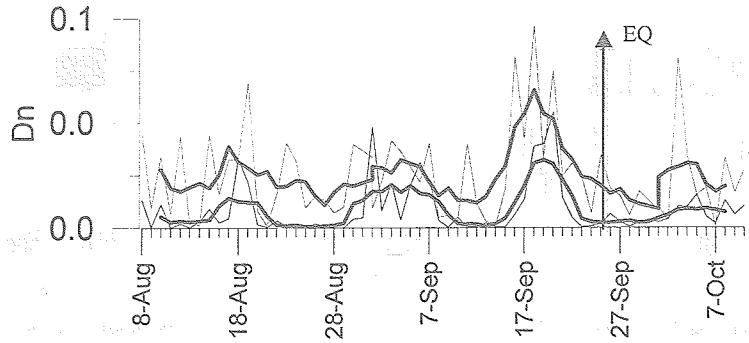


Fig. 6. Synchronous 16-day wave packets observed on the variations of the signals received at Moshiri (upper curve) and at Petropavlovsk-Kamchatski (lower curve) before the Tokachi earthquake on September 25, 2003. Thin curves refer to the daily value and thick curves are the 5-day running means.

specific propagation conditions on this path. Wavelet diagrams showing the time evolution of the spectral content of deviations in both signals are presented in the lower part of the graphs. We can recognize the intensification of oscillations with period corresponding to the quasi 16-day PW in both diagrams started approximately one month before the earthquake. This kind of intensification is found to be very consistent with our previous work (Molchanov and Hayakawa, 1998). A magnified view of the variations of negative fractions of signal dispersion combined for both observation points is shown in Fig. 6. It is important to note that the wave-like variations of the dispersion of signals propagating on those two different paths become almost synchronous during about one month period before the earthquake as is clearly seen from 5-day running means presented in Fig. 6.

Then we analyze an extended data set over the time span of about one year obtained for the JJY–Petropavlovsk-Kamchatski propagation path to compare LF data with the seismic ones. For this analysis we selected relatively shallow earthquakes with magnitude grater than or equal to 5 with depth less than 50 km within the area bounded by the 3rd Fresnel zone and circles of 150 km radius around the transmitter and the receiver. The day-to-day variations of the negative fraction of the dispersion and its 5-day running mean (thin and thick black curves respectively) are presented in Fig. 7 together with the selected earthquakes marked by vertical bars. As we can see from this figure the period from the beginning of the year to the beginning of May (DOY=122) is characterized by appearance of deviations which are comparable to or stronger than those preceding the main event, *i.e.* the Tokachi-oki earthquake. The number of such anomalies approximately corresponds to the number of earthquakes answering the above selection criteria. The most of them can be associated with earthquakes by the time of occurrence. Then from the beginning of May we observe rather quiet behavior of the signal fluctuations excluding two strong one-day anomalies. Then on the background of relative seismic silence from the end of July (DOY=213) to the end of September (DOY=274) we can observe a gradual intensification of signal dispersion with period of the quasi 16-days. This intensification is observed in the signals

This document is provided by JAXA.

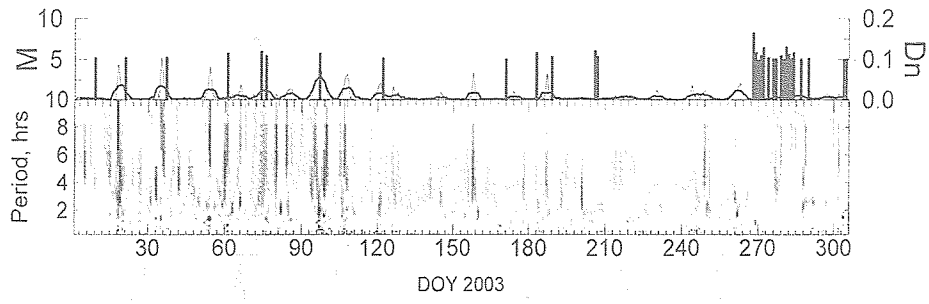


Fig. 7. A comparison between the seismic activity and intensification of fluctuation in the period of gravity and planetary waves in the signal received at Petropavlovsk-Kamchatski during January–October, 2003

propagating over the both paths, as was noted before.

Gravity waves (GWs) are considered as the most probable agent for the energy transportation from the earthquake preparatory processes to the lower ionosphere (see Pilipenko *et al.*, 2001; Hayakawa and NASDA's Earthquake Remote Sensing Frontier Research, 2001; Molchanov *et al.*, 2001; Hayakawa *et al.*, 2004). To demonstrate a correspondence between the PWs manifestation in the day-to-day variations of the LF signal and its fluctuations in the frequency range of GWs, a survey of the frequency spectra of the nighttime fluctuations is presented in the lower part of Fig. 7. The frequency dependence of the average spectra of nighttime fluctuations is well described by a power law with spectral index which is approximately equal to 2 (see *e.g.* Shvets *et al.*, 2004). To emphasize the higher frequency components we have compensated the power dependence in the spectra shown in Fig. 7. We can find a correspondence between the peaks of the dispersion and the intensification of oscillations within the GW frequency range (1–8 hours). The intensification of such fluctuations occurs as a quasi-periodic process with the PW periodicity. This circumstance seems to provide a good evidence for the modulation of GW by PW appearing in the observations.

4. Discussion and conclusion

As was shown previously PW periodicity is found in the day-to-day variations in both the transitional terminator times (Molchanov and Hayakawa, 1998; Hayakawa and NASDA's Earthquake Remote Sensing Frontier Research, 2001) and the nighttime fluctuations (Shvets *et al.*, 2004) in VLF signals. We should note that some precursory signatures found by Hayakawa *et al.* (1996) using the terminator time method also appeared as a development and intensification of oscillations with the PW periodicity in the VLF signal before the Kobe earthquake. So, in searching for anomalous deviations of the VLF/LF signal parameters related to the seismic activity, we need to consider the influence of the PWs on the lower ionosphere as a background process.

Atmospheric processes can crucially affect GW propagation from the ground to the ionosphere. So, we do not expect the existence of strong dependence between the value of subionospheric signal anomaly and the power of a probable GW source. In our

This document is provided by JAXA.

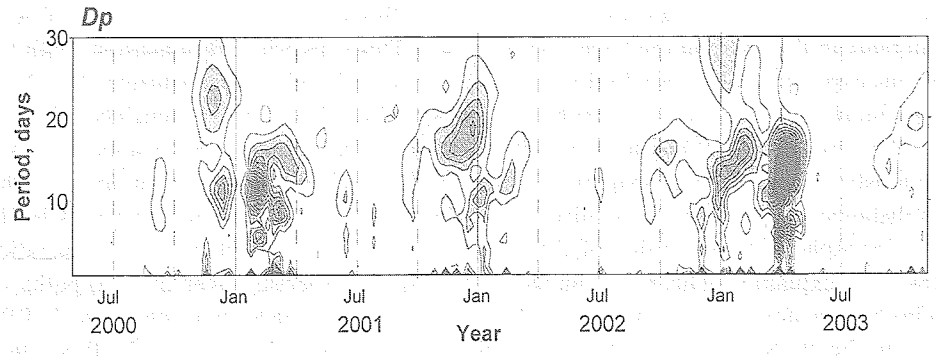


Fig. 8. Wavelet diagram of the positive fraction of dispersion of the LF signal on the propagation path JJY–Petropavlovsk-Kamchatski during the period of 2000–2003.

supposition concerning a seismic origin of the observed LF perturbations, the contradiction between these perturbation values and magnitudes of associated earthquakes can be explained by nonlinear interaction between GWs and PWs accounting for seasonal variability of PW activity in the lower ionosphere. The observed deviations in the LF signal during several winter-spring months are stronger in comparison with the case of the huge Tokachi-oki earthquake. They could be explained by enhanced penetration of the PWs to the lower ionospheric heights and their nonlinear interaction with GWs. Under such a consideration we also expect that the phase relationship between possible precursory effects and seismic events will be exposed to an external factor, *i.e.* PWs.

Shown in Fig. 8 is the wavelet diagram of the positive fraction of nighttime dispersion variations in the JJY signal measured at Kamchatka. It demonstrates clear seasonal variability of the nighttime amplitude fluctuations. We can observe the repeating maxima of them during winter months over the time span of more than 3 years. The maximal spectral density of these variations is concentrated in the range of the 16-day planetary waves periods. Such a seasonal variability can be explained by the seasonal dependence of the PW penetration to the lower ionosphere driven by stratospheric winds. The minor peaks observed during summer–autumn months are rather characterized by the GW activity. It is expected to be dominating during summer months when westward stratospheric background winds trap the PWs and prevent them from direct penetration into the lower ionospheric heights. The results of analysis of LF data set obtained during 2000–2003 show clear seasonal variations of the PW activity with maxima occurring in January–February. It is sufficiently close to the results of radar measurements of winds at MLT region cited in a number of papers (Mitchell *et al.*, 1999; Namboothiri *et al.*, 2002; Luo *et al.*, 2002).

Two concurring mechanisms can be used for explanation of the nighttime amplitude fluctuations: (1) modal interference that can induce the strong variations of the signal due to changes of the effective height of the lower ionosphere or/and (2) electromagnetic wave scattering from local inhomogeneities in the ionospheric profile along the propagation path accompanied with the change of losses. Since the amplitude of negative anomalous deviations corresponding to the signal fading, tends to

This document is provided by JAXA.

prevail over the positive ones, we can suppose that this process is mainly connected with an increase in the losses in the lower ionosphere. This supposition is consistent with the previous experimental results by Lastovicka *et al.* (1993) who demonstrated the effects of loss increase in the lower ionosphere related to the GW activity intensification.

The observed perturbations in the LF signals are found to have appeared synchronously on both the propagation paths before the Tokachi-oki earthquake. This circumstance would seem to require dimensions of corresponding irregularities in the lower ionosphere of the order of 300–500 km or more, to overlap both propagation paths. To explain synchronous changes of the signal dispersion over the two paths we can invoke the next mechanisms. The first one is the intensification of global scale PWs affecting the properties of the lower ionosphere. But as it follows from the theoretical predictions, the maximal intensity of the PWs at lower ionospheric heights is reached during winter months. So, the second mechanism seems to be preferred involving the penetration of IGWs modulated by the PWs in the troposphere, stratosphere and ionosphere for the considered autumn period. In this case the influence on the ionosphere will be relatively local and the observed synchronous perturbations of LF signals on the monitored propagation paths provide a possibility for the localization of ionospheric perturbations which are close to their possible source at the earth surface.

Thus, the next scheme of the seismo-ionospheric interaction that includes both GW and PW influence is summarized to explain the observed effects on the LF propagation. The IGWs excited by any processes in the Earth's crust connected with earthquake preparation, propagate to mesopause heights, dissipate increasing turbulence and create additional losses in the lower ionosphere. The intensity of IGW is modulated by PWs due to nonlinear interconnection between them in the troposphere and stratosphere and at the lower ionospheric heights.

Acknowledgments

This research was partly supported by a grant from Ministry of Education, Culture, Sports and Technology (MEXT) (No. 15403012) and by "R and D promotion scheme funding international joint research" by NiCT. One of the authors (M.H.) is grateful to the Mitsubishi Foundation and Hôsô-Bunka Foundation for their support. The authors would like to thank V.F. Voropaev and A.A. Smirnov of the Petropavlovsk-Kamchatski observatory (Institute of Geophysical Survey, Russian Academy of Sciences, Far-East Branch, Petropavlovsk-Kamchatski, Kamchatka, Russia) for their contribution to the LF/VLF observation there.

The editor thanks Drs. K. Hattori and A.P. Nickolaenko for their help in evaluating this paper.

References

Dowden, R.L. and Adams, C.D.D. (1988): Phase and amplitude perturbations on subionospheric signals explained in terms of echoes from lightning-induced electron precipitation ionization patches. J. Geophys. Res., 93, 543–550.

Gokhberg, M.B., Gufeld, I.L., Rozhnoy, A.A., Marenko, V.F., Yampolsky, V.S. and Ponomarev, E.A.

This document is provided by JAXA.

(1989): Study of seismic influence on the ionosphere by super long wave probing of the Earth-ionosphere waveguide. Phys. Earth Planet. Inter., **57**, 64–67.

Gokhberg, M.B., Nekrasov, A.K. and Shalimov, S.L. (1996): On the influence of unstable release of green-effect gases in seismically active regions on the ionosphere. Izvestiya AN SSSR, Fizika Zemli, **8**, 52–55.

Hayakawa, M., ed. (1999): Atmospheric and Ionospheric Electromagnetic Phenomena Associated with Earthquakes. Tokyo, Terra Sci. Publ., 996 p.

Hayakawa, M. and Molchanov, O.A., ed. (2002): Seismo Electromagnetics; Lithosphere-Atmosphere-Ionosphere Coupling. Tokyo, Terra Sci. Publ., 478 p.

Hayakawa, M. and NASDA's Earthquake Remote Sensing Frontier Research (2001): Seismo-electromagnetic Phenomena in the Lithosphere, Atmosphere and Ionosphere, Final Report. Univ. of Electro-Comms., 228 p.

Hayakawa, M., Molchanov, O.A., Ondoh, T. and Kawai, E. (1996): Precursory signature of the Kobe earthquake on VLF subionospheric signal. J. Atmos. Electr., **16**, 247–257.

Hayakawa, M., Molchanov O.A. and NASDA/UEC Team (2004): Achievements of NASDA's Earthquake Remote Sensing Frontier Project. Terr. Atmos. Oceanic Sci., **15**, 311–328.

Lastovicka, J., Boska, J. and Buresova, D. (1993): Digital measurements of LF radio wave absorption in the lower ionosphere and inferred gravity wave activity. Ann. Geophys., **11**, 937–946.

Lin'kov, E.M., Petrova, L.N. and Zuroshvili, D.D. (1989): Seismogravity oscillations of the Earth and related atmosphere perturbations. Doklady AN SSSR, **306**, 314–317.

Luo, Y., Manson, A.H., Meek, C.E., Meyer, C.K., Burrage, M.D., Fritts, D.C., Hall, C.M., Hocking, W.K., MacDougall, J., Riggin, D.M. and Vincent, R.A. (2002): The 16-day planetary waves: multi-MF radar observations from the arctic to equator and comparisons with the HRDI measurements and the GSWM modelling results. Ann. Geophys., **20**, 691–709.

Maekawa, S. and Hayakawa, M. (2005): Dependence of characteristics of VLF/LF terminator times on the propagation direction: Statistical study. submitted to Special Issue on EMC, Inst. Electr. Engrs, Japan.

Mitchell, N.J., Middleton, H.R., Beard, A.G., Williams, P.J.S. and Muller, H.G. (1999): The 16-day planetary wave in the mesosphere and lower thermosphere. Ann. Geophys., **17**, 1447–1456.

Molchanov, O.A. and Hayakawa, M. (1998): Subionospheric VLF signal perturbations possibly related to earthquakes. J. Geophys. Res., **103** (A8), 17489–17504.

Molchanov, O.A., Hayakawa, M. and Miyaki, K. (2001): VLF/LF sounding of the lower ionosphere to study the role of the atmospheric oscillations in the lithosphere-ionosphere coupling. Adv. Polar Upper Atmos. Res., **15**, 146–158.

Morgounov, V.A., Ondoh, T. and Nagai, S. (1994): Anomalous variation of VLF signal associated with strong earthquakes ($M>7$). Electromagnetic Phenomena Related to Earthquake Prediction, ed. by M. Hayakawa and Y. Fujinawa. Tokyo, Terra Sci. Publ., 409–428.

Namboothiri, A.P., Kishore, P. and Igarashi, K. (2002): Climatological studies of the quasi 16-day oscillations in the mesosphere and lower thermosphere at Yamagawa (31.2N, 130.6E), Japan. Ann. Geophys., **20**, 1239–1246.

Pilipenko, V., Shalimov, S., Uyeda, S. and Tanaka, H. (2001): Possible mechanism of the over-horizon reception of FM radio waves during earthquake preparation period. Proc. Jpn. Acad., **77**, Ser. B, No. 7, 125–130.

Salby, M.L. (1981a): Rossby normal modes in nonuniform background configurations, Part I, Simple fields. J. Atmos. Sci., **38**, 1803–1826.

Salby, M.L. (1981b): Rossby normal modes in nonunoform background configurations, Part II, Equinox and solstice conditions. J. Atmos. Sci., **38**, 1827–1840.

Shvets, A.V., Hayakawa, M., Molchanov, O.A. and Ando, Y. (2004): A study of ionospheric response to regional seismic activity by VLF radio sounding. Phys. Chem. Earth, **29/4–9**, 627–637.

Smith, A.K. (1996): Longitudinal variations in mesospheric winds: Evidence for gravity wave filtering by planetary waves. J. Atmos. Sci., **53**, 1156–1173.

Soloviev, O.V. and Hayakawa, M. (2004): 3D modelling method of VLF subionospheric radio wave propagation allowing for a localized ionospheric perturbation. Inst. Electr. Engrs. Japan, Trans.

This document is provided by JAXA.

Fundamentals and Materials, Special Issue on Recent Progress in Electromagnetic Theory and Its Application, 124, No. 12, 1216–1224.

Uyeda, S., Nagao, T., Hattori, K., Noda, Y., Hayakawa, M., Miyaki, K., Molchanov, O., Gladychev, V. *et al.* (2002): Russian-Japanese complex geophysical observatory in Kamchatka for monitoring of phenomena connected with seismic activity. Seismo Electromagnetics: Lithosphere-Atmosphere-Ionosphere Coupling, ed. by M. Hayakawa and O.A. Molchanov. Tokyo, Terra Sci. Publ., 413–419.

Voitov, G.I. and Dobrovolsky, I.P. (1994): Chemical and isotropic-carbon instabilities of the native gas flows in seismically active regions. Izvestiya AN SSSR, Fizika Zemli, 3, 20–31.

This document is provided by JAXA.

Adv. Polar Upper Atmos. Res., 19, 55–62, 2005
© 2005 National Institute of Polar Research

Model calculations of possible ionospheric backscatter echo area for a mid-latitude HF radar

Nozomu Nishitani[1]* and Tadahiko Ogawa[1]

[1]*Solar-Terrestrial Environment Laboratory, Nagoya University, Toyokawa 442-8507*
**Corresponding author. E-mail: nisitani@stelab.nagoya-u.ac.jp*

(Received February 4, 2005; Accepted April 5, 2005)

Abstract: HF ray path calculation is performed in order to identify possible ionospheric backscatter echo area for an HF radar at mid-latitude. The calculation is made on the basis of the R.M. Jones and J.J. Stephenson (U.S. Dept. of Commerce, OT Rep. 75–76, 1975) HF ray path tracing algorithm plus the IRI-2001 ionosphere model. It is shown that depending on the local time and geomagnetic activity, the possible ionospheric backscatter regions have different distributions. In any case the backscatter region is large enough, indicating the capability of a planned HF radar in Hokkaido (43.5°N, 143.6°E), Japan.

key words: ionospheric echoes, SuperDARN, mid-latitude, ray-path tracing

1. Introduction

Super Dual Auroral Radar Network (SuperDARN) (Greenwald *et al.*, 1995) is a powerful tool for monitoring the ionospheric plasma dynamics over a global extent. Figure 1 shows the coverage of the present SuperDARN network as of January 1, 2005. Each radar has spatial resolution of 15 to 45 km in radial direction and up to about 100 km in azimuthal direction, temporal resolution of 1 s to 2 min per one beam, operating frequency of 8 to 20 MHz, peak output power of 10 kW and 16 beam directions. There are total of 16 radars operating in the polar ionosphere (9 in the northern and 7 in the southern hemisphere), under the international cooperation of 11 countries.

Although all of the present radars are located at geomagnetic latitudes higher than 54°, there are plans to expand this network to lower latitudes, in United States, Europe, Japan, and so on. One of these proposals is a mid-latitude HF radar in Hokkaido, Japan (43.5°N, 143.6°E in geographic coordinates), which is designed to monitor the upper atmosphere with the geomagnetic latitude between 38° to 63°. The field of view of the radar is shown in Fig. 2. With this radar we expect to deal with a wide variety of scientific topics, ranging from the magnetosphere, ionosphere, thermosphere to upper mesosphere.

There are several points which should be considered when deploying mid-latitude HF radars to observe ionospheric backscatter echoes. The most important point is that the ambient geomagnetic field lines at mid-latitudes are not vertical to the ground, but rather inclined to the horizontal direction. This may greatly affect the receiving con-

This document is provided by JAXA.

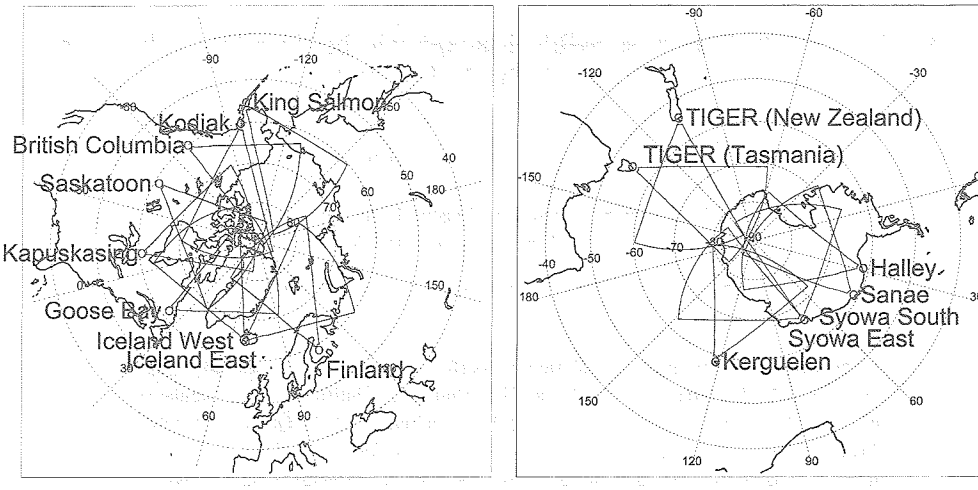


Fig. 1. Fields of view of the existing SuperDARN radars in both hemispheres. The plots are given in Altitude Adjusted Corrected Geomagnetic (AACGM) coordinates, which is an updated version of the PACE geomagnetic coordinate system (Baker and Wing, 1989).

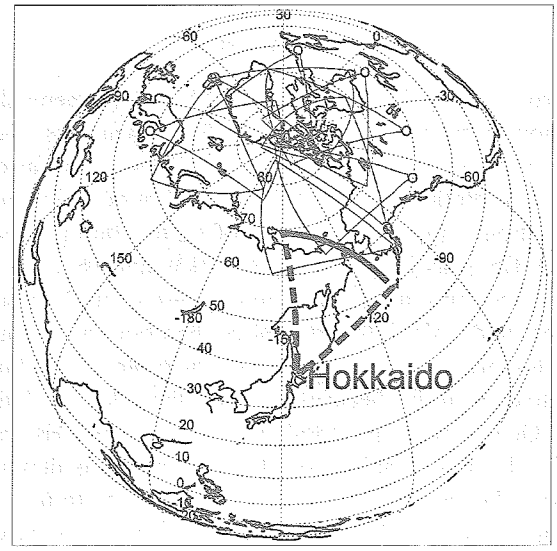


Fig. 2. Field of view of the planned Hokkaido HF radar.

ditions of ionospheric backscatter echoes, because the radar wave propagation vector should be normal to the geomagnetic field vector in order to detect echoes from ionospheric field-aligned irregularities (Greenwald *et al.*, 1995). For the HF radar the situation is complicated because the radar waves are highly deflected when they pass through the ionosphere, and the amount of deflection depends on the ionospheric plasma

This document is provided by JAXA.

densities, which is highly variable as a function of several parameters. In order to estimate the echo receiving conditions for the mid-latitude HF radar accurately, it is necessary to execute HF ray path tracing by using reliable ionospheric models.

Ogawa *et al.* (1990) calculated the possible ionospheric backscatter regions for the Syowa South HF radar, by using the Chapman model ionosphere, but things might be completely different for mid-latitude radars. In this paper, we show examples of the calculation of the HF ray path tracing under a model ionosphere (IRI-2001) and estimate ionospheric backscatter for the planned Hokkaido HF radar.

2. Model description

The HF ray path tracing program used in this study was originally developed by Jones and Stephenson (1975). With this program we can calculate the ray paths of HF radio waves under a simple model ionosphere such as Chapman layer with a limited number of ionospheric parameters. In the present study we introduced International Reference Ionosphere-2001 (IRI-2001) model ionosphere (Bilitza, 2001) to this HF ray tracing program. With the IRI model we can use various parameters as input, so that we can estimate the echo reception under variable conditions such as geomagnetic/solar activities, season and local time, and can perform more realistic calculation. For the geomagnetic field modeling, the International Geomagnetic Reference Field (IGRF) model is used.

3. Result of calculation

Figure 3 shows examples of the model calculation result of the echo receiving situation for the Hokkaido HF radar. The horizontal axis is the ground distance from the radar site, and the vertical axis is the ground height (both axes have the same scale). The calculation was made for the central beam of the planned Hokkaido radar, at a horizontal angle of 30° clockwise from the geographic north and the elevation angles of 10° to 40°, every 5 degrees. The vertical antenna pattern of standard SuperDARN radars depend on radar HF frequency, but at 10 MHz the maximum sensitivity occurs between 20° and 30° elevation angle, and the sensitivity is −5 to 0 dB for 10° to 40° (Y. Kato, unpublished data). In order to observe ionospheric backscatter echoes, it is required that the radar wave vector is normal to the ambient magnetic field vector; the × labels indicate the points where the angles between these two vectors are within the range of 90°±1°. The calculation was made by using the IRI-2001 model ionosphere for quiet nighttime (2003/03/26, 00 JST, JST=UT+9 hours, $Ap=4$), disturbed nighttime (2003/05/30, 00 JST), quiet daytime (2002/04/23, 0900 JST) and disturbed daytime (2002/04/18, 09 JST) conditions, and the IGRF geomagnetic field model. The Ap geomagnetic indices indicate 3-hour averaged mid-latitude geomagnetic activity level with a linear scale. The calculation was made for various radar HF wave frequencies (9, 11 and 13 MHz).

It can be seen that the distribution of × points highly depends on local time, geomagnetic activity and radar HF frequency. In the nighttime, the 9 MHz case seems to be most suitable for observing ionospheric backscatter echoes over wide range, both

This document is provided by JAXA.

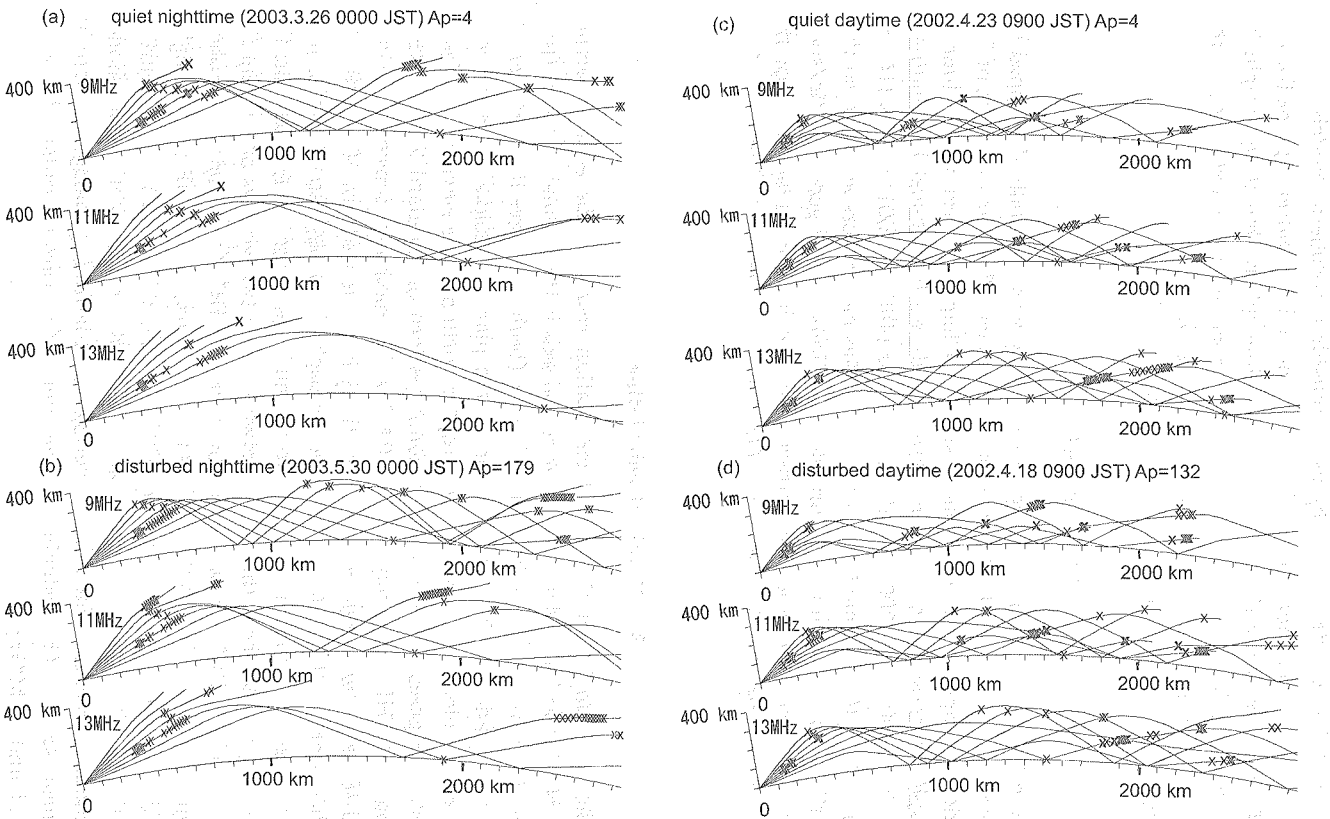


Fig. 3. Vertical profile of HF ray paths (solid curves) in the model ionosphere. The horizontal axis is the distance from the radar antenna, and the vertical axis is the height. The radar wave is emitted at a horizontal angle of 30° clockwise from the geographic north. At × points, where the angle between radar HF ray vector and the ambient magnetic field vector is within the range of 90° ±1°, HF waves are expected to be backscattered by ionospheric field-aligned irregularities (if they exist). Four sets of 3 panels show the results for (a) quiet nighttime (2003/03/26, 00 JST), (b) disturbed nighttime (2003/05/30, 00 JST), (c) quiet daytime (2002/04/23, 09 JST) and (d) disturbed daytime (2002/04/18, 09 JST) conditions respectively, with 3 different frequencies.

This document is provided by JAXA.

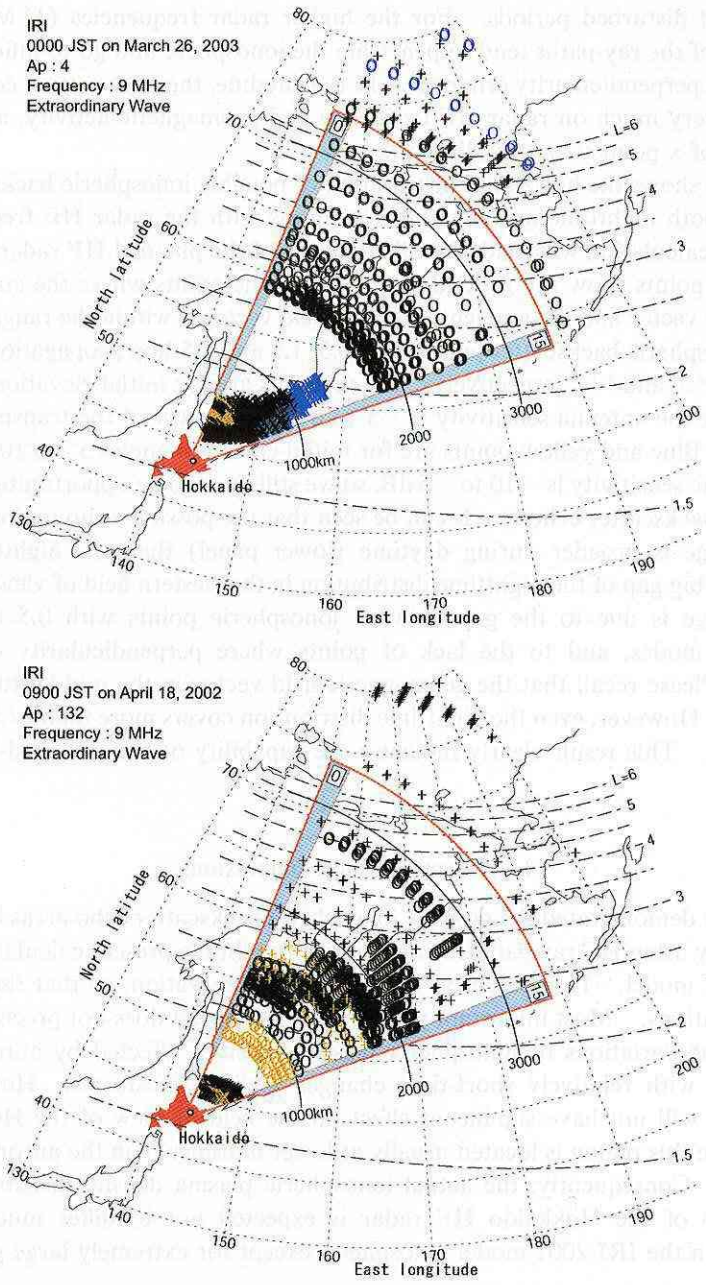


Fig. 4. Horizontal profile of possible HF ionospheric backscatter receiving points where the angle between radar HF ray vector and the ambient magnetic field vector is within the range of 90° ±1°. The upper and lower panels show the results for nighttime (2003/03/26, 00 JST) and daytime (2002/04/18, 09 JST) conditions. The points labeled '×', '○' and '+' are for 0.5-hop, 1.5-hop and 2.5-hop propagation modes, respectively. The black points are for initial elevation angles 10° to 40°, blue are for elevation angles 5° to 10°, and yellow are for elevation angles 40° to 50°. The calculation is made for every 2.5° elevation angle.

This document is provided by JAXA.

for quiet and disturbed periods. For the higher radar frequencies (11 MHz and 13 MHz) most of the ray-paths tend to penetrate the ionosphere and go to infinity without satisfying the perpendicularity criterion. In the daytime, the propagation conditions do not depend very much on radar HF frequency and geomagnetic activity, although the distribution of x points changes slightly.

Figure 4 shows the horizontal distribution of possible ionospheric backscatter echo regions for both nighttime and daytime conditions with the radar HF frequency of 9 MHz. The calculation was made for all 16 beams of the planned HF radar. The '×', '○' and '+' points show the ground projection of the points where the angle between radar HF ray vector and the ambient magnetic field vector is within the range of $90^\circ \pm 1^\circ$. Possible ionospheric backscatter points with 0.5, 1.5 and 2.5-hop propagation modes are labeled '×', '○' and '+' respectively. Black points are for initial elevation angles 10° to 40°, where the antenna sensitivity is -5 to 0 dB, and most of the transmitter power is radiated. Blue and yellow points are for initial elevation angles 5° to 10° and 40° to 50°, where the sensitivity is -10 to -5 dB, so we still have some opportunities to receive ionospheric backscatter echoes. It can be seen that the possible echo region within the 2000 km range is broader during daytime (lower panel) than the nighttime (upper panel). The big gap of the nighttime distribution in the western field of view in the 500–1700 km range is due to the gap between ionospheric points with 0.5 and 1.5-hop propagation modes, and to the lack of points where perpendicularity condition is satisfied. (Please recall that the geomagnetic field vector in the mid-latitude region is not vertical.) However, even the nighttime distribution covers more than 2/3 of the total field of view. This result clearly indicates the capability of the new mid-latitude HF radar.

4. Discussion and conclusions

We have demonstrated the possible ionospheric backscatter echo areas based on the calculation by using HF ray path tracing algorithm. In the present calculation we used the IRI-2001 model. It is based on the statistical observation, so that the model has several limitations. Most important point is that the model does not precisely describe the short-time variations of ionospheric plasma densities affected by auroral particle precipitation with relatively short-time changes such as substorms. However, such precipitation will not have significant effect on the field of view of the Hokkaido HF radar because this region is located usually at lower latitudes than the auroral precipitation region. Consequently, the actual ionospheric plasma density distribution in the field of view of the Hokkaido HF radar is expected not to differ much from the distribution in the IRI-2001 model ionosphere, except for extremely large geomagnetic storms.

There are other conditions which affect the ionospheric backscatter receiving conditions. The most important factor is the presence/absence of ionospheric field-aligned plasma irregularities of the spatial scale of $\lambda/2$, where λ is the wavelength of the radar HF wave. Without such irregularities, the radar HF waves are not backscattered even if the perpendicularity condition is satisfied in the ionosphere. Since plasma irregularities are often observed in the *F*-region ionosphere at sub-auroral and mid-

This document is provided by JAXA.

latitude regions (Hosokawa *et al.*, 2001; Fukao *et al.*, 1988), we can expect to observe *F*-region echoes at mid-latitude regions. The occurrence of mid-latitude *F* region irregularities is one of the key scientific questions we hope to address with the new HF radar.

The actual ionospheric echoes are also affected by the HF ray absorption in the D-layer ionosphere at high latitudes, which are enhanced by particle precipitation during high geomagnetic activity such as substorms (Milan *et al.*, 1996; Gauld *et al.*, 2002). However, such effects are weaker for the mid-latitude radar than the existing high-latitude radars, because the HF ray paths cross the D-layer ionosphere at much lower latitudes than the auroral oval where the significant particle precipitation is expected. It is interesting to examine whether this hypothesis is true or not, by analyzing the actual data of the planned mid-latitude HF radar.

It should be noticed that the daytime D-layer ionosphere is produced by solar photoionization, which at mid-latitudes will lead to high absorption. This might have some impact on dayside observation of the HF radar, but the amount of absorption highly depends on the selection of HF radar frequency. It should be important to select proper radar HF frequency for observation.

In the present study we have estimated the possible ionospheric backscatter echo regions by using HF ray path tracing algorithm. This ray path tracing algorithm is applicable for various other purposes. Here are some examples: (1) estimation of the HF ray path refraction in the high-latitude D-region and E-region ionosphere during geomagnetically active periods and during solar proton events. (2) estimation of the change of HF ray paths due to the sporadic E layer in the ionosphere, which is often observed in Japan area during summer. Moreover, although we have discussed here only the ray paths of the radar HF waves, we can also the estimate the rate of attenuation, phase shift and Doppler shift of the HF waves.

The mid-latitude HF radar also aims at detecting two-dimensional images of thermospheric phenomena such as MSTIDs (Samson *et al.*, 1990). When we employ SuperDARN radars for the measurement of TIDs, ground scatter echoes become important. Figure 3 shows that for the quiet nighttime ionosphere and 9 MHz frequency, 1.0-hop ground scatter echoes have ionospheric reflection points for 500 to 1500 km range continuously. For daytime and disturbed periods these ranges become shorter, but this highly depends on the selection of radar HF frequency. Again, the selection of proper radar HF frequency is important, as in the case of suppressing dayside D-layer absorption.

With mid-latitude HF radars we expect to deal with a wide variety of scientific topics, ranging from the magnetosphere, ionosphere, thermosphere to the upper mesosphere. Mid-latitude HF radars such as Hokkaido HF radar will provide many important parameters for studying particle transport/acceleration in the inner magnetosphere, response of ionospheric convection to changes in solar wind parameters, generation/propagation/decay of gravity waves in the upper atmosphere, and many other dynamic processes in the geospace environment.

This document is provided by JAXA.

Acknowledgments

The ray path tracing program was obtained from the NOAA Environment Technology Laboratory anonymous-ftp site.

The editor thanks Drs. K. Hosokawa and S.E. Milan for their help in evaluating this paper.

References

Baker, K.B. and Wing, S. (1989): A new magnetic coordinate system for conjugate studies at high latitudes. J. Geophys. Res., **94**, 9139–9144.

Bilitza, D. (2001): International Reference Ionosphere 2000. Radio Sci., **36**, 261–275.

Fukao, S., McClure, J.P., Ito, A., Sato, T., Kimura, I., Tsuda, T. and Kato, S. (1988): First VHF radar observation of midlatitude *F*-region field-aligned irregularities. Geophys. Res. Lett., **15**, 768–771.

Gauld, J.K., Yeoman, T.K., Davies, J.A., Milan, S.E. and Honary, F. (2002): SuperDARN radar HF propagation and absorption response to the substorm expansion phase. Ann. Geophys., **20**, 1631–1643.

Greenwald, R.A. *et al.* (1995): DARN/SUPERDARN: A global view of the dynamics of high-latitude convection. Space Sci. Rev., **71**, 761–796.

Hosokawa, K., Iyemori, T., Yukimatu, A.S. and Sato, N. (2001): Source of field-aligned irregularities in the subauroral *F* region observed by the SuperDARN radars. J. Geophys. Res., **106**, 24713–24731.

Jones, R.M. and Stephenson, J.J. (1975): A versatile three-dimensional ray tracing computer program for radio waves in the ionosphere. U.S. Department of Commerce, OT Report 75–76.

Milan, S.E., Jones, T.B., Lester, M., Warrington, E.M. and Reeves, G.D. (1996): Substorm correlated absorption on a 3200 km trans-auroral HF propagation path. Ann. Geophys., **14**, 182–190.

Ogawa, T., Hirasawa, T., Ejiri, M., Sato, N., Yamagishi, H., Fujii, R. and Igarashi, K. (1990): HF radar experiment at Syowa Station for the study of high-latitude ionosphere-2: A capability (extended abstract). Proc. NIPR Symp. Upper Atmos. Phys., **3**, 91–95.

Samson, J.C., Greenwald, R.A., Ruohoniemi, J.M., Frey, A. and Baker, K.B. (1990): Goose Bay observations of earth-reflected, atmospheric gravity waves in the high-latitude ionosphere. J. Geophys. Res., **95**, 7693–7709.

This document is provided by JAXA.

Adv. Polar Upper Atmos. Res., 19, 63-70, 2005
© 2005 National Institute of Polar Research

Research note

Relationship between thermospheric vertical wind and the location of ionospheric current in the polar region

Mamoru Ishii

National Institute of Information and Communications Technology, Koganei-shi, Tokyo 184-8795
E-mail: mishii@nict.go.jp

(Received November 5, 2004; Accepted January 25, 2005)

Abstract: We have been observing vertical winds in the polar thermosphere with a Fabry-Perot interferometer (FPI) installed at Poker Flat Research Range, Alaska. To introduce a new method to understand thermospheric wind system in the polar region, the vertical wind variations are compared with the peak location of ionospheric current deduced from magnetic field measurements on the ground in a case observed on December 5, 1999. The magnetometer data were obtained at Kaktovik, Fort Yukon, Poker Flat, and Gakona. The method of estimating ionospheric current was obtained from H. Lühr *et al.* (J. Atmos. Terr. Phys., **56**, 81, 1994). The eastward current dominant interval was clearly separated from the westward current dominant one at 1130 UT (~0030 MLT) in this case. The relation between the vertical wind and the location of the ionospheric current was clearly different before and after the boundary. Namely, the downward (upward) vertical wind was found to be dominant equatorward (poleward) of the ionospheric current after 1130 UT, which is consistent with results obtained in many previous works. However, this relation was found to be opposite before 1130 UT: the upward (downward) vertical wind was seen to be equatorward (poleward) of current.

key words: vertical wind, thermosphere-ionosphere coupling, ionospheric current, Fabry-Perot Interferometer, magnetometer

1. Introduction

Since large vertical winds have been found near the auroral zone with Fabry-Perot interferometers (FPIs; Rees *et al.*, 1984), many studies focused attention on the phenomenon (Crickmore *et al.*, 1991; Price and Jacka, 1991; Conde and Dyson, 1995; Aruliah and Rees, 1995; Smith and Hernandez, 1995; Price *et al.*, 1995; Innis *et al.*, 1996, 1997; Ishii *et al.*, 1999, 2001). These vertical winds play a significant role in determining the composition, large scale circulation and energy balance of the upper atmosphere. Several sources are considered to generate such large vertical winds; (1) Joule and particle heating, (2) divergence and convergence of horizontal winds, and (3) gravity waves propagating from the lower atmosphere. Joule heating is one of the most likely sources of the vertical winds in the polar thermosphere. Although a number of

This document is provided by JAXA.

studies have been conducted on this subject, there have been few studies that discuss the relationship between lower thermospheric vertical wind and ionospheric current, which is the source of Joule heating (Rees *et al.*, 1984; Peteherych *et al.*, 1985).

In this study, we estimate temporal variation of the ionospheric current peak using the Alaskan magnetometer chain, and research the relation between the deduced current peak and the vertical winds in the lower thermosphere. The typical height of OI 557.7 nm emission layer is 110–140 km which is close to the peak height of ionospheric current and appropriate to discuss the effect of current to neutral wind. The method shown in Lühr *et al.* (1994) was used for estimating the current peak. Some of the previous studies have stated that the direction of vertical wind depends on the relative location of the auroral oval (Innis *et al.*, 1996, 1997; Crickmore *et al.*, 1991). However, most studies deduced the location of the oval from optical measurements on the ground, and it has not been confirmed whether the observed boundary is the real one between open and closed magnetic field lines.

The first motivation for the paper is to investigate the vertical wind system on the vicinity of ionospheric current, instead of optical aurora. In our method, the location of the dominant ionospheric current can be estimated without auroral images. This paper introduces this new method for discussing the relation between Joule heating and vertical wind, and shows an initial result obtained in a case study measured on December 5, 1999.

Some analysis of magnetometer data corresponding to thermospheric vertical wind events were reported in Innis *et al.* (1996). They had a spectral analysis of fluxgate magnetometer data obtained at Mawson on the nights when significant periodicities were seen in the FPI data. The vertical component of the magnetic field exhibited evidence of a correlation with the wind data, where an interval of upward wind was likely to be associated with an interval of increased upward field strength.

We need many of the information such as electric field, ionospheric conductivity and horizontal component of neutral winds to understand completely the neutral wind system in the polar thermosphere including vertical winds. For these, several additional observations are required such as incoherent scatter radar, HF radar and Doppler Imaging FPI. This paper will be placed as a small but practical step toward these simultaneous observations, with showing that the magnetometer data also gives us important information.

2. Instrumentation and observations

The Communications Research Laboratory FPI (CRLFPI) project operates two types of FPIs, one with a narrow field of view and the other with a wide field of view (details of these instruments were described in Ishii *et al.*, 1997). The narrow field-of-view FPI (scanning FPI) was installed at Poker Flat, Alaska in September 1998. A single, 116 mm aperture etalon with servo-control of the etalon spacing is operated at a 20.49 mm gap. The field of view is 1.4 deg full-angle and is fixed to the zenith direction. Each fringe pattern image of the λ630.0 nm and λ557.7 nm emissions of atomic oxygen are recorded simultaneously on each of two output channels every 2 min. Each image has 3 orders of interference for 630.0 nm and 4 order for 557.7 nm at the etalon. We use two kinds of laser for calibration; a He-Ne green laser (543.5 nm) for the shorter

This document is provided by JAXA.

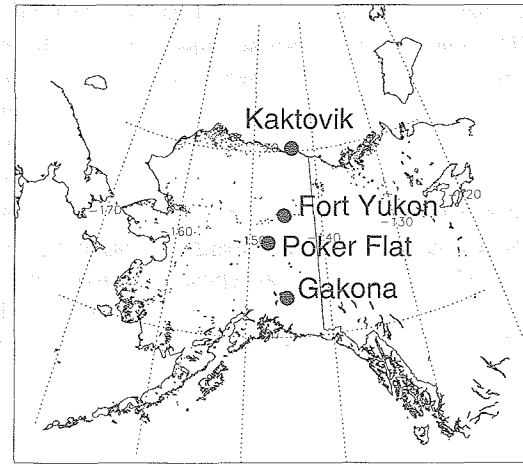


Fig. 1. Location of the observatories. The CRLFPI was operated at Poker Flat Research Range. The magnetic field was measured at Fort Yukon, Gakona, and Poker Flat. This map is plotted with geographic coordinates.

wavelength and a frequency-stabilized He-Ne red laser for the longer wavelength. We obtain one laser image per every ten observations (every~20 min), which allows us to characterize and correct for the effect of etalon gap drift. Wind velocities deduced from both channel images are also calibrated with the same frequency-stabilized laser.

A one-night average of vertical wind measurement was used to determine the zero Doppler shift, keeping in mind the possibility of constant offset in wind velocity. Another study using the same system shows high correlation over 0.7 between the wind velocity variations obtained two independent FPIs 300 km distant from each other along auroral arc (Ishii *et al.*, 2004). This result will be an evidence that our baseline determination is acceptable.

The magnetometer used here (The Geophysical Institute Magnetometer Array) has a basic fluxgate design using a triaxial set of cores (Narod ring-core magnetometer, Narod Geophysics Lt., Canada). Figure 1 shows the location of the four observatories at which the geomagnetic field was recorded; Poker Flat (65.12 N, 147.43 W), Kaktovik (70.16 N, 143.67 W), Gakona (62.12 N, 145.14 W) and Fort Yukon (66.56 N, 145.22 W). The magnetometer electronics are controlled by an S-100 computer that uses internal calibrations to produce digital output in units of nano-Tesla. The nominal data rate is 8 samples per second and 1 s-average data were obtained for this study. The temperature instability of the sensor is less than 0.1 nT/degree and the long-term drift is less than 10 pT/day. The noise level is $7\,\mathrm{pT}/\sqrt{Hz}$ at 1 Hz. The error in orthogonality is less than 0.1 degrees.

3. Method of analysis and results

We adopted the method described in Lühr *et al.* (1994) for deducing the ionospheric current distribution. We assumed a single, magnetic east-west ionospheric

This document is provided by JAXA.

current with Gaussian-shape distribution as the first approximation, following Lühr *et al.* (1994). The ΔH-components of magnetometer data at four sites were used to determine three parameters: peak location, height and width. Since four-point data of the magnetic field did not provide enough information to determine the peak of ionospheric current with Gaussian-fitting in many cases, the magnitude of the ΔH-component at infinite North and South was assumed to be zero. The baseline of magnetic field variation was calculated from the averaged value over five quiet days for each observatory. Zonal direction of the ionospheric current was deduced from the signature of the height of the fitting Gaussian (positive: eastward).

Figure 2 shows the result obtained on December 5, 1999. The top panel shows auroral luminosity with OI 557.7 nm fringes. The solid and dotted lines show the intensities at the maximum and minimum counts in the inner fringe data. The

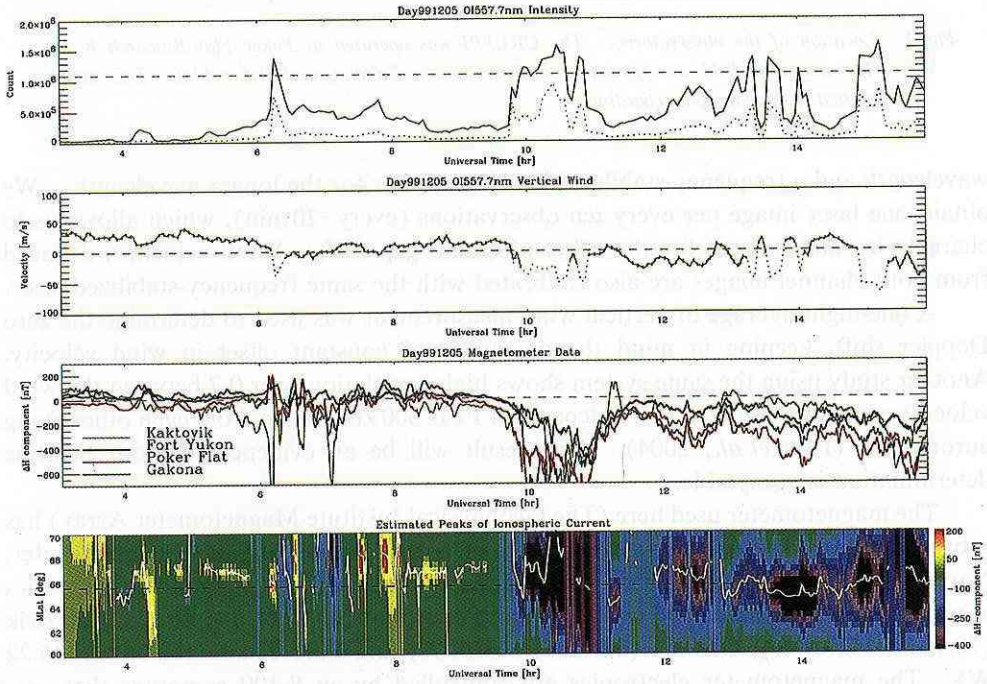


Fig. 2. The result of comparison between the vertical wind and the location of ionospheric current deduced from December 5, 1999 observation. Top panel: auroral luminosity with OI557.7 nm fringes. The solid and dotted lines show the intensities at the top and bottom of the innermost fringe. Second panel: vertical winds estimated from OI557.7 nm emission (upward positive). When the fringe is saturated with bright aurora ($>1.10\times10^6$ count), it is shown by a dotted line. Third panel: the ΔH-component of magnetic field perturbations. Results were obtained at Kaktovik (green), Fort Yukon (blue), Poker Flat (red), and Gakona (black). Bottom panel: "estimated peaks of ionospheric currents." The vertical axis shows latitudinal distribution of ionospheric currents assuming single Gaussian distribution. The broken line shows the latitude of PFRR, in which the vertical winds were measured. White lines in this panel show the peak location of ionospheric currents.

This document is provided by JAXA.

magnetic midnight corresponds to ~1100 UT. The second panel shows vertical winds in the OI 557.7 nm emission layer whose altitude is generally ~110 km (*e.g.*, Shepherd *et al.*, 1995). The upward velocity shows a positive signature. Ishii *et al.* (2001) show the detailed method of analysis to obtain the vertical winds. When the observed aurora was too bright, the recorded fringes saturate; this can lead to overestimation of temperature and large errors in velocity. The maximum count in two minutes was 1.206×10^6 and we show wind velocity with a dotted line when the peaks of fringe images had a count of greater than 1.10×10^6. The third panel shows ΔH-components of magnetometer data at four sites, subtracted the average of five quiet days as baselines. The fourth panel shows estimated peaks of ionospheric current, with the vertical axis showing latitudinal distribution of ionospheric currents assuming single Gaussian distribution. The equivalent current was used in this study which is proportional to the variation of magnetic field on the ground: the unit is nT. The color code in the forth panel shows equivalent current (or estimated distribution of ΔH-components of magnetic field) along the magnetic latitude. The broken line shows the latitude of the Poker Flat Research Range (PFRR), which the vertical winds were measured. The white lines in the panel show the location of estimated peaks of ionospheric currents.

Figure 3 is given as an aid for discussing the relation between vertical wind and the

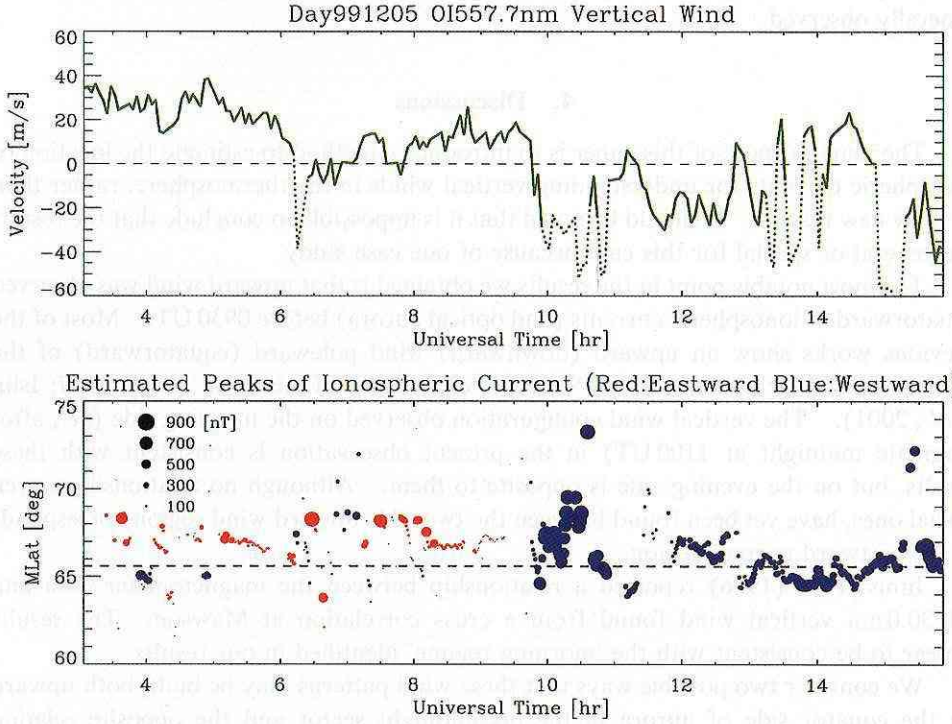


Fig. 3. Top panel: the same as the second panel of Fig. 2. Bottom panel: the location of estimated peaks of ionospheric currents. The size and color of circles show the current magnitude and the direction of the current (red: eastward, blue: westward).

This document is provided by JAXA.

location and direction of ionospheric currents. The top panel of the figure is the same as the second panel of Fig. 2. The bottom panel shows the location of estimated peaks of ionospheric currents. The size of the points shows the current magnitude and the color shows the direction of the currents (red: Eastward, blue: Westward). This panel shows a boundary at around 0930 UT; eastward currents existed only before the boundary. The relation between the vertical wind and the location of ionospheric currents changed both before and after the boundary. Namely, before 0930 UT, there was a relatively eastward current poleward of PFRR that was dominant. During this period the vertical wind flowed upward.

The magnetic field was considerably disturbed from 1000 to 1100 UT. During this interval there was a strong westward current poleward of PFRR and the vertical wind accelerated downward strongly (It should be noted that the absolute value of wind velocity is not accurate in this interval because of fringe saturation with bright aurora). Just after 1100 UT a weak westward current was detected when upward acceleration was observed in the vertical wind. After this event the current was poleward of PFRR, and the vertical wind kept flowing downward until 1300 UT. There was some fluctuation from 1300 to 1500 UT, but generally the current reached the equatorwardmost location at 1400 UT and then moved poleward again. The vertical wind variation showed the different tendency from the previous interval, namely, when the current located poleward (equatorward) of PFRR, downward (upward) vertical wind was generally observed.

4. Discussions

The main purpose of this paper is to introduce a method to estimate the location of ionospheric currents for understanding vertical winds in the thermosphere, rather than to show new results. It should be noted that it is impossible to conclude that the results are general or special for this case because of one case study.

The most notable point in the results we obtained is that upward wind was observed equatorward of ionospheric currents (and optical aurora) before 0930 UT. Most of the previous works show an upward (downward) wind poleward (equatorward) of the auroral oval (Crickmore *et al.*, 1991; Price *et al.*, 1995; Innis *et al.*, 1996, 1997; Ishii *et al.*, 2001). The vertical wind configuration observed on the morning side (*i.e.*, after magnetic midnight at 1100 UT) in the present observation is consistent with these results, but on the evening side is opposite to them. Although no relationships, even casual ones, have yet been found between the two, this upward wind region corresponds to the eastward current region.

Innis *et al.* (1996) reported a relationship between the magnetometer data and OI630.0 nm vertical wind found from a cross correlation at Mawson. The results appear to be consistent with the 'morning regime' identified in our results.

We consider two possible ways that these wind patterns may be built, both upward on the equator side of aurora in the pre-midnight sector and the opposite relation between vertical wind and aurora in the post-midnight sector. The first of these is variation of the ionospheric current source in the auroral oval. Kamide (1988) shows schematic distribution of electric field/conductivity dominant regions. The Harang

This document is provided by JAXA.

discontinuity is clearly manifested as a switch from the eastward to the westward electrojet, and more specifically as a switch from the "electric field" dominant electrojet to the "conductivity" dominant electrojet. There is another boundary in the morning sector that divides the electric field/conductivity dominant region (Fig. 9.6 in Kamide's paper). Because the ionospheric Joule heating rate is proportional to conductivity and the square of the electric field, the neutral gas is heated more effectively in the electric field dominant region than in the conductivity dominant region. The electric field dominant region shown in Kamide (1988) is equatorward of the oval in the pre-midnight region, and poleward of the oval in the post-midnight region; the Joule heating rate can be stronger in the region than in others.

Second, Lorentz force may contribute to the building of the wind patterns. A similar idea is discussed in Peteherych *et al.* (1985). They mentioned that $J \times B$ force is downward (upward) when the westward (eastward) electrojets are observed. This idea sounds persuasive because our case shows that the direction of the ionospheric current are opposite to each other where the relation between vertical wind and the location of aurora is opposite: the correlation between vertical wind and estimated peaks of ionospheric current is positive (negative) during the eastward (westward) current was observed (Fig. 3). In this case, the direction of Lorentz force is perpendicular to the magnetic field and the inclination of the magnetic field is 77.49 deg at PFRR. This means that if the observed vertical wind was driven by Lorentz force, there should be a horizontal wind about 4.5 times (~tan 77.49) larger than the vertical winds. However, our results shows more complicated relation between ionospheric currents and the vertical winds: vertical wind velocity varied significantly even when the current direction did not change. It means that we need any other mechanism to explain the phenomena, even if the Lorentz force may be one of the sources of the vertical winds.

5. Concluding remarks

The temporal variation of vertical winds in the polar thermosphere deduced from OI557.7 nm observation with an FPI was compared with the location and intensity of the ionospheric current estimated from geomagnetic field data obtained from Alaska chain observatories. A case study observed on December 5, 1999 was presented in this study.

The eastward current dominant interval was clearly separated from the westward current dominant one at 1130 UT in this case. The relation between the vertical wind and the location of ionospheric current between before and after the boundary was clearly different. Namely, the downward (upward) vertical wind was found to be dominant equatorward (poleward) of the ionospheric current after 1130 UT (~0030 UT), which is consistent results obtained in many previous works. Before this time, however, the opposite relation held. This difference may be explained by the MLT dependence of effective Joule heating rate and/or Lorentz force driving, but more observational results will be required before this can be ascertained with precision.

Acknowledgments

The magnetometer data was provided by John Olson, Geophysical Institute,

This document is provided by JAXA.

University of Alaska, Fairbanks. We thank June Pelehowski and Brian Lawson for supporting the operation of the Fabry-Perot interferometers, Meridian Scanning Photometer, and the observatory at Poker Flat. This study has been supported in part by the U.S.-Japan International Research Project to observe the middle atmosphere, NICT.

The editor thanks Dr. J. L. Innis and another referee for their help in evaluating this paper.

References

Aruliah, A.L. and Rees, D. (1995): The trouble with thermospheric vertical winds: geomagnetic, seasonal and solar cycle dependence at high latitudes. J. Atmos. Terr. Phys., **57**, 597–609.

Conde, M. and Dyson, P. (1995): Thermospheric vertical winds above Mawson, Antarctica. J. Atmos. Terr. Phys., **57**, 589–596.

Crickmore, R.I., Dudeney, J.R. and Rodger, A.S. (1991): Vertical thermospheric winds at the equatorward edge of the auroral oval. J. Atmos. Terr. Phys., **53**, 485–492.

Innis, J.L., Greet, P.A. and Dyson, P.L. (1996): Fabry-Perot spectrometer observations of the auroral oval/polar cap boundary above Mawson, Antarctica. J. Atmos. Terr. Phys., **58**, 1973–1988.

Innis, J.L., Dyson, P.L. and Greet, P.A. (1997): Further observations of the thermospheric vertical wind at the auroral oval/polar cap boundary above Mawson station, Antarctica. J. Atmos. Terr. Phys., **59**, 2009–2022.

Ishii, M., Okano, S., Sagawa, E., Watari, S., Mori, H., Iwamoto, I. and Murayama, Y. (1997): Development of Fabry-Perot interferometers for airglow observations. Proc. NIPR Symp. Upper Atmos. Phys., **10**, 97–108.

Ishii, M., Oyama, S., Nozawa, S., Fujii, R., Sagawa, E., Watari, S. and Shinagawa, H. (1999): Dynamics of neutral wind in the polar region observed with two Fabry-Perot Interferometers. Earth Planets Space, **51**, 833–844.

Ishii, M., Conde, M., Smith, R.W., Krynicki, M., Sagawa, E. and Watari, S. (2001): Vertical wind observations with two Fabry-Perot interferometers at Poker Flat, Alaska. J. Geophys. Res., **106**, 10537–10551.

Ishii, M., Kubota, M., Conde, M., Smith, R.W. and Krynicki, M. (2004): Vertical wind distribution in the polar thermosphere during Horizontal E Region Experiment (HEX) campaign. J. Geophys. Res., **109**, doi: 10.1029/2004JA010657.

Kamide, Y. (1988): Electrodynamic Processes in the Earth's Ionosphere and Magnetosphere. Kyoto, Kyoto Sangyo Univ. Press, 756 p.

Lühr, H., Geisler, H. and Schlegel, K. (1994): Current density models of the eastward electrojet derived from ground-based magnetic field and radar measurements. J. Atmos. Terr. Phys., **56**, 81–91.

Peteherych, S., Shepherd, G.G. and Walker, J.K. (1985): Observation of vertical E-region neutral winds in two intense auroral arcs. Planet. Space Sci., **33**, 869–873.

Price, G.D. and Jacka, F. (1991): The influence of geomagnetic activity on the upper mesosphere/lower thermosphere in the auroral zone. I. Vertical winds. J. Atmos. Terr. Phys., **53**, 909–922.

Price, G.D., Smith, R.W. and Hernandez, G. (1995): Simultaneous measurements of large vertical winds in the upper and lower thermosphere. J. Atmos. Terr. Phys., **57**, 631–643.

Rees, D., Smith, R.W., Charleton, P.J., McCormac, F.G., Lloyd, N. and Steen, A. (1984): The generation of vertical winds and gravity waves at auroral latitudes -I. Observations of vertical winds. Planet. Space Sci., **38**, 667–684.

Shepherd, G.G., Thuillier, G., Solheim, B.H., Rochon, Y.J., Criswick, J., Gault, W.A., Peterson, R.N., Wiens, R.H. and Zhang, S.-P. (1995): WINDII on UARS—Status report and preliminary results. The Upper Mesosphere and Lower Thermosphere, ed. by R.M. Johnson and T.L. Killeen. Washington, D.C., Am. Geophys. Union, 297–304 (Geophysical Monograph **87**).

Smith, R.W. and Hernandez, G. (1995): Vertical winds in the thermosphere within the polar cap. J. Atmos. Terr. Phys., **57**, 611–620.

This document is provided by JAXA.

Adv. Polar Upper Atmos. Res., 19, 71–79, 2005
© 2005 National Institute of Polar Research

Research note

High-resolution simulation of propagation of interplanetary shock wave caused by a coronal mass ejection observed on November 13, 2003

Tomoya Ogawa[1]*, Mitsue Den[1], Takashi Tanaka[2] and Kazuyuki Yamashita[3]

[1] *Space Simulation Group, National Institute of Information and Communications Technology, Nukuikita-Machi 4–2–1, Koganei-shi, Tokyo 184-8795*
[2] *Department of Earth and Planetary Sciences, Kyushu University, Hakozaki 6–10–1, Higashi-ku, Fukuoka 812-8581*
[3] *The Center for Educational Research, University of Yamanashi, Takeda 4, Kofu 400-8510*
**Corresponding author. E-mail: ogawa@nict.go.jp*

(Received December 18, 2004; Accepted April 12, 2005)

Abstract: We simulated the three-dimensional (3D) propagation of a shock wave caused by a coronal mass ejection (CME) on November 13, 2003. The 3D simulations were performed using a high-resolution adaptive mesh refinement (AMR) technique. The AMR technique enabled us to resolve near the sun with $(0.06R_\odot)^3$-sized cells and to resolve the entire shock front with $(0.24R_\odot)^3$-sized cells in an interplanetary simulation within a $(500R_\odot)^3$-sized computational box. The solar wind was measured by an imaginary spacecraft positioned at point L1 in the simulations. A model fitted for solar wind density fluctuations observed by the ACE spacecraft was employed, and models in which some CME parameters were changed were employed for comparison. The relationships between the CME parameters and the solar wind fluctuations were also investigated, and the results were compared with the solar wind data observed at point L1 by the ACE spacecraft.

key words: coronal mass ejection, interplanetary shock wave, three-dimensional simulation

1. Introduction

Fast coronal mass ejections (CMEs) cause shock waves in interplanetary space. The shock waves may continue to fluctuate strongly when they arrive at Earth, leading to space weather phenomena in the Earth's magnetosphere and ionosphere.

Three-dimensional (3D) simulations of interplanetary shock wave propagation are difficult to perform in one simulation box spanning the orbit of Earth as long as a regular mesh structure is used because of limitations in computational resources (CPU power and memory capacity). The use of a spherical mesh is one effective solution to this problem. Odstrcil and Pizzo (1999) and Odstrcil *et al.* (2004) used a fan-shaped spherical mesh to investigate CME-caused structures within a streamer belt. However, a spherical mesh cannot resolve CME-caused shock waves with a high resolution once

This document is provided by JAXA.

the shock waves are distant from the sun. The use of an adaptive mesh refinement (AMR) technique (Khokhlov, 1998) is an excellent solution to this problem. The AMR technique dynamically adapts the meshes to suit the physical state. Running structures can be monitored using fine meshes and coarse meshes can be allocated to quiet regions. This feature makes it possible to simulate interplanetary shock wave propagations with high resolution. Manchester *et al.* (2004) performed AMR simulations of interplanetary CME propagation, but they localized their fine meshes for the CME to a narrow region along a sun-to-earth line.

We used a 3D AMR hydrodynamic code to simulate an interplanetary shock wave caused by a CME that occurred at 0930 UT on November 13, 2003. The CME was observed by SOHO/LASCO with a velocity of 1141 km/s (see the SOHO LASCO CME Catalog available on the SOHO web page). We selected this CME because it produced a clear shock wave on a quiet solar wind. The relevant shock wave was observed by the ACE spacecraft about 43.8 hours after the detection of the CME. In our simulations, the plane of the shock wave was processed using small cells, and a high resolution was maintained throughout the simulation.

2. Simulation

Simulations of CME-caused shock waves were performed using our 3D AMR code. With the AMR technique, the areas, positions, and shapes of the regions of fine meshes can be adapted to suit the physical state in progress. This makes it possible to monitor the shock wave structure using fine meshes and to monitor the ambient solar wind using coarse meshes, enabling high-resolution simulations to be performed using available computer resources.

The equations for the system are

$$\begin{cases} \dfrac{\partial \rho}{\partial t} + \nabla \cdot (\rho \mathbf{u}) = 0, \\ \dfrac{\partial (\rho \mathbf{u})}{\partial t} + \nabla \cdot (\rho \mathbf{u}\mathbf{u}) = \rho \mathbf{g}, \\ \dfrac{\partial e}{\partial t} + \nabla \cdot (e+P)\mathbf{u} = \rho \mathbf{g} \cdot u + (\gamma - 1)Q, \end{cases} \tag{1}$$

where ρ, $\mathbf{u}$, $\mathbf{g}$, e, P, γ, and Q are mass density, velocity, gravitational acceleration, total energy density, pressure, specific heat ratio, and heating function, respectively. We set

$$\gamma = \frac{5}{3}, \tag{2}$$

and

$$\mathbf{g} = G\frac{M_\odot}{r^3}\mathbf{r}, \tag{3}$$

where G, $M_\odot$, $\mathbf{r}$, and $r = |\mathbf{r}|$ are the gravitational constant, the solar mass, the position vector from the solar center, and the distance from the solar center, respectively. And we set the heating function as

This document is provided by JAXA.

$$Q=-\rho q_0(T-T_0)\exp\left[-\frac{(r-R_\odot)^2}{\sigma_0^2}\right], \tag{4}$$

where T, r, and $R_\odot$ are temperature, distance from the sun, and the solar radius, respectively. We choose $\sigma_0=4.5R_\odot$, which was the minimum value used by Manchester *et al.* (2004) and

$$\begin{cases} q_0=10^6\text{erg/g/s/K}, \\ T_0=2.7\times10^6\text{K}, \end{cases} \tag{5}$$

to reproduce the density and the velocity of the solar wind observed by the ACE spacecraft at point L1. We set the density at the inner boundary to $\rho=1.3\times10^6$ protons/cm^3. The above parameters were used to reproduce the velocity and the density of the solar wind in the pre-shock region.

The equations were then rewritten into difference equations that can be solved using the Roe-MUSCL algorithm (Roe, 1981; Van Leer, 1977, 1979; Fujii, 1994). The size of the computational box was $(500R_\odot)^3$. The sun was positioned at the conter of the box. The inner boundary was set at $1.1R_\odot$. The cell size was $(0.06R_\odot)^3$ near the sun, $(0.24R_\odot)^3$ in the area of the shock wave, and $(7.8R_\odot)^3$ for the maximum cells. We first obtain a steady-state solar wind and then inputted the model CME into the inner boundary. The CME model is described in the next section.

3. CME model

Once a steady-state solar wind was produced, we inputted a model CME into the inner boundary. We focused on a CME that occurred at 0930 UT on November 13, 2003. The speed of the CME was measured as 1141 km/s by SOHO/LASCO. We modeled the CME as follows:

$$\begin{cases} A(\xi)=\cos\left(\dfrac{\pi\xi}{2\xi_0}\right) \\ B(t)=\begin{cases} \dfrac{t}{\tau_r} & (0<t<\tau_r) \\ 1 & (\tau_r<t<\tau_r+\tau_d) \\ \dfrac{2\tau_r+\tau_d-t}{\tau_r} & (\tau_r+\tau_d<t<2\tau_r+\tau_d) \end{cases} \\ V(t,\xi)=V_{\max}A(\xi)B(t) \\ \rho(t,\xi)=\rho_{SW}+\rho_{CME}A(\xi)B(t), \end{cases} \tag{6}$$

where V_{CME} is the radial velocity of the input CME, V_{max} is the maximum of V_{CME}, ρ_{SW} is the density of the pre-CME solar wind, ρ_{CME} is the additional density of the input CME, and ξ, ξ_0, τ_r, and τ_d are the angle to the axis of the CME cone, the angular radius of the CME, the stand-up time, and the duration of the CME, respectively (Odstrcil and Pizzo, 1999). We adopted $\xi_0=15^\circ$ and $\tau_r=1$ hour; these values are the ones used by Odstrcil and Pizzo (1999). And we set V_{max} as the observed CME velocity. The *Joint*

This document is provided by JAXA.

Table 1. Density, duration, position, and mass of the CME in each of the models.

Model	ρ_{CME} (cm^{-3})	τ_d (hour)	Longitude	Mass (g)
1	1.0×10^6	4	E25°	1.1×10^{15}
2	1.0×10^6	4	E15°	1.1×10^{15}
3	2.6×10^6	4	E30°	3.8×10^{15}
4	0.5×10^6	10	E25°	1.7×10^{15}

ρ_{CME}, density; τ_d, duration. All other parameters were fixed, as described in the text.

USAF/NOAA Report of Solar and Geophysical Activity reported that the CME appeared to erupt off an east limb. We therefore assumed that the CME occurred on the east side of the equator. The longitude, together with the ρ_{CME} and τ_d, were adjusted as a temporal plot of the solar wind density at point L1 to fit the ACE data. These fitted values were used in model 1, shown in Table 1. For comparison, we simulated three other models that deviated from the fitted point. Model 2 was the same as model 1 except for the direction of the eruption of the CME. Model 3 had a higher density and the longitude was adjusted so that the density peak at point L1 agreed with the observed value. Model 4 had a longer duration time and the same longitude as model 1. The density of model 4 was adjusted so that the density peak at point L1 agreed with the observed value. These models are summarized in Table 1.

4. Results

The density distributions of model 1 on the solar equator plane at 24 and 52 hours after the CME are shown in Fig. 1. An imaginary spacecraft placed at point L1 in a simulation box was used to observe the time variations of the solar wind. The density and velocity of model 1 are plotted in Fig. 2, together with the ACE data. The density of models 2, 3, and 4 are plotted in Fig. 3, while the velocities of these models are shown in Fig. 4. The upper-left panels of Figs. 3 and 4 are the same as the left and right panels of Fig. 2, respectively. These plots were adjusted so that the rise time of the simulated shocks coincided with the observed one. Shock waves were detected in each model. The arrival times of the shock waves in each model were 51.6, 47.2, 50.2, and 51.6 hours after the beginning of the CME input. A shock wave was seen in the ACE data 43.8 hours after SOHO/LASCO detected a bright loop. Of note, the data were measured at the center of the cell nearest to point L1, not just at point L1. This method produced apparent discontinuities in the temporal plots when the cell size was changed. For instance, the jumps in the post-shock region seen in Figs. 2, 3, and 4 are not real discontinuities. Such jumps were small near the shock front well because the size of the cells near the shock front was small. The density plot of model 1 agreed with the observations, but the peak was somewhat higher. The velocity of model 1 had a somewhat lower peak and was difficult to decrease. Model 2 was the same as model 1, but the erupting direction was turned toward Earth. The density plot of model 2 had a higher peak and a subsequent second peak. The velocity of model 2 was 10^1 km/s higher than that of model 1. Model 3 erupted a larger mass directed away from Earth. The density peak of model 3 moved backward from the shock. The velocity plot of

This document is provided by JAXA.

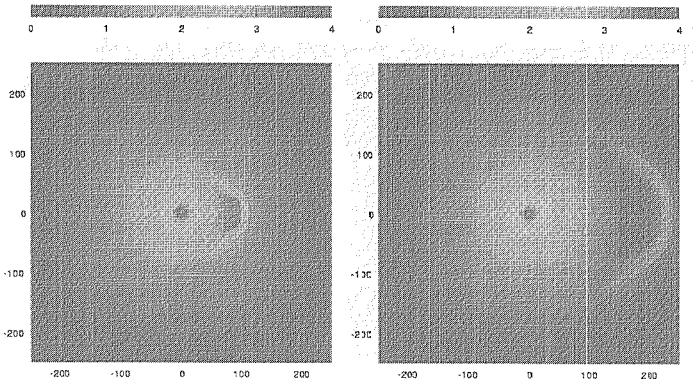


Fig. 1. Density distributions of model 1 on the solar equator plane at 24 (left) and 52 (right) hours after the occurrence of the CME. The logarithm of the density is expressed by the gray scale. The unit of length is the solar radius. The sun is located at the center (0,0,0). The horizontal axis faces the direction of the CME eruption. The earth is located at (195,91,0).

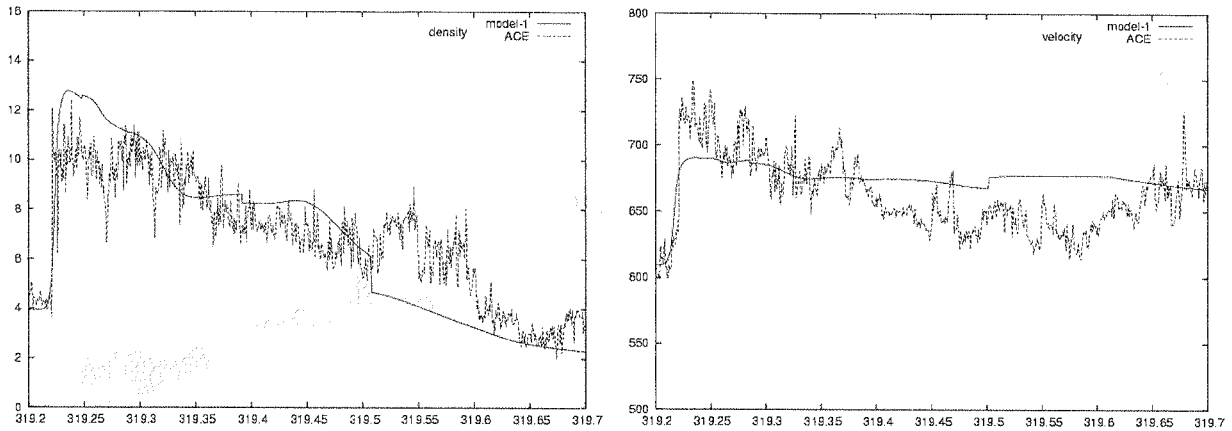


Fig. 2. Density plot (left) and velocity plot (right) for model 1 compared with the ACE data. The unit of the horizontal axis is Day of Year. The units of the vertical axes in the two panels are cm^{-3} (left) and km/s (right), respectively. The simulated results were adjusted so that the rise time coincided with the observed one.

This document is provided by JAXA.

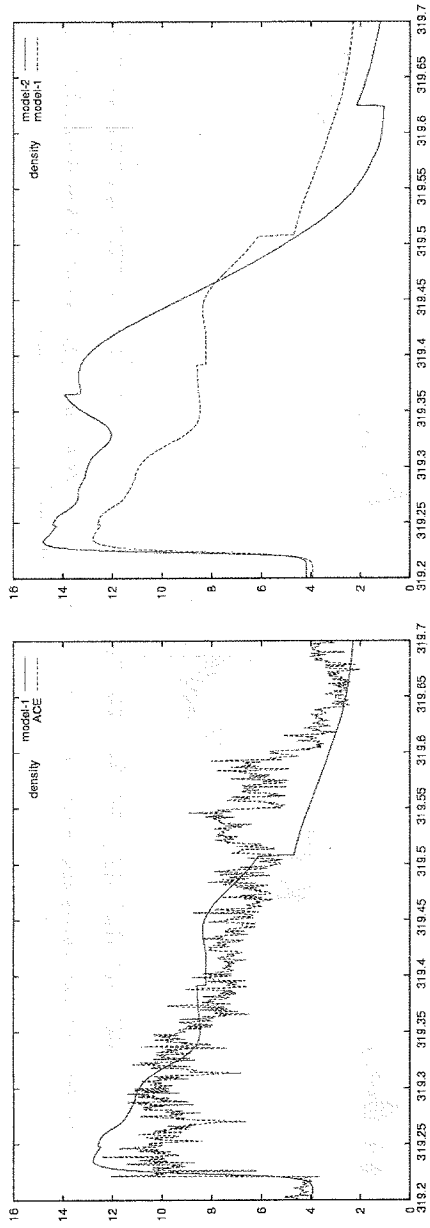


Fig. 3. Density plot of model 1 compared with the ACE data (upper left) and density plots of models 2–4 compared with that of model 1 (upper right, lower left, and lower right). The units of the horizontal and vertical axes are Day of Year and cm^{-3}, respectively. The simulated results were adjusted so that the rise time coincided with the observed one.

This document is provided by JAXA.

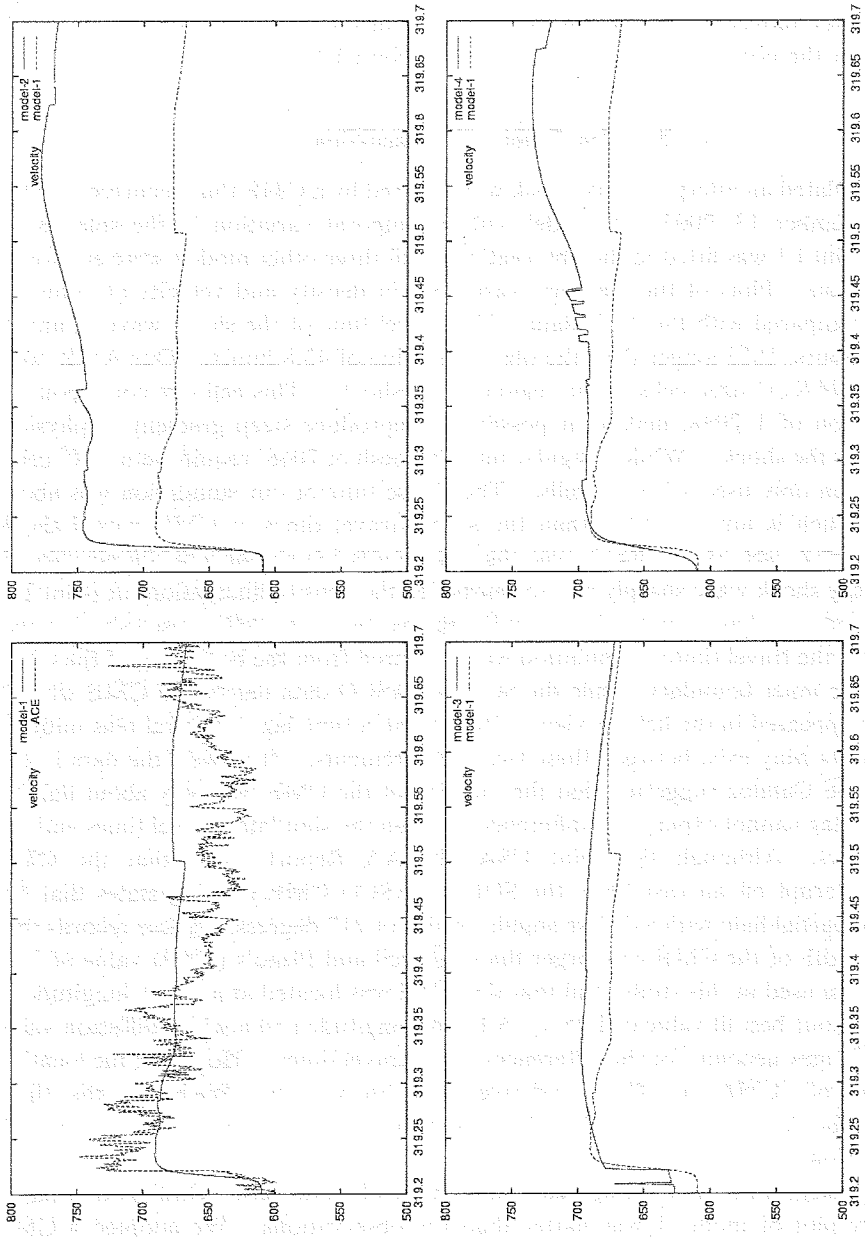


Fig. 4. Velocity plot of model 1 compared with the ACE data (upper left) and velocity plots of models 2–4 compared with that of model 1 (upper right, lower left, and lower right). The units of the horizontal and vertical axes are Day of Year and km/s, respectively.

This document is provided by JAXA.

model 3 was similar to model 1, but a bit higher. Model 4 erupted a low density for a long duration. The density plot of model 4 had a flat profile. In these plots, some discontinuous profiles with small jumps were observed. These apparent variations were caused by switching from fine cells to coarse cells at point L1, since the merging of the cells implies the movement of the observation point of the imaginary spacecraft, which was placed at the center of the cell nearest to the point L1.

5. Conclusions and discussion

We simulated an interplanetary shock wave caused by a CME that occurred at 0930 UT on November 13, 2003. A model with a temporal variation in the solar wind density at point L1 was fitted to the observations, and three other models were employed for comparison. Plots of the temporal variations in density and velocity at point L1 were then compared with the ACE data. The travel time of the shock wave in model 1 was 51.6 hours, 18% longer than the observed value of 43.8 hours. Our AMR code allocated $(0.24R_{\odot})^3$-sized cells to the region of the shock. This cell size corresponded to a resolution of 1/2048, making it possible to reproduce steep gradient of physical quantities for the shock. While a regular interval mesh of 2048^3 requires 8.6×10^9 cells, our simulation only used 1.8×10^7 cells. The elapse time of our simulation was about 11 hours, which is much shorter than the actual travel times of CME-caused shock waves. In the present paper, we showed that our simulation was able to characterize an interplanetary shock wave sharply and to reproduce the density fluctuations at point L1. Our AMR code also has the potential to predict the passage of a CME-caused shock wave.

Of note, the travel time in simulation was measured from the beginning of the CME input into the inner boundary, while the SOHO/LASCO data detected a CME when a bright loop appeared in the field of view. In general, a time lag of several tens minutes to a few hours May exist between these two measurements. However, the data in the LASCO CME Catalog suggested that the time lag of the CME was only about half an hour. This lag cannot explain the difference between the simulated travel times and the observed ones. Although the Joint USAF/NOAA Report states that the CME appeared to erupt off an east limb, the SOHO LASCO CME Catalog states that the CME was a partial halo with a diffuse angular width of 217 degrees. These records that the actual width of the CME was larger than Odstrcil and Pizzo's (1999) value of $\xi_0=15^\circ$, which we used in this study, and that the CME was located at a larger longitude in the east than our best fit value of E25°. A larger longitude and a wider diffusion value for the CME may account for the differences in the travel times. However, the location and diffusion of a CME are difficult to derive from observations. We believe that these parameters should be adjusted so that the solar wind variation at point L1 agrees with the observations.

The density plot of model 1 agreed well with the observations. On the other hand, the velocity plot of model 1 was flatter than the observations. We adopted a CME model that was similar to Odstrcil and Pizzo's model (Odstrcil and Pizzo, 1999). However, we placed the inner boundary at $1.1R_{\odot}$, very close to the sun surface, while Odstrcil and Pizzo placed the inner boundary at $30R_{\odot}$, distant from the sun. A different CME may be required when the inner boundary is set close to the solar surface.

This document is provided by JAXA.

The CME model should be improved to reproduce both density and velocity plots more accurately. Furthermore, the solar magnetic field may influence the evolution of CMEs. CME observations show a nearly constant velocity of the shock front from about $3R_\odot$ to $27R_\odot$ (see the SOHO LASCO CME Catalog). The magnetic effects on the shock front of the CME seem to be small, but they may affect the post-shock region. The effects of the solar magnetic field will be examined in our next study. Odstrcil and Pizzo (1999) and Odstrcil *et al.* (2004) demonstrated that interactions between a CME-caused shock wave and the ambient solar wind distort the shock front. In the present paper, we selected a CME that had a quiet pre-shock solar wind to allow this effect to be ignored. In general, a structured solar wind should be modeled in a simulation of an interplanetary shock wave propagation. In the future, we hope to introduce a realistic model of a solar magnetic field through which the solar wind structure can be reproduced.

Acknowledgments

Data from the SOHO LASCO CME Catalog was used in the present study. This CME catalog is generated and maintained by NASA and The Catholic University of America in cooperation with the Naval Research Laboratory. SOHO is an international cooperation between ESA and NASA. Data from the Joint USAF/NOAA Report of Solar and Geophysical Activity was also used. We are grateful for the production of these useful and well-ordered data.

The editor thanks Drs. M. Tokumaru and T. Nakagawa for their help in evaluating this paper.

References

Fujii, K. (1994): Numerical Methods for Computational Fluid Dynamics (Ryutai Rikigaku no Suchi Keisan-ho). Tokyo, University of Tokyo Press (in Japanese).

Khokhlov, A.M. (1998): Fully threaded tree algorithms for adaptive refinement fluid dynamics simulations. J. Comput. Phys., **143**, 519–543.

Manchester, W.B., Gombosi, T.I., Roussev, I., Ridley, A., De Zeeuw, D.L., Sokolov, I.V. and Powell, K.G. (2004): Modeling a space weather event from the Sun to the Earth: CME generation and interplanetary propagation. J. Geophys. Res., **109**, A02107.

Odstrcil, D. and Pizzo, V.J. (1999): Three-dimensional propagation of coronal mass ejections (CMEs) in a structured solar wind flow 1.CME launched within the streamer belt. J. Geophys. Res., **104** (A1), 483–492.

Odstrcil, D., Riley, P. and Zhao, X.P. (2004): Numerical simulation of the 12 May 1997 interplanetary CME event. J. Geophys. Res., **109**, A02116.

Roe, P.L. (1981): Approximate riemann solvers, parameter vectors, and difference schemes. J. Comput. Phys., **43**, 357–372.

Van Leer, B. (1977): Toward the ultimate conservative difference scheme. 4, A new approach to numerical convection. J. Comput. Phys., **23**, 276–299.

Van Leer, B. (1979): Toward the ultimate conservative difference scheme. 5, A second-order sequel to Godunov's method. J. Comput. Phys., **32**, 101–136.

This document is provided by JAXA.

Adv. Polar Upper Atmos. Res., 19, 80–83, 2005
© 2005 National Institute of Polar Research

Research note

Plasma flow characteristics in converging field line geometry in anisotropic plasmas

Osuke Saka

Kurume National College of Technology, Kurume 830-8555
E-mail: saka@kurume-nct.ac.jp

(Received November 30, 2004; Accepted March 23, 2005)

Abstract: Plasma flow characteristic in the anisotropic plasmas was examined in converging field lines by assuming the double adiabatic condition. When the pressure anisotropy disappears, the plasma flows behave as isotropic fluids; flows are decelerated/accelerated above/below the sound velocity. When the pressure anisotropy defined by $P_\perp/P_z$ was below unity, the critical velocity that separates acceleration and deceleration increased above the sound velocity. In the opposite case where $P_\perp/P_z > 1$, the critical velocity decreased below the sound velocity. We suggest that a kinetic energy of the flow varies as the pressure anisotropy changes.

key words: field-aligned plasma flows, anisotropic plasmas, converging field lines

1. Introduction

It is natural to consider that plasma pressures are often anisotropic in magnetized plasmas. In this research note, we examine the field-aligned flow in the converging field geometry by assuming anisotropic plasma pressure condition. We assumed double adiabatic equations of state, where perpendicular and parallel motion with respect to the field lines is decoupled. We show a role of pressure ratio (perpendicular to parallel) on the plasma flows. Present results could be applied to the plasma flows along the field-lines, particularly in low altitudes of Earth's dipole fields.

2. Plasma flow in converging field lines

We assume anisotropic plasma pressures ($P_\perp \neq P_z$). Here, $\perp$ and z denote "perpendicular" and "parallel" to the field lines. We discuss the field-aligned behavior of the steady state plasma flow.

The equation of motion along the field lines can be written as,

$$\rho(V \cdot \nabla)V = -\nabla P_z + \frac{P_z - P_\perp}{B}\nabla B. \quad (1)$$

Here, B is the strength of the magnetic field, ρ is mass density, V is a field-aligned

This document is provided by JAXA.

component of the fluid velocity, ∇ is a gradient operator along the field lines. The second term of the right-hand side of the equation describes the net parallel pressure force associated with the changing area along the flux tube and the magnetic mirror force averaged over the particles (Comfort, 1988). This term, however vanishes for the isotropic plasmas.

Plasmas considered are magnetized and motions normal and along the field lines are assumed to be decoupled. Such conditions are represented by the double adiabatic equations of state (*e.g.*, Parks, 1991)

$$\frac{\mathrm{d}}{\mathrm{d}t}\left(\frac{P_\perp}{\rho B}\right)=0, \tag{2}$$

$$\frac{\mathrm{d}}{\mathrm{d}t}\left(\frac{P_z B^2}{\rho^3}\right)=0. \tag{3}$$

The equation of the mass conservation along the converging field line geometry can be expressed as

$$\rho \cdot A \cdot V=\text{const.} \tag{4}$$

Here, A denotes a cross-section of the flux tube.

Equations (1) through (4) can be written as

$$\frac{\mathrm{d}P_z}{\rho}=-V\mathrm{d}V-\frac{1}{\rho}\frac{P_\perp-P_z}{B}\mathrm{d}B, \tag{1'}$$

$$\frac{\mathrm{d}P_\perp}{\rho}-\frac{P_\perp}{\rho}\frac{\mathrm{d}\rho}{\rho}-\frac{P_\perp}{\rho}\frac{\mathrm{d}B}{B}=0, \tag{2'}$$

$$\frac{\mathrm{d}P_z}{P_z}-3\frac{\mathrm{d}\rho}{\rho}+2\frac{\mathrm{d}B}{B}=0, \tag{3'}$$

$$\frac{\mathrm{d}\rho}{\rho}+\frac{\mathrm{d}A}{A}+\frac{\mathrm{d}V}{V}=0. \tag{4'}$$

To merge eq. (1') through (4'), we assume a conservation of magnetic flux along flux tube.

$$B \cdot A=\text{const.} \tag{5}$$

After few steps of algebraic manipulations, we have following expression that describes flow velocity in the changing area of flux tube.

$$\frac{P_\perp}{P_z}\frac{\mathrm{d}A}{A}=\frac{1}{V}\left(\frac{V^2}{C_z^2}-3\right)\mathrm{d}V. \tag{6}$$

Here, C_z is a sound velocity along the field lines defined by $\sqrt{P_z/\rho}$.

The expression of $P_\perp/P_z$ and C_z^2 in eq. (6) can be obtained from double adiabatic eqs. (2) and (3) by incorporating initial conditions at the starting point of the flow in the converging nozzle. In addition, we utilize in equations pressure anisotropy α defined by $P_\perp/P_z$ and total pressure P_t defined by $2P_\perp+P_z$, instead of using $P_\perp$, and P_z. Then, $P_\perp/P_z$ can be written as β_2 (V^2/A), and $1/C_z^2$ as $\beta_1 V^2$. Here, $\beta_1=(2\alpha_0+1)\ 1/(C_0^2 \cdot V_0^2)$ and $\beta_2=\alpha_0(A_0/V_0^2)$ are calculated by use of initial pressure anisotropy α_0, initial sound velocity C_0 defined by $\sqrt{P_{0t}/\rho_0}$, initial flow velocity V_0, and initial cross-section A_0.

Finally, eq. (6) may be written as,

This document is provided by JAXA.

$$\beta_2 \frac{dA}{A^2} = (\beta_1 V^4 - 3)\frac{dV}{V^3}. \tag{7}$$

By integrating eq. (7) from A_0 to A_1 of the cross section, and from V_0 to V_1 of the flow velocity, we have following expression.

$$\alpha_0 \int_1^{a_1} \frac{da}{a^2} = (2\alpha_0+1)M_0^2 \int_1^{v_1} v dv - 3\int_1^{v_1} \frac{dv}{v^3}.$$

Here, $a_1 = \frac{A_1}{A_0}$, $v_1 = \frac{V_1}{V_0}$, $\alpha_0 = \frac{P_{0\perp}}{P_{0z}}$ and $M_0 = \sqrt{\frac{V_0^2}{C_0^2}}$.

Finally, we have following relation.

$$a_1 = -\frac{2\alpha_0 v_1^2}{M_0^2(2\alpha_0+1)v_1^4 - [2+2\alpha_0+1+M_0^2(2\alpha_0+1)]v_1^2+3}. \tag{8}$$

Again, α_0 is pressure anisotropy defined by $\alpha_0 = P_{0\perp}/P_{0z}$, and M_0 is Mach number defined by $M_0 = \sqrt{V_0^2/C_0^2}$. Those values α_0 and M_0 are initial values where the flow started.

We analyze eq. (8) to examine whether the initial flow at $A = A_0$ is accelerated ($(da_1/dv_1) < 0$) or decelerated ($(da_1/dv_1) > 0$). It is a function of pressure anisotropy α_0 and Mach number M_0. When pressure anisotropy is unity at a flow start, the flow below/above $M_0 = 1$ is accelerated/decelerated as is shown in Fig. 1. It is a well-known result in fluid dynamics where the supersonic/subsonic flows are decelerated/accelerated in the converging nozzle (Ikui and Matsuo, 1995). When the initial pressure anisotropy α_0 decreases below unity, the flow above $M_0 = 1$ can be accelerated. Mach number that separates acceleration and deceleration of the flow (critical Mach number) varies as a function of initial pressure anisotropy α_0 as is shown in Fig. 1.

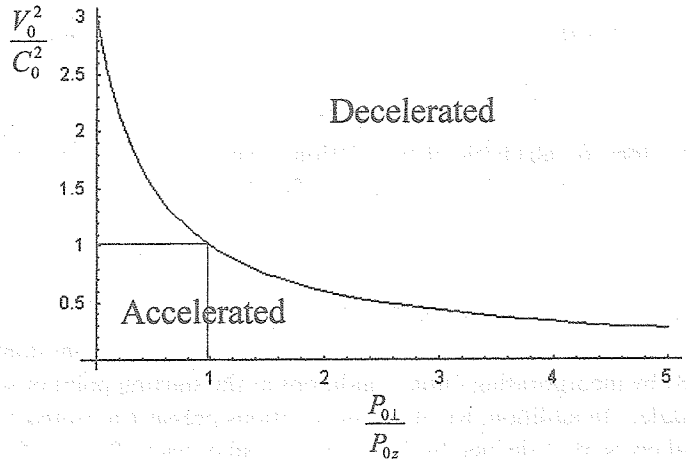


Fig. 1. A line of critical Mach number as a function of pressure anisotropy in the horizontal axis and Mach number in the vertical axis. Flows above the critical Mach number are decelerated. The vertical and horizontal lines indicate that the critical Mach number becomes unity when $P_{0\perp} = P_{0z}$.

This document is provided by JAXA.

3. Discussion

In some analogy to fluid dynamics, we could demonstrate that deceleration takes place when flow velocity exceeds the critical Mach number, M_c, because of a compressive nature in converging field line geometry. Conversely, acceleration takes place because flow is in-compressive when flow velocity is below the critical Mach number. The magnetic mirror force is force acting on a single particle. It is a multiple of a perpendicular kinetic energy and gradient of the field magnitudes. When the magnetic mirror force of individual particle is averaged over the particles in volume element, it can be written as $(-P_\perp/B)\nabla_z B$. In addition, a net parallel pressure associated with the changing area along the flux tube can be shown as $(P_z/B)\nabla_z B$ (*e.g.* Comfort, 1988). Therefore the second term of the right-hand side of the eq. (1) is consisted of the magnetic mirror force averaged over the particles and net parallel pressure force. It was found that the net parallel pressure raise the critical Mach number while the magnetic mirror force lower it. We have demonstrated the initial flow condition in the flux tube in terms of acceleration/deceleration of flow. However, the flow penetrates some distance after it leaved the starting point by changing the pressure anisotropy thereafter. The depth of the penetration will be deep when the flow is initially accelerated, while it is shallow when the flow is initially decelerated. Such a flow characteristic will be a subject of our future work.

Acknowledgments

The editor thanks Dr. M.P. Freeman and another referee for their help in evaluating this paper.

References

Comfort, R.H. (1988): The magnetic mirror force in plasma fluid models. Modeling Magnetospheric Plasma, ed. by T.E. Moore and J.H. Waite, Jr. Washington, D.C., Am. Geophys. Union, 51–53 (Geophysical Monograph Series 44).

Ikui, T. and Matsuo, K. (1995): Mechanical Dynamics of Compressive Fluids. Rikogaku-sha (in Japanese), 38 p.

Parks, G.K. (1991): Physics of Space Plasmas : An Introduction. New York, Addison-Wesley, 267 p.

This document is provided by JAXA.

Adv. Polar Upper Atmos. Res., 19, 84–88, 2005
© 2005 National Institute of Polar Research

Research note

The effect of magnetic mirror force on the field-aligned acceleration of plasmas

Osuke Saka[1]*, Shigeru Fujita[2] and Daniel N. Baker[3]

[1]*Department of Physics, Kurume National College of Technology, Kurume 833-8555*
[2]*Meteorological College, Asahi, Kashiwa 277-0852*
[3]*Laboratory for Atmospheric and Space Physics, University of Colorado, Boulder, CO 80309, U.S.A.*
**Corresponding author. E-mail: saka@kurume-nct.ac.jp*

(Received December 13, 2004; Accepted May 13, 2005)

Abstract: A magnetic mirror effect on the field-aligned acceleration of plasma flow is discussed for anisotropic plasma conditions by incorporating double adiabatic equations of state. In a non-uniform distribution of the field magnitude along the field lines, it is found that the field-aligned acceleration is toward higher field intensity region for the fluid of low thermal energy, while the acceleration is toward lower field intensity region for the fluid of high thermal energy. We infer that perpendicular pressure would cause such an energy-dependent behavior of the field-aligned acceleration through the magnetic mirror force.

key words: anisotropic plasma pressure, diamagnetic condition, field-aligned acceleration

1. Introduction

MHD waves in space plasmas are categorized as Alfvén, fast mode and slow mode waves. The Alfvén wave has an incompressible nature. It carries a curl of the cross-field plasma displacement, $\xi_\perp$ (Southwood and Kivelson, 1991), which is the reason why the Alfvén wave has been suggested to carry field-aligned currents. On the other hand, the fast and slow mode waves can carry the divergence of the cross-field plasma displacement $\xi_\perp$ (*e.g.*, Kadomtsev, 1976). For this reason, the fast and slow mode waves are referred to as a compressible mode. For those compressible modes, a spatial gradient of div$\xi_\perp$ along the field line would result in a field-aligned inertial force. Such a force would drive the plasma flows along the field lines. In anisotropic plasma where the perpendicular and parallel pressures differ, the magnetic mirror force averaged over the particles and the net field-aligned force associated with the changing area along the flux tube are added (Comfort, 1988).

In this report, we examine the field-aligned acceleration of plasmas in anisotropic fluid pressure.

This document is provided by JAXA.

2. An equation of motion for field-aligned plasma acceleration

We examine field-aligned flow acceleration by assuming anisotropic plasma pressure condition ($P_\perp \neq P_z$). Here, $\perp$ and z denote "perpendicular" and "parallel" to the field lines.

We start with the field-aligned acceleration of the plasma flow by the following equation (*e.g.*, Parks, 1991).

$$\rho \frac{d\mathbf{V}_z}{dt} = -\nabla_z P_z - (P_z - P_\perp)\mathbf{b}(\nabla \cdot \mathbf{b}). \tag{1}$$

Here, $\mathbf{b}$ is unit vector of the magnetic field $\mathbf{B}$, ρ is mass density, $\mathbf{V}_z$ is field-aligned component of the fluid velocity $\mathbf{V}$. The second term of the right-hand side of the equation can also be written as $-[(P_z - P_\perp)/B]\nabla_z B$, because $\mathbf{b}(\nabla \cdot \mathbf{b}) = -(\mathbf{B}/B^2)\nabla_z B$. Equations of motion perpendicular to the field lines in anisotropic plasma can be given by the equation (*e.g*, Parks, 1991)

$$\rho \frac{d\mathbf{V}_\perp}{dt} = \mathbf{j} \times \mathbf{B} - \nabla_\perp P_\perp - (P_z - P_\perp)(\mathbf{b} \cdot \nabla)\mathbf{b}. \tag{2}$$

Here, $\mathbf{j}$ is current vector.

From the field equation, $\partial \mathbf{B}/\partial t = \nabla \times (\mathbf{V} \times \mathbf{B})$, we can relate field and plasma displacement $\boldsymbol{\xi}$ as,

$$\mathbf{B} = \nabla \times (\boldsymbol{\xi} \times \mathbf{B}). \tag{3}$$

In addition, double adiabatic equations of state are given by (*e.g.*, Parks, 1991)

$$\frac{d}{dt}\left(\frac{P_\perp}{\rho B}\right) = 0, \tag{4}$$

$$\frac{d}{dt}\left(\frac{P_z B^2}{\rho^3}\right) = 0. \tag{5}$$

We examine first order perturbations of eqs. (1) through (5) assuming uniform background field geometries and uniform distribution of background plasma density, pressure. The pressure is however anisotropic. Those are expressed as,

$$\rho_0 \frac{\partial \mathbf{V}_{1z}}{\partial t} = -\nabla_z P_{1z} + \frac{(P_{0z} - P_{0\perp})}{B_0}\nabla_z B_1, \tag{1'}$$

$$\mathbf{j}_1 \times \mathbf{B}_0 = \nabla_\perp P_{1\perp}, \tag{2'}$$

$$\mathbf{B}_1 = \nabla \times (\boldsymbol{\xi}_1 \times \mathbf{B}_0), \tag{3'}$$

$$P_{1\perp} = \frac{P_{0\perp}}{\rho_0}\rho_1 + \frac{P_{0\perp}}{B_0}B_1, \tag{4'}$$

$$P_{1z} = -2\frac{P_{0z}}{B_0}B_1 + 3\frac{P_{0z}}{\rho_0}\rho_1. \tag{5'}$$

Here, the suffix "0" and "1" indicate the background and perturbed quantities. We assume no background flow, $\mathbf{V}_0$ and no background currents, $\mathbf{J}_0$. To derive the eq. (2′), we assumed that the force balance across the field lines is maintained primarily by the diamagnetic condition where the inertial currents in the left-hand side of the equation and centrifugal term ($(\mathbf{b} \cdot \nabla)\mathbf{b} = \mathbf{n}/R$, $\mathbf{n}$ is unit vector normal to the field lines, R is

This document is provided by JAXA.

radius of the field line curvature) in the last part of the right-hand side of the eq. (2) are neglected. Such conditions can be justified when field variations are slow to be able to neglect the inertial force as compared to the pressure gradient force and when scale length of the pressure gradient across the field lines is smaller than the radius of the field line curvature.

From the eq. (3′) we can calculate the first order perturbation of the field line vector $\mathbf{B}_1=-\mathbf{B}_0\mathrm{div}\hat{\boldsymbol{\xi}}_\perp+(\mathbf{B}_0\cdot\nabla)\hat{\boldsymbol{\xi}}_\perp$ (Kadomtsev, 1976). Here, $\hat{\boldsymbol{\xi}}_\perp$ is plasma displacement across the field lines. The first order quantity of the field magnitude can be obtained by the following relation.

$$B_1=\sqrt{(\mathbf{B}_0+\mathbf{B}_1)^2}-\sqrt{(\mathbf{B}_0)^2}\approx\frac{\mathbf{B}_0\cdot\mathbf{B}_1}{B_0}.$$

Substituting $\mathbf{B}_1=-\mathbf{B}_0\mathrm{div}\hat{\boldsymbol{\xi}}_\perp+(\mathbf{B}_0\cdot\nabla)\hat{\boldsymbol{\xi}}_\perp$ into the above relation, we have the following expression.

$$B_1=-B_0\cdot\mathrm{div}\hat{\boldsymbol{\xi}}_\perp. \tag{3″}$$

The left-hand side of the eq. (2′) may be expressed as (Kadomtsev, 1976),

$$-\frac{1}{\mu_0}\nabla_\perp(\mathbf{B}_0\cdot\mathbf{B}_1)+\frac{B_0^2}{\mu_0}(\mathbf{b}\cdot\nabla)\mathbf{b}.$$

We again neglect the centrifugal term in the equation. Then, pressure perturbations in the right-hand side of eq. (2′) may be written as,

$$P_{1\perp}=\rho_0C_A^2\cdot\mathrm{div}\hat{\boldsymbol{\xi}}_\perp. \tag{2″}$$

Here, C_A is Alfvén velocity defined by $B_0/\sqrt{\mu_0\rho_0}$, μ_0 is the magnetic permeability in vacuum. Because the term "$\mathrm{div}\hat{\boldsymbol{\xi}}_\perp$" in the eqs. (2″) and (3″) is common for both the perturbations B_1 and $P_{1\perp}$, the field-aligned gradient of the pressure and field magnitude along the flux tube can be related as,

$$\nabla_zB_1=-\frac{\mu_0}{B_0}\cdot\nabla_zP_{1\perp}. \tag{6}$$

Substituting eq. (6) into (1′), we obtain

$$\rho_0\frac{\partial\mathbf{V}_{1z}}{\partial t}=-\nabla_zP_{1z}+\frac{(P_{0\perp}-P_{0z})}{B_0}\frac{\mu_0}{B_0}\nabla_zP_{1\perp}. \tag{7}$$

Substituting (2″), (3″), (4′) and (5′) into eq. (7), we have

$$\rho_0\frac{\partial\mathbf{V}_{1z}}{\partial t}=-\frac{P_{0z}}{B_0}\left[\frac{P_{0\perp}}{P_{0z}}-3\cdot\left(2+\frac{B_0^2}{\mu_0P_{0\perp}}\right)\right]\frac{\partial B_1}{\partial z}. \tag{8}$$

We define the pressure anisotropy, α, and the ratio of field and fluid energy density, γ by the equations,

$$\alpha=\frac{P_{0\perp}}{P_{0z}},$$

$$\gamma=\frac{1}{N_0E_0}\cdot\frac{B_0^2}{\mu_0}.$$

Here, N_0 is number density, E_0 is total fluid energy define by the following relations,

$$N_0E_0=P_0,\ \text{and}\ P_0=P_{0\perp}+P_{0z}.$$

This document is provided by JAXA.

Substituting above relations into (8), we have

$$\rho_0 \frac{\partial V_{1z}}{\partial t} = -\frac{P_0}{B_0}\left[\frac{\alpha-6}{\alpha+1} - \frac{3}{\alpha}\cdot\gamma\right]\frac{\partial B_1}{\partial z}. \tag{9}$$

The field-aligned acceleration is in the parallel/anti-parallel direction of $\partial B_1/\partial z$ as the total fluid energy is above/below the critical value, E_{0c} defined by

$$E_{0c} = \frac{B_0^2}{N_0\mu_0}\cdot\frac{3(\alpha+1)}{\alpha(\alpha-6)}.$$

3. Discussion

The magnetic mirror force is force acting on a single particle. It is a multiple of a perpendicular kinetic energy and gradient of the field magnitude. When the magnetic mirror force of individual particle is averaged over the particles in a volume element, it can be written by $-(P_\perp/B)\nabla_z B$. In addition, a net parallel pressure associated with the changing area along the flux tube can be shown as $(P_z/B)\nabla_z B$ (*e.g.* Comfort, 1988). Therefore the second term of the right-hand side of the eq. (1′) consists of the magnetic mirror force averaged over the particles and net parallel pressure force, though the field gradient is in a first order quantity. The direction of magnetic mirror force is opposite to both the pressure gradient force of fluid perturbation in the first term and the net parallel pressure force. When the background perpendicular pressures exceed that of the parallel pressures, the magnetic mirror force might exceed the sum of the remaining forces. Then, it is apparent that field-aligned acceleration would show two different behaviors as the anisotropy of fluid pressure varies. Because the fluid pressure can be expressed by the thermal energy of fluid, the field-aligned acceleration is a function of the pressure anisotropy and thermal energy. In our calculation, the field-aligned flow acceleration and $\partial B_1/\partial z$ are oppositely directed, when the fluid energy was above E_{0c}. This means that the fluid energy above E_{0c} is accelerated toward weaker field intensity region, if the field intensity changes along the field lines. Substituting typical plasma sheet parameters, $B_0 = 10\,\mathrm{nT}$, $N_0 = 10^{-1}\mathrm{cm}^{-3}$, E_{0c} is estimated to be 16.8 keV when the pressure anisotropy α is 7.0. The fluid energy E_{0c} decreases to 4.0 keV at $\alpha = 10.0$. There appears no upper limit in E_{0c} when α is below 6.0. It asymptotically approaches to zero as α increases.

In the present study, we examined the pressure anisotropy effect on the field-aligned flow acceleration by assuming the diamagnetic condition where inertia force and the centrifugal term are neglected. The results presented here are valid when $\nabla_\perp P_\perp \gg \rho(\partial V_\perp/\partial t)$ and $\nabla_\perp \gg 1/R$, R is radius of the field line curvature.

Acknowledgments

The editor thanks Drs. M. Watanabe and A. Yoshikawa for their help in evaluating this paper.

This document is provided by JAXA.

References

Comfort, R.H. (1988): The magnetic mirror force in plasma fluid models. Modeling Magnetospheric Plasma, ed. by T.E. Moore and J.H. Waite, Jr. Washington, D.C., Am. Geophys. Union, 51–53 (Geophysical Monograph, Series 44).

Kadomtsev, B.B. (1976): Collective Phenomena in Plasmas. Tokyo, Iwanami Shoten (in Japanese).

Parks, G.K. (1991): Physics of Space Plasmas: An Introduction. New York, Addison-Wesley, 267 p.

Southwood, D.J. and Kivelson, M.G. (1991): An approximate description of field-aligned currents in a planetary magnetic field. J. Geophys. Res., **96**, 67–75.

This document is provided by JAXA.

Adv. Polar Upper Atmos. Res., 19, 89–105, 2005
© 2005 National Institute of Polar Research

Research note

VHF data transmission experiments using MBC equipment conducted during the period from JARE-43 to JARE-45

Kaiji Mukumoto[1]*, Akira Fukuda[1], Masashi Nagasawa[2], Yasuaki Yoshihiro[1], Kei Nakano[1], Satoshi Ohichi[1], Hisao Yamagishi[3], Natsuo Sato[3], Akira Kadokura[3], Huigen Yang[4], Ming Wu Yao[5], Sen Zhang[5], Guojing He[5] and Li-Jun Jin[5]

[1] *Shizuoka University, 3-5-1, Johoku, Hamamatsu 432-8561*
[2] *Numazu College of Technology, 3600, Ooka, Numazu 410-8501*
[3] *National Institude of Polar Research, Kaga 1-chome, Itabashi-ku, Tokyo 173-851*
[4] *Polar Research Institute of China, 451 Jinqiao Road, Pudong, Shanghai 200129, China*
[5] *Xidian University, 2 Taibai Road, Xi'an, 710071, China*
**Corresponding author. E-mail: tekmuku@ipc.shizuoka.ac.jp*

(Received December 17, 2004; Accepted March 30, 2005)

Abstract: In order to study the ability of meteor burst communications (MBC) as a new medium of data collection networks in Antarctica, we have performed a series of VHF data transmission experiments. In the experiment during the period of JARE-43 (the 43rd Japanese Antarctic Research Expedition), a remote station at Zhongshan Station sent data packets to a master station at Syowa Station using a commercial MBC system. Together with meteor burst propagations, non-meteoric propagations were frequently observed during local nighttime. We found that they worked effectively for packet transmissions and greatly increased the data throughput. Overall data throughput obtained by this experiment was 0.63 bps. In JARE-44, we added another remote station at Dome Fuji Station. Since the transmitted power from the master unit was split into two directions, data throughput from Zhongshan Station was reduced to 0.36 bps. That from Dome Fuji Station was only 0.13 bps. For the experiment in JARE-45, we replaced the commercial MBC system with a RANDOM (RAdio Network for Data Over Meteor) system developed by the authors. The experiment is being conducted between Syowa and Zhongshan Stations. The estimated data throughput during the period from April 1st, 2004 to August 31st, 2004 was 2.9 bps.

key words: meteor burst communications, Antarctica, VHF, software modem, aurora

1. Introduction

MBC (Meteor Burst Communication) is known to have superiority over other BLOS (Beyond Line of Sight) communications (*e.g.* those using HF and satellite channels) in many respects such as simplicity of implementation and operation, lower initial and running costs, and reliability (Fukuda, 1997; Schanker, 1990). At high latitudes, in particular, MBC has a strong advantage over HF communications (Weitzen

This document is provided by JAXA.

et al., 1993). Since MBC uses higher frequencies (low VHF band) than HF communications, it is less subject to anomalous absorption events (such as polar cap and aurora absorption). Moreover, it is also known that MBC is very suitable for non-real time, slow rate data acquisition networks consisting of one (or few) master station(s) and many remote stations. This is because the primary drawback of MBC, that is, the low duty cycle of the intermittent channel between two stations is largely mitigated in such a star network. Thus, the authors have proposed to use MBC network for the Antarctic survey and conducted some basic experiments in Antarctica since December 2001 to study the ability of MBC for such a data collection network.

Some experiments were conducted in Arctic region such as Greenland and Alaska to study the properties of MB (Meteor Burst) channels at high latitudes. However, in the Antarctic region, there have been few experiments on MBC, even to study the properties of MB channels in that region except for the ones with backscatter meteor radars (Ogawa *et al.*, 1985; Tsutsumi *et al.*, 2001).

At high latitudes, MB propagation is not the only BLOS propagation mode in the VHF band. Others may include some kinds of sporadic E (E_s), auroral scatter and F layer propagation modes. Auroral E_s over Syowa Station is known to occur mainly at local nighttime (Ose, 1962) and its formation is related to electrojet which appears with aurora phenomenon (Fukunishi *et al.*, 1983). Cannon *et al.* (1994, 1996) reported that "wind shear E_s", known as mid-latitude E_s, is also frequently observed at high latitudes. E_s propagation modes are generally characterized by low multipath spread, slow fading, and high signal levels (Weitzen *et al.*, 1987; Weitzen and Ralston, 1988). In the high latitude E layer, VHF signals are also scattered by magnetic-field-aligned plasma irregularities. This mode of propagation is known as auroral scatter and is widely investigated in the fields of aurora and ionosphere observations (Koustov *et al.*, 2001; Makarevitch *et al.*, 2002). Signals scattered by this mode are generally subject to severe multipath, rapid fading, relatively large Doppler shift, and broader Doppler spread, so that auroral scatter is thought to have properties not compatible with usual coherent signaling techniques commonly used in MBC (Ostergaard *et al.*, 1985; Weitzen *et al.*, 1987). Some mechanisms related to the F layer can also propagate VHF signals. While such F layer propagations can increase system duty cycle, they may cause multi-path signals that result in high bit error rates due to inter-symbol interference (Maynard, 1968). Another important phenomenon related to MBC at high latitudes is anomalous ionospheric absorption, both polar cap and auroral. It may significantly reduce system duty cycle and cause long lasting blackout (McDonough *et al.*, 1993).

In this paper, all BLOS propagation modes other than MB are lumped and referred to as NMB (Non-Meteor Burst) propagation modes from a communication viewpoint. In our experiment, NMB propagation phenomena are frequently observed mainly at local nighttime.

Our experiments started in December 2001. In the first year, during the period of JARE-43 (the 43rd Japanese Antarctic Research Expedition, December 2001–March 2003), two kinds of experiments, 'tone experiment' and 'data experiment', were conducted between Syowa and Zhongshan Stations. In the former experiment, a continuous tone signal was sent from Zhongshan Station (69.4°S, 76.4°E geographic; 74.6°S, 96.5°E corrected geomagnetic) and the signal level observed at Syowa Station (69.0°S,

This document is provided by JAXA.

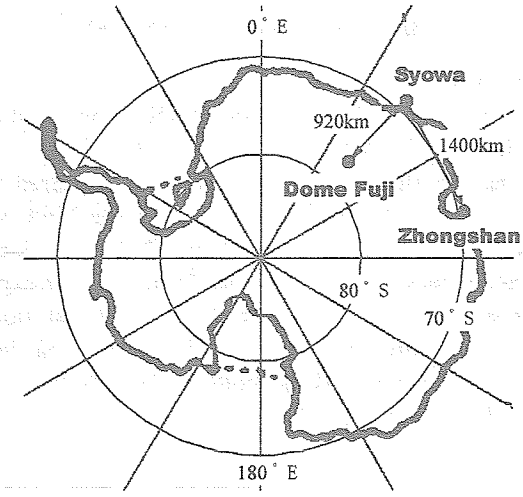


Fig. 1. Location of the stations.

39.6° E geographic; 66.2° S, 72.0° E corrected geomagnetic) was recorded to study the basic properties of the MB channel. In the latter one, a remote station located at Zhongshan Station sent data packets to a master station at Syowa Station to evaluate the performance of a commercial MBC system in this region. The radio units used in the experiment were manufactured by MCC (Meteor Communications Co., Wash., USA). In JARE-44 (December 2002–March 2004), we added another MCC remote station at Dome Fuji Station (77.3° S, 39.7° E geographic; 70.8° S, 56.7° E corrected geomagnetic) and tried to collect data from two remote stations simultaneously. Figure 1 illustrates the path geometry. While Syowa and Zhongshan Stations are located at almost the same latitude, Dome Fuji Station is located at almost the same longitude as Syowa Station. By this configuration, we can examine the effect of path direction and length on the system performance. In JARE-45 (December 2003–March 2005), we have replaced the MCC system by a RANDOM (RAdio Network for Data Over Meteor) system designed and developed by the authors. This experiment is now being conducted between Syowa and Zhongshan Stations. Dome Fuji Station was not used for this experiment since no wintering party was sent there in JARE-45. The tone experiment has been continuously conducted between Syowa and Zhongshan Stations during the periods of JARE-44 and JARE-45.

In this paper, we show the results of the data experiments conducted during the periods from JARE-43 to JARE-45 from the viewpoint of communications. Detailed geophysical considerations are left to future papers, which will discuss the issue with the result of the tone experiment. Overall descriptions of our MBC experiments in Antarctica are found in Fukuda *et al.* (2003, 2004). Some results of the tone experiment are described in Nagasawa *et al.* (2004).

This document is provided by JAXA.

2. Data experiment in JARE-43

2.1. *Description of the experiment*

In the data experiment during the period of JARE-43, we used a commercial MBC system, in which the radio units were manufactured by MCC. The radio units are designed for general use, so that system designers are required to properly set the parameters of the units for their networks. Moreover, the MCC system can transmit various types of data such as messages, positional data, and data logger data. Its transmission procedure changes with the type of data. In our experiment, we set the parameters assuming a star network consisting of one master station and many remote stations, although there was only one remote station in the real experimental system. Also, we assumed that the network would collect scientific data, so that the remote station was set to send data stored in a data logger.

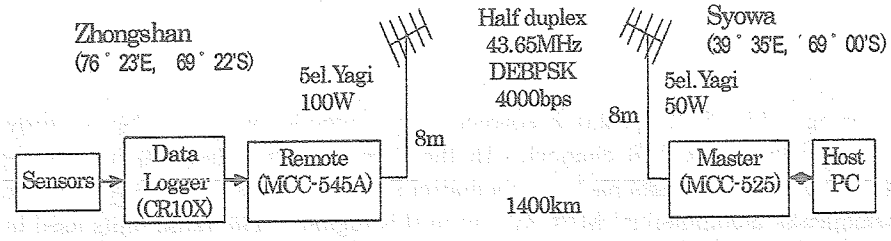


Fig. 2. Equipment for the data experiment during the period of JARE-43.

Figure 2 shows the equipment for the data experiment conducted during the period of JARE-43. The remote and master units are designated MCC-545A and MCC-525, respectively. The remote unit equipped at Zhongshan Station was set to acquire data of 20 bytes from a data logger designated CR10X (manufactured by Campbell Scientific Ut. USA) with an interval of 5 min. The acquired data is sent as a DP (Data Packet) when the remote station receives a PP (Probe Packet) sent by the master unit installed at Syowa Station. When the master unit successfully receives the DP, it sends an AP (Acknowledge Packet) to the remote station. If the remote station receives the AP, then it removes the transmitted data set from the transmission buffer and proceeds to the next data set. We set the lifetime of DPs to 2 hours in the experiment. *i.e.*, if the remote station cannot receive an AP for a DP within 2 hours, then it discards the DP. Figure 3 shows the length and transmission timing of packets used in the experiment.

In the experiment, the master station was set to operate only 5 min in each 10 min interval to avoid interference with the tone experiment. At Syowa Station, we had to use a long coaxial cable (10D2E of length 150 m) for connecting the master unit with the antenna since there was no suitable antenna site near the equipment house. Nominal attenuation of the cable is about 31 dB/km at 50 MHz. Thus, the estimated power radiated from the antenna was about 50 W though the power output from the master unit was 150 W. Also, at Zhongshan Station, we used the same cable (10D2E) of length 60 m to connect between the remote unit and the antenna. The power output

This document is provided by JAXA.

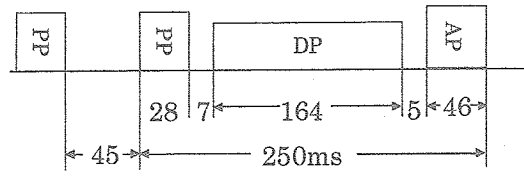


Fig. 3. The length and transmission timing of packets used in the data experiment during the period of JARE-43.

from the remote unit was around 150 W. Thus, the estimated radiation power from the antenna was about 100 W. More detailed descriptions of the experiment can be found in Fukuda *et al.* (2003, 2004) and Mukumoto *et al.* (2004).

2.2. *Results and discussion*

The data experiment in JARE-43 started April 1st, 2002 and lasted until December 31st, 2002. Figure 4 shows hourly data and PP reception ratios averaged over this period together with the 10 dB duty cycle obtained by the tone experiment. Here, data reception ratio is defined by the number of received data sets during a specified period divided by the number of data sets generated during that period. In the experiment, we have set the remote station to generate 12 data sets per hour. Similarly, PP reception ratio is defined by the number of received PPs in a specified period divided by the number of transmitted PPs in that period. In the calculation of the hourly PP reception ratio in Fig. 4, we have used a fixed value (24658) as the denominator although it is not precisely constant. This value is obtained by assuming that PPs are constantly transmitted with the interval shown in Fig. 3. This is apparently an overestimate but may be a good estimate since the cause of decreasing the number of PP transmissions is DP arrivals and, in this experiment, the number of DP generations per hour is limited to 12. On the other hand, 10 dB duty cycle is obtained from the tone experiment according to the process described in Fukuda *et al.* (2004) and Yoshihiro

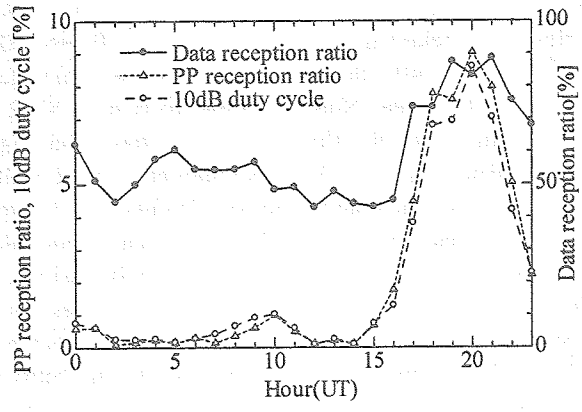


Fig. 4. Hourly variations of data reception ratio, PP reception ratio and 10 dB duty cycle (April 1st–December 31st, 2002).

This document is provided by JAXA.

Table 1. List of days excluded from the analysis.

Statistics	Days excluded from the analysis
Data reception ratio	April 18, April 21–22, June 15–16, Aug. 29–Sep. 17, Oct. 16–29, Dec. 6–10, Dec. 30–31
PP reception ratio	April 21–22, May 15–17, May 28–29, June 15–16, Aug. 29–Sep. 17, Oct. 16–29, Dec. 23–26, Dec. 30–31
10 dB duty cycle	April 4, April 21–23, Dec. 24–25

et al. (2001). We have used two antennas with different tower length for the reception of tone signals. The hourly 10 dB duty cycle shown in Fig. 4 is obtained by analyzing tone signal received by the lower antenna and averaging over the same period with the data experiment, *i.e.*, from April 1st, 2002 to December 31st, 2002.

In the analyses of these hourly statistics, we have excluded days listed in Table 1 from the averaging because the system stopped operation or operated under some different parameter settings in those days.

In Fig. 4, all curves exhibit an increase during the period around 15–24 UT. Local time at the midpoint of the path between Syowa and Zhongshan Stations proceeds about 4 hours from UT. Thus, the period of 15–24 UT corresponds to local nighttime. As mentioned in Nagasawa *et al.* (2004), the increment observed during local nighttime is thought to be caused by NMB propagation phenomena. It should be noted that the NMB propagations have very different properties from those mentioned in Weitzen *et al.* (1993) and Cannon *et al.* (1994, 1996). They are also different from NMB propagations observed at mid-latitude, which are known to occur mainly during daytime in summer.

Curves of 10 dB duty cycle and PP reception ratio are very similar not only in their shapes but also in their values. If Syowa and Zhongshan Stations had the same noise environment, received PP power with SNR of 4.2 dB corresponds to received signal level of 10 dB above the noise power in the tone experiment. This is deduced from the fact that 1) the radiation power of PP transmission was 50 W while that of tone signal was 115 W and 2) packet transmission speed of the MCC system is 4000 bps while the assumed noise bandwidth to determine the threshold levels in the tone experiment is 2400 Hz. Considering that packets in the MCC system are BPSK (Binary Phase Shift Keying) modulated and coherently demodulated, it seems plausible in case of ideal AWGN (Additional White Gaussian Noise) channel to require SNR of more than 4.2 dB for receiving PPs. Thus, it implies that the channel has good characteristics *i.e.*, it can be modeled as an intermitted fading AWGN channel without multipath or frequency shift. Moreover, we can see the coincidence of the curves of PP reception ratio and 10 dB duty cycle even in local nighttime. Thus, we can conclude that the NMB propagations also work effectively for coherent packet transmissions.

On the other hand, the curve of data reception ratio changes not proportionally to that of 10 dB duty cycle although their shapes show some resemblance. This is because the transmission buffer at the remote station is frequently being empty during the period with large duty cycle since DPs are generated with the interval of 5 min and their lifetime is set to 2 hours. It should be noted that there may exist some other minor reasons such as 1) a DP reception requires 250 ms of continuous channel open, 2) the master station

This document is provided by JAXA.

Table 2. Averages over April 1st–December 31st, 2002.

	10 dB duty cycle (%)	PP reception ratio (%)	Data reception ratio (%)
Total average	2.15	2.01	59.1
Average over 00–16 UT	0.36	0.46	51.4
Average over 16–24 UT	5.73	5.12	74.4

stops PP transmissions for a few hundred milliseconds after a DP reception.

In the figure, we also find that there is small increment in PP reception ratio and 10 dB duty cycle around 10 o'clock. This increment stems from a propagation phenomenon occurred in the period from December 10th to 18th. We have not yet identified the propagation phenomenon (Geminids meteor shower is suspected).

Table 2 is a list of the results averaged over the period from April 1st, 2002 to December 31st, 2002 excluding days listed in Table 1. Total data reception ratio averaged over all hours is about 59.1% while those averaged over the periods of 00–16 UT and 16–24 UT are 51.4% and 74.4%, respectively. The difference is caused by NMB propagations that have been frequently observed after 16 UT. Since the system has operated only 5 min in each 10 min interval and a DP has contained 20 bytes of information, the data throughputs is 0.63 bps for the whole hours, 0.55 bps for the hours before 16 UT and 0.79 bps for the hours after 16 UT, respectively. On the other hand, from PP reception ratios, we can estimate the ratio of the time during which the channel can transmit data at the speed of 4000 bps to the operating period. The estimated values are 2% for the whole hours, 0.46% for the hours before 16 UT and 5.12% for the hours after 16 UT. Channel capacities or possible maximum data throughputs calculated from these results are 80 bps, 18.4 bps and 204.8 bps, respectively. Of course, no system can attain these data throughputs since DPs generally need some overheads and their transmissions are controlled by some transmission procedure. In case of the MCC system, to transmit 20 bytes of data, it requires at least 250 ms of continuous channel opening as previously shown in Fig. 3. Thus, data throughput of the MCC system is greatly reduced from the channel capacities obtained above even if the remote station always has DPs in its transmission buffer.

It should be noted that the proportion of PP reception ratio to 10 dB duty cycle for the hours before 16 UT is 1.28 whereas that for the hours after 16 UT is 0.89. This may implies that NMB channels have characteristics somewhat worse than the MB channel.

Figure 5 shows daily averaged data reception ratio, PP reception ratio, and 10 dB duty cycle for July 2002. In this figure, we also find good coincidence between the daily variations of PP reception ratio and 10 dB duty cycle. On the other hand, correlations between the daily variation of data reception ratio and those of PP reception ratio and 10 dB duty cycle are very little. This is because the transmission buffer at the remote station is frequently being empty during the period with large duty cycle, so that the increase of duty cycle does not directly bring about the increase of data reception ratio as mentioned before. It should be noted that the daily variations of PP reception ratio and 10 dB duty cycle are dominated by the occurrence of NMB phenomena and their durations.

This document is provided by JAXA.

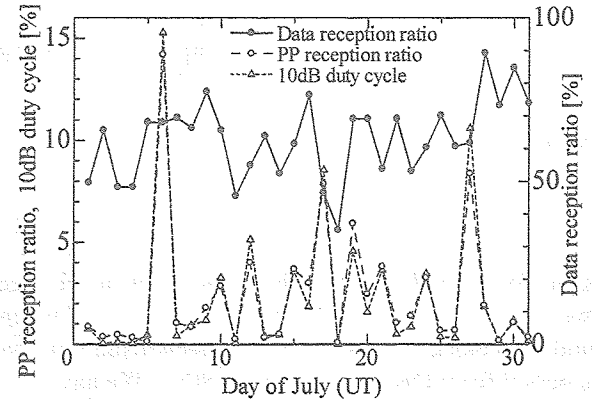


Fig. 5. Daily variations of data reception ratio, PP reception ratio and 10 dB duty cycle (April 1st–December 31st, 2002).

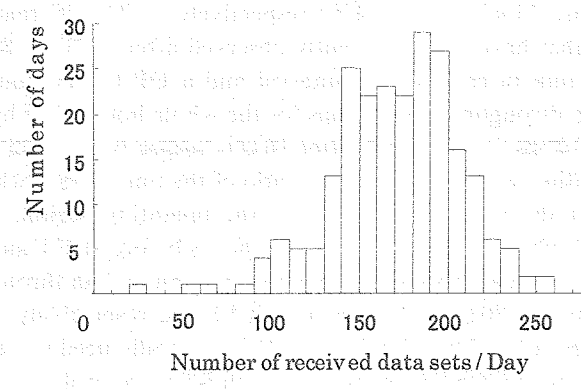


Fig. 6. Histogram of the number of received data sets per day (April 1st–December 31st, 2002).

Figure 6 shows a histogram of the number of days classified by the number of received data sets per day with the resolution of 10 packets. We find that the graph exhibits the shape of a mountain with somewhat flat top since there exist two kinds of days *i.e.*, days with and without NMB phenomena. This implies that, during the experimental period, there were no serious blackout events that retarded MBC data transmission for a long time. Specifically, days with the number of received data sets less than 100 were 8 days divided into three periods. They were 22 Aug. (67), 24 Aug. (58), 25 Aug. (93), 30 Oct. (90), 31 Oct. (82), 10 Nov. (22), 11 Nov. (94). Here, numbers in parentheses represent the number of data sets received in each day.

3. Data experiment in JARE-44

3.1. Description of the experiment

Figure 7 shows the system of the data experiment conducted during the period of

This document is provided by JAXA.

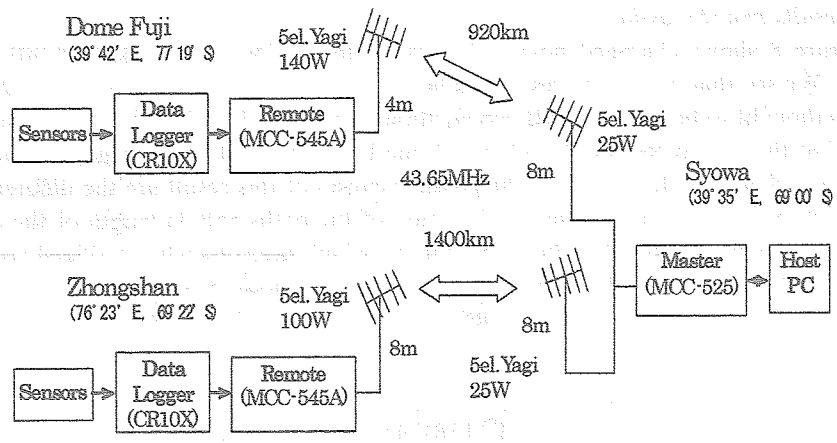


Fig. 7. Equipment for the data experiment during the period of JARE-44.

JARE-44. In this experiment, we added another MCC remote station at Dome Fuji Station, which had the same configuration as the remote station at Zhongshan Station except for the antenna tower length and the radiation power. At Dome Fuji Station, the antenna tower with the length of 4 m was installed near the equipment house. The measured output power from the remote unit at Dome Fuji Station was around 140 W. The antenna cable used in Dome Fuji Station was short, so that the loss was negligible. At Syowa Station, two antennas, each directed to Zhongshan and Dome Fuji Stations respectively, were connected to the master unit using a split cable. Because of this configuration, the transmission power from the master unit was divided into two coaxial cables connected to each antenna. Thus, the radiation power of each antenna was estimated to be only about 25 W. On the other hand, when receiving a DP, input to the master unit was the sum of power from the antenna directed to the signal source and that from the antenna without signal arrival. Thus, SNR of DP was lowered about 3 dB.

Prior to the experiment shown in Fig. 7, we also carried out another short term experiment where only the Dome Fuji remote station was operated as a remote station and the master unit at Syowa Station was connected solely to the antenna directed to Dome Fuji Station.

In both the experiments, the operation of the system was the same with that in the data experiment in JARE-43, *i.e.*, the master station transmitted PPs only 5 min in each 10 min, the remote stations acquired 20 byte data with the interval of 5 min and lifetime of data was set to be 2 hours. The three kinds of data experiments and their durations are:

① From Zhongshan to Syowa, April 1st, 2002–December 31st, 2002,
② From Dome Fuji to Syowa, February 27th, 2003–March 23rd, 2003,
③ From Zhongshan and Dome Fuji to Syowa, March 25th, 2003–December 31st, 2003.

As mentioned before, we exclude days listed in Table 1 in the analysis of the experiment during the period of JARE-43. As for the analysis of the experiment in JARE-44, we exclude days from July 30th, 2003 to August 8th, 2003 since the system was not operated during that period due to a hardware problem at the master station.

This document is provided by JAXA.

3.2. Results and discussion

Figure 8 shows averaged hourly data reception ratios for the experiments listed above. We see that all the curves shows larger values during the period of 16–24 UT, which is thought to be due to NMB propagations. Comparing the results of ① and ②, we see that the data reception ratio from Dome Fuji remote station is smaller than that from Zhongshan remote station. The possible causes of this result are the difference in 1) location of the remote stations, 2) direction of the paths and 3) length of the paths. However, we cannot exclude other possibilities, which are somewhat artificial reasons, such as difference of the radio units, antenna height and noise conditions. Thus, to get a conclusion for this issue, we need additional carefully designed experiments.

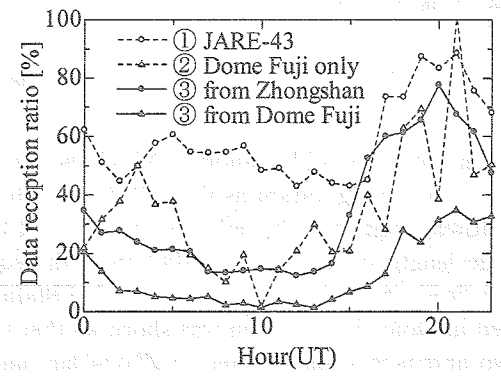


Fig. 8. Hourly variations of data reception ratios (①: April 1st–December 31st, 2002, ②: February 27th–March 23rd, 2003, ③: March 25th–December 31st, 2003).

Next, we compare data reception ratios from Zhongshan Station in the experiments of ① and ③. During 00–15 UT, the latter is less than one half of the former. This is because effective radiation power of PPs in the experiment of ③ is a half of that in the experiment of ① since the transmission power is separated into two antennas. On the other hand, during the period of 16–24 UT, the effect of reduced radiation power in PP transmission on the data reception ratio is not large since NMB propagations effectively reflect radio signals.

Comparing data reception ratios from Dome Fuji and Zhongshan Stations in the experiment of ③, we find that, as in the case of comparison between ① and ②, the former is fairly lower than the latter. We also find that the peak of the former is slightly delayed from that of the latter. This may be due to the fact that midpoint of the path between Syowa and Dome Fuji Stations is located to the west of that between Syowa and Zhongshan Stations.

The data reception ratios and the data throughputs for the experiments are summarized in Table 3. Here, data throughput is defined by the number of data bits successfully transferred divided by the operational period in second.

In Fig. 9, we show the seasonal variations of data reception ratios by averaging over month-by month. It is seen that the variations of all the curves are not large but exhibit

This document is provided by JAXA.

Table 3. Data reception ratios and data throughputs.

Experiment	Data reception ratio (%)			Data throughput (bps)		
	Total	00–16 UT	16–24 UT	Total	00–16 UT	16–24 UT
①	59.1	51.4	74.4	0.63	0.55	0.79
②	34.4	24.2	54.7	0.37	0.26	0.58
③ from Zhongshan	34.0	20.3	61.8	0.36	0.21	0.66
③ from Dome Fuji	12.3	5.8	25.4	0.13	0.06	0.27

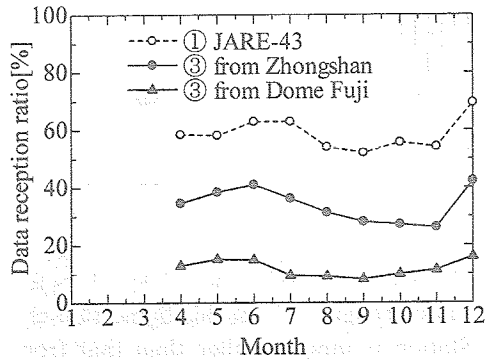


Fig. 9. Seasonal variation of data reception ratios.

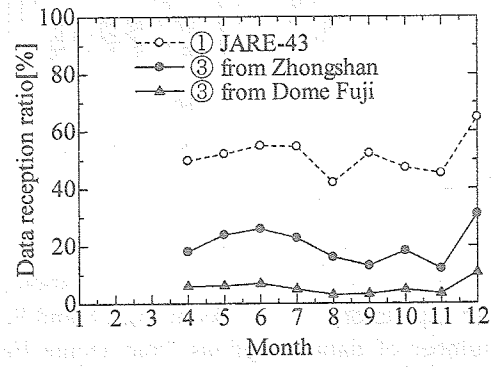


Fig. 10. Seasonal variation of data reception ratios (averaged over 00–16 UT).

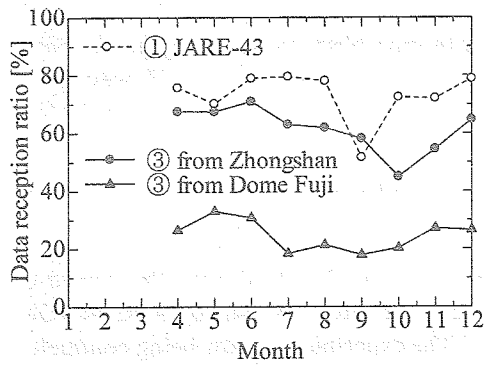


Fig. 11. Seasonal variation of data reception ratios (averaged over 16–24 UT).

a similar shape. To examine the cause of the seasonal variation, we show the monthly data reception ratios for MB hours (00–16 UT) and NMB hours (16–24 UT) in Figs. 10 and 11, respectively. In Fig. 10, the data reception ratios of the JARE-44 experiment exhibit a similar shape to that of the JARE-43 experiment. On the other hand, as shown in Fig. 11, we can see no apparent correlation between the seasonal variations in the case of NMB hours. Thus, we can conclude that the seasonal variation in the occurrence of MBs is the cause of the variations of the data reception ratios appeared in Fig. 9.

Figure 12 shows histograms of the number of days classified by the number of

This document is provided by JAXA.

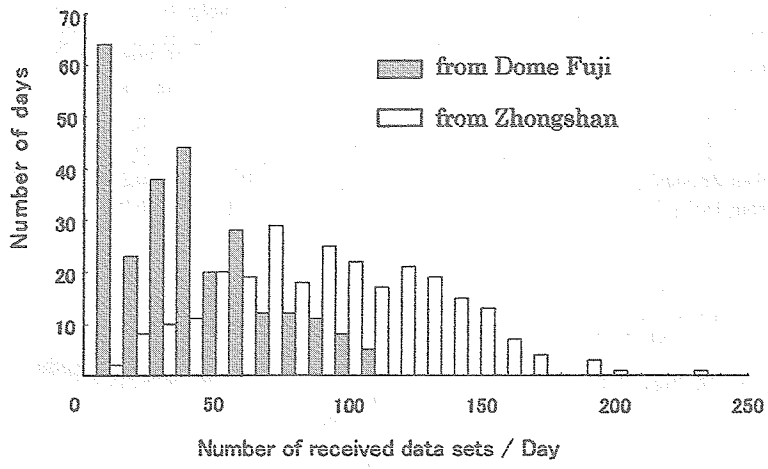


Fig. 12. Histogram of the number of received data sets per day (March 25th–December 31st, 2003).

received data sets from each remote station per day with the resolution of 10 packets for the experiment of ③. As in Figs. 8 and 9, we also recognize from this figure that the number of data receptions from Dome Fuji Station is much smaller than that from Zhongshan Station. The shape of distribution of the number of data receptions per day from Zhongshan Station is a symmetric flat top mountain whereas that from Dome Fuji Station is asymmetric having its maximum of 64 days at less than 10 packets per day. Moreover, among the 64 days, no data receptions were observed in 27 days. This number is almost 10 percent of the total number of days observed (265 days). Possible cause for no data receptions is some sort of absorption phenomenon. However, the number of data receptions from Dome Fuji Station is not enough to have a conclusion.

4. Data experiment in JARE-45

4.1. Description of the experiment

Figure13 is the system for the data experiment conducted during the period of JARE-45. In this experiment, we have replaced the MCC system by a RANDOM system designed and developed by the authors. The experiment is now being conducted between Syowa and Zhongshan Stations. Radio equipment used in the experiment is named IT-5000. The transmission power output from IT-5000 is rather accurately adjusted to 100 W. At Syowa Station, we have replaced the long antenna cable (10D 2E) with a thicker one (12DSFA) before the experiment. Nominal attenuation of the new cable is about 15.5 dB/km. Thus, estimated radiation power from the antenna of the master station is about 60 W. At Zhongshan Station, we have not changed the cable, so that estimated radiation power from the remote station is about 65 W.

The hardware of IT-5000 consists of radio, control, and DSP (Digital Signal Processor) units as shown in Fig. 14. The radio unit is responsible for 1) frequency conversion between low VHF and low IF (0.3–9.0 kHz) bands, 2) RF filtering and amplification, and 3) high speed switching between receiving and transmitting RF

This document is provided by JAXA.

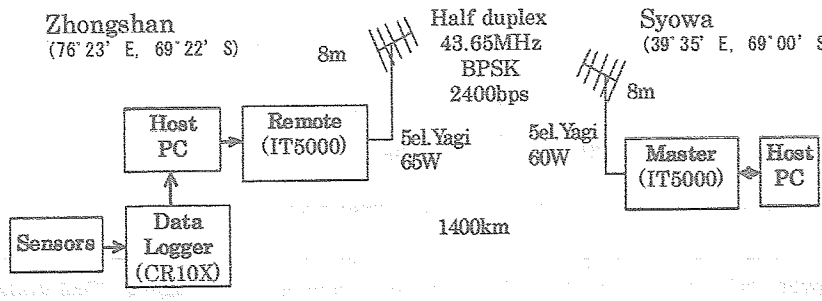


Fig. 13. Equipment for the data experiment during the period of JARE-45.

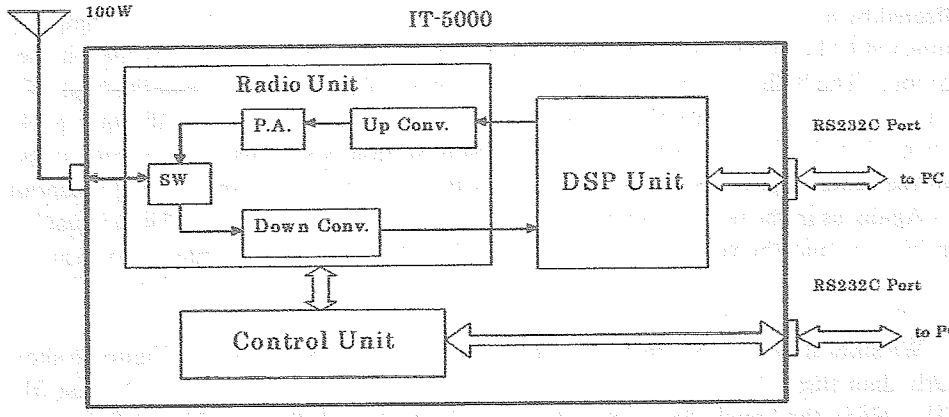


Fig. 14. Block diagram of IT-5000.

signal. The control unit monitors the radio unit. In case of detecting anomalous operation, it stops the radio unit and announces the cause to the operator. The software loaded in the DSP provides all other functions needed as an MBC equipment, which include 1) packet detection, 2) carrier and bit synchronization, 3) modulation and demodulation in low IF band, 4) coding and decoding, 5) protocol handling, 6) interfacing between the radio and the host computer, and so on.

Since almost all communication functions are accomplished by software, IT-5000 can be applied to various communication systems by changing the software on the DSP (Mahmud *et al.*, 2001). The software developed for the experiment in JARE-45 is named SMR2003. It can treat BPSK and QPSK (Quadrature Phase Shift Keying) packets with symbol speed of less than 4800 baud. Taking into account of relatively small transmission power, we have selected BPSK modulation with transmission speed of 2400 bps for the experiment. In SMR2003, packets are accurately detected and coherently demodulated by means of newly developed methods suitable for software modem (Mukumoto *et al.*, 2002). The transmission protocol installed is essentially the same as the MCC protocol described in Section 2.1. Figure 15 shows length of the packets and the transmission timing. Note that required duration of channel opening for sending a 20-byte data is 140 ms. This is shorter than that of MCC system in spite

This document is provided by JAXA.

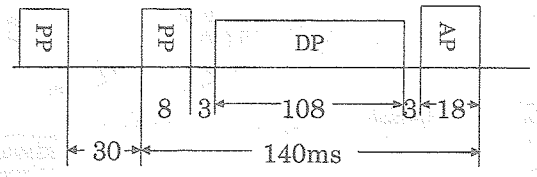


Fig. 15. Length of the packets and the transmission timing in RANDOM system.

of the lower transmission speed. This is because packets in the RANDOM system are greatly shortened using new techniques realized by the software modem.

Further, in this experiment, the lifetime of a DP is not limited. Instead, the size of the transmission buffer in the remote station is limited. In the RANDOM system, data collected by a data logger are first stored in memory in a host PC (Personal Computer) connected to IT-5000. Then, the host PC sends the data set to a buffer in DSP if there is room. The buffer can accommodate 4 data sets. The memory size in the host PC is set to 100 data sets. Another difference from the MCC protocol is dummy packet transmission, *i.e.*, in this experiment, the remote station is set to send a dummy packet with the same length as a DP when it has no data to transmit in spite of PP reception.

Again, as in the previous experiments, the master station sends PPs 5 min in each 10 min interval and the remote station acquires 20 byte data with the interval of 5 min.

4.2. Results and discussion

We show here only one figure as the first report of the experiment. Figure16 shows hourly data throughput averaged over the period from April 1st, 2004 to August 31st, 2004. Here, the hourly data throughput is calculated as follows: 1) count the number of DPs including duplicated ones and dummy packets received at the master station during an hour, 2) multiply by 160, the number of information bits in a packet, and 3) divide by 1800, the length of the period in operation.

In the figure, we also show the hourly data throughput for the MCC system obtained from the experiment during the period of JARE-43, from April 1st, 2002 to

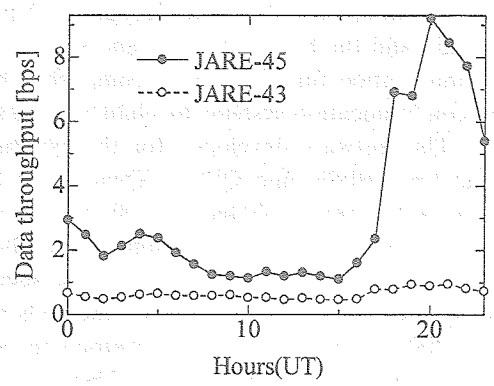


Fig. 16. Hourly data throughputs (April 1st–August 31st, 2004 for the experiment in JARE-45, April 1st–December 31st, 2002 for the experiment in JARE-43).

This document is provided by JAXA.

December 31st, 2002, for the purpose of comparison. This data throughput is calculated from the data reception ratio shown in Fig. 4, so that duplicated data is not included in this case.

Overall data throughput for the RANDOM system obtained by averaging over the whole hours is 3.2 bps while that for the MCC system is 0.63 bps. However, it should be noted that the result for the RANDOM system is somewhat overestimated since it includes duplicated receptions. By examining the received data, we find that duplicated DPs are about 10 percent of the received DPs. Thus, the data throughput without duplicated receptions is estimated to 2.9 bps.

In order to estimate data throughput precisely, we need information of AP receptions at Zhongshan Station that is to be brought from Antarctica after the experiment is completed. More precise performance evaluations using such information and other interesting results will be presented in the near future.

5. Conclusions

This paper showed the results of data experiments conducted during the period from JARE-43 to JARE-45. In JARE-43, we performed the data transmission experiment between Syowa and Zhongshan Stations using a commercial MBC system manufactured by MCC. Comparing with 10 dB duty cycle obtained by the tone experiment, hourly and daily averaged data and PP reception ratios were examined. We found that NMB propagation phenomena frequently observed at local nighttime work effectively for packet transmissions and greatly increase the data throughput. Overall data throughput obtained by this experiment was 0.63 bps. During the experiment, we did not observe serious blackout events that retarded MBC data transmission for a long time. In JARE-44, we added another MCC remote station at Dome Fuji Station. Since the power from the master unit was split into two antennas each directed to the remote stations, data throughput from Zhongshan Station was reduced to 0.36 bps and that from Dome Fuji Station was only 0.13 bps. There were some days without data receptions from the Dome Fuji remote station. For the experiment conducted during the period of JARE-45, we replaced the MCC system with a RANDOM system developed by the authors. The experiment is being conducted between Syowa and Zhongshan Stations. It is expected that the software modem and newly developed techniques greatly improve the performance. In fact, the estimated data throughput during the period from April 1st, 2004 to August 31st, 2004 was 2.9 bps, corresponding to 31.32 kbyte per day. This is enough ability for some kinds of scientific data transmission such as meteorological monitoring, telemetering magnetic activity data and so on.

Acknowledgments

This research is supported by the Grant-in-Aid for Scientific Research (C2 14550353) from Japan Society for the Promotion of Science. The installation and operation of the meteor burst communication system at Zhongshan and Syowa Stations were supported by the 18th, 19th, and 20th Chinese Antarctic Research Expeditions and

This document is provided by JAXA.

the 43rd, 44th, and 45th Japanese Antarctic Research Expeditions, respectively.

The editor thanks Drs. T. Ogawa and P.S. Cannon for their help in evaluating this paper.

References

Cannon, P.S., Weitzen, J.A., Ostergaard J. and Rasmussen, J.E. (1994): Meteor burst and other long distance high latitude propagation modes in the low VHF band. Proc. IEE HF Radio Systems and Techniques, 353–357.

Cannon, P.S., Weitzen, J.A., Ostergaard, J. and Rasmussen, J.E. (1996): Relative impact of meteor scatter and other long-distance high-latitude propagation modes on VHF communication systems. Radio Sci., **31**, 1129–1140.

Fukuda, A. (1997): Meteor Burst Communications. Tokyo, Corona Publ. (in Japanese).

Fukuda, A., Mukumoto, K., Yoshihiro, Y., Nagasawa, M., Yamagishi, H., Sato, N., Yang, H., Yao, M. and Jin, L. (2003): Experiments on Meteor Burst Communications in the Antarctic. Adv. Polar Upper Atmos. Res., **17**, 120–136.

Fukuda, A., Mukumoto, K., Yoshihiro, Y., Nakano, K., Ohichi, S., Nagasawa, M., Yamagishi, H., Sato, N., Kadokura, A., Yang, H., Yao, M., Zhang, S., He, G. and Jin, L. (2004): Meteor burst communications in the Antarctica: Description of experiments and first results. IEICE Trans. Commun., **E87-B**, 2767–2776.

Fukunishi, H., Kokubun, S. and Matuura, N. (1983): Nankyoku no Kagaku, 2. Ôrora to Chôkôsô Taiki (Science in Antarctica 2). Tokyo, Kokon Shoin, 255–256 (in Japanese).

Koustov, A.V., Igarashi, K., Andre, D., Ohta, K., Sato, N., Yamagishi, H. and Yukimatu, A. (2001): Observations of 50- and 12-MHz auroral coherent echoes at the Antarctic Syowa Station. J. Geophys. Res., **106** (A7), 12875–12887.

Mahmud, K., Mukumoto, K. and Fukuda, A. (2001): A bandwidth efficient variable rate transmission scheme for meteor burst communications. IEICE Trans. Commun., **E84-B**, 2956–2966.

Makarevitch, R.A., Koustov, A.V., Igarashi, K., Ohtaka, K., Ogawa, T., Nishitani, N., Sato, N., Yamagishi, H. and Yukimatu, A.S. (2002): Comparison of flow angle variations of E-region echo characteristics at VHF and HF. Adv. Polar Upper Atmos. Res., **16**, 59–83.

Maynard, L.A. (1968): Meteor burst communication in the Arctic. Ionospheric Radio Communications: Proc. NATO Institute on Ionospheric Radio Communications in the Arctic, Finse, Apr. 13–19, 1967. New York, Plenum, 165–173.

McDonough, A.K., Desourdis, R.I., Jr. and Katan, J.R. (1993): "Blackout" of simultaneous HF skywave and VHF meteor burst communication links. Proc. IEEE MILCOM'93, Boston, U.S., 402–406.

Mukumoto K., Ohichi S. and Fukuda, A. (2002): A new packet detection and CPSK demodulation method for the MBC software modem. IEICE National Convention Record B-2-20 (in Japanese).

Mukumoto, K., Fukuda, A., Yoshihiro, Y., Nakano, K., Ohichi, S., Nagasawa, M., Yamagishi, H., Sato, N., Kadokura, A., Yang, H., Yao, M., Zhang, S., He, G. and Jin, L. (2004): On the MBC data transmission experiment in Antarctica. Technical Report in IEICE **SANE2003-95**, 13–17 (in Japanese).

Nagasawa, M., Mukumoto, K., Fukuda, A., Yoshihiro, Y., Nakano, K., Ohichi, S., Yamagishi, H., Sato, N., Kadokura, A., Yang, H., Yao, M., Zhang, S., He, G. and Jin, L. (2004): Observation of Antarctic meteor burst communication channel using tone signal. Technical Report in IEICE **SANE2003-96**, 19–24 (in Japanese).

Ogawa, T., Igarashi, K., Kuratani, Y., Fujii, R. and Hirasawa, T. (1985): Some initial results of 50 MHz meteor radar observation at Syowa Station. Mem. Natl Ins. Polar Res., Spec. Issue, **36**, 254–263.

Ose, M. (1962): Auroral E_s and blackout under the ionospheric observation. Nankyoku Shiryô (Antarct. Rec.), **15**, 25–31.

Ostergaard, J.C., Rasmussen, J.E., Sowa, M.J., Quinn, J.M. and Kossey, P.A. (1985): Characteristics of high latitude meteor scatter propagation parameters over the 45–104 MHz band. Paper presented at AGARD Conf. Publ., CP-382.

This document is provided by JAXA.

Schanker J.Z. (1990): Meteor Burst Communications. Boston, Artech House Inc.

Tsutsumi, M., Aso, T. and Ejiri, M. (2001): Initial results of Syowa MF radar observations in Antarctica Adv. Polar Upper Atmos. Res., **15**, 103–116.

Weitzen, J.A. and Ralston, W.T. (1988): Meteor Scatter: An Overview. IEEE Trans. Antennas Propag., **36** (12), 1813–1819.

Weitzen, J.A., Sowa, M.J., Scofidio, R.A. and Quinn, J. (1987): Characterizing the multipath and Doppler spreads of the high-latitude meteor burst communication channel. IEEE Trans. Commun., **35**, 1050–1057.

Weitzen, J.A., Cannon, P.S., Ostergaard , J.C. and Rasmussen, J.E. (1993): High-latitude seasonal variation of meteoric and nonmeteoric oblique propagation at a frequency of 45 MHz. Radio Sci., **28**, 213–222.

Yoshihiro, Y., Nagasawa, M., Mukumoto, K. and Fukuda, A. (2001): Measurements of the Antarctic meteor burst communication channel. IEICE National Convention Record B-2-24 (in Japanese).

This document is provided by JAXA.

Adv. Polar Upper Atmos. Res., 19, 106–134, 2005
© 2005 National Institute of Polar Research

Review

Inner magnetospheric plasma interactions and coupling with the ionosphere

Mei-Ching Fok[1]*, Yusuke Ebihara[2] and Thomas E. Moore[1]

[1]*NASA Goddard Space Flight Center, Greenbelt, Maryland 20771, U.S.A.*
[2]*National Institute of Polar Research, Kaga 1-chome, Itabashi-ku, Tokyo 173-8515*
**Corresponding author. E-mail: mei-ching.h.fok@nasa.gov*

(Received March 18, 2005; Accepted June 13, 2005)

Abstract: The inner magnetosphere occupies a vast volume in space containing a relatively low-density mixture of hot and cold plasmas: the ring current, plasmasphere and radiation belt. Energy is transferred from the ring current to the cold plasmas through Coulomb collisions and wave-particle interactions, producing temperature enhancements in the plasmasphere. The plasma waves generated in the plasmasphere cause pitch-angle and energy diffusion of the energetic particles. The magnetic disturbances generated from the ring current alter the drift paths of radiation belt particles, causing radiation belt flux dropout during magnetic storm main phases. The ionosphere is filled with dense and cold plasmas in a 1000-km-thick shell above the Earth's surface at ~100 km altitude. Despite the distinct differences in size, location and physical properties, the ionosphere and the inner magnetosphere are tightly connected to each other. The ionosphere is an important source of magnetospheric ions. Energy transported down from the inner magnetosphere to the ionosphere produces observable temperature enhancements and optical emissions in the ionosphere. The electric coupling between the ionosphere and magnetosphere explains features such as shielding field, non-linear response of the ring current to the plasma-sheet source, and the post-midnight enhancement of the storm-time ring current flux. Even though many signatures are well described from the perspective of magnetosphere-ionosphere coupling, there are still unanswered questions, for example, the precise roles of wave-particle interactions in ring current loss and plasmaspheric heating, the cause of rapid storm initial recovery, the source of O^+ enhancement at substorm expansion, and the causes of outer radiation belt enhancement during storm recovery. The unresolved questions can be answered through careful cross analysis of the observational data from the ongoing and future imaging and multi-point missions with simulation results of large-scale modeling.

key words: inner magnetosphere, hot-cold interactions, magnetosphere-ionosphere coupling

1. Introduction

The ionosphere is a region in the upper atmosphere (~100–1000 km altitude) that consists of significant amount of cold (< 1 eV) ions and electrons (Comfort *et al.*,

This document is provided by JAXA.

1985), which are produced through ionizations of the neutral atmosphere by solar radiations and collisions with energetic particles (Schunk and Nagy, 2000). Plasma drifts in the ionosphere are determined by the electric field impressed by magnetospheric plasma motions and local collision frequencies. In the topside ionosphere where collisions are negligible, electrons and ions basically execute E×B drift. At lower altitudes where collisions are significant, plasma drift velocity is inclined at an angle of $\tan^{-1}(\nu/\omega)$, where ν and ω are collision and cyclotron frequencies, respectively. In the ionosphere, currents flow according to the Ohm's law with conductivity tensor consisting Hall, Pedersen and Cowling conductivities. Electric field can be expressed as negative gradient of a potential since magnetic field is basically constant with time in the ionosphere.

The inner magnetosphere consists of plasma populations that vary widely in characteristics, *i.e.*, the plasmasphere, ring current and the radiation belt (Wolf, 1995). The plasmasphere is basically the outward extension of the ionosphere. It is often outlined by a sharp boundary called the plasmapause, which separates the corotating dense region from the low-density exterior. The size and shape of the plasmasphere is largely controlled by the convection electric field reflecting global magnetospheric plasma circulation. During quiet periods, the plasmasphere has a tear-drop shape with the tip located around dusk local time. During active times, strong convection sweeps the plasmas toward dayside and forms an elongated extension of the plasmasphere known as plasma plume (or less precisely, tail) (Grebowsky, 1970; Grebowsky and Chen, 1976). Almost forty years since the discovery of the plasmapause (Carpenter, 1963), all our knowledge about the plasmasphere dynamics and configuration came from theoretical studies, ground-based or *in-situ* measurements. With the launch of the Imager for Magnetopause-to-Aurora Global Exploration (IMAGE) mission in 2000 (Burch, 2000), the global structures of the plasmasphere were finally revealed through the EUV images of the region (Sandel *et al.*, 2001). The predicted development of plasma plumes was confirmed and new features such as plasmasphere 'shoulders' and 'voids' were discovered (Burch *et al.*, 2001).

The ring current is a population of energetic (~1−300 keV) ions and electrons flowing in the inner magnetosphere in the range of L shells from ~2 to 8. Major ion species in the ring current are H^+, O^+, He^+, N^+ and He^{++} (Gloeckler and Hamilton, 1987; Daglis *et al.*, 1993). During active periods, enhanced ring current fluxes produce worldwide perturbations to the surface magnetic field, which are used to identify magnetic storms (Daglis, 2003). The ring current contains plasmas from the solar wind and ionosphere. Ring current H^+ is supplied from the solar wind and ionosphere, while O^+, He^+ and N^+ are mainly from the ionosphere, and He^{++} is from the solar wind. Solar wind plasmas enter the ring current region primarily *via* the flanks, and to a less extend through the cusp and plasma sheet. Ionospheric particles enter the inner magnetosphere predominantly through the plasma sheet and then convect earthward to the ring current region (Moore *et al.*, 2005a). During storm main phase of strong convection, the ring current is highly asymmetric and peaks on the nightside (Stüdemann *et al.*, 1987; Ebihara *et al.*, 2002). When the convection strength subsides, the ring current becomes more symmetric in local time as more particles are drifting in closed paths (Liemohn *et al.*, 1999; Pollock *et al.*, 2001; Ebihara *et al.*, 2002). An

This document is provided by JAXA.

in-depth and comprehensive discussion on the ring current sources, buildup and decay can be found in the excellent review by Daglis *et al.* (1999).

Explorer I and III in 1958 revealed the existence of energetic electrons and protons (up to MeV's for electrons and tens of MeV for protons) trapped in the magnetosphere, later named as the Van Allen radiation belt (Van Allen, 1959). Since its discovery, the radiation belt has been a subject of active research owning to its scientific significance and its impacts to space borne electronic systems and humans in space. The radiation belt populates about the same region as the ring current. Particles in the radiation belt are believed to originate from the solar wind, ionosphere and cosmic ray albedo (Walt, 1996; Baker *et al.*, 1996). During geomagnetic active periods, the intensities of radiation belt particles vary significantly. A flux decrease is often seen during the main phase of a magnetic storm, the signature that is known as the "Dst effect". When a storm intensifies, the magnetic field produced by the ring current inflates the main field. The drift shells of energetic particle in the radiation belt expand outward correspondingly (conversation of the third adiabatic invariant) and particles decelerate (Dessler and Karplus, 1961; Kim and Chen, 1997). This de-energization causes a decrease in particle fluxes since the energy spectrum slope is usually negative in the radiation belt energy range. During the storm recovery, the radiation belt fluxes recover as well, to a level higher than, equal to, or lower than the pre-storm intensity, seeming to depend on the solar wind velocity (Reeves *et al.*, 2003). The radiation belt is also be greatly enhanced when the magnetosphere is compressed by interplanetary shocks (Blake *et al.*, 1992; Hudson *et al.*, 1996).

The hot and cold plasma populations in the inner magnetosphere interact with each other. Energy transfer between the ring current and the plasmasphere causes decay of the hot population and heating in the cold plasmasphere (Kozyra *et al.*, 1987; Fok *et al.*, 1993). Anisotropies in ring current and radiation belt particles excite plasma wave growth in the plasmasphere. These waves, in turn, give rise to pitch-angle and energy diffusion of the energetic plasmas (Jordanova *et al.*, 2001; Khazanov *et al.*, 2003b; Tsurutani and Smith, 1977; Summer *et al.*, 1998). Wave-particle interactions are thus important mechanisms in ring current and radiation belt decay and buildup. The magnetic field produced by the ring current alters the drift paths of radiation belt particles causing reversible (adiabatic) changes or irreversible losses of the radiation belt (Kim and Chan, 1997).

Despite distinct differences in size, location and physical properties, the ionosphere and the magnetosphere are tightly connected to each other through magnetic field lines (Wolf, 1975; Khazanov *et al.*, 2003a). Variations and disturbances that occur on one side will induce corresponding changes on the other side (Schulz, 1997). Certain features observed in the magnetosphere cannot be understood without examining the contribution from the ionosphere, and vice versa. Likewise, some interactions between magnetospheric plasma populations have to be linked through the ionosphere. For instance, asymmetries in the ring current particle pressure tensor produce field aligned currents flowing into and out from the ionosphere. These currents control the ionospheric electric potential distributions and couple plasma convection in both the ionosphere and magnetospheric plasmas (Harel *et al.*, 1981; Wolf, 1983). Another crucial element in determining the convection pattern is the ionosphere conductivity

This document is provided by JAXA.

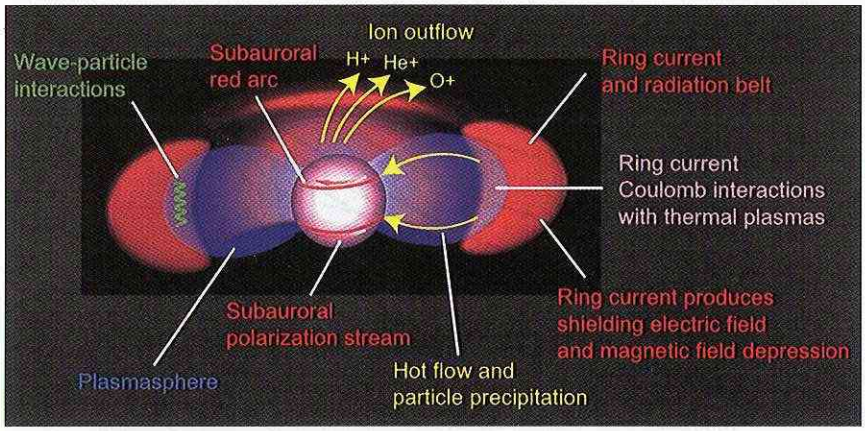


Fig. 1. Cartoon sketch shows major interactions between plasmas in the inner magnetosphere and coupling with the ionosphere.

(Wolf, 1970; Ebihara *et al.*, 2004), which is strongly moderated by precipitation of magnetospheric electrons and ions. In addition to electric coupling, the ionosphere also serves as a source (Daglis and Axford, 1996) and a sink to the magnetospheric plasmas. Figure 1 summarizes the major processes coupling plasmas in the inner magnetosphere and ionosphere. In this paper, we review the progress in understanding the interactions between magnetospheric plasmas and coupling with the ionosphere. We then conclude with questions that need further investigation.

2. Magnetospheric plasma interactions

2.1. hot-cold interactions through Coulomb collisions

In this paper, hot-cold interactions refer to coupling between the ring current (hot) and the plasmasphere (cold) particles. In the region of overlap between the ring current and the plasmasphere, the two plasma populations interact with each other *via* Coulomb collisions. Strong interactions especially occur between cold plasmasphere electrons and hot ring current ions due to their comparable velocities (Fok *et al.*, 1991a). Energy is transferred from the hot ions to the plasmaspheric particles. The hot ions thus lose energy and when their energies are reduced to below the ring current energy range (< 1 keV), these ions are treated as lost from the ring current. The hot ions also suffer angular deflection but the effect is minimal (Wentworth *et al.*, 1959). Coulomb interaction with the plasmasphere is one of the major loss mechanisms for ring current ions other than charge exchange loss. In fact, at low energies, Coulomb loss are often dominant over charge exchange loss. Figure 2 (taken from Fok *et al.*, 1991a) shows a comparison of Coulomb decay lifetimes with charge exchange lifetimes for ring current H^+, He^+ and O^+. As shown in the figure, Coulomb lifetimes are often shorter than charge exchange lifetimes for ring current H^+ below a few keV, for He^+ and O^+ below tens of keV. Jordanova *et al.* (1998) simulated the ring current development during the storm on October 18–26, 1995. They found Coulomb collisions to be the second

This document is provided by JAXA.

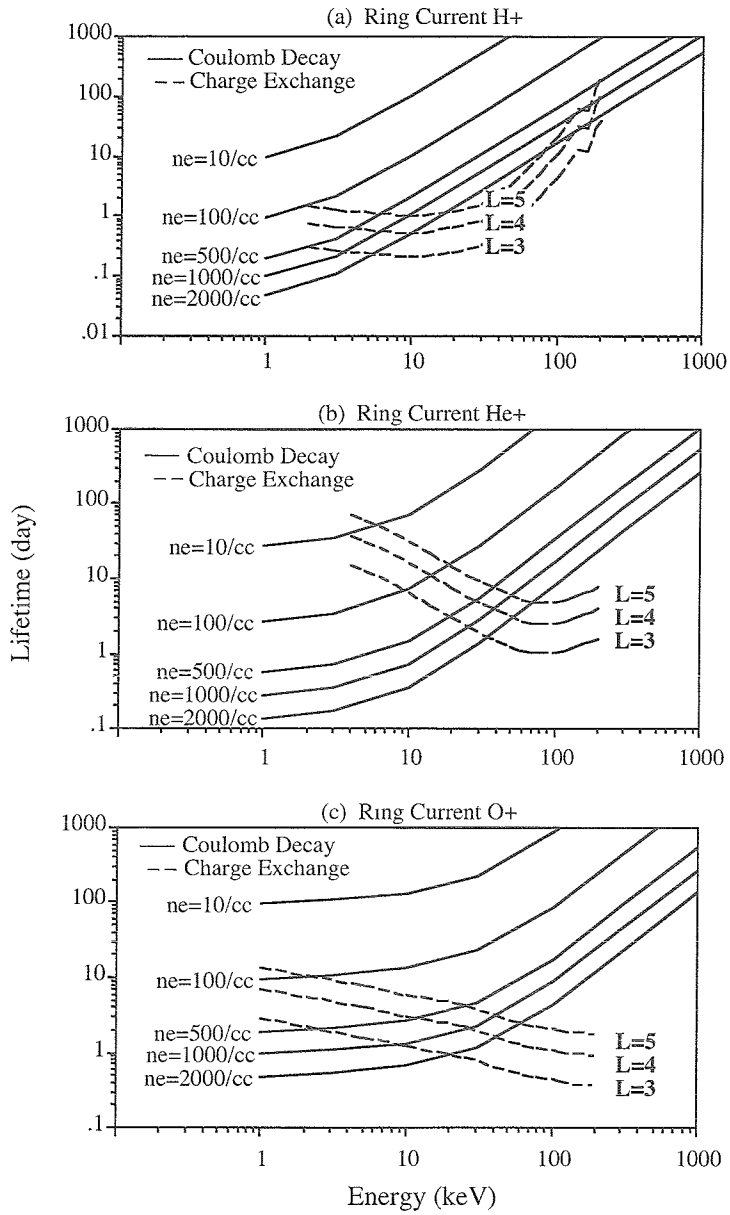


Fig. 2. Comparison of Coulomb decay lifetimes (solid lines) with charge exchange lifetimes (dashed lines) for ring current H^+ (top panel), He^+ (middle panel), and O (bottom panel). Coulomb decay lifetimes are calculated using plasmasphere density (ne) = 2000, 1000, 500, 100, and 10 cm^{-3} (taken from Fok et al., 1991a).

important loss process, followed the charge exchange loss.

As mentioned above, Coulomb drag from cold plasmas causes energy degradation in the ring current. In a simulation study, Fok *et al.* (1993) found a population of

This document is provided by JAXA.

low-energy (10–500 eV) ions is intensified during the storm recovery at $L=2$–4. Enhanced 10–500 eV fluxes of H^+, He^+ and O^+ were developed a few hours into the recovery phase. After 2 days of recovery, the low-energy H^+ flux decreases in an order of magnitude. In contrast, there is an order of magnitude increase in the low-energy O^+ flux with the peak flux located at $L=2$–3. Fok *et al.* (1993) confirmed that these low-energy ions are not injected from the nightside but generated locally from energy degradation of ring current ions. The different times of appearance for H^+ and O^+ low-energy fluxes can be accounted for by their different Coulomb decay lifetimes. Ring current H^+ of energies of 1–10 keV lose their energies to the plasmasphere faster than ring current O^+ of the same energy range. After the low-energy (10–500 eV) H^+ is built up, they lose energy to below 10 eV in a few more hours due to continued Coulomb drag from the plasmasphere. The Coulomb lifetime for ring current O^+ is longer, so it takes ~1 day for low-energy O^+ to develop and the high flux lasts for a few days. Kistler *et al.* (1989) calculated the ring current ion fluxes during the storm on 19 September 1984, considering ion drifts and charge exchange loss. The simulated H^+ flux at $L=3$–4 at storm early recovery was compared with the CCE/CHEM measurement. They found very good agreements except below 5 keV. Their model underestimated the H^+ flux at low energies. We suspect this discrepancy came from the exclusion of low-energy ion buildup due to Coulomb collisions between ring current ions and the plasmasphere. A buildup of suprathermal ions was also observed by Shelley *et al.* (1985) during the storm main phase and recovery on 4 September 1984. The temporal and spatial distributions of this observed suprathermal ions are consistent with the theoretical calculation by Fok *et al.* (1993) as presented above.

While the hot ring current ions are degraded in energy when they have Coulomb collisions with the plasmasphere, the energy transfer from the hot ions to the cold plasmas will cause high electron and ion temperatures in the plasmasphere if no compensating loses occur. No electron temperature measurement in the plasmasphere has been made because of technical difficulties. However, enhanced plasmaspheric ion temperatures were observed during magnetic active times by the Retarding Ion Mass Spectrometer (RIMS) on Dynamics Explorer 1 (DE 1) (Comfort *et al.*, 1988). Fok *et al.* (1995) calculated the plasmaspheric ion temperature during the recovery phase of the magnetic storm on 6–11 February 1986 using the Field Line Interhemispheric Plasma (FLIP) model, taking into account the additional heat source from the ring current. Figure 3 shows the calculated altitude profiles of ion temperature at different times in storm recovery at $L=4$, 0900 LT (left panel) and 2200 LT (right panel). The figure shows that the ion temperature does not change with time if there is no heating from the ring current. However, with the additional magnetospheric heat source, ion temperatures above 500 km increase rapidly in the early recovery phase and then gradually return toward the quiet-time level. For comparison, the mean DE-1/RIMS H^+ temperatures during October and November of 1981 (Comfort *et al.*, 1988) are also shown. Both high and low altitude data on the morning side are shown and only the high altitude measurement is plotted on the evening side. It is clearly seen in the figure that the observed high ion temperature cannot be explained without additional heat input from the magnetosphere.

This document is provided by JAXA.

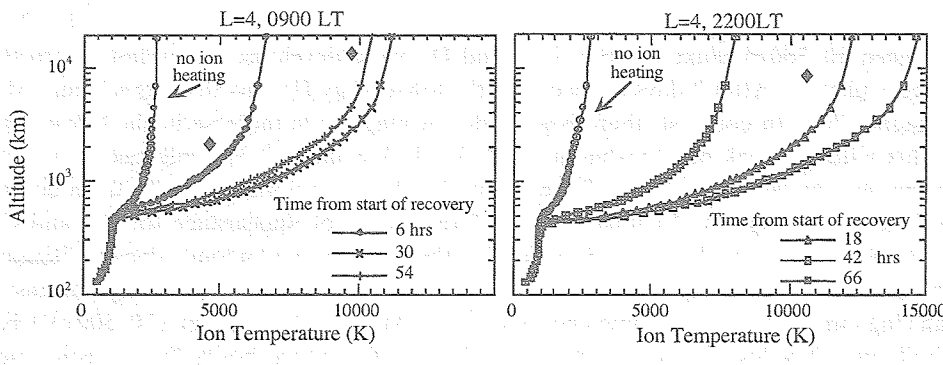


Fig. 3. Calculated altitude profiles of ion temperature at L=4 on the morning side (left) and evening (right). Average DE-1/RIMS data in October to November 1981 are shown with the ◆ (taken from Fok et al., 1995).

2.2. *Magnetospheric plasma interactions through waves*

Three kinds of plasma wave will be discussed: electromagnetic ion cyclotron (EMIC) waves, whistler mode chorus, and plasmaspheric hiss. These waves are generated in the inner magnetosphere and serve as channels for transferring energy from one plasma population to the others. They are important in plasmasphere heating, ring current-radiation belt loss and buildup.

2.2.1. EMIC Waves

EMIC waves are left-hand polarized with frequencies near ion cyclotron frequencies. EMIC waves propagate along magnetic field lines, reflecting at the ionosphere and bouncing between conjugate ionospheric points. Ion cyclotron modes grow when the ring current ion pitch-angle distribution is sufficiently anisotropic, with more energy perpendicular than parallel to the magnetic field (Kennel and Petschek, 1966). Magnetospheric processes such as convection, Coulomb and charge exchange interactions tend to reduce the field-parallel flux of ring current ions, providing the free energy for EMIC wave excitations. The amplification of EMIC waves also depends on the cold plasma density. Near the plasmapause where the density gradient is steep, EMIC waves bounce several times across the equator and thus experience multiple wave gains (Thorne and Horne, 1992). EMIC waves have been observed in the inner magnetosphere, especially in the vicinity of the plasmapause (Anderson *et al.*, 1992; Fraser *et al.*, 1992, 1996). The occurrence and intensity of EMIC waves are much higher during storms than quiet times (Fraser *et al.*, 1992; Erlandson and Ukhorskiy, 2001). The active wave regions move to lower latitudes as storm develops (Braysy *et al.*, 1998), along with the storm time plasmas.

EMIC waves cause pitch-angle diffusions and eventually precipitation losses of ring current ions. Jordanova *et al.* (2001) simulated the ring current ion fluxes during the 14–16 May 1997 storm, including losses due to wave-particle interactions. They found the global patterns of proton precipitation moved to lower L shells during storm main phase and receded back toward larger L shells in storm recovery, consistent with the EMIC wave observations mentioned above (Braysy *et al.*, 1998). Kozyra *et al.* (1997a) studied the contribution of EMIC wave-induced precipitation to ring current decay

This document is provided by JAXA.

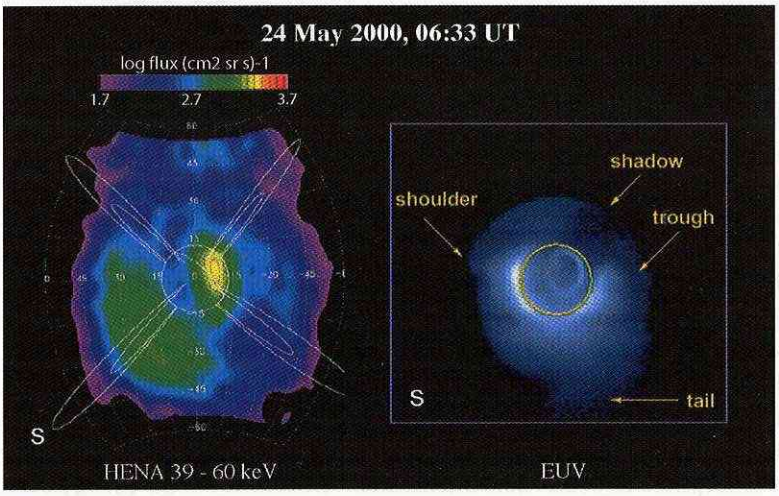


Fig. 4. IMAGE HENA (left) and EUV (right) images at 0633 UT on 24 May 2000. "S" represents the sun direction in both panels.

during the storm on 2–6 November 1993. They found an additional ~8 nT recovery in the Dst index. Since the launch of the IMAGE spacecraft in 2000, simultaneous images of the ring current and the plasmasphere have been obtained. To illustrate the advantage of multiple imaging, the left panel of Fig. 4 shows the ring current ion image from the High Energy Neutral Atom (HENA) imager (Mitchell *et al.*, 2000) on IMAGE taken at 0633 UT on 24 May 2000. Dipole field lines of $L=4$ and 8 at 4 local times are overlaid. The Sun direction is indicated by an "S". As shown in the figure, ENA flux peaks around noon at high altitude. At low altitude another peak is found in the dusk-midnight sector as a result of ring current precipitation. The right panel is the image of the plasmasphere taken at the same time from the Extreme Ultraviolet (EUV) imager (Sandel *et al.*, 2000). The EUV image is orientated the same as the ENA image. The dark area in the anti-sunward direction is the shadow of the Earth. Features such as plasmaspheric tail, shoulder and trough are clearly seen in the EUV image. As shown in Fig. 4, the plasmasphere bulge-tail collocates with the high altitude trough in ENA flux at dusk. It is possible that strong EMIC waves in the bulge region deplete ring current ions by scattering them into the loss cone and causing strong precipitation at low altitude (Burch *et al.*, 2001).

Radiation belt electrons also interact with EMIC waves through cyclotron resonance. Using balloon-borne X-ray detectors, Lorentzen *et al.* (2000) found intense X-ray event associated with atmospheric bremsstrahlung from 1.7 MeV precipitation electrons during a substorm. They interpreted the event as electron pitch-angle scattering and precipitation caused by resonance with EMIC waves. Based on quasi-linear theory, Summers and Thorne (2003) calculated the electron pitch-angle diffusion coefficients for cyclotron resonance with EMIC waves. They found, under typical storm condition in the duskside plasmasphere, only electrons with energy above 1 MeV to be resonant with EMIC waves. The time scale for removing these energetic

This document is provided by JAXA.

electrons by EMIC wave scattering during magnetic storms is as short as several hours to one day. The location of the calculated precipitation is consistent with the observation by Lorentzen *et al.* (2000).

EMIC waves resonant with ring current ions and radiation belt electrons cause precipitation losses of energetic particles. On the other hand, these waves are sources of heating to thermal electrons as they go through Landau damping. The ion cyclotron phase velocity, essentially the Alfvén speed, is comparable to the thermal velocity of plasmaspheric electrons. This suggests that Landau resonance with the thermal electrons is important. Since more electrons are moving slower than the wave phase velocity than those are moving faster, EMIC waves are damped and thermal electrons are heated by the waves. Cornwall *et al.* (1971) estimated the energy absorbed by plasmasphere electrons through Landau damping of EMIC waves. Together with energy deposition from Coulomb interactions with ring current ions, they found the combined heat flux to the ionosphere is sufficient to drive the stable aurora red (SAR) arcs in the ionosphere to observable intensities. Gorbachev *et al.* (1992) calculated the wave energy transfer to the thermal plasmas by means of Landau damping. The heat flux to electrons was found to be $\sim 3 \times 10^{10}$ eV cm^{-2}s^{-1} and 4×10^{8} eV cm^{-2}s^{-1} for ions. The predicted plasmaspheric temperatures with this additional heat source agreed well with observations for various satellites. This is an excellent example demonstrating that EMIC waves serve as media for energy transfer from hot plasmas to the cold plasmasphere. The hot plasmas provide the free energy for wave generation and the subsequent damping of these waves heats up the cold plasmas.

2.2.2. Whistler mode chorus

Whistler mode waves are right-hand polarized with frequencies less than the electron gyro-frequency. They travel along magnetic field lines or are refracted across field lines. Whistler mode chorus is identified as quasi-periodic, series of overlapping rising and falling tones (Shawhan, 1979). Two separated chorus emissions were observed in two distinct regions: high-latitude and low-latitude magnetosphere (Tsurutani and Smith, 1977; Meredith *et al.*, 2001). Both studies found the high-latitude chorus is principally on the dayside. The low-latitude chorus was observed mostly outside the plasmasphere at all local times but predominantly in the post-midnight to dayside magnetosphere. A close relationship between substorm activities and the low-latitude chorus is found and it is suggested that these chorus emissions are generated by injection of 10–100 keV electrons (Tsurutani and Smith, 1977; Isenberg *et al.*, 1982; Meredith *et al.*, 2001). As substorm ring current electrons are injected on the nightside, they gradient-curvature drift to the dayside through dawn. During their earthward transport, the electrons are energized preferentially in the perpendicular direction. The resulting anisotropy in perpendicular and parallel electron temperatures generates instability or excitation of whistler mode chorus.

Whistler mode chorus cause energy and pitch-angle diffusion of radiation belt electrons. During the recovery phases of magnetic storms, the fluxes of outer belt electrons are often seen to increase, exceeding the pre-storm level (Reeves *et al.*, 2003). Two types of mechanism are suggested to be responsible for this storm-time enhancement: earthward diffusion of injected particles from the plasma sheet and internal energization processes. Green and Kivelson (2004) examined the radial profiles of

This document is provided by JAXA.

electron phase space density using data from the Polar High Sensitivity Telescope energetic detector. They concluded that their results are best explained by an internal acceleration process at $L \sim 5$. Energy diffusion due to interaction with the whistler mode chorus is the most accepted candidate for this energization process. Summers and Ma (2000) developed a kinetic (Fokker-Planck) model of relativistic electrons, considering energy diffusion based on gyroresonance electron-whistler mode waves and precipitation due to pitch-angle scattering by EMIC and whistler mode waves. They assumed a constant background plasma density and whistler amplitudes on the order of 100 pT. Their model is able to generate the observable increases in relativistic electrons during storm recovery phases. On the other hand, MeV electrons experience pitch-angle scattering when interact with the whistler mode chorus and precipitate into the atmosphere. This diffusion loss is evident in the collocation of observed chorus emissions and MeV electron microburst precipitation (O'brien *et al.*, 2003).

2.2.3. Plasmaspheric hiss

Another type of whistler mode turbulence propagates in the magnetosphere is the plasmaspheric hiss. These waves have the same frequency range (100 Hz–5 kHz) as the chorus. However, plasmasphere hiss emissions are mostly seen inside the plasmapause and for this reason they are named. Plasmaspheric hiss is relatively steady, persistently seen throughout the plasmasphere. It is proposed that plasmaspheric hiss is generated through cyclotron resonant instability with 10–100 keV electrons that diffuse inward to the plasmasphere from the outer belt (Thorne *et al.*, 1973; Shawhan, 1979). The generation region is presumed to lie in the outer plasmasphere. From the source, waves propagate to fill the plasmasphere (Lyons *et al.*, 1972). However, ray-tracing and growth rate calculation carried out by Huang *et al.* (1983) produced significantly lower wave intensity than observed hiss emissions, suggesting that wave sources other than anisotropic electron cyclotron resonance are needed to inject sufficient wave energy in the outer plasmasphere (Church and Thorne, 1983). Lightning is another possible source of plasmaspheric hiss. Lightning generates a broad electromagnetic wave spectrum in the lower ionosphere. These wave transmit through the ionosphere into the plasmasphere and experience dispersion as they propagate. Using data from DE 1 satellite, Sonwalkar and Inan (1989) observed close relation between lightning and hiss emission. They suggested that lightning-generated whistler is an important embryonic source for VLF hiss. Recent work by Green *et al.* (2005) also supports that lightning is the dominant source for plasmaspheric hiss.

Whistler mode plasmaspheric hiss is believed to be the source of the slot region that separates the inner and outer radiation belts during quiet periods. Plasmaspheric hiss interacts with radiation belt electrons through gyroresonance, causing pitch-angle diffusion and subsequent precipitation loss of these energetic electrons. The slot region is located at L shells ~2–3.5, where precipitation decay rates are comparatively high and radial diffusion is weak to balance the loss. Lyons *et al.* (1972) computed the pitch-angle diffusion coefficients of energetic electrons due to interaction with plasmaspheric hiss and solve the diffusion equation of electron distribution function. In their calculation, they considered cyclotron-harmonic and Landau resonances, as well as oblique propagation of waves. Their calculated pitch-angle distribution and precipitation lifetimes are in good agreement with satellite observations. Albert (1994) extended the

This document is provided by JAXA.

calculation of Lyon *et al.* (1972) by considering more harmonics, but in an efficient way such that the computation is still manageable. They found the improved precipitation lifetimes for electron energies above 500 keV and L shells greater than 3 are shorter than those previously reported by Lyon *et al.* (1972).

As mentioned above, plasmaspheric hiss emissions are generated in the lower ionosphere by lightning and probably further excited by the ring current electrons. On the other hand, part of the hiss wave energy is damped by the ring current and radiation belt ions. Kozyra *et al.* (1994, 1995) calculated the energy, pitch-angle and cross diffusion coefficients of energetic ($\geq$80 keV) ions when they undergo resonant interactions with the ducted plasmaspheric hiss. Their model produced high-energy proton enhancement as a result of energy diffusion. The diffusion timescale is on the order of tens of days, which seems to be long but it is comparable to charge exchange and Coulomb loss lifetimes of H^+ at these energies. Once again, we have demonstrated the roles of whistler mode waves in ionosphere-plasmasphere-ring-current-radiation-belt coupling: the ionosphere and plasmasphere provide the environment for whistler mode wave generation and excitation; in turn, these waves cause precipitation of the radiation belt electrons and energization of the ring current ions.

2.3. *Magnetic depression produced by the ring current*

The magnetic field disturbances generated by the ring current produce noticeable signatures on both ground-based and satellite magnetometers. In fact, the magnetic disturbances measured on ground are used to define a magnetic storm as indicated by the Dst (disturbance, storm-time) index (Daglis, 2003). During extreme active periods, the magnetic depression produced by the ring current on the surface of the Earth reaches a maximum of 300–600 nT, which is about 1–2% of the main field. In the magnetosphere, the relative importance of the ring current field is much higher. Using magnetometer data from several satellites during storm-times ($Dst \leq -65$ nT), Tsyganenko *et al.* (2003) found strong distortion of the magnetic field in the inner magnetosphere. The disturbed field reaches 30–50% of the main field at 3 earth radii (R_E) at the equator during major storms.

The drift paths of charged particles in the magnetosphere are altered by the distorted magnetic field, especially for radiation belt particles, for which magnetic drifts are dominant over electric drifts. To demonstrate this effect, Fig. 5 plots the drift paths of energetic electrons with magnetic moment 1.2×10^{10} keV/T and pitch angle 90°, which have been significantly distorted by the ring current field perturbations. The magnetic field is modeled by the Tsyganenko 1996 (T96) model (Tsyganenko, 1995). Input parameters for T96: solar wind dynamic pressure, interplanetary magnetic field (IMF) By and Bz are set to be 3 nPa, 0 nT and -5 nT, respectively. The Dst index, which is also an input parameter of the T96 model, is set to be 0 nT (left panel) and -80 nT (right panel) to represent weak and strong disturbances from the ring current. In Fig. 5, drift paths (solid lines) are calculated including corotation and convection, which is assumed to be Volland-Stern type (Volland, 1973; Stern, 1975) with cross polar cap potential drop of 60 kV. Dashed lines indicate the energy of the electrons. As shown in the left panel, electrons with this particular magnetic moment, at 5.5 R_E, 00 MLT, have energy of 1.5 MeV and travel in closed drift paths. However, in the

This document is provided by JAXA.

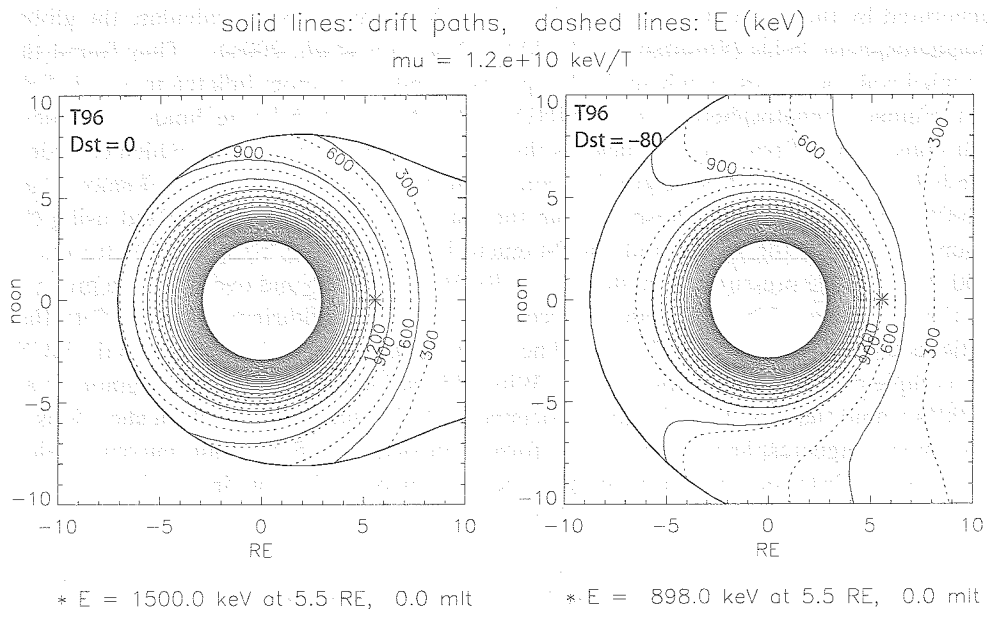


Fig. 5. Drift paths of equatorially mirroring electrons with magnetic moment equal 1.2×10^{10} keV/T. Left panel shows the drift paths (solid lines) and energy contours (dashed lines) in T96 model with input parameters: solar wind dynamic pressure=3 nPa, Dst=0, IMF By=0, and Bz=−5 nT. The right panel is the same as the left one except Dst in T96 model is equal to −80 nT.

magnetosphere that is inflated by the ring current (right panel), the same particles (same all three adiabatic invariants) cross midnight at a distance greater than $5.5R_E$ in open drift path, with a much lower energy (<900 keV). This calculation illustrates the effect of the ring current on radiation belt dynamics through the magnetic field produced by the ring current.

It is well-observed that radiation belt electron fluxes decrease during storm main phases and then gradually increase toward pre-storm level during recovery. As discussed in the Introduction, the flux dropout during storm intensification is an adiabatic effect as radiation belt particles are drifting in a field strongly distorted by the ring current. However, both studies from Kim and Chan (1997) and Reeves *et al.* (2003) indicated that the fully adiabatic effect accounts for a significant fraction not all of observed flux variations. Other loss and source mechanisms have to be involved. In order to separate influences from adiabatic and non-adiabatic processes, ring current-generated field has to be considered in analytical or simulation studies of the radiation belt. Zheng *et al.* (2003) included the Dst effect in their radiation belt environment model by simply employing the T96 model with Dst as one of the parameters. They were able to reproduce the flux dropout observed during the main phase of the storm on 12 August 2000. On the other hand, a number of models and studies take into account the ring current effects in a self-consistent manner. Modelers at the University of Michigan have coupled the Block-Adaptive-Tree-Solarwind-Roe-Upwind-Scheme (BATSRUS) MHD with the Rice Convection Model (RCM) such that particle pressure

This document is provided by JAXA.

generated by the ring current is included in the MHD equation to calculate the global magnetospheric fields (Gombosi *et al.*, 2003; De Zeeuw *et al.*, 2004). They found the coupled code produces significant higher pressure and much more inflated magnetic field in the inner magnetosphere than the MHD model alone. Another technique to achieve self-consistency of particles and fields is the force equilibrium approach, which considers the balance between pressure gradient and magnetic stress ($J \times B = \nabla p$). Lemon *et al.* (2004) simulated plasma transport from the plasma sheet to the ring current using the coupled code of the RCM and the Magneto-Friction (MF) code (Toffoletto *et al.*, 2001). Particle pressure calculated by the RCM is passed to and overrides the pressure in the MF code. The MF code then computes a new equilibrium magnetic field that satisfies the force balance condition. The new magnetic field is passed back to the RCM to complete the computation cycle. With this self-consistent model, Lemon *et al.* (2004) found that the perturbation associated with the injection of plasma sheet ions in the inner magnetosphere prevents the formation of a significant ring current, unless there is a substantial reduction of the specific entropy $PV^{5/3}$ in inner plasma sheet. Here, P is particle pressure and V is flux volume per unit magnetic flux.

3. Magnetosphere-ionosphere coupling

3.1. *Magnetospheric sources of ionosphere heating*

As discussed in detail in the last section, the plasmasphere is heated by the ring current plasmas through Coulomb and wave-particle interactions. The interesting remaining question is whether the ring current energy deposited in the plasmasphere is transported down to the ionosphere and produce observable signatures there. One possible transport mechanism is heat conduction along magnetic field lines. In a fully ionized gas, the plasma is considered as collisional and conduction is effective when the mean free path of self-collision (Coulomb) is less than the particle scale height. Cole (1965) estimated the electron mean free path and scale height along a flux tube of $L = 2.5$, assuming an equatorial plasmaspheric density n_e of $10^3\,cm^{-3}$ and $n_e \propto B$. He found heat conduction at the equator is poorly justified but is acceptable at higher latitudes ($\lambda > 25^\circ$) where thermal density is higher. It thus requires a flux of electrons to carry the heat energy out of the equator. Bounce motion is the ideal process to bring the heated electrons from the equator to the collisional region of higher latitudes. As a result, the criterion for heat conduction is instead determined by the relative collision time to the bounce period. If the collision time t_c is shorter than the bounce period t_b, the plasma is considered to be collisional. The Coulomb electron-electron collision time is $t_c \sim 1.6 \times 10^4 n_e^{-1} T_e^{3/2}$ (Spitzer, 1962) where t_c is in seconds, n_e is density in cm^{-3} and T_e is electron temperature in eV. At $L = 3$, $t_b \sim 1.2 \times 10^2 T_e^{-1/2}$. For a typical plasmasphere of $T_e = 1$ eV and $n_e = 1000\,cm^{-3}$, t_c is less than t_b and the plasmaspheric electrons are collisional.

Cornwall *et al.* (1971) proposed that the ring current energy dissipation to the plasmasphere electrons via Coulomb and wave-particle interactions, conducts along the flux tube as a heat flux to the ionosphere. This magnetospheric influx heats the ionospheric electrons and produces the subauroral T_e peak and the associated optical signature named by stable auroral red (SAR) arc which is often observed during the recovery of magnetic storm (Fig. 1). The subauroral T_e peak is an enhancement in the

This document is provided by JAXA.

latitudinal profile of electron temperature in the subauroral F region (Brace *et al.*, 1967, 1974; Kozyra *et al.*, 1986; Fok *et al.*, 1991b). The peak values are typically in excess of ~3000 K and the latitudinal extent is ~2–3°. SAR arc is formed at the location of electron temperature enhancements. It is narrow in latitude but extends in longitude around the nightside and even possibly to the dayside. When the electron temperature is high and above 3000 K, significant amount of electrons with energies in excess of 1.96 eV exist in the high-energy tail of the Maxwellian distribution. These electrons collisionally excite O atoms to the ^1D state. The excited O atoms radiatively relax with the emission of photons at 6300 or 6364 Å. SAR arc emission rate ranges from barely above the airglow level to several kilorayleighs (Rees and Roble, 1975). Simulation studies performed by Kozyra *et al.* (1987) and Fok *et al.* (1993) suggested that Coulomb collisions alone are sufficient to extract energy from the storm-time ring current, mainly from ring current O^+, to the cold plasmasphere to generate the SAR arc emissions to the observable levels. The role of wave-particle interactions is still unclear.

The Coulomb proton-proton collision time is 43 times of that of the electrons because the collision time is proportional to the square root of the atomic mass. Ions trapped in the plasmasphere could be considered as collisionless. Comfort *et al.* (1995) calculated the ion conductivity in the plasmasphere considering contribution only from ions that lie inside the loss cone. Using this reduced ion conductivity in their hydrodynamic model, they were able to reproduce the high ion temperatures (1–2 eV) observed in the outer plasmasphere and obtained substantially lower ion temperatures in the topside ionosphere. Since the ion conductivity is low, thermal energy from the heated plasmaspheric ions may hardly conduct to the ionosphere to cause enhanced ion temperature there. Ion temperature within the SAR arc has been measured but in one case enhancement was found but in another case no enhancement at all (Rees and Roble, 1975). Therefore it is still not clear how much of the ring current energy deposited in plasmaspheric ions is transported down to the ionosphere and lost there.

3.2. *Ionosphere as a source of magnetospheric ions*

The ionospheric source consists of a highly variable flow of heavy ions superposed upon a relatively steady flow of hydrogen (and to a lesser extent, helium) ions. The local H^+ flux may exceed $1\times10^{12}\,m^{-2}s^{-1}$ (Moore *et al.*, 1999) when "normalized" to 1000 km altitude using a dipolar magnetic flux tube area profile. The H^+ source is weakly dependent on solar EUV radiation and therefore on solar cycle phase, with lower fluxes at solar maximum. This results from reductions in H density in the altitude range where free H^+ is produced by charge exchange of O^+ produced by solar photoionization. The outer flux tubes of the magnetosphere circulate on paths linking the boundary layers, and exhaust plasma to the solar wind faster than it is refilled from the ionosphere. These polar flux tubes are perpetually in a state of disequilibrium with a steadily flowing light ion polar wind (Moore *et al.*, 1999).

Somewhat deeper in the magnetosphere, where flux tube circulation occasionally links to the boundary layers (Goldstein *et al.*, 2002), a slower form of the polar wind is known as "refilling flows". In the innermost magnetosphere, the plasmasphere, closed circulation traps outflowing plasma and accumulates it to pressure equilibrium, effectively shutting down the outflow. The plasmasphere is severely depleted in O^+ and other

This document is provided by JAXA.

heavy ions, relative to the ionosphere. Varying solar illumination modulates electron densities and temperatures, producing a diurnal "breathing" of the plasmasphere. But heavy ion scale heights remain much smaller than the height of the closed region, so these ions remain confined by gravity to relatively low altitudes.

The variable component of plasma outflow consists principally of escaping oxygen ions (O^+), typically with ~10% N^+, which we term the auroral wind. Highly variable amounts of the molecular species N_2^+, NO^+, and O_2^+ escape with the O^+, but these fluxes are important mainly for the largest solar wind disturbances. The total heavy ion flux varies in space and time from essentially zero to greater than $1\times10^9\,cm^{-2}s^{-1}$ (at the standard altitude of 1000 km). Appreciable heavy ion outflow fluxes are found only in the auroral zones or within polar cap auroral features where electrons or ions are heated and heavy ion scale heights increase substantially. Such flows respond directly to the deposition of solar wind energy in the topside ionosphere (Strangeway *et al.*, 2000). The dayside auroral zone, or cusp "footprint" is the most productive region of auroral wind, and the most directly responsive to solar wind conditions (Moore *et al.*, 1999). Figure 6 illustrates the gross dependence of auroral wind outflows on solar wind dynamic pressure fluctuations, which appear to play a significant role in delivering energy to the ionosphere.

The sources of heavy ion plasma outflows are localized and depend strongly on solar wind conditions, but the resulting outflows circulate throughout the magnetosphere on high latitude flux tubes that participate in all aspects of magnetospheric dynamics. The large outflows from the dayside auroral zone are circulated antisunward across the polar cap, forming a fountain of plasma that is strongly influenced by both gravity and solar wind electromagnetism. In particular, the cooler component

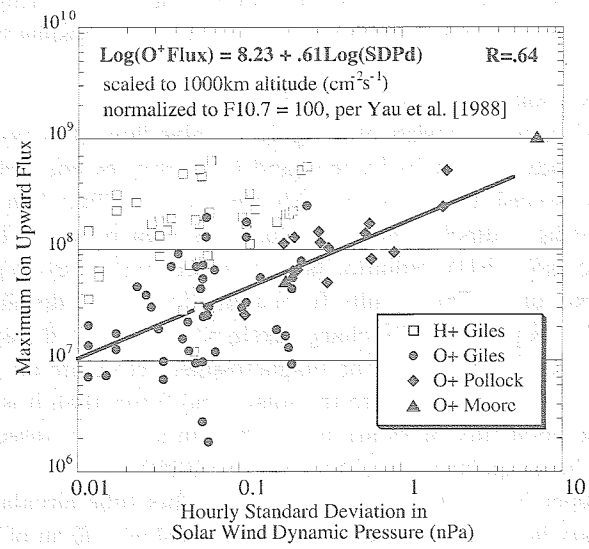


Fig. 6. The observed relationship between ionospheric auroral wind fluxes and the hourly average standard deviation of the solar wind dynamic pressure. Here the long term solar cycle of F10.7 has been removed according to the scaling of Yau and Lockwood (1988).

This document is provided by JAXA.

of the plasma launched upward in the dayside cusp region falls back into the polar ionosphere, while the hotter, faster component continues along lobe field lines to the magnetotail. Thus we typically have simultaneous outflow at high altitude and downflow at lower altitudes on polar cap/lobe field lines (Chandler, 1995). As the fountain of heavy-ion plasma expands along each flux tube, both inward and outward, the high altitude O^+ density drops.

Polar ionospheric outflows are channeled directly into the night side plasma sheet. The strong dynamics of this region are known to contribute to the formation of storm time plasmas in the inner magnetosphere. However, both simple calculations (Hill, 1974) and elaborate simulations (Moore *et al.*, 2005a) agree on the conclusion that the polar wind H^+ pressure in the inner magnetosphere is for typical conditions overwhelmed by the pressure of solar wind protons entering into the magnetosphere, mostly through the flank magnetopause. However, polar wind protons are sufficiently plentiful to produce densities comparable with the density of solar wind ions finding their way into the inner magnetosphere. However, they are not typically heated or energized sufficiently to become a competitive pressure contribution. Observations (Hamilton *et al.*, 1988) and recent simulations (Moore *et al.*, 2005b) agree on the conclusion that the auroral wind produces substantial pressure in the inner magnetosphere and competes with the solar wind proton pressure contribution. This requires both strong energy dissipation in the auroral zone ionosphere and strong circulation flows in the magnetosphere as a whole.

3.3. Electric coupling between magnetosphere and ionosphere

3.3.1. Field aligned currents

The magnetosphere and ionosphere are tightly connected through magnetic field lines and the current flow along them. The divergence of gradient-curvature drift currents generated by plasmas in the magnetosphere, mainly from ring current ions, produces field-aligned currents that flow into or out from the ionosphere. These currents must close through the ionosphere. The thickness of the ionospheric current layer is relatively small in comparison with that in the magnetosphere. In the thin-layer assumption, the continuity of current satisfies the equation:

$$\nabla \cdot (-\Sigma \cdot \nabla \Phi_i) = J_{\parallel} \sin I, \tag{1}$$

where Σ is the height-integrated conductivity tensor, Φ_i is the electric potential and I is the inclination of the geomagnetic field. The ring current acts as a current generator. For given Σ and $J_{\parallel}$, the electric potential distribution in the ionosphere is obtained by solving (1). The above formulation is valid if temporal changes in the driver (perpendicular current in the magnetosphere for this particular case) are much longer than the Alfvén wave propagation time between the magnetosphere and the ionosphere. Information in the magnetospheric usually takes a few minutes to propagate in the form of Alfvén wave from the equatorial plane to the ionosphere (Baumjohann and Glaßmeier, 1984).

The field-aligned currents generated by the ring current modulate the ionospheric electric potential and plasma flow distribution. The newly restructured electric potential is mapped to the magnetosphere along field lines, placing a load on the magneto-

This document is provided by JAXA.

spheric electric generator, which is powered by plasma convection. The motion of magnetospheric particles is thus significantly influenced by this self-consistently coupled system (Vasyliunas, 1970; Wolf, 1970).

3.3.2. Shielding electric field

Non-uniformity in the plasma pressure in the inner magnetosphere produces the Region 2 field-aligned current generally flowing into the ionosphere on the duskside and away from the ionosphere on the dawnside. The Region 2 field-aligned current thus produces an ionospheric electric field that is opposite to the dawn-to-dusk convection electric field. This additional electric field shields or partially shields the inner region of the magnetosphere from the convection electric field. For this reason, the additional electric field is called the shielding electric field. When the dawn-to-dusk convection field is suddenly weakened while the Region 2 field-aligned current remains fairly constant, the shielding electric field may dominate over the convection field and overshield the region earthward of the Region 2 field-aligned current (Spiro *et al.*, 1988; Peymirat *et al.*, 2000). Simulation results from the RCM have shown that overshielding takes place when the IMF turns northward after a prolonged southward IMF condition, and the lifetime of the overshielding condition lasts for about 10–20 min (Spiro *et al.*, 1988). This prediction is consistent with observations of the ionospheric electric field at the MillStone Hill, Chatanika, and Jicamarca radars reported by Kelley *et al.* (1979) and Fejer *et al.* (1990).

Ebihara *et al.* (2004) calculated the ionospheric potential pattern using the Comprehensive Ring Current Model (CRCM) (Fok *et al.*, 2001), with the aurora-associated conductivity based on the IMAGE/FUV observation. They found that the overshielding condition is established when the auroral conductivity rapidly decreases after a prolonged southward IMF condition. When the conductivity reduces abruptly, the shielding electric field becomes strong. A dusk-to-dawn electric field (or the antisunward plasma flow) is expected to exist in the region where the aurora-associated conductivity is lower than ambient. Overshielding also happens during northward turning of the IMF. Goldstein *et al.* (2002) performed simulations by the Magnetospheric Specification Model (Freeman *et al.*, 1993) and produced dusk-to-dawn overshielding electric field triggered by sudden, strong northward turning of the IMF. They found the antisunward flow caused by overshielding creates a shoulder-shaped bulge in the morning sector plasmapause, named as the plasmaspheric shoulder (Burch *et al.*, 2001).

The shielding effect tends to impede the plasma injection from the plasma sheet. When the magnetosphere is not coupled with the ionosphere, doubling the plasma sheet density simply doubles the ring current strength (*e.g.*, Chen *et al.*, 1994; Kozyra *et al.*, 1998; Jordanova *et al.*, 1998). However, the degree of the shielding increases with increasing the plasma sheet density (Garner, 2003). When the magnetosphere is electrically coupled with the ionosphere, doubling the plasma sheet density does not double the ring current strength because of the increasing shielding field. The CRCM simulation showed that the ring current total energy is roughly proportional to $N_{ps}^{1/2}$, where N_{ps} is the plasma sheet density (Ebihara *et al.*, 2005). This non-linear response comes from the intense shielding electric field for dense plasma sheet.

The drift trajectories of magnetospheric ions are drastically skewed by the shielding

This document is provided by JAXA.

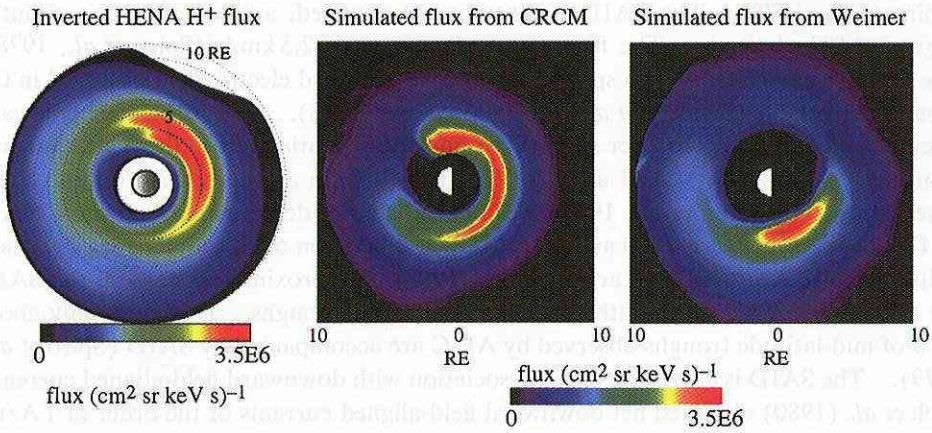


Fig. 7. Left panel: equatorial flux of 27–39 keV H^+ inverted from the HENA image at 0900 UT on 12 August 2000. Middle panel: simulated flux at the same energy range and time calculated by the CRCM. Right panel: simulated flux using the Weimer electric field model. Sun is to the left in all panels. Note that the colors of the HENA flux and that of the simulated fluxes are slightly different.

electric field. Conventionally, the tens-of-keV ions originating from the nightside plasma sheet are thought to reach a minimum L-value in the pre-midnight region as predicted by drift calculation using statistical electric field models (*e.g.*, Stern, 1973; Volland, 975; Weimer, 2001). However, during major storms when shielding electric field is strong, the CRCM predicted that the tens-of-keV ions originating from the nightside plasmas sheet reaches a minimum L-value in the post-midnight region instead (Fok *et al.*, 2003; Ebihara and Fok, 2004). Fok *et al.* (2003) have shown that, for the same storm condition, calculations with Weimer type convection electric field produced peak ion flux in the pre-midnight sector, while the self-consistent model of the CRCM predicted the peak in the post-midnight sector. Figure 7 shows the equatorial flux of 27–39 keV H^+ inverted from the HENA image (Perez *et al.*, 2001) at 0900 UT on 12 August 2000 (left panel), showing a flux maximum near dawn. The middle panel plots the simulated flux at the same energy range and time calculated by the CRCM. As shown in the figure, the CRCM produces a comparable flux level and a similar local-time distribution as the HENA invert ion flux. In contrast, the simulation using the empirical electric field model of Weimer (1995) gives the peak flux at the dusk-midnight sector (right panel). The post-midnight enhancements of ring current ion fluxes with energy of tens of keV are consistent with ENA observations by the IMAGE/HENA during over 10 storms in 2000–2002 (Brandt *et al.*, 2002). The strong shielding electric field established in the inner magnetosphere is believed to be the main contributor of this newly found feature (Ebihara and Fok, 2004).

3.3.3. Subauroral polarization stream

In the dusk-to-midnight region during geomagnetic active times, very often there is a rapid westward flow in the ionosphere just equatorward of the auroral oval, called the Polarization Jet (PJ) (Galperin *et al.*, 1974) or the SubAuroral Ion Drift (SAID)

This document is provided by JAXA.

(Spiro *et al.*, 1978). The SAID is latitudinally confined, and usually, it is about 1 degree wide in latitude. The flow speed often exceeds 2.5 km/s (Spiro *et al.*, 1978). The SAID is associated with a spike of an intense poleward electric field observed in the subauroral region (Smiddy *et al.*, 1977; Maynard; 1978). The associated poleward electric field ranges up to over 400 mV/m and the potential across these structures is approximated to lie between 1 and 10 kV at 600–1750 km altitudes, according to Freja observations (Karlsson *et al.*, 1998). Statistical studies demonstrate that most of the SAID occurs in between 1800 and 0200 MLT and between 55 deg and 70 deg invariant latitude (Spiro *et al.*, 1979; Karlsson *et al.*, 1998). Approximately 85% of the SAID are observed in association with well-defined *F*-region troughs. However, only about 20% of mid-latitude troughs observed by AE-C are accompanied by SAID (Spiro *et al.*, 1979). The SAID is also observed in association with downward field-aligned currents. Rich *et al.* (1980) observed net downward field-aligned currents of the order of 1 A/m^2 in the region of strong subauroral electric fields ranging up to 350 mV/m. The close connection with the net downward field-aligned current supports the following scenario for the formation of SAID: the field-aligned currents flow into the subauroral ionosphere and close through the low-conductivity region equatorward of the auroral oval, producing a strong poleward directed electric field (Southwood and Wolf, 1978; Banks and Yasuhara, 1978; Anderson *et al.*, 1993).

Recently, based on observations of the MillStone Hill radar, Foster and Burke (2002) introduced the name SubAuroral Polarization Stream (SAPS) to encompass both types of observed subauroral electric fields, the SAID/PJ signatures and the similar feature in broader regions described by Yeh *et al.* (1991). The SAPS structure has an average peak amplitude of 900 m/s or higher and spans 3–5 degrees in latitude (Foster and Vo, 2002). Foster and Vo (2002) suggested that SAPS is associated with magnetosphere-ionosphere (M-I) coupling and is caused by field-aligned current trying to close across the subauroral ionosphere, as same as the proposed formation mechanism for the SAID.

It has been observed that rapid westward flow also exists in the magnetosphere (Maynard *et al.*, 1980; Rowland and Wygant, 1998), appeared to be associated with the SAPS. Rowland and Wygant (1998) carried out a statistical study of the dawn-to-dusk electric field observed by the Combined Radiation and Release Satellite (CRRES) near the equatorial plane. The averaged dawn-to-dusk electric field shows that for low *Kp* values (between 0 and 3), the magnitude of the electric field increases with L. This is consistent with a simple convection electric field model with a shielding effect (Stern, 1975; Volland, 1978). However, for moderate *Kp* values (between 4 and 7^-), the magnitude of the dawn-to-dusk electric field has a local peak near $L=3$–4. Then when *Kp* ranges between 7 and 9, the magnitude decreases with L. These *in-situ* measurements in the magnetosphere illustrate that simple Volland-Stern type model cannot represent disturbed conditions. The actual convection electric field is far more complicated by processes coupling the magnetosphere and ionosphere, such as the shielding field and the SAPS.

3.4. *Roles of ionospheric conductivities in M-I coupling*

The ionospheric conductivity plays an active role in the M-I coupling. Equation

This document is provided by JAXA.

(1) illustrates that for a given field-aligned current, the magnitude of the electric field (potential gradient) decreases with increasing the conductivity. This implies that the magnitude of the shielding electric field and the SAPS electric field will be weakened when conductivity is high. Spiro and Wolf (1984) found that the total energy of the ring current increases by a factor of 1.4 when the ionospheric conductivity is doubled. Using the CRCM, Ebihara *et al.* (2004) investigated how the ionospheric conductivity influences the ring current development. They found the conductivity for F10.7=250 $\times 10^4$ Jy (solar maximum condition) results in the ring current that is about 29% stronger than for that for F10.7=70$\times 10^4$ Jy (solar minimum condition). The conductivity at equinox results in the ring current that is about 5% stronger than at solstice. The ionospheric conductivity in the subauroral region is the higher at the solar maximum and equinox, therefore the magnitude of the shielding electric field is weaker. During these time periods, the plasma originating from the plasma sheet drifts further earthward by the convection electric field because the inner magnetosphere is less shielded. As a consequence, a more robust ring current is developed.

The relative latitude of the auroral oval also influences the ring current formation. Both expansion and contraction of the auroral oval from an optimal latitude is found through simulation to weaken the ring current strength (Ebihara *et al.*, 2004). Mesoscale structures in the conductivity associated with auroral precipitation are shown to result in a significant modification of the electric field distribution and the plasma distribution as mentioned in the previous section. When the auroral conductivity decreases, the overshielding condition is produced, causing the anti-sunward plasma flow in the magnetosphere.

The already low conductivity in the SAPS region is further reduced by the increased frictional heating of the ionospheric ions. The frictional heating increases the rate of ion-atom interchange between O^+ and N_2. Subsequent fast recombination of NO^+ with electrons further reduces the subauroral *F* region conductivity. The heating also leads to a thermal expansion, substantial field-aligned plasma flow and large depression in the concentration in the *F* region, known as the mid-latitude trough. When the ionospheric concentration is reduced, the conductivity is decreased and then speed of the SAPS is increased. Fast SAPS increases the frictional heating, in turn resulting in the reduction of the conductivity. This self-enhanced mechanism has been proposed by Anderson *et al.* (1993). The ring current thus tightly links with not only the ionosphere but also the thermosphere.

4. Discussions and summary

We have illustrated the close connections between plasma populations in the inner magnetosphere and the ionosphere. Even though numerous observation and simulation studies have been carried out to tackle this subject, the linkage is so extensive and complex that there are still missing pieces in understanding the overall picture of these coupled systems. The impact of wave-particle interactions is one of the major unresolved questions. Ring current precipitation loss due to interactions with EMIC waves is often thought to be important and should not be ignored (Kozyra *et al.*, 1997a; Jordanova *et al.*, 2001). However, it is not clear how this process contributes to the

This document is provided by JAXA.

ring current loss and especially, the rapid decay of the ring current often seen during early recovery. Kozyra *et al.* (1997a) included EMIC wave scattering in their ring current simulation and found just an additional ~8 nT recovery of the Dst index at the early recovery phase of a storm with minimum Dst of −150 nT. Moreover, EMIC waves are rarely observed in the magnetosphere at $L < 5$ (Anderson *et al.*, 1992), where the peak of the ring current located during the main and early recovery phases. The relative roles of EMIC waves and Coulomb interaction in heating the plasmasphere are still controversial. Simulations including either one of the two mechanisms alone provide sufficient heating to the plasmasphere and produce observable high temperatures there (Gorbachev *et al.*, 1992; Fok *et al.*, 1993, 1995).

SAR arcs provide an excellent display of energy transport from the ring current to the magnetically connected underlying ionosphere. Observations reveal significant amounts of O^+ (major source of plasmaspheric electron Coulomb heating) in the storm time ring current (Hamilton *et al.*, 1988; Daglis *et al.*, 1993). The lack of EMIC waves in the SAR energy source region (Anderson *et al.*, 1992), implicates Coulomb collision as a favorable energy exchange process over wave-particle interaction. However, this deduction is not yet decisive (Kozyra *et al.*, 1997b). Another puzzle in SAR arc physics is the co-existence of a soft (~1 eV) electron precipitation over SAR arcs (Gurgiolo *et al.*, 1982; Slater *et al.*, 1987). Any SAR arc energy source theory should provide the explanation of this electron precipitation. Even though Coulomb collision mechanism is very convincing, it is not certain whether Coulomb collisions alone will produce such field-aligned soft electron distribution.

As we have discussed above, magnetospheric O^+ is a one of the key players in the coupling processes in the M-I system. Auroral O^+ outflow provides substantial pressure in the ring current comparable with the solar wind protons (Moore *et al.*, 2005b). O^+ is the dominant source of plasmaspheric electron heating (Kozyra *et al.*, 1987). In fact, O^+ in the ring current would suppress the growth of EMIC waves and lower the frequency of maximum wave growth (Kozyra *et al.*, 1984). Recent observations from IMAGE/HENA revealed important but relatively short-lived enhancements of 52–180 keV O^+ at substorm expansions (Mitchell *et al.*, 2003). It is not certain that how these heavy ions get energized and injected into the ring current region. It may be through direct injection from the ionosphere or energization of the pre-existing lower-energy ions. Further observational and simulation investigations are needed to understand the transport and energization of the O^+ ions and their influences in coupled M-I system.

We have demonstrated the effects of ring current-generated magnetic distortion on radiation belt development. Work has been done to include the ring current field in global modeling (De Zeeuw *et al.*, 2004; Lemon *et al.*, 2004). However, none of them has incorporated the self-consistent fields into radiation belt calculation.

In recent years, the space physics community has recognized the need for multi-point measurements and global imaging to monitor the coupling and simultaneous responses of various plasma populations in the magnetosphere and ionosphere to solar activity and to the resultant disturbances in the interplanetary medium. The IMAGE mission, launched on 25 March 2000, is the first mission dedicated to imaging the aurora, ring current, plasmasphere and ionosphere outflow (Burch, 2000). Later in the same year, the 4 satellites of the Cluster II missions were launched, carrying plasma

This document is provided by JAXA.

instruments to measure electric and magnetic fields, electron and ion distributions. This tetrahedral constellation was designed to study the small-scale plasma structures and macroscopic turbulence in three-dimensions in the regions of the solar wind, bow shock, magnetopause, cusps, auroral zone and the magnetotail (Escoubet *et al.*, 2001). The complementary capabilities of these two missions have enabled many unique observations and scientific discoveries (http://image.gsfc.nasa.gov/poetry/IMAGEdisc.html/, http://sci.esa.int/cluster/). At least three multi-point and global imaging missions are being implemented and scheduled to launch in the next 10 years: TWINS (Two Wide-angle Imaging Neutral-atom Spectrometers), THEMIS (Time History of Events and Macroscale Interactions during Substorms), and MMS (Magnetospheric MultiScale Mission).

In parallel on the theory-modeling side, end-to-end global models have been developed that transmit the disturbances on the surface of the Sun through the interplanetary space to the Earth's magnetosphere, ionosphere and lastly, the atmosphere. These modeling activities have been vigorously pursued in several modeling centers such as the Center for Space Environment Modeling at the University of Michigan, the Community Coordinated Modeling Center at the Goddard Space Flight Center, and the Center for Integrated Space Weather Modeling at NSF. Measurements from current and future imaging and multi-point missions are vital for testing the theories and refining the models. On the other hand, theories and models would be used to guide the interpretations of observational data and to provide assistance in future mission designs. Combining the efforts and strengths of global missions and large-scale modeling, we foresee major breakthroughs will be made in unveiling the physics that governs the interactions in the entire M-I system and their responses to the solar wind.

We have reported results from investigations on coupling between plasmas in the inner magnetosphere and their connection with the ionosphere:

(1) Significant energy is transferred from ring current ions to the plasmasphere through Coulomb collisions and produces observable plasmaspheric electron and ion temperature enhancements.

(2) Anisotropies in ring current particle distributions provide the free energy for plasma wave excitation. EMIC waves, whistler mode chorus and plasmaspheric hiss are commonly observed in the inner magnetosphere. These waves cause pitch-angle and energy diffusion of the ring current and radiation belt plasmas. The damping of these waves in the plasmasphere is a source of plasmaspheric heating.

(3) The magnetic field generated by the ring current during storm intensification modifies the main field in the inner magnetosphere and alters the drift paths of radiation belt particles, causing reversible adiabatic decrease and irreversible loss in radiation belt flux.

(4) Energy from the high-temperature plasmaspheric electrons is transported along field lines to the ionosphere and produces the observed electron temperature enhancements in the subauroral *F*-region during magnetic storms. These electron temperature enhancements are energy sources for the SAR arc emissions at mid-latitude ionosphere.

(5) The auroral zone is the vital source of the heavy ion pressure seen in the magnetosphere and this source is highly modulated by the fluctuations in the solar wind dynamic pressure as reflected in local auroral conditions. The ionosphere also provides proton

This document is provided by JAXA.

density in the magnetosphere comparable to the solar wind source.
(6) The magnetosphere and the ionosphere are tightly linked together through magnetic field lines and the field-aligned currents.
(7) The shielding electric field is a result of electric coupling between the magnetosphere and ionosphere. The non-linear response of the ring current to the plasma-sheet source and several newly observed features in the inner magnetosphere, such as plasmasphere shoulder, post-midnight enhancement in storm-time ring current flux, are effectively explained by the shielding effect.
(8) SAPS and SAID are typical signatures of M-I coupling, caused by field-aligned current trying to close across the low-conductivity region in the subauroral ionosphere.
(9) Ionospheric conductivities play a crucial role in determining the convection electric fields in the ionosphere and the inner magnetosphere, and thus the transport and development of the ring current.

We have identified the following unanswered issues in inner-magnetosphere-ionosphere interactions that need further investigation.
(1) The precise roles of EMIC waves in ring current decay.
(2) The relative importance of plasma waves and Coulomb collisions in plasmasphere heating.
(3) The exact cause of the ring current rapid decay at the early recovery phase.
(4) The source of the soft-electron precipitation associated with the SAR arcs.
(5) The sources of the instant O^+ enhancement in response to substorm expansion.
(6) The relative roles of wave induced energy-diffusion versus earthward radial diffusion in producing the radiation belt electron enhancements often seen in the recovery phases of magnetic storms.

The above unresolved questions can be addressed through the careful cross analysis of observations from the ongoing and future imaging and multi-point missions with simulation results of large-scale modeling.

Acknowledgments

We thank Drs. Janet Kozyra, Pontus Brandt, Adolfo Vinas, Robert Benson, George Khazanov, Dimitris Vassiliadis, Richard Wolf, and Vania Jordanova for useful discussions. The HENA inverted H^+ flux shown in Fig. 7 is provided by Dr. Joseph Perez. This work is supported by the NASA Office of Space Science Sun-Earth Connection Guest Investigator Program under RTOP Grant 370-16-00-11 and IMAGE mission under UPN 370-28-12.

The editor thanks Dr. J. Burch and another referee for their help in evaluating this paper.

References

Albert, J.M. (1994): Quasi-linear pitch angle diffusion coefficients: Retaining high harmonics. J. Geophys. Res., **99**, 23741–23745.

Anderson, P.C., Heelis, R.A. and Hanson, W.B. (1991): The ionospheric signatures of rapid subauroral ion drift. J. Geophys. Res., **96**, 5785–5792.

This document is provided by JAXA.

Anderson, B.J., Erlandson, R.E. and Zanetti, L.J. (1992): A statistical study of Pc 1-2 magnetic pulsations in the equatorial magnetosphere, 1. Equatorial occurrence distributions. J. Geophys. Res., **97**, 3075-3088.

Anderson, P.C., Hanson, W.B., Heelis, R.A., Craven, J.D., Baker, D.N. and Frank, L.A. (1993): A proposed production model of rapid subauroral ion drifts and their relationship to substorm evolution. J. Geophys. Res., **98**, 6069-6078.

Baker, D.N., Kanekal, S.G., Looper, M.D., Blake, J.B. and Mewaldt, R.A. (1996): Jovian, Solar, and other possible sources of radiation belt particles. Radiation Belts: Models and Standards, ed. by J.F. Lemaire *et al.* Washington, D.C., Am. Geophys. Union, 49-55 (Geophysical Monograph Vol. 97).

Banks, P.M. and Yasuhara, F. (1978): Electric fields and conductivity in the nighttime E region: A new magnetosphere-ionosphere-atmosphere coupling effect. Geophys. Res. Lett., **5**, 1047-1050.

Baumjohann, W. and Glaßmeier, K.H. (1984): The transient response mechanism and Pi 2 pulsations at substorm onset-review and outlook. Planet. Space Sci., **32**, 1361-1370.

Blake, J.B., Kolasinski, W.A., Fillius, R.W. and Mullen, E.G. (1992): Injection of electrons and protons with energies of tens of MeV into $L<3$ on 24 March 1991. Geophys. Res. Lett., **19**, 821-824.

Brace, L.H., Reddy, B.M. and Mayr, H.G. (1967): Global behavior of the ionosphere at 1000-kilometer altitude. J. Geophys. Res., **72**, 265-283.

Brace, L.H., Maier, E.J., Hoffman, J.H., Whitteker, J. and Shepherd, G.G. (1974): Deformation of the night side plasmasphere and ionosphere during the August 1972 geomagnetic storm. J. Geophys. Res., **79**, 5211-5218.

Brandt, P.C., Ohtani, S., Mitchell, D.G., Fok, M.-C., Roelof, E.C. and Demajistre, R. (2002): Global ENA observations of the storm mainphase ring current: Implications for skewed electric fields in the inner magnetosphere. Geophys. Res. Lett., **29** (20), 1954, doi: 10.1029/2002GL015160.

Braysy, T., Mursula, K. and Marklund, G. (1998): Ion cyclotron waves during a great magnetic storm observed by Freja double-probe electric field instrument. J. Geophys. Res., **103**, 4145-4155.

Burch, J.L. (2000): IMAGE mission overview. Space Sci. Rev., **91**, 1-14.

Burch, J.L., Mitchell, D.G., Sandel, B.R., Brandt, P.C. and Wuest, M. (2001): Global dynamics of the plasmasphere and ring current during magnetic storms. Geophys. Res. Lett., **28**, 1159-1162.

Carpenter, D.L. (1963): Whistler evidence of a 'knee' in the magnetospheric ionization density profile. J. Geophys. Res., **68**, 1675-1682.

Chandler, M.O. (1995): Observations of downward moving O^+ in the polar topside ionosphere. J. Geophys. Res., **100**, 5795-5800.

Chen, M.W., Lyons, L.R. and Schulz, M. (1994): Simulations of phase space distributions of storm time proton ring current. J. Geophys. Res., **99**, 5745-5760.

Chua, D., Brittnacher, M., Parks, G., Germany, G. and Spann, J. (1998): A new auroral feature: The nightside gap. Geophys. Res. Lett., **25**, 3747-3750.

Church, S.R. and Thorne, R.M. (1983): On the origin of plasmaspheric hiss: Ray path integrated amplification. J. Geophys. Res., **88**, 7941-7957.

Cole, K.D. (1965): Stable auroral red arc, sinks for energy of D_{st} main phase. J. Geophys. Res., **70**, 1689-1706.

Comfort, R.H., Waite, J.H., Jr. and Chappell, C.R. (1985): Thermal ion temperatures from the retarding ion mass spectrometer on DE 1. J. Geophys. Res., **90**, 3475-3486.

Comfort, R.H., Newberry, I.T. and Chappell, C.R. (1988): Preliminary statistical survey of plasmaspheric ion properties from observations by DE 1/RIMS. Modeling Magnetospheric Plasma, ed. by T.E. Moore and J.H. Waite, Jr. Washington, D.C., Am. Geophys. Union, 107-114 (Geophysical Monograph Vol. 44).

Comfort, R.H., Craven, P.D. and Richards, P.G. (1995): A modified thermal conductivity for low density plasma magnetic flux tubes. Geophys. Res. Lett., **22**, 2457-2460.

Cornwall, J.M., Coroniti, F.V. and Thorne, R.M. (1971): Unified theory of SAR arc formation at the plasmapause. J. Geophys. Res., **76**, 4428-4445.

Daglis, I. (2003): Magnetic storm-still an adequate name? Eos, **84** (22), 3 June.

Daglis, I.A. and Axford, W.I. (1996): Fast ionospheric response to enhanced activity in geospace: Ion feeding of the inner magnetotail. J. Geophys. Res., **101**, 5047-5065.

Daglis, I.A., Sarris, E.T. and Wilken, B. (1993): AMPTE/CCE CHEM observations of the energetic ion

This document is provided by JAXA.

population at geosynchronous altitudes. Ann. Geophys., **11**, 685–696.
Daglis, I.A., Thorne, R.M., Baumjohann, W. and Orsini, S. (1999): The terrestrial ring current: origin, formation, and decay. Rev. Geophys., **37**, 407–438.
Dessler, A.J. and Karplus, R. (1961): Some effects of diamagnetic ring currents on Van Allen radiation. J. Geophys. Res., **66**, 2289–2295.
De Zeeuw, D.L., Sazykin, S., Wolf, R.A., Gombosi, T.I., Ridley, A.J. and Tóth, G. (2004): Coupling of a global MHD code and an inner magnetospheric model: Initial results. J. Geophys. Res., **109**, A12219, doi: 10.1029/2003JA010366.
Ebihara, Y. and Fok, M.-C. (2004): Postmidnight storm-time enhancement of tens-of-keV proton flux. J. Geophys. Res., **109**, A12209, doi: 10.1029/2004JA010523.
Ebihara, Y., Ejiri, M., Nilsson, H., Sandahl, I., Milillo, A., Grande, M., Fennell, J.F. and Roeder, J.L. (2002): Statistical distribution of the storm-time proton ring current: POLAR measurements. Geophys. Res. Lett., **29** (20), 1969, doi: 10.1029/2002GL015420.
Ebihara, Y., Fok, M.-C., Wolf, R.A., Immel, T.J. and Moore, T.E. (2004): Influence of ionosphere conductivity on the ring current. J. Geophys. Res., **109**, A08205, doi: 10.1029/2003JA010351.
Ebihara Y., Fok, M.-C., Wolf, R.A., Thomsen, M.F. and Moore, T.E. (2005): Nonlinear impact of plasma sheet density on the ring current. J. Geophys. Res., **110**, A02208, doi: 10.1029/2004JA010435.
Erlandson, R.E. and Ukhorskiy, A.J. (2001): Observations of electromagnetic ion cyclotron waves during geomagnetic storms: Wave occurrence and pitch angle scattering. J. Geophys. Res., **106**, 3883–3895.
Escoubet, C.P., Fehringer, M. and Goldstein, M. (2001): The cluster mission. Ann. Geophys., **19**, 1197–1200.
Fejer, B.G., Spiro, R.W., Wolf, R.A. and Foster, J.C. (1990): Latitudinal variation of perturbation electric fields during magnetically disturbed periods: 1986 SUNDIAL observations and model results. Ann. Geophys., **8**, 441–454.
Fok, M.-C., Kozyra, J.U., Nagy, A.F. and Cravens, T.E. (1991a): Lifetime of ring current particles due to Coulomb collisions in the plasmasphere. J. Geophys. Res., **96**, 7861–7867.
Fok, M.-C., Kozyra, J.U., Warren, M.F. and Brace, L.H. (1991b): Seasonal variations in the subauroral electron temperature enhancement. J. Geophys. Res., **96**, 9773–9780.
Fok, M.-C., Kozyra, J.U., Nagy, A.F., Rasmussen, C.E. and Khazanov, G.V. (1993): Decay of equatorial ring current ions and associated aeronomical consequences. J. Geophys. Res., **98**, 19381–19393.
Fok, M.-C., Craven, P.D., Moore, T.E. and Richards, P.G. (1995): Ring current—plasmasphere coupling through Coulomb collisions. Cross-Scale Coupling in Space Plasmas, ed. by J.L. Horwitz *et al.* Washington, D.C., Am. Geophys. Union, 161–171 (Geophysical Monograph Vol. 93).
Fok, M.-C., Wolf, R.A., Spiro, R.W. and Moore, T.E. (2001): Comprehensive computational model of the Earth's ring current. J. Geophys. Res., **106**, 8417–8424.
Fok, M.-C., Moore, T.E., Wilson, G.R., Perez, J.D., Zhang, X.X., Brandt, P.C., Mitchell, D.G., Roelof, E. C., Jahn, J.-M., Pollock, C.J. and Wolf, R.A. (2003): Global ENA IMAGE simulations. Space Sci. Rev., **109**, 77–103.
Foster, J.C. and Burke, W.J. (2002): SAPS: A new characterization for subauroral electric fields. Eos AGU Trans., **83**, 393–394.
Foster, J.C. and Vo, H.B. (2002): Average characteristics and activity dependence of the subauroral polarization stream. J. Geophys. Res., **107**, 1475, doi: 10.1029/2002JA009409.
Fraser, B.J., Samson, J.C., Hu, Y.D., McPherron, R.L. and Russsell, C.T. (1992): Electromagnetic ion cyclotron waves observed near the oxygen cyclotron frequency by ISEE 1 and 2. J. Geophys. Res., **97**, 3063–3074.
Fraser, B.J., Singer, H.J., Hughes, W.J., Wygant, J.R., Anderson, R.R. and Hu, Y.D. (1996): CRRES Poynting vector observations of electromagnetic ion cyclotron waves near the plasmapause. J. Geophys. Res., **101**, 15331–15343.
Freeman, J.W. *et al.* (1993): Magnetospheric Specification Model Development code and Documentation. Report for USAF contract F19,628-90-K-0012, Rice University, Houston, TX.
Galperin, Y.I., Ponomarev, V.N. and Zosimova, A.G. (1974): Plasma convection in polar ionosphere. Ann. Geophys., **30**, 1–7.
Gloeckler, G. and Hamilton, D.C. (1987): AMPTE ion composition results. Physica Scripta, **T18**, 73–84.
Goldstein, J., Spiro, R.W., Reiff, P.H., Wolf, R.A., Sandel, B.R., Freeman, J.W. and Lambour, R.L. (2002):

This document is provided by JAXA.

IMF-driven overshielding electric field and the origin of the plasmaspheric shoulder of May 24, 2000. Geophys. Res. Lett., **29** (16), 1819, doi: 10.1029/2001GL014534.

Gombosi, T.I., DeZeeuw, D.L., Powell, K.G., Ridley, A.J., Sokolov, I.V., Stout, Q.F. and Toth, G. (2003): Adaptive mesh refinement for global magnetohydrodynamic simulation. Space Plasma Simulation, ed. by J. Buchner *et al.* Berlin, Springer, 247–274.

Gorbachev, O.A., Khazanov, G.V., Gamayunov, K.V. and Krivorutsky, E.N. (1992): A theoretical model for the ring current interaction with the earth's plasmasphere. Planet. Space Sci., **40**, 859–872.

Grebowsky, J.M. (1970): Model study of plasmapause motion. J. Geophys. Res., **75**, 4329–4333.

Grebowsky, J.M. and Chen, A.J. (1976): Effects on the plasmasphere of irregular electric fields. Planet. Space Sci., **24**, 689–696.

Green J.C. and Kivelson, M.G. (2004): Relativistic electrons in the outer radiation belt: Differentiating between acceleration mechanisms. J. Geophys. Res., **109**, A03213, doi: 10.1029/2003JA010153.

Green, J.L., Boardsen, S., Garcia, L., Taylor, W.W.L., Fung, S.F. and Reinisch, B.W. (2005): On the origin of whistler mode radiation in the plasmasphere. J. Geophys. Res., **110**, A03201, doi: 10.1029/2004JA 010495.

Hamilton, D.C., Gloeckler, G., Ipavich, F.M., Studemann, W., Wilken, B. and Kremser, G. (1988): Ring current development during the great geomagnetic storm of February 86. J. Geophys. Res., **93**, 14343–14355.

Harel, M., Wolf, R.A., Reiff, P.H., Spiro, R.W., Burke, W.J., Rich, F.J. and Smiddy, M. (1981): Quantitative simulation of a magnetospheric substorm, 1, Model logic and overview. J. Geophys. Res., **86**, 2217–2241.

Hill, T.W. (1974): Origin of the plasma sheet. Rev. Geophys., **12**, 379–388.

Huang, C.Y., Goertz, C.K. and Anderson, F.R. (1983): A theoretical study of plasmaspheric hiss generation. J. Geophys. Res., **88**, 7927–7940.

Hudson, M.K., Elkington, S.R., Lyon, J.G., Marchenko, V.A., Roth, I., Temerin, M. and Gussenhoven, M. S. (1996): MHD/particle simulations of radiation belt formation during a storm sudden commencement. Radiation Belts: Models and Standards, ed. by J.F. Lemaire *et al.* Washington, D.C., Am. Geophys. Union, 57–62 (Geophysical Monograph Vol. 97).

Isenberg, P.A., Koons, H.C. and Fennell, J.F. (1982): Simultaneous observations of energetic electrons and dawnside chorus in geosynchronous orbit. J. Geophys. Res., **87**, 1495–1503.

Jordanova, V.K., Farrugia, C.J., Janoo, L., Quinn, J.M., Torbert, R.B. *et al.* (1998): October 1995 magnetic cloud and accompanying storm activity: Ring current evolution. J. Geophys. Res., **103**, 79–92.

Jordanova, V.K., Farrugia, C.J., Thorne, R.M., Khazanov, G.V., Reeves, G.D. and Thomsen, M.F. (2001): Modeling ring current proton precipitation by electromagnetic ion cyclotron waves during the May 14–16, 1997, storm. J. Geophys. Res., **106**, 7–22.

Karlsson, T., Marklund, G.T., Blomberg, L.G. and Mälkki, A. (1998): Subauroral electric fields observed by the Freja satellite: A statistical study. J. Geophys. Res., **103**, 4327–4341.

Kelley, M.C., Fejer, B.G. and Gonzales, C.A. (1979): An explanation for anomalous equatorial ionospheric electric fields associated with a northward turning of the inter planetary magnetic field. Geophys. Res. Lett., **6**, 301–304.

Kennel C.F. and Petschek, H.E. (1966): Limit on stably trapped particle fluxes. J. Geophys. Res., **71**, 1–28.

Khazanov, G.V., Liemohn, M.W., Newman, T.S., Fok, M.-C. and Spiro, R.W. (2003a): Self-consistent magnetosphere-ionosphere coupling: Theoretical studies. J. Geophys. Res., **108** (A3), 1122, doi: 10.1029/2002JA009624.

Khazanov, G.V., Gamayunov, K.V. and Jordanova, V.K. (2003b): Self-consistent model of magnetospheric ring current and electromagnetic ion cyclotron waves: The 2–7 May 1998 storm. J. Geophys. Res., **108** (A12), 1419.

Kim, H.-J. and Chan, A.A. (1997): Fully relativistic changes in storm time relativistic electron fluxes. J. Geophys. Res., **102**, 22107–22116.

Kistler, L.M., Ipavich, F.M., Hamilton, D.C., Gloeckler, G., Wilken, B., Kremser, G. and Stüdemann, W. (1989): Energy spectra of the major ion species in the ring current during geomagnetic storms. J. Geophys. Res., **94**, 3579–3599.

Kozyra, J.U. and Nagy, A.F. (1991): Ring current decay-Coupling of ring current energy into the thermo-

This document is provided by JAXA.

sphere/ionosphere system. J. Geomagn. Geoelectr., 43, Suppl., 285–297.
Kozyra, J.U., Brace, L.H., Cravens, T.E. and Nagy, A.F. (1986): A statistical study of the subauroral electron temperature enhancement using Dynamics Explorer 2 Langmuir probe observations. J. Geophys. Res., 91, 11270–11280.
Kozyra, J.U., Shelley, E.G., Comfort, R.H., Brace, L.H., Cravens, T.E. and Nagy, A.F. (1987): The role of ring current O^+ in the formation of stable auroral red arcs. J. Geophys. Res., 92, 7487–7502.
Kozyra, J.U., Rasmussen, C.E., Miller, R.H. and Lyons, L.R. (1994): Interaction of ring current and radiation belt protons with ducted plasmaspheric hiss 1. Diffusion coefficients and timescales. J. Geophys. Res., 99, 4069–4084.
Kozyra, J.U., Rasmussen, C.E., Miller, R.H. and Villalon, E. (1995): Interaction of ring current and radiation belt protons with ducted plasmaspheric hiss 2. Time evolution of the distribution function. J. Geophys. Res., 100, 21911–21919.
Kozyra, J.U., Jordanova, V.K., Horne, R.B. and Thorne, R.M. (1997a): Modeling of the contribution of electromagnetic ion cyclotron (EMIC) waves to stormtime ring current erosion. Magnetic Storms, ed. by B.T. Tsurutani *et al.* Washington, D.C., Am. Geophys. Union, 187–202 (Geophysical Monograph Vol. 98).
Kozyra, J.U., Nagy, A.F. and Slater, D.W. (1997b): High-altitude energy source(s) for stable auroral red arcs. Rev. Geophys., 35, 155–190.
Kozyra, J.U., Jordanova, V.K., Borovsky, J.E., Thomsen, M.F., Knipp, D.J., Evans, D.S., McComas D.J. and Cayton, T.E. (1998): Effects of a high-density plasma sheet on ring current development during the November 2–6, 1993, magnetic storm. J. Geophys. Res., 103, 26285–26306, 10.1029/98JA01964.
Lemon, C., Wolf, R.A., Hill, T.W., Sazykin, S., Spiro, R.W., Toffoletto, F.R., Birn, J. and Hesse, M. (2004): Magnetic storm ring current injection modeled with the Rice Convection Model and a self-consistent magnetic field. Geophys. Res. Lett., 31, L21801.
Liemohn, M.W., Kozyra, J.U., Jordanova, V.K., Khazanov, G.V., Thomsen, M.F. and Cayton, T.E. (1999): Analysis of early phase ring current recovery mechanisms during geomagnetic storms. Geophys. Res. Lett., 26, 2845–2848.
Lorentzen, KR., McCarthy, M.P., Parks, G.K., Foat, J.E., Millan, R.M., Smith, D.M., Lin, R.P. and Treilhou, J.P. (2000): Precipitation of relativistic electrons by interaction with electromagnetic ion cyclotron waves. J. Geophys. Res., 105, 5381–5389.
Lui, A.T.Y., Elphinstone, R.D., Murphree, J.S., Henderson, M.G., Vo, H.B., Cogger, L.L., Lühr, H., Ohtani, S., Newell, P.T. and Reeves, G.D. (1995): Special features of a substorm during high solar wind dynamic pressure. J. Geophys. Res., 100, 19095–19108.
Lyons, L.R., Thorne, R.M. and Kennel, C.F. (1972): Pitch-angle diffusion of radiation belt electrons with the plasmasphere. J. Geophys. Res., 77, 3455–3474.
Maynard, N.C. (1978): On large poleward directed electric fields at sub auroral latitudes. Geophys. Res. Lett., 5, 617–618.
Meredith P.N., Horne, R.B. and Anderson, R.R. (2001): Substorm dependence of chorus amplitudes: Implications for the acceleration of electrons to relativistic energy. J. Geophys. Res., 106, 13165–13178.
Mitchell, D.G. *et al.* (2000): High energy neutral atom (HENA) imager for the IMAGE mission. Space Sci. Rev., 91, 67–112.
Mitchell, D.G., Brandt, P.C., Roelof, E.C., Hamilton, D.C., Retterer, K. and Mende, S. (2003): Global imaging of O^+ from IMAGE/HENA. Space Sci. Rev., 109, 63–75.
Moore, T.E. *et al.* (1999): Source processes in the high-latitude ionosphere. Space Sci. Rev., 88 (1–2), 7–84.
Moore, T.E., Fok, M.-C., Chandler, M.O., Chappell, C.R., Christon, S.P. *et al.* (2005a): Plasma sheet and (nonstorm) ring current formation from solar and polar wind sources. J. Geophys. Res., 110, A02210, doi: 10.1029/2004JA010563.
Moore, T.E., Fok, M-C., Christon, S.P., Chen, S.-H., Chandler, M.O., Delcourt, D.C., Fedder, J., Slinker, S. and Liemohn, M. (2005b): Solar and ionospheric plasmas in the ring current. Global Physics of the Coupled Inner Magnetosphere, Wshington, D.C., Am. Geophys. Union (Geophysical Monograph) (in press).
O'brien T.P., K.R., Lorentzen, I.R., Mann, N.P., Meredith, J.B., Blake, J.F., Fennell, M.D., Looper, Milling,

This document is provided by JAXA.

D.K. and Anderson, R.R. (2003): Energization of relativistic electrons in the presence of ULF power and MeV microbursts: Evidence for dual ULF and VLF acceleration. J. Geophys. Res., **108** (A8), 1329.

Peymirat, C., Richmond, A.D. and Kobea, A.T. (2000): Electrodynamic coupling of high and low latitudes: Simulations of shielding/overshielding effects. J. Geophys. Res., **105**, 22991–23003.

Pollock, C.J. *et al.* (2001): First medium energy neutral atom (MENA) images of Earth's magnetosphere during substorm and storm-time. Geophys. Res. Lett., **28**, 1147–1150.

Rees, M.H. and Roble, R.G. (1975): Observations and theory of the formation of stable auroral red arcs. Rev. Geophys., **13**, 201–242.

Reeves, G.D., McAdams, K.L. and Friedel, R.H.W. (2003): Acceleration and loss of relativistic electrons during geomagnetic storms. Geophys. Res. Lett., **30**, 1529.

Rich, F.J., Burke, W.J., Kelley, M.C. and Smiddy, M. (1980): Observations of field-aligned currents in association with strong convection electric fields at subauroral latitudes. J. Geophys. Res., **85**, 2335–2340.

Rowland, D.E. and Wygant, J.R. (1998): Dependence of the large-scale, inner magnetospheric electric field on geomagnetic activity. J. Geophys. Res., **103**, 14959–14964.

Sandel, B.R. *et al.* (2000): The extreme ultraviolet imager investigation for the IMAGE mission. Space Sci. Rev., **91**, 197–242.

Sandel, B.R., King, R.A. Forrester, W.T. Gallagher, D.L. Broadfoot, A.L. and Curtis, C.C. (2001): Initial result from the IMAGE Extreme Ultraviolet Imager. Geophys. Res. Lett., **28**, 1439–1442.

Schulz, M. (1997): Direct influence of ring current on auroral oval diameter. J. Geophys. Res., **102**, 14149–14154.

Schunk, R.W., and Nagy, A.F. (2000): Ionospheres—Physics, Plasma Physics, and Chemistry. Cambridge, Cambridge Univ. Press.

Shawhan, S.D. (1979): Magnetospheric plasma wave research 1975–1978. Rev. Geophys. Space Phys., **17**, 705–724.

Shelley, E.G., Klumpar, D.M., Peterson, W.K., Ghielmetti, A., Balsiger, H., Geiss, J. and Rosenbauer, H. (1985): AMPTE/CCE observations of the plasma composition below 17 keV during the September 4, 1984 magnetic storm. Geophys. Res. Lett., **12**, 321–324.

Slater, D.W., Gurgiolo, C., Kozyra, J.U., Kleckner, E.W. and Winningham, J.D. (1987): A possible energy source to power stable auroral red arcs: Precipitating electrons. J. Geophys. Res., **92**, 4543–4552.

Smiddy, M., Kelly, M.C., Burke, W., Rich, F., Sagalyn, R., Shuman, B., Hays, R. and Lai, S. (1977): Intense poleward directed electric fields near the ionospheric projection of the plasmapause. Geophys. Res. Lett., **4**, 543–546.

Sonwalkar, V.S. and Inan, U.S. (1989): Lightning as an embryonic source of VLF hiss. J. Geophys. Res., **94**, 6986–6994.

Southwood, D.J. and Wolf, R.A. (1978): An assessment of the role of precipitation in magnetospheric convection. J. Geophys. Res., **85**, 5227–5232.

Spiro, R.W. and Wolf, R.A. (1984): Electrodynamics of convection in the inner magnetosphere. Magnetospheric Currents, ed. by T.A. Potemra. Washington, D.C., Am. Geophys. Union, 247–259 (Geophysical Monograph Vol. 28).

Spiro, R.W., Heelis, R.A. and Hanson, W.B. (1978): Ion convection and the formation of the midlatitude F region ionization trough. J. Geophys. Res., **83**, 4255–4264.

Spiro, R.W., Heelis, R.A. and Hanson, W.B. (1979): Rapid subauroral ion drifts observed by Atmosphere Explorer C. Geophys. Res. Lett., **6**, 657–660.

Spiro, R.W., Wolf, R.A. and Fejer, B.G. (1988): Penetration of high-latitude-electric field effects to low latitudes during SUNDIAL 1984. Ann. Geophys., **6**, 39–49.

Spitzer, L. (1962): Physics of Fully Ionized Gases, 2nd ed., chap. 5. New York, Interscience.

Stern, D.P. (1975): The motion of a proton in the equatorial magnetosphere. J. Geophys. Res., **80**, 595–599.

Strangeway, R.J., Russell, C.T., Carlson, C.W., McFadden, J.P., Ergun, R.E., Temerin, M., Klumpar, D.M., Peterson, W.K. and Moore, T.E. (2000): cusp field-aligned currents and ion outflows. J. Geophys. Res., **105** (A9), 21129.

Stüdemann, W., Wilken, B., Kremser, G., Korth, A., Fennell, J.F. *et al.* (1987): The May 2–3, 1986 magnetic

This document is provided by JAXA.

storm: First energetic ion composition observations with the MICS instrument on Viking. Geophys. Res. Lett., **14**, 455–458.

Summers, D. and Ma, C.-Y. (2000): A model for generating relativistic electrons in the Earth's inner magnetosphere based on gyroresonant wave-particle interactions. J. Geophys. Res., **105**, 2625–2639.

Summers, D. and Thorne, R.M. (2003): Relativistic electron pitch-angle scattering by electromagnetic ion cyclotron waves during geomagnetic storms. J. Geophys. Res., **108** (A4), 1143.

Thorne, R.M. and Horne, R.B. (1992): The contribution of ion-cyclotron waves to electron heating and SAR-arc excitation near the storm time plasmapause. Geophys. Res. Lett., **19**, 417–420.

Thorne, R.M., Smith, E.J., Burton, R.K. and Holzer, R.E. (1973): Plasmaspheric hiss. J. Geophys. Res., **78**, 1581–1596.

Toffoletto, F.R., Spiro, R.W., Wolf, R.A., Birn, J. and Hesse, M. (2001): Modeling inner magnetospheric electrodynamics. Space Weather, ed. by Song *et al.* Washington, D.C., Am. Geophys. Union, 265–272 (Geophysical Monograph Vol. 125).

Tsurutani, B.T. and Smith, E.J. (1977): Two types of magnetospheric ELF chorus and their substorm dependences. J. Geophys. Res., **82**, 5112–5128.

Tsyganenko, N.A. (1995): Modeling the Earth's magnetospheric magnetic field confined within a realistic magnetopause. J. Geophys. Res., **100**, 5599–5612.

Tsyganenko, N.A., Singer, H.J. and Kasper, J.C. (2003): Storm-time distortion of the inner magnetosphere: How severe can it get. J. Geophys. Res., **108** (A5), 1209, doi: 10.1029/2002JA009808.

Volland, H. (1973): A semiempirical model of large-scale magnetospheric electric fields. J. Geophys. Res., **78**, 171–180.

Van Allen, J.A. (1959): The geomagnetically trapped corpuscular radiation. J. Geophys. Res., **64**, 1683–1689.

Vasyliunas, V.M. (1970): Mathematical models of magnetospheric convection and its coupling to the ionosphere. Particles and Fields in the Magnetosphere, ed. by B. McCormac. Norwell, D. Reidel, 60–71.

Volland, H. (1978): A model of the magnetospheric electric convection field. J. Geophys. Res., **83**, 2695–2699.

Walt, M. (1996): Source and loss processes for radiation belt particles. Radiation Belts: Models and Standards, ed. by J.F. Lemaire *et al.* Washington, D.C., Am. Geophys. Union, 1–13 (Geophysical Monograph Vol. 97).

Weimer, D.R. (1995): Models of high-latitude electric potentials derived with a least error fit of spherical harmonic coefficients. J. Geophys. Res., **100**, 19595–19607.

Weimer, D.R. (2001): An improved model of ionospheric electric potentials including substorm perturbations and applications to the Geospace Environment Modeling November 24, 1996, event. J. Geophys. Res., **106**, 407–416.

Wentworth, R.C., MacDonald, W.M. and Singer, S.F. (1959): Lifetimes of trapped radiation belt particles determined by Coulomb scattering. Phys. Fluids, **2**, 499–509.

Wolf, R.A. (1970): Effects of ionospheric conductivity on convective flow of plasma in the magnetosphere. J. Geophys. Res., **75**, 4677–4698.

Wolf, R.A. (1975): Ionosphere-magnetosphere coupling. Space Sci. Rev., **17**, 537–562.

Wolf, R.A. (1983): The quasi-static (slow-flow) region of the magnetosphere. Solar Terrestrial Physics, ed. by R.L. Carovillano and J.M. Forbes. Norwell, D. Reidel, 303–368.

Wolf, R.A. (1995): Magnetospheric configuration. Introduction to Space Physics, ed. by M.G. Kivelson and C.T. Russell, Chap. 10. Cambridge, Cambridge University Press, 288–329.

Yau, A.W. and Lockwood, M. (1988): Vertical ion flow in the polar ionosphere. Modeling Magnetospheric Plasma, ed. by T.E. Moore and J.H Waite, Jr. Washington, D.C., Am. Geophys. Union, 229–244 (Geophysical Monograph Vol. 44).

Yeh, H.-C., Foster, J.C., Rich, F.J. and Swider, W. (1991): Storm time electric field penetration observed at mid-latitude. J. Geophys. Res., **96**, 5707–5721.

Zheng, Y., Fok, M.-C. and Khazanov, G.V. (2003): A radiation belt-ring current forecasting model. Space Weather, **1** (3), 1013.

This document is provided by JAXA.

Adv. Polar Upper Atmos. Res., 19, 135-151, 2005
© 2005 National Institute of Polar Research

Report

Development of the Virtual Earth's Magnetosphere System (VEMS)

Ken T. Murata[1]*, Kazunori Yamamoto[1], Daisuke Matsuoka[1], Eizen Kimura[1], Hiroshi Matsumoto[2], Masaki Okada[3], Toshifumi Mukai[4], John B. Sigwarth[5], Shigeru Fujita[6], Takashi Tanaka[7], Kiyohumi Yumoto[8], Tatsuki Ogino[9], Kazuo Shiokawa[9], Nikolai A. Tsyganenko[10], James L. Green[10] and Tsugunobu Nagai[11]

[1]*Center for Information Technology, Ehime University, 3, Bunkyo-cho, Matsuyama 790-8577*
[2]*Research Institute for Sustainable Humanosphere, Kyoto University, Gokasho, Uji 611-0011*
[3]*National Institute of Polar Research, Kaga 1-chome, Itabashi-ku, Tokyo 173-8515*
[4]*Institute of Space and Astronautical Science, Japan Aerospace Exploration Agency, 3-1-1, Yoshinodai, Sagamihara 229-8510*
[5]*Iowa University, Iowa City, Iowa 52242, U.S.A.*
[6]*Meteorological College, 7-4-81, Asahi, Kashiwa 277-0852*
[7]*Graduate School of Sciences, Kyushu University,*
[8]*Space Environment Research Center, Kyushu University, 6-10-1, Hakozaki, Higashi-ku, Fukuoka 812-8581*
[9]*Solar-Terrestrial Environment Laboratory, Nagoya University, 3-13, Honohara, Toyokawa 442-8507*
[10]*Goddard Space Flight Center, National Aeronautics and Space Administration, Greenbelt Road, Greenbelt, MD 20771-0001, U.S.A.*
[11]*Tokyo Institute of Technology, 2-12-1, O-okayama, Meguro-ku, Tokyo 152-8550*
**Corresponding author. E-mail: murata@cs.ehime-u.ac.jp*

(Received December 27, 2004; Accepted March 18, 2005)

Abstract: We have constructed a new research environment for geo-space science based on 3-D visualization tool and network database; Virtual Earth's Magnetosphere System (VEMS). With an interactive research environment researchers can visually understand structures of the Earth's magnetosphere using VEMS. On the VEMS, computer simulation results and observation data are simultaneously visualized, having a potential to data assimilation for geo-space studies in the future. Since the VEMS deals with time-dependent data, it also helps researchers to study dynamics of the Earth's magnetosphere. We found that immersive data analyses are possible using the VEMS on a virtual reality system.

key words: computer simulation, Earth's magnetosphere, 3-D visualization, network database, satellite and ground-based observation

1. Introduction

There are two major research methods for geo-space science; computer simulations, satellite observations, and remote ground-based observations. Both methods have advantages and disadvantages: Computer simulations can provide data in whole time

This document is provided by JAXA.

and space in the simulation domain. However, since they are based on model equations, the simulation results are not necessarily accurate. On the other hand, satellite observation data are hopefully more accurate. However, the data are restricted in time and space. To combine both methods is important in order to develop our understandings of the structure and dynamics of geo-space. 3-D visualizations would be effective for combinations and analyses of both data (Murata *et al.*, 2004).

So far many global MHD simulations have been 3-D visualized (*e.g.*, Winglee *et al.*, 1998; Ogino, 2002; Shao *et al.*, 2003). Recently Boston University (Glenn, 2004) demonstrated 3-D global MHD simulations on a virtual reality system at the SC2004 conference (SC04 Home page, 2004). These are visualizations of simulation data, but satellite or ground-based observation data are not included.

In the present study, we propose a new research environment for geo-space science. This system is named VEMS (Virtual Earth's Magnetosphere System). The basic concept of the VEMS is "to reproduce the past Earth's magnetosphere virtually in a personal computer". It visualizes both satellite and ground-based observation data and global MHD simulation data together in 3-D space and 1-D time domain.

2. Backgrounds for geo-space science

2.1. Satellite observations

During the final decade in the 20th century, most of the satellite observations for geo-space were still *via* singular spacecraft. In the near future, many missions will be with multi-spacecraft. To study the static or dynamic structures of the Earth's magnetosphere *via* simultaneous multipoint observations, we often map the observation data on their orbits on 2-D planes (as will be shown in Fig. 2c).

However, as the number of spacecraft increase, the mapping results become complicated and their 3-D structures would be hard to be recognized. In case of the studies to compare spacecraft observation data with ground-based phenomena on the Earth, 3-dimensional relative locations of the spacecraft are important. For example, if one compares the regions of aurora breakup on the Earth with plasma jet observed by spacecraft located in the magnetotail, one may be interested in the footpoint of the magnetic field line on the Earth from the spacecraft (as will be discussed in Fig. 6).

2.2. Computer simulations

During these two decades, many space plasma computer simulations were one- or two-dimensional. However, as power and performance of super computers develop, the data sizes in the computer simulations become larger and larger. During these 30 years, computational power of super-computers shows exponential progresses according to Moore's law (Intel Research, 2004). Both main memory size and data storage size also show tremendous developments. At the SC2004 conference, the peak values of super-computers are presented (SC04 Home page, 2004). The best performance of super-computers, Blue Gene/L, measured by the Linpack benchmark was 72 TFlops. This CPU power is as twice as of the Earth Simulator in Japan (The Earth Simulator Center, 2004) which used to be at the top from 2002 to 2003.

This document is provided by JAXA.

2.3. *Requirement to introduce*

Through the above discussions on the background for geo-space science, it is implied that we should introduce new information technologies (IT) in this research field. To compare and analyze a variety of data, we need an integrated system for data-download, data-read, data-plot and data-analysis. Recently powerful super-computers yield a huge size of data, and most of them are in 3-D format. The visualization of simulations must be, therefore, in 3-D format since it is not easy to get 3-D images of the magnetosphere from 2-D plots.

In the next section we discuss a data analysis and reference system which has been developed by some of the present authors. Therein a network database technology plays an important role. Using the network database, in the present paper, we propose a 4-dimensional data visualization and analysis system in Section 4. Both observation data and simulation data are to be visualized in 3-D space and 1-D time via visualization techniques and network database.

3. STARS (Solar-Terrestrial data Analysis and Reference System)

3.1. *Concept of STARS*

In 1992, under the collaborations between the NASA, the ESA and the ISAS, an international project started, which is called the ISTP (International Solar-Terrestrial Physics) project. In the project, many satellites are launched and observe the wide area in the geo-space and interplanetary regions. The more scientific satellites are launched, with higher quality and quantity the data are provided by the satellites. The software programs to analyze and plot the data become complex as more data are included into the programs. A new software system was required that refers to and analyzes such a wide variety of data.

Some of the authors (Murata, Kimura and Yamamoto) have been developing a data analysis system for satellite and ground-based observation data for solar-terrestrial physics: Solar-Terrestrial data Analysis and Reference System (STARS) (Murata, 2003). The STARS application works with a wide variety of spacecraft data and ground-based observation data. The construction of the STARS is fully based on an object-oriented software methodology that is called Object Modeling Technique (OMT) (Rumbaugh, 1991). It is usually said that the addition of new program, class and function is rather easy if a system is designed with the OMT.

3.2. *Properties of STARS application*

Figure 1 is a network configuration of the STARS application, the STARS meta-database and data sites for solar-terrestrial physics observations. The STARS meta-database provides meta-information of observation data files managed at the observation data sites (Murata *et al.*, 2002; Murata, 2003). Users download data files through the STARS application. The downloads are done backend of the STARS application, thus users don't know where the data files are managed over the Internet. In December 2004, the numbers of mission record, data record and data file record are 25, 140 and 1,219,056, respectively. These numbers still continue to increase.

This document is provided by JAXA.

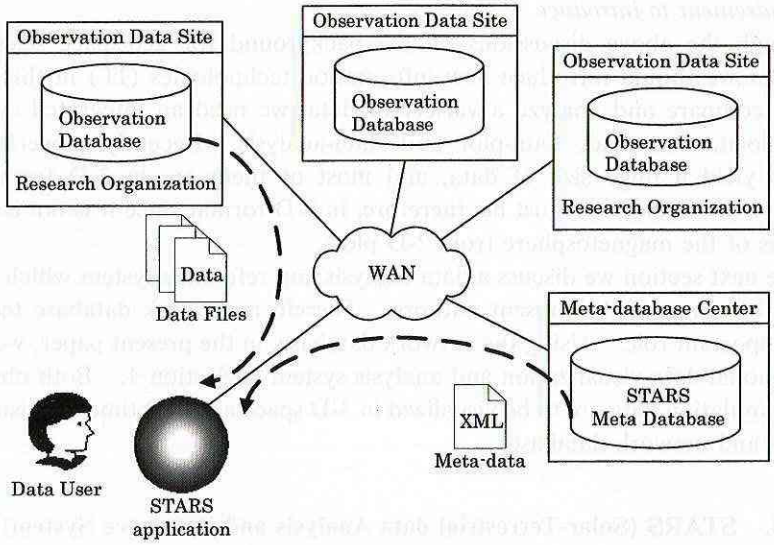


Fig. 1. The network configuration of the STARS application, STARS meta-database and observation data site.

(a)

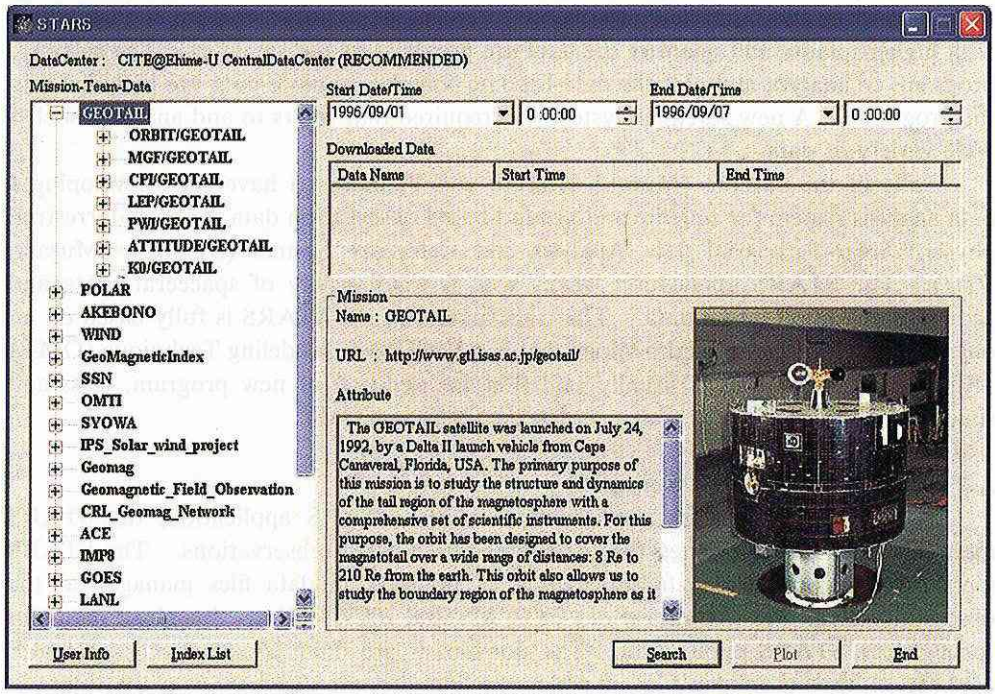
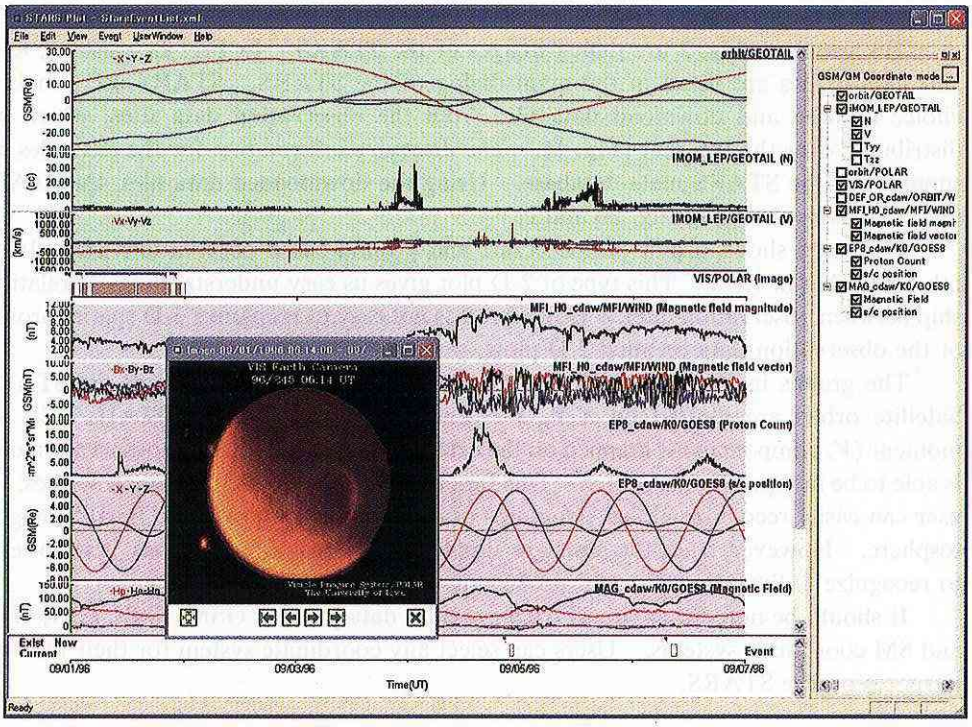


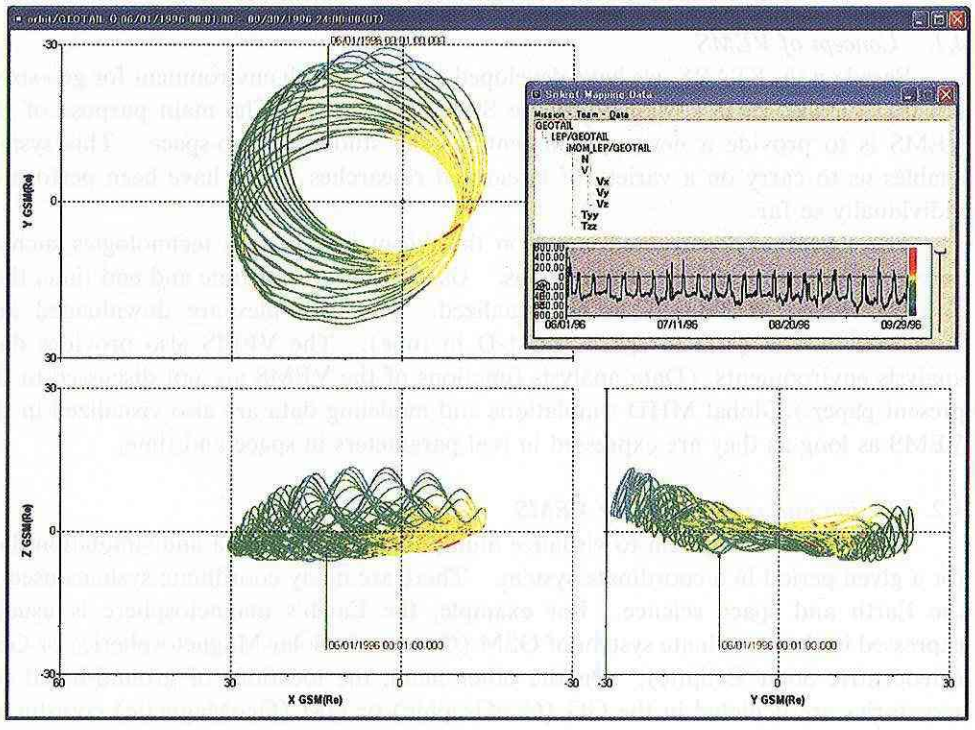
Fig. 2. Dialog images of the STARS (Solar-Terrestrial data Analysis and Reference System) from 1st to 6th September in 1996. (a) Main window of the STARS. (b) A plot window of the STARS. (c) An orbit window of STARS. Any observation data is mapped on a satellite orbit.

This document is provided by JAXA.

(b)



(c)



This document is provided by JAXA.

3.3. 2-D Data plots of STARS

The panels in Fig. 2 are dialog images of the STARS. In Fig. 2a, mission, team and data names are listed in the main dialog of the STARS. STARS users make a choice of data and download data files from the observation data sites, which are distributed over the Internet (Fig. 1). The directory information for the data files are supplied by the STARS meta-database. Using the downloaded data files, the STARS makes plots as shown in Fig. 2b and c.

Figure 2b shows a plot of spacecraft and ground-based observations from 1st to 6th September in 1996. This type of 2-D plot gives us easy understandings of relationship between observation data. However, it is not easy to recognize 3-D spatial profiles of the observation data on such 2-D plots.

The graphs in Fig. 2c are plotted using one of the plot functions of the STARS. Satellite orbits are plotted on *X-Y*, *Y-Z* and *Z-X* planes and GEOTAIL/LEP ion moment (V_x component) is mapped on the orbits. On the STARS any observation data is able to be mapped on the orbits. This function may help user's statistical studies: the user can easily recognize global structures of observation data over the Earth's magnetosphere. However, since the plots are simple projections on 2-D planes, it is not easy to recognize 3-dimentional spatial profiles of the data.

It should be noted that the STARS provides data plots in GSM, GSE, GEI, GEO and SM coordinate systems. Users can select any coordinate system for their research purposes on the STARS.

4. Virtual Earth's Magnetosphere System (VEMS)

4.1. Concept of VEMS

Based on the STARS, we have developed a new research environment for geo-space science; Virtual Earth's Magnetosphere System (VEMS). The main purpose of the VEMS is to provide a new environment for the studies of geo-space. This system enables us to carry on a variety of integrated researches which have been performed individually so far.

The VEMS is constructed based on the recent information technologies such as network database and 3-D visualizations. User first sets start time and end time, then make a choice of datasets to be visualized. The data files are downloaded and visualized in 4-D (3-D in space and 1-D in time). The VEMS also provides data analysis environments. (Data analysis functions of the VEMS are not discussed in the present paper.) Global MHD simulations and modeling data are also visualized in the VEMS as long as they are expressed in real parameters in space and time.

4.2. Design and construction of VEMS

The VEMS is a system to visualize multiple observation data and simulation data for a given period in a coordinate system. There are many coordinate systems used in the Earth and space science. For example, the Earth's magnetosphere is usually expressed in the coordinate system of GSM (Geocentric Solar Magnetospheric) or GSE (Geocentric Solar Ecliptic). On the other hand, the locations of ground-based observatories are depicted in the GG (GeoGraphic) or GM (GeoMagnetic) coordinate.

This document is provided by JAXA.

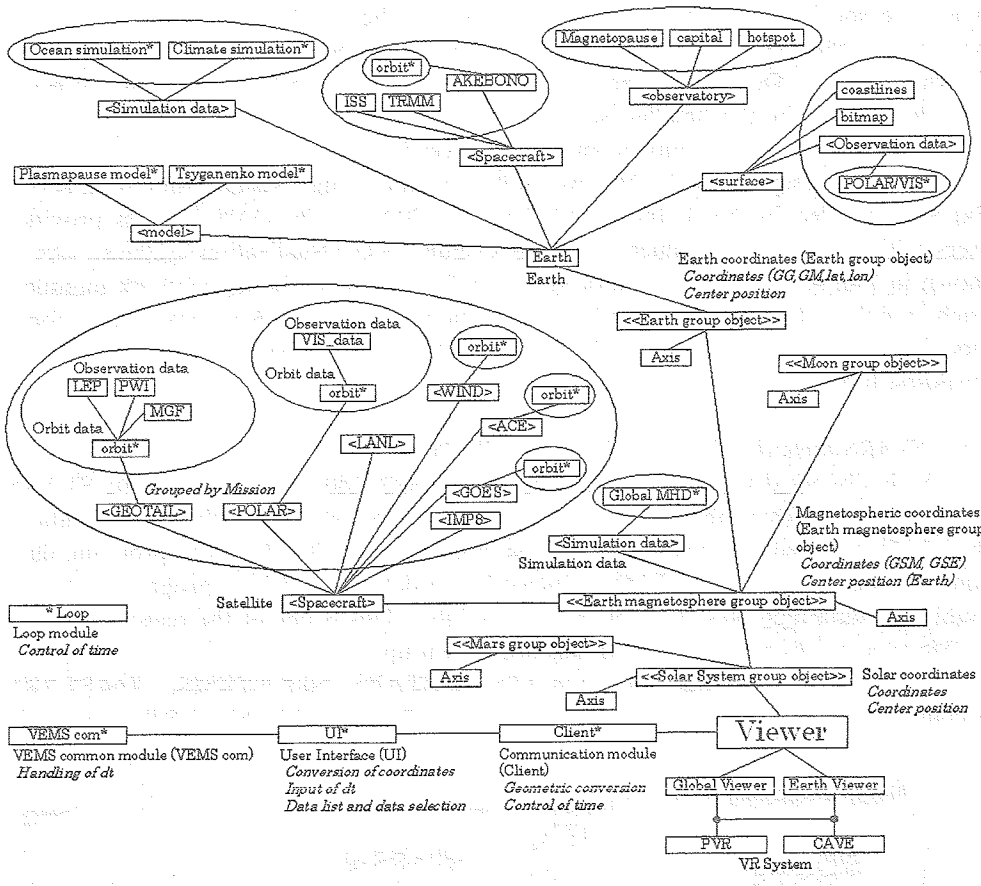


Fig. 3. The VEMS framework. Note that symbol "" represents a reference of Loop module, symbol "< >" represents folder and symbol "≪ ≫" represents coordinates.*

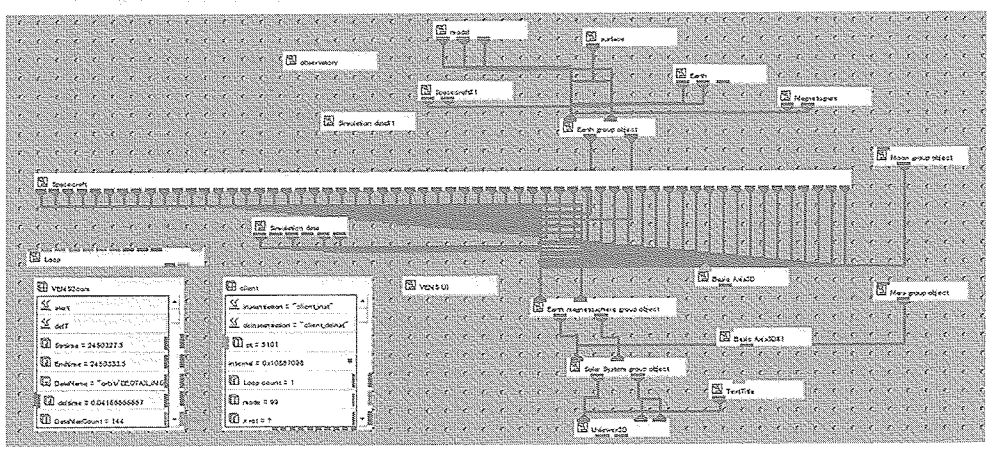


Fig. 4. The module network of the VEMS on AVS/Express.

This document is provided by JAXA.

It is unreasonable to express the observatories on the Earth in the GSE coordinate system. In the VEMS, a smaller scale coordinate system is laid on a larger one as shown in Fig. 3. Due to this hierarchical structure of coordinate systems, any observation data given in the smaller scale coordinate system is expressed in the larger coordinate system without any geometrical conversion.

After the design of the VEMS, we implemented it using a visualization tool: AVS/Express provided by KGT Inc. (AVS/Express, 2004). The AVS/Express provides users with an easy environment to build original 3-D visualization systems. As is shown in Fig. 4, the construction of system is done with combining network modules. Each module of the AVS/Express has one or more functions. A variety of functional modules are supplied. Users are able to make his/her own original modules for special purposes, too.

4.3. STARS meta-database and XML for VEMS

As is discussed in Section 3.2, there are already 140 data stored in the STARS meta-database in December 2004. In order to include a variety of observation data in the VEMS, we need to prepare a set of programs for each data; data read program, data conversion program to the VEMS framework and data visualization program. As the number of data increases, it becomes a heavy job. This is one of the reasons that the VEMS type of visualization system has not shown up.

Figure 5 shows data handling process for the STARS and the VEMS. The STARS is composed of two programs: STARSdb and STARSplot. The STARSdb downloads

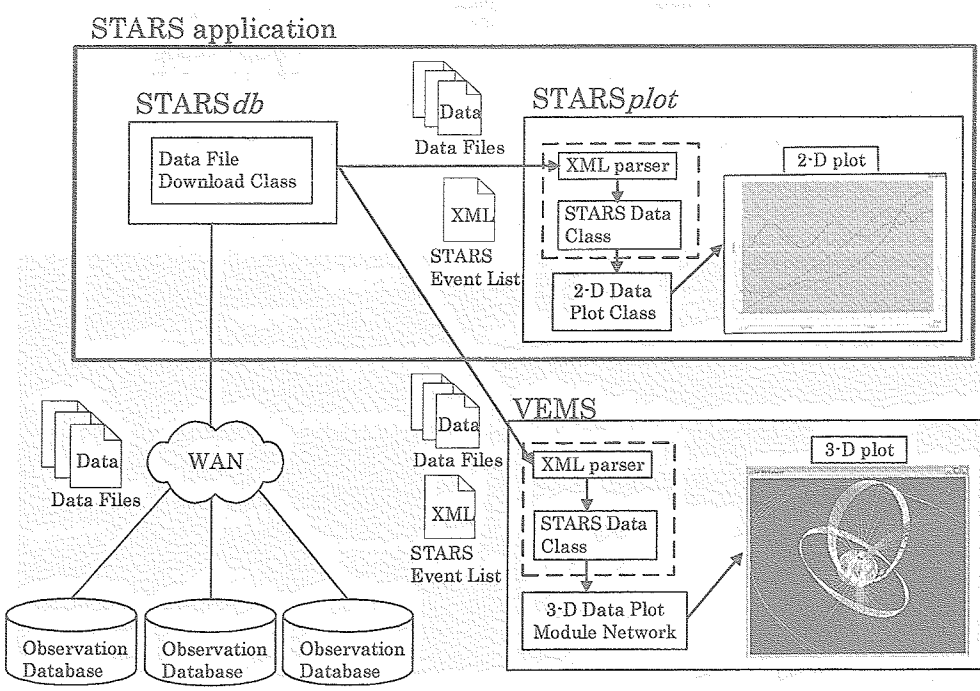


Fig. 5. VEMS cooperates with STARS.

This document is provided by JAXA.

Table 1. A list of dataset to be visualized in the VEMS (December 2004).

Magnetic field model	Tsyganenko 2003 model
Simulation data	Global MHD simulations
Satellite observation data and ground observation data	GEOTAIL (Orbit, ion density, ion velocity and Electromagnetic field) POLAR (Orbit, Visible Imaging System data, Magnetic field) GOES-6, -7, -8, -9, -0, -12 (Orbit, Proton, Electron, Solar X-ray Fluxes and Magnetic field) WIND (Orbit and Magnetic field) AKEBONO (Orbit) ACE (Orbit and *Magnetic field*) LANL-89, -90, -91, -94, -97 (Orbit, keV proton and MeV proton) IMP8 (Orbit, Plasma and Magnetic field) IMAGE (Orbit) Interball tail (*Orbit, Magnetic field, Electron and AKR*) Interball aurora (*Orbit, Magnetic field and Electron*) SOHO (*Orbit, Proton flux and Electron flux*) Cluster (*Orbit, Electromagnetic field in the equatorial and Electron*) FAST (*Orbit, Electromagnetic field on polar, ion and Electron*) Equator-S (*Orbit, Electromagnetic field in the equator and Electron*) Ground Geomagnetic Field Data Along the 210 degree Magnetic Meridian: (position coordinates of station and geomagnetic field)

(*Italic character: data list scheduled to be included*)

data files for the periods set by users. The list of downloaded data files are described as an XML file named STARS Event List. The XML parser program in the STARSplot resolves the STARS Event List to bring data files from the STARSdb to the STARSplot. To read data files and convert them into the STARS data format, the STARS project prepared a data class named STARS Data Class. The STARS Data Class defines schemata for several types of data. This class encapsulates data files to users: users simply get a data stored in a data format regulated by the STARS data schemata.

For the construction of the VEMS, we make full use of the STARS. As shown in Fig. 5, we replicate the XML parser and STARS Data Class of the STARSplot to the VEMS. For the VEMS, we simply make as many AVS modules for 3-D visualization as is given by the STARS Data Class (Fig. 5). Table 1 shows a list of datasets which are ready for visualizations on the VEMS.

5. Application of VEMS

5.1. 2-D plot via STARS and 4-D visualization via VEMS

Figure 6a is a 2-D plot via STARS from 0000 UT on 1st September to 0000 UT on 7th September in 1996. There are 5 spacecraft orbits and magnetic fields observed by them. Ground-based magnetogram data are also shown at the bottom of the plot.

Figure 6b is its 4-D visualization (3-D in space and 1-D in time). Spacecraft are depicted as spheres. The color of each sphere shows one scalar data and arrows show vector data. There are two arrows at each spacecraft. Bold arrows represent magnetic fields given by Tsyganenko model, while thin arrows for observed magnetic fields.

This document is provided by JAXA.

(a)

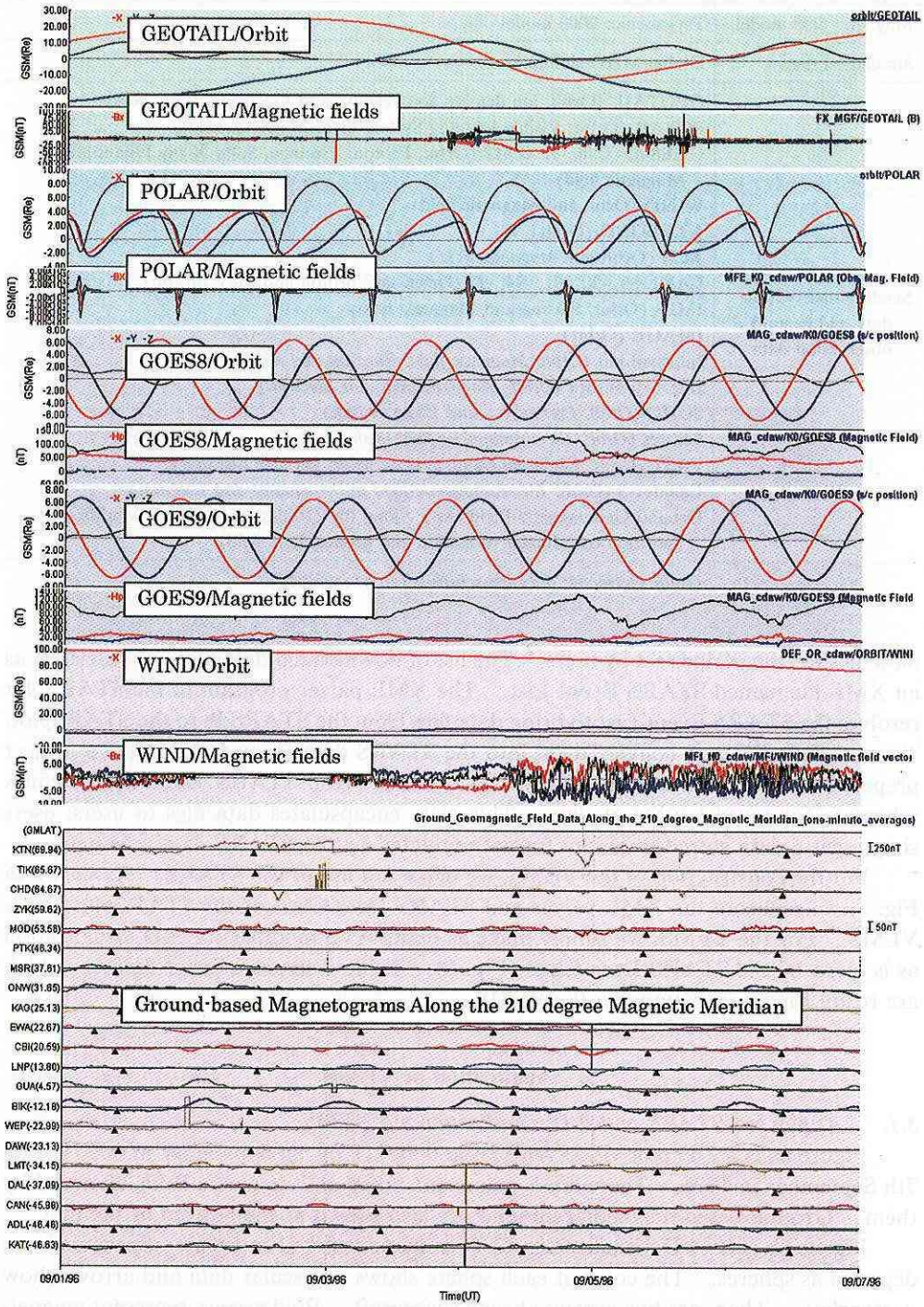


Fig. 6a.

This document is provided by JAXA.

(b)

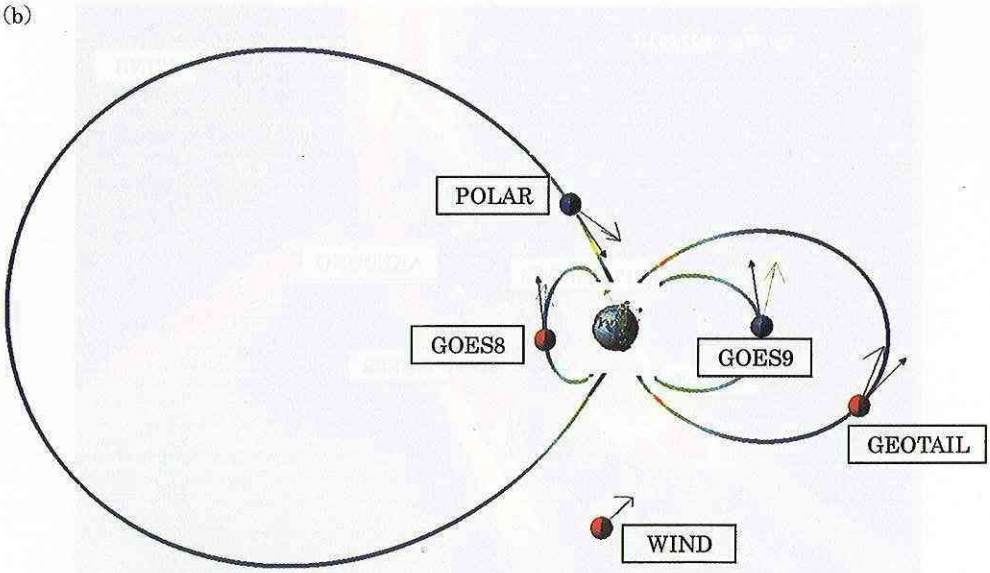


Fig. 6. Traditional 2-D and present 3-D visualization of satellite orbits and observation data from 1st to 6th September in 1996: (a) Traditional 2-D plot by the STARS. (b) 3-D visualization of observation data by the VEMS. A magnetic field lines are given by Tsyganenko model 2003. Bold arrows represent magnetic fields given by Tsyganenko 2003 model, while thin arrows are observed magnetic fields. The coordinate system is GSM.

The magnetic field lines which go through spacecraft are drawn based on Tsyganenko 2003 model. The magnetic field lines move with spacecraft, thus the footpoints of magnetic field line in the vicinity of the spacecraft are visible. This may help our studies on relationship between spacecraft observation and ground-based observation such as aurora activities or magnetograms (Yumoto *et al.*, 1996).

One may find arrows on the Earth if he/she carefully take a look of Fig. 6b. These correspond to magnetogram data from Fig. 6a. Time-dependent sequences from the changes in the solar wind to the fluctuations of the Earth magnetic field are comprehensive if one uses the VEMS replay mode.

5.2. *Combination of observation and simulation on VEMS*

Figure 7 is an example of the VEMS from 0816 to 0935 UT on 6th September in 1996, in which observation data and simulation data are visualized in 3-D space and 1-D time. In Table 2 a list of data in Fig. 7 is shown. Figure 7 depicts a screen shot of the VEMS at 0829 UT. The positions of multiple satellites (POLAR, AKEBONO, WIND and GOES) are expressed in 3-D sphere, thus relative positions between satellites are visible. It should be noted that one can change his/her viewpoints in any direction or walk through regions in the magnetosphere.

One scalar data and one or more vector data *via* spacecraft are able to be visualized on the VEMS. In Fig. 7 the color on each sphere shows one scalar data, such as plasma density, observed by the satellite. Note that any scalar data, even one component of

This document is provided by JAXA.

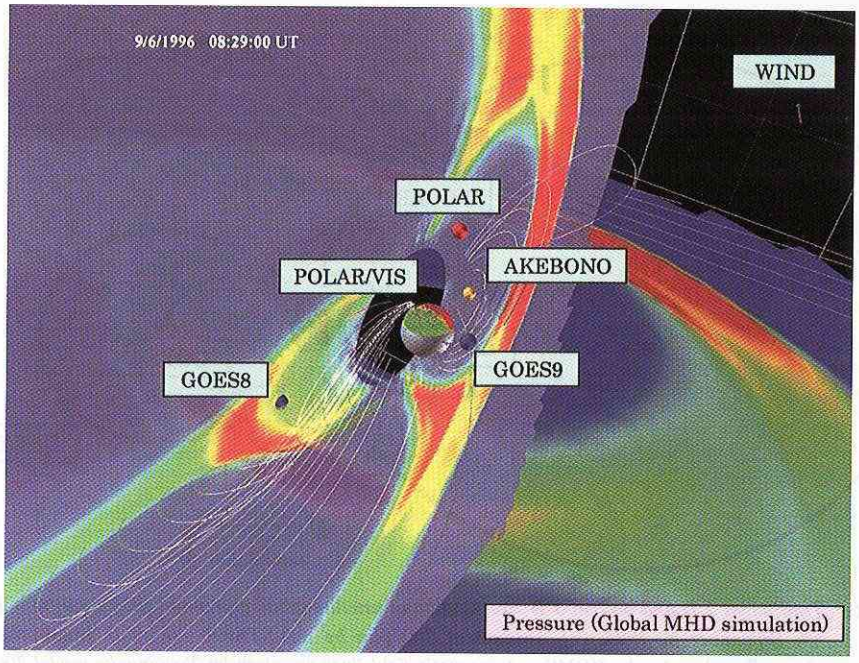


Fig. 7. Global MHD simulation and satellite observations. Only the magnetic field lines which pass along the X-axis are extracted. Pressure (Global MHD simulation) is expressed as a cross section. The coordinate system is GSM.

Table 2. Global MHD simulation and satellite observations. The visualized period is from 09/06/1996 0816 UT to 09/06/1996 0935 UT.

Global MHD simulation data	Magnetic field: streamline Pressure: cross section
Observation data	GOES8: Orbit, Magnetic field and Proton count GOES9: Orbit, Magnetic field and Proton count GEOTAIL: Orbit and Magnetic field POLAR: Orbit WIND: Orbit and Solar wind AKEBONO: Orbit

vector or one channel data of multi-channel observation, is able to be expressed in color. The arrow at each sphere shows an vector data like magnetic fields. Since the VEMS provides time-dependent visualization, the color and vector changes as time goes on. On the Earth, ground-based magnetogram data (not shown in Fig. 7) or aurora image data are also depicted (Murata *et al.*, 2004).

On the VEMS, in addition to the observation data, global MHD simulation data are also visualized in 4-D format as long as the simulation is performed with real parameters. In Fig. 7 plasma pressure is shown in color contours. The AVS/Express pro-

This document is provided by JAXA.

vides a variety of 3-D visualization. The plasma pressure contours are given on two-planes: the X-Y plane and the X-Z plane in GSM coordinates, respectively. If one carefully see, he/she may find that the GOES 8 spacecraft is on both planes. One can directly compare GOES8 observation data (scalar or vector) with global MHD simulation results. These planes move with the satellite so that this direct comparison is possible at any moment.

5.3. *Magnetic field models on VEMS*

Instead of global MHD simulations, magnetic filed modeling data in 4-D format are also visualized on the VEMS. Figure 8 is a long durational 3-D visualized data of satellite orbits from 0000 UT on 1st September 1996 to 0000 UT on 1st October 1996 with magnetic filed lines given by Tsyganenko 2003 model (Tsyganenko, 2002). Table

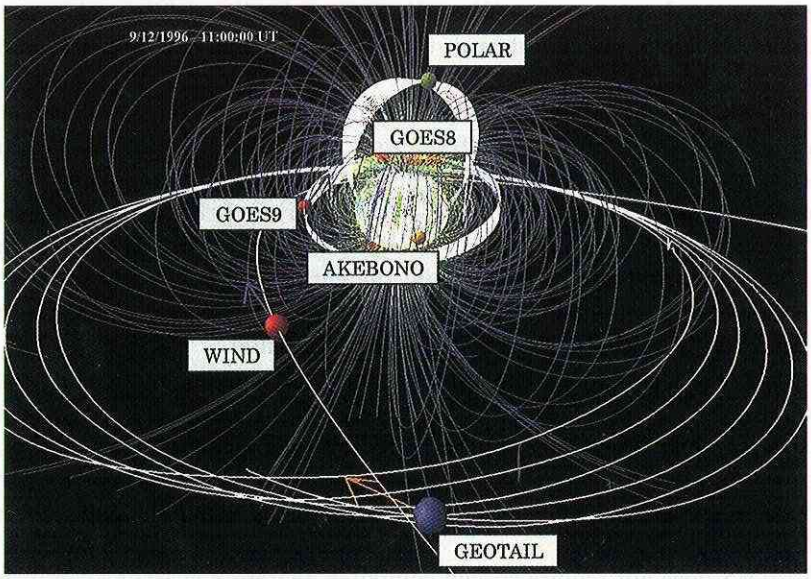


Fig. 8. Satellite orbits and the Earth's magnetic field lines which go through the satellites. The magnetic fields are given by Tsyganenko 2003 model.

Table 3. Magnetic field model and satellite observations. The visualized period is from 09/01/1996 to 10/01/1996.

Tsyganenko 2003 model	Magnetic field: streamline
Observation data	GOES8: Orbit, Magnetic field and Proton count GOES9: Orbit, Magnetic field and Proton count GEOTAIL: Orbit and Ion moment POLAR: Orbit and Magnetic field WIND: Orbit and Solar wind AKEBONO: Orbit

This document is provided by JAXA.

3 shows a list of visualization data in Fig. 8. Using the replay mode of the AVS/Express, these satellites move along with the orbits and the model magnetic filed lines follow them. (Note that the Tsyganenko model is a time-dependent model.) This view looks simple, but helps researchers or nonspecialists to understand the positions of spacecraft in the Earth's magnetosphere.

6. Summary and discussions

Taking into account the backgrounds of geo-space science discussed in Sections 2.1 and 2.2, we conclude that a new research environment is required in order to achieve break-through results. For the development of the researches, we need to make full use of up-to-date information technologies (IT). In the present paper, we propose a new 4-D visualization system, Virtual Earth's Magnetosphere System (VEMS). The basic concept of the VEMS is to reproduce the past Earth's magnetosphere for given period virtually in personal computers. We gather (download) satellite and ground-based observation data public on the Internet, then drop them into the VEMS. The VEMS visualizes these data in 4-dimentional format (3-D in space and 1-D in time).

The VEMS also visualizes 3-D computer simulation results or magnetic field models (*e.g.*, Tsyganenko, 2002) in the same framework with observations if the simulation is performed based on real parameters. In this case, direct comparison between observations and simulations are possible. The direct comparison helps the data interpretation by allowing researchers to put the data into a global context and allows the modellers to directly compare the results to data within the entire system. This kind of research environment has a potential to lead to data assimilations in the future. Nevertheless, it requires the helps of adequate filters, such as Kalman filter.

After the basic design, we implemented the VEMS using visualization software, AVS/Express (AVS/Express, 2004). The VEMS provides us with several visualization and analysis environments, such as re-scaling, rotation, draw of stream lines, particle trace, orthogonal slice, iso-surface and others with help of the AVS functional modules. We can handle and analyze the Earth's magnetosphere in our computers from our own viewpoints.

The VEMS does not require special computer, therefore everyone can install it on his/her personal computer (Windows PC). Generally, it is not easy for nonspecialists to search and download observation data files. In case of the VEMS, downloads of data files are supported by the STARS (Solar-Terrestrial data Analysis and Reference System), which has been developed at the Center for Information Technology, Ehime University (Murata, 2003). The operation of the STARS is not difficult: even high school students can easily download and visualize data. Consequently, the VEMS is a powerful tool. This implies that the VEMS can be used for outreach activities and educations.

It should be noted that the VEMS works on a virtual reality system. We installed the VEMS on PVR (Portable VR, 2004) which is a low-price virtual reality system (Fig. 9). Using the VEMS on the PVR, we could obtain an immersive experience of the Earth's magnetosphere: it was as if we could see the Earth and magnetosphere from the space (Watari *et al.*, 2003). Not only the immersive experience, but the VR system

This document is provided by JAXA.

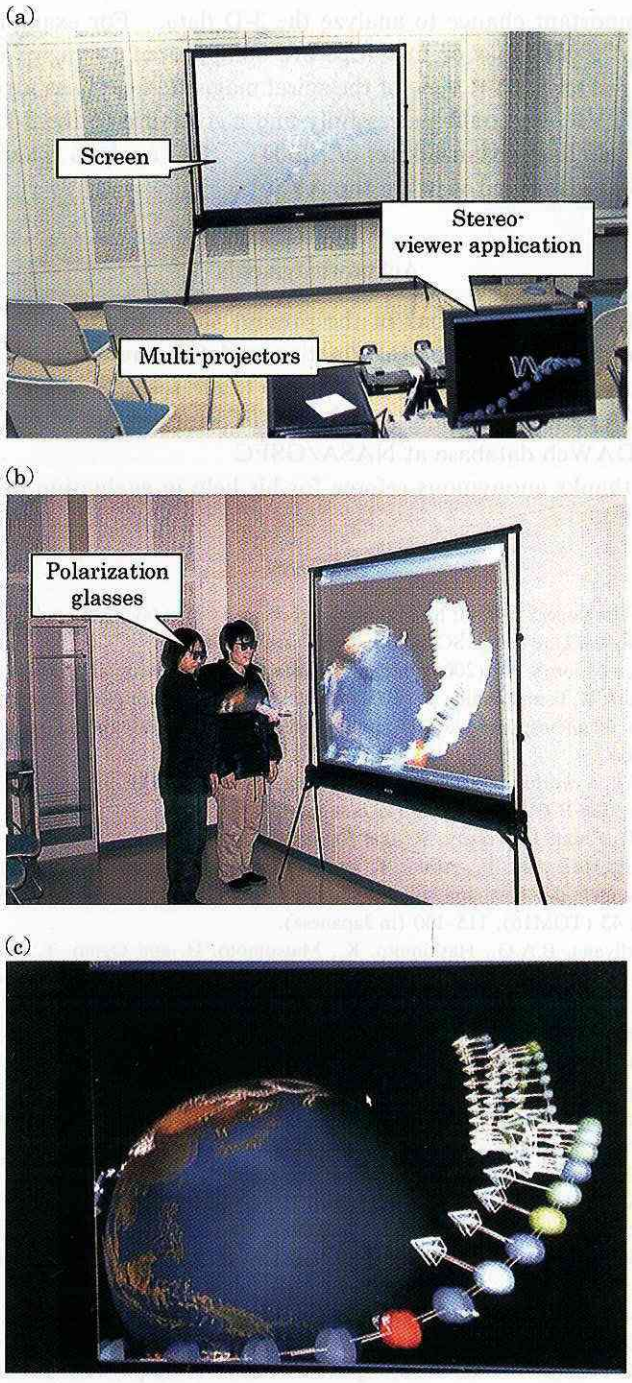


Fig. 9. (a) and (b) A portable virtual reality system (Portable VR, 2004) at the Center for Information Technology, Ehime University. (c) VEMS on PVR.

This document is provided by JAXA.

gives us more important chance to analyze the 3-D data. For example, the magnetic field lines around a plasmoid or flux rope are complicated (Winglee *et al.*, 1998), in general. When we took a VR view of the spiral magnetic field lines around a magnetic flux rope on the PVR, we could successfully find a structure of the 3-D configurations of the magnetic field lines (Matsuoka *et al.*, 2004). This analysis is hard to be done on the traditional 3-D visualized view on the AVS.

Acknowledgments

The Global MHD simulations in the present study are done on the SX-6 super computer in National Institute of Information and Communications Technology; we thank to T. Obara and his co-workers. We also thank to H. Singer (NOAA SEC), C. T. Russell (UCLA) and R. Lepping (NASA/GSFC) for our use of their magnetic field data through CDAWeb database at NASA/GSFC

The editor thanks anonymous referee for his help in evaluating this paper.

References

AVS/Express (Viz/Developer) (2004): http://www.kgt.co.jp/product/avs/express/viz/index.html.

Glenn, B. (2004): Boston University. SC2004 Exhibit Directory, 45.

Intel Research-Silicon-Moore's law (2004): http://www.intel.com/research/silicon/mooreslaw.htm.

Matsuoka, D., Murata, K.T. and Fujita, S. (2004): Data analyses of space plasma computer simulations for the Earth's magnetosphere via 3-D visualization and visual data mining. submitted to Journal of Visualization.

Murata, K.T. (2003): A world-wide distributed database system for ISTP project. IEICE Transactions on Electronics, **J86-B** (7), 1331–1343 (in Japanese).

Murata, K.T. (2004): Ehime University. SC2004 Exhibit Directory, 56.

Murata, K.T., Okada, M., Abe, F., Araki, T. and Matsumoto, H. (2002): A design and estimation of distributed meta-database for solar-terrestrial physics observation data. IPSJ Transactions on Databases, **43** (TOM16), 115–130 (in Japanese).

Murata, K.T., Nurdiyana. B.A.G., Hashimoto. K., Matsumoto. H. and Ogino. T. (2004): Proposal of a Virtual Earth Magnetosphere System. IEICE Transactions on Electronics, **J87-B** (2), 309–313 (in Japanese).

Ogino, T. (2002): Three-dimensional global MHD simulation code for the Earth's magnetosphere using HPF/JA. Concurrency Computat: Pract. Exper., **14**, 631–646.

Portable VR (2004): http://www.kgt.co.jp/product/avs/pvr/.

Rumbaugh, J., Blaha, M., Premerlani, W., Eddy, F. and Lorenson, W. (1991): Object-Oriented Modeling and Design. Prentice Hall.

SC04 Home page (2004): http://www.sc-conference.org/sc2004/.

Shao, X., Sitnov, M.I., Sharma, S.A., Papadopoulos, K., Goodrich, C.C., Guzdar, P.N., Milikh, G.M., Wiltberger, M.J. and Lyon, J.G. (2003): Phase transition-like behavior of magnetospheric substorms: Global MHD simulation results, J. Geophys. Res., **108** (A1), 1037, doi: 10.1029/2001JA009237.

The Earth Simulator Center (2004): http://www.es.jamstec.go.jp/esc/eng/index.html.

Tsyganenko, N.A. (2002): A model of the near magnetosphere with a dawn-dusk asymmetry 1. Mathematical structure, 2. Parameterization and fitting to observations. J. Geophys. Res., **107** (A8), doi: 10.1029/2001JA000219/220.

Watari, S., Iwamoto, I., Igarashi, K., Isogai, M. and Arakawa, Y. (2003): 3-D visualization of the IRI model. Adv. Space Res., **31** (3), 781–783.

Winglee, R.M., Kokubun, S., Lin, R.P. and Lepping, R.P. (1998): Flux rope structures in the magnetotail:

This document is provided by JAXA.

Comparison between Wind/Geotail observation and global simulations. J. Geophys. Res., 103 (A1), 135–150.

Yumoto, K. and the 210° MM Magnetic Observation Group (1996): The STEP 210° magnetic meridian network project. J. Geomagn. Geoelectr., 48, 1297–1309.

This document is provided by JAXA.

Advances in Polar Upper Atmosphere Research
NOTE TO CONTRIBUTORS

Editorial policy

Advances in Polar Upper Atmosphere Research is an annual publication from National Institute of Polar Research (NIPR) including contributed papers on the upper atmosphere physics in the polar regions as well as papers presented at the NIPR Symposium on Space and Upper Atmospheric Sciences in the Polar Regions. *Advances in Polar Upper Atmosphere Research* accepts the following categories of papers; scientific papers, research notes, review papers and reports. Scientific papers are original articles dealing with major problems related to the polar upper atmosphere physics. Research notes are short articles dealing with a significant topic, new findings, and preliminary interpretation, etc. Review papers deal with overview of researches on specific issues. Reports include scientific and technical information on the activities related to polar upper atmosphere research.

Submission of manuscripts

Authors are requested to submit, with their manuscripts, a sheet of submission to indicate the contact address, telephone and fax numbers and e-mail address, etc. In case of more than one author, please indicate to whom the correspondence should be addressed. The format of the sheet is available upon request to:

Editorial Board of Advances in Polar Upper Atmosphere Research
National Institute of Polar Research
Kaga 1-9-10, Itabashi-ku, Tokyo 173-8515, Japan
Tel: +81-3-3962-6482 Fax: +81-3-3962-6482 E-mail: editor@uap.nipr.ac.jp

Three copies of the manuscript prepared according to the **Technical details** should be submitted. Arrival date of the manuscripts to the Editorial Board is registered as the received date. Manuscript (and cover letter) can also be submitted as e-mail attachments. If you plan to submit by e-mail, please contact the editorial committee for instruction (*e.g.*, file types and sizes).

Review processes

The received scientific papers and research notes are reviewed by at least two referees. Review papers and reports are reviewed by at least one referee. Referees and the editors may request modification/revision of the papers, and the acceptance of the paper and its final category is determined by the Editorial Committee of NIPR.

Proofs

One set page proofs will be sent to the corresponding author, to be checked for typesetting/editing. The author is not allowed to make changes or corrections that constitute departures from the article in its accepted form. Proofs should be returned within 2 days.

Submission of final revised manuscript

Authors are requested to submit digital files of the text and tables as e-mail attachments together with one hard copy of the manuscript (including a complete set of figures). We accept files generated by Microsoft Word and plain ASCII text files.

Reprints

It is free of charge for submission and publication. The corresponding author can receive free 50 reprints. Additional reprints can be ordered on a reprint order form.

Acknowledgment to the referee

In your final manuscript, the authors are requested to append the following lines below the acknowledgment paragraph as "The editor thanks *** and another referee for their help in evaluating this paper."

This document is provided by JAXA.

Copyright agreement

The copyright of any published articles (hereafter referred to as papers) in the Journal belongs to the National Institute of Polar Research. Republication, translation and other uses to any extent of papers in this Journal require written permission from the Library Director, the National Institute of Polar Research and acknowledgment of the source. In exception of the above requirement, use of several figures, tables and brief excerpts from the Journal in scientific and educational publications does not require the permission from the National Institute of Polar Research provided that the source is acknowledged.

Technical details

(1) All manuscripts must be written in English.
(2) All pages of the manuscripts must be typed double spaced on one side of the A4 paper with wide margins, and assembled in the order; *title, abstract, text, acknowledgment, references, appendices, tables, figure captions* and *figures*.
(3) An abstract is within 200 words.
(4) Key words of less than five are required. (new item)
(5) Use of the International System of Units (SI) is recommended.
(6) The title page should include the category of contribution, the title, the name(s) of author(s), their affiliations and addresses. In case the title contains more than 50 letters, a running title should also be given.

References

(1) References in the text consist of the surname of the author(s), followed by the year of publication in parentheses. All references cited in the text should be given in the reference list and *vice versa*.
(2) The reference list should be in alphabetical order.
(3) References should be in the following format:

Akasofu, S.-I. and Chapman, S. (1972): Solar-Terrestrial Physics. Oxford, Clarendon Press, 100 p.

Kawahara, T.D., Gardner, C.S. and Nomura, A. (2004): Observed temperature structure of the atmosphere above Syowa Station, Antarctica (69°S, 39°E). J. Geophys. Res., **109**, D12103, doi: 10.1029/2003JD003918.

Ogawa, T., Hirasawa, T., Ejiri, M., Sato, N. Yamagishi, H., Fujii, R. and Igarashi, K. (1992): HF radar experiment at Syowa Station for the study of high-latitude ionosphere-2: A capability. Proc. NIPR Symp. Upper Atmos. Phys., **3**, 91–95.

Sato, N. and Saemundsson, Th. (1987): Conjugacy of electron auroras. Mem. Natl Inst. Polar Res., Spec. Issue, **48**, 58–71.

Urashima, A., Fujita, A. and Aso, T. (1997): A study of the reconstruction algorithm for auroral tomography by numerical simulation. Nankyoku Shiryô (Antarct. Rec.), **41**, 469–496 (in Japanese with English abstract).

Yamagishi, H., Fujita, Y., Sato, N., Nishino, M., Stauning, P., Liu, R. and Saemundsson, T. (2000): Interhemispheric conjugacy of auroral poleward expansion observed by conjugate imaging riometers at ~67° and 75°–77° invariant latitude. Adv. Polar Upper Atmos. Res., **14**, 12–33.

Tables/Figures

Each table should be typed by on a separate sheet of A4 paper and numbered according to their sequence in the text. All figures should be numbered consecutively and referred to in the text. Color figures can be accepted upon request. But the final decision rests with the editorial board.

This document is provided by JAXA.

AUTHOR INDEX

Baker, Daniel N. 84

Den, Mitsue 71

Ebihara, Yusuke 106

Fok, Mei-Ching 106
Fujita, Shigeru 84, 135
Fukuda, Akira 89

Green, James L. 135

Hayakawa, Masashi 42
He, Guojing 89
Hori, Tomoaki 1

Iizima, Masahide 10
Ishii, Mamoru 63

Jin, Li-Jun 89

Kadokura, Akira 89
Kimura, Eizen 135
Kumamoto, Atsushi 10

Maekawa, Shinko 42
Matsumoto, Hiroshi 135
Matsuoka, Daisuke 135
Moore, Thomas E. 106
Mukai, Toshifumi 1, 135
Mukumoto, Kaiji 89
Murata, Ken T. 135

Nagai, Tsugunobu 135
Nagasawa, Masashi 89
Nakano, Kei 89
Nishitani, Nozomu 55

Ogawa, Tadahiko 55
Ogawa, Tomoya 71
Ogino, Tatsuki 135
Ohichi, Satoshi 89
Okada, Masaki 135
Ono, Takayuki 10

Saka, Osuke 80, 84
Sakurai, Tohru 21
Sato, Natsuo 89
Shiokawa, Kazuo 135
Shirai, Hisato 1
Shvets, Alexandre V. 42
Sigwarth, John B. 135

Tanaka, Takashi 71, 135
Tonegawa, Yutaka 21
Tsyganenko, Nikolai A. 135

Yamagishi, Hisao 89
Yamamoto, Kazunori 135
Yamashita, Kazuyuki 71
Yang, Huigen 89
Yao, Ming Wu 89
Yoshihiro, Yasuaki 89
Yumoto, Kiyohumi 135

Zhang, Sen 89

This document is provided by JAXA.

Acknowledgments to Referees

The editorial board wishes to thank the following and anonymous referees.

Burch, J. (SWRI)
Cannon, P.S. (QinetiQ U)
Freeman, M.P. (BAS)
Hattori, K. (Chiba U)
Hosokawa, K. (UEC)
Innis, J.L. (AAD)
Kasaba, Y. (JAXA/ISAS)
Menk, F.W. (U Newcastle)
Milan, S.E. (U Leicester)
Nakagawa, T. (Tohoku Inst. Tech.)
Nickolaenko, A.P. (IRE)
Nose, M. (Kyoto U)
Ogawa, T. (Nagoya U)
Sergeev, V.A. (St.Petersburg State U)
Shiokawa, K. (Nagoya U)
Tokumaru, M. (Nagoya U)
Watanabe, M. (U Saskatchewan)
Yoshikawa, A. (Kyushu U)

The proceedings of past Symposia on Upper Atmosphere Physics were published as follows:

The 1st Symposium: Nankyoku Shiryô (Antarctic Record), **63**, 310 p., **64**, 176 p., **65**, 1-118, 1979
The 2nd Symposium: Nankyoku Shiryô (Antarctic Record), **68**, 319 p., **69**, 252 p., 1980
The 3rd Symposium: Memoirs of National Institute of Polar Research, Special Issue (Mem. Natl Inst. Polar Res., Spec. Issue), **18**, 502 p., 1981
The 4th Symposium: Mem. Natl Inst. Polar Res., Spec. Issue, **22**, 287 p., 1982
The 5th Symposium: Mem. Natl Inst. Polar Res., Spec. Issue, **26**, 201 p., 1983
The 6th Symposium: Mem. Natl Inst. Polar Res., Spec. Issue, **31**, 179 p., 1984
The 7th Symposium: Mem. Natl Inst. Polar Res., Spec. Issue, **36**, 353 p., 1985
The 8th Symposium: Mem. Natl Inst. Polar Res., Spec. Issue, **42**, 154 p., 1986
The 9th Symposium: Mem. Natl Inst. Polar Res., Spec. Issue, **47**, 224 p., 1987
The 10th Symposium: Proceedings of the NIPR Symposium on Upper Atmosphere Physics (Proc. NIPR Symp. Upper Atmos. Phys.), **1**, 214 p., 1988
The 11th Symposium: Proc. NIPR Symp. Upper Atmos. Phys., **2**, 144 p., 1989
The 12th Symposium: Proc. NIPR Symp. Upper Atmos. Phys., **3**, 108 p., 1990
The 13th Symposium: Proc. NIPR Symp. Upper Atmos. Phys., **4**, 120 p., 1991
The 14th Symposium: Proc. NIPR Symp. Upper Atmos. Phys., **5**, 80 p., 1992
The 15th Symposium: Proc. NIPR Symp. Upper Atmos. Phys.. **6**, 138 p., 1993
The 16th Symposium: Proc. NIPR Symp. Upper Atmos. Phys., **7**, 76 p., 1994
The 17th Symposium: Proc NIPR Symp. Upper Atmos. Phys., **8**, 76 p., 1995
The 18th Symposium: Proc. NIPR Symp. Upper Atmos. Phys., **9**, 86 p., 1996
The 19th Symposium: Proc. NIPR Symp. Upper Atmos. Phys., **10**, 180 p., 1997
The 20th Symposium. Proc. NIPR Symp. Upper Atmos. Phys., **11**, 170 p., 1998
The 21st Symposium: Proc. NIPR Symp. Upper Atmos. Phys., **12**, 180 p., 1998
The 22ed Symposium: Advances in Polar Upper Atmosphere Research (Adv. Polar Upper Atmos. Res.), **13**, 199 p., 1999
The 23rd Symposium: Adv. Polar Upper Atmos. Res., **14**, 243 p., 2000
The 24th Symposium: Adv. Polar Upper Atmos. Res., **15**, 203 p., 2001
The 25th Symposium: Adv. Polar Upper Atmos. Res., **16**, 195 p., 2002
The 26th Symposium: Adv. Polar Upper Atmos. Res., **17**, 179 p., 2003
The 27th Symposium: Adv. Polar Upper Atmos. Res., **18**, 151 p., 2004

Copyright 2005 by the National Institute of Polar Research,
Research Organization of Information and Systems

9-10, Kaga 1-chome, Itabashi-ku, Tokyo 173-8515

Printed by Soubun Printing Co., Ltd.

This document is provided by JAXA.

This document is provided by JAXA.